Strength and Durability of Steel to Composite Joints for Marine Application

Stephen William Boyd

Submitted for the Degree of Doctor of Philosophy
School of Engineering Sciences
University of Southampton
Southampton, UK

April 2006

UNIVERSITY OF SOUTHAMPTON

ABSTRACT

SCHOOL OF ENGINEERING SCIENCES

SHIP SCIENCE

Doctor of Philosophy

STRENGTH AND DURABILIUTY OF STEEL TO COMPOSITE JOINTS FOR MARINE APPLICATION

By Stephen William Boyd

This thesis deals with the assessment of the strength and durability of steel to composite joints for composite superstructures on ships where reduced weight is a design driver. The purpose of the work is to understand the long-term performance characteristics of hybrid connections to allow for improvements to the design of hybrid structures. Two joints were investigated in the present research. The first was a full-scale connection suitable for application in superstructures of marine vehicles, specifically a helicopter hanger on a naval vessel. The second was a generic steel/composite connection for testing performance after hygrothermal ageing.

The strength and durability of the full-scale connection were examined in compression, the loading scenario representative of in-service conditions. The results indicated that the static and fatigue performance were in excess of the realistic in-service loading conditions. Failure for both static and fatigue tests were comparable and therefore good confidence in the prediction of the joint's failure was achieved. The generic hybrid connection was artificially aged through immersion in water. The results indicated that there was no significant reduction in the performance of the joint in either static tension or bending.

The numerical modelling highlighted a number of issues. Due to the geometry of the joint high stress concentration factors were observed in some locations. It is in these areas that failure of the joint was predicted in the numerical modelling. Similar results were obtained experimentally and this gave confidence in the modelling of the joint. Numerical parametric and optimisation studies were conducted to assess the influence of the joint geometry on performance characteristics obtained from both the experimental and numerical studies. This highlighted that improvements to the performance of the joint could be obtained through geometric changes alone.

Dedication

To Hayley, the love of my life, you have made my life complete. Without your constant support, encouragement and love, I could never have completed this work. I will love you always.

To my parents, Dave and Ann, for your continuing support throughout my university career.

Contents

List of Tables

List of Illustrations

Nomenclature

CFRP	Carbon Fibre Reinforced Plastic
CSM	Chopped Strand Mat
DCB	Double Cantilever Beam
DLHC	Double Lap Hybrid Connection
FEA	Finite Element Analysis
FRP	Fibre Reinforced Plastic
GA	Genetic Algorithm
GRP	Glass Reinforced Plastic
HSC	Hybrid Structural Connection
MCMV	Mine Counter Measure Vessel
PDM	Progressive Damage Model
SRMH	Single Role Mine Hunter
TSRL	Transport Systems Research Laboratory
VMC	Von Mises Criterion
WCDF	Weibull Cumulative Density Function
UCS	Ultimate Compressive Strength
UTS	Ultimate Tensile Strength

Acknowledgments

I would like to thank the following:

My supervisors, Prof. Ajit Shenoi and Dr. James Blake for their continual guidance and encouragement throughout the course of this research.

Dr Jagath Mawella for his sponsorship of the current research and his colleagues at the UK Ministry of Defence for advice and discussions.

My colleagues past and present for informal chats and discussions on the subject of composite materials and structures, Elouan Jarry, Gleb Makarov, Narasimhan Sampathkumar, Dan Holmes, Richard Trask and others who I may have forgotten.

Dr Mingy Tan and Dr. James Blake for the development of the genetic algorithm and multi-objective function modules for the optimisation routines

The technical staff in the School of Engineering Sciences that helped sort out various problems, Dave Beckett, Erik Roszkowiak, Bob Barnes and James Chitty.

James, Dominic, Janice and anyone else who joined me in the bar for a discussion on anything but work and putting the world to right!

The people at Southampton Hockey Club for giving me something to do outside of work to relieve the pressure of completing this research, whether it be hockey, golf, an occasional quiz night or meeting my future wife.

And last, but by no means least, to me, for deciding to stick with this research through some of my darkest times, it was a battle that has been won and I am a better and stronger person for sticking with it and completing this work.

Chapter 1

Introduction

Steel has been the material of choice for the construction of large ships since the late 1800's. From the 1940's onwards welding began to replace riveting as the most common joining method. Steel is still extensively, if not exclusively, used for the construction of large transoceanic cargo carrying vessels such as oil carriers, bulk carriers and gas carriers and in the foreseeable future this is unlikely to change. The majority of naval vessels at present are constructed from steel however the use of more lightweight materials for the construction of naval platforms has been under investigation for a number of years. Aluminium became the material of most interest. However, due to its relatively low melting point and its loss of structural integrity at relatively low elevated temperatures, it is no longer used for structural applications in the Royal Navy.

Composites are a group of structural materials that are being increasingly used for the construction of ships less than 100 metres and boats due to the ease of mass production and favourable properties e.g. strength to weight ratio. In the context of this work they can be defined as the combination of fibre reinforcement in a polymer matrix. However, in general a composite can be the combination of any two or more materials which when combined provide the benefits of each of the materials and often some additional benefits. Composite materials, in the form of fibre reinforced plastic (FRP), made their mark on the marine industry by their extensive use in the pleasure craft industry. A large number of sailing and motor yachts are constructed using FRP every year. By reducing structural weight an increase in speed or payload capacity can be achieved, the former being important to the consumer in the pleasure craft industry, the latter for the commercial industry. In recent years the use of composite materials for vessels greater than 60 metres has extended the knowledge and experience in their application to alternative sectors of the marine market. For example, composite materials can now be found in the offshore oil industry and naval platforms. The Royal Navy Single Role Mine Hunters (SRMH) and the Mine Counter Measure Vessels (MCMV) are built entirely from glass reinforced polyester resin. These vessels up until recently were the largest composite vessels. The advantage of using composite materials in this application is to remove the threat of magnetic mines by having a non-metallic mine hunter. More recently, the Swedish Navy has introduced a fully composite corvette (Visby) constructed from carbon fibre reinforced epoxy sandwich and even more recently the largest composite vessel “Mirabella V” was launched, a 75m sailing yacht. For very large composite ships, longitudinal strength is an issue. This requires substantial FRP laminate thicknesses to create an efficient hull girder. Thick laminates have their own problems associated with the polymerisation of the resin being an exothermic reaction producing heat, which is exacerbated when in large volumes (i.e. thick sections).

At present, for ships over 100 m in length, steel is still the preferred material for main hull girder construction where longitudinal strength is the main design consideration. In order to take advantage of lightweight materials such as FRP composites, consideration must be given to their application in secondary structures i.e. superstructures. The construction of the superstructure block is relatively easy given the advances in FRP processing technology. The key difficulty is the connection between the FRP composite and the steel hull. Steel is joined traditionally by welding (i.e. hot work) while FRP to FRP joints in ships are usually adhesive bonds. Composite to steel connections can therefore be either bonded or bolted. Bolting is largely avoided in ships since it introduces problems of watertightness. Therefore bonded connections are the preferred option.

The hybrid joint has been developed provide the structural connection between the FRP superstructure and the steel hull. Figure 1.1 describes the advantages and disadvantage of steel versus FRP construction highlighting the possibility of a combination construction employing a hybrid connection. Areas of required research for hybrid structures are identified through the literature study in Chapter 2.

In recent times the design of new engineering structures, not solely in the marine industry, has focused on small refinements of design rather than huge technological leaps. One design refinement that is of particular interest to the marine industry is to assess the weight distribution of the structure. Structural engineers are beginning to investigate the feasibility of using a mixture of materials within a single structure to tailor the weight distribution for its particular application. In the marine industry, stability of the vessel is an important design aspect. This is especially true in naval applications, where the ship must be an efficient and stable platform from which to launch ordinance, aircraft or conduct other activities in a wide range of sea and manoeuvring conditions. In this application it is the weight distribution vertically that is of importance to the naval architect. By reducing weight aloft, the centre of gravity of the ship can be lowered and hence the roll and pitch stability characteristics of the ship can be improved. The use of a mixture of materials in the design of such naval platforms, incorporating lightweight materials, could provide significant advantages for the marine industry as a whole.

The aim of the present research is to examine the performance of hybrid connections and gain an understanding of how the load is transferred through the joint, how the stresses develop within the joint that induce failure, how failure occurs and progresses for present joint designs. Finally, based on this research of how current hybrid connections perform, a new generation of hybrid joints is proposed and their structural performance assessed. Previous studies investigating the use of hybrid connections have concentrated mainly on static strength [1-4]. The objectives of the current research are to:

- Identify the strength and durability characteristics of a hybrid structural connection (HSC), which is representative of a full-scale structural element;
- Identify the strength and fatigue characteristics of a small-scale double lap hybrid connection (DLHC) in an unaged condition and after artificial hygrothermal ageing to identify the effect if any of moisture ingress;
- Investigate possible changes to the joint design to improve the performance of the HSC through numerical studies.

The present research firstly investigates in Chapter 2 the background to the use of composites, adhesive joints and the application of steel-to-composite joints. In addition, the ageing of composite materials and the physical processes involved are outlined. Chapter 2 finally looks at the use of numerical techniques for the identification of progressive damage in structures. Chapter 2 identifies the gaps in the present knowledge of hybrid connections and the analysis of adhesively bonded joint damage progression and addresses how the present research will provide information to future structural engineers and naval architect so that improvements can be made to the design of hybrid connections.

Chapter 3 introduces the joint design philosophy, materials and manufacturing methods for hybrid connections. The thought processes for the design of the HSC and the DLHC are described. Chapter 4 outlines the experimental facilities used for the present research. There is also a clear description of the tests that will be carried out and the methods used in the data analyses. The accelerated ageing process is also outlined in this chapter. The numerical methods used in the present research are outlined in Chapter 5. This chapter aims to describe the progressive damage method, beginning with the finite element analyses (FEA), through the failure criteria that are applied to the progressive damage model (PDM) and the property degradation post-initial failure. It is hoped that the combination of these three numerical methods can be brought together to help in the development of a tool to aid in the design of hybrid connections. In addition, this chapter outlines the methods used to investigate performance improvement of the HSC joint through parametric variations and formal optimisation routines.

The results from the experimental strength and durability characterisation of the hybrid joints are presented in Chapter 6 incorporating, static axial and bending strength, fatigue performance, residual strength and the influence of hygrothermal ageing. Chapter 7 investigates the numerical simulation of the joint with respect to performance under quasi-static loading and incorporates the methods outlined in Chapter 5.

Chapter 8 investigates the effects of geometric changes to the HSC by finite element analysis. The parametric changes to the joint will be assessed with respect to a base design. In addition an optimisation technique involving genetic algorithms is used to obtain the optimal solution with respect to weight, maximum stress and global stiffness. Chapter 9 draws conclusions on the work carried out under the present research.

The knowledge obtained through the present research is vital to the naval architect who will require such information to ensure the prolonged performance of hybrid connections during their service life. The combination of experimental and numerical investigations into the strength, durability, damage progression and optimisation within the hybrid connections will aid future designs of such joints. The aim of this thesis is to provide further knowledge on hybrid joints and increase the confidence levels required to apply such jointing technology to full-scale structures in the near future.

Chapter 2

Background and literature review

2.1. INTRODUCTION

This chapter involves the examination of ship structures and their evolution which has lead to the desire to match traditional ship construction materials such as steel with more modern lightweight materials such as fibre reinforced plastic (FRP). The reasons for the application of hybrid structures to modern marine vessels are examined through the literature on the application of such structures.

The use of composite materials involves different production processes compared to traditional shipbuilding methods. Therefore the methods whereby the steel and GRP materials can be connected are an important factor in the success of hybrid structures. The methods used to connect dissimilar materials are wide and varied and the method in which the hybrid connection is manufactured will influence the performance of the joint when subjected to loads encountered onboard a marine vehicle.

It is important to understand that although the use of hybrid connections has many advantages there are design issues that must be addressed to ensure the success of the application.

2.2. EVOLUTION OF SHIP STRUCTURES

Ship structures have developed rapidly from the days when wood was the material used to construct large sailing ships for trade and naval applications. Iron and then its derivative steel, which has become the backbone of ship construction worldwide, superseded wooden construction [5]. Aluminium was introduced as a ship building material where ship operators were looking for faster and more efficient vessels. The high-speed ferry market where faster and faster crossings were required drove this construction materials usage. As the search for further gains in structural efficiency continued GRP or composite materials were the next material destined for use in marine structures

Composite materials made their first appearance in the marine industry soon after the Second World War in the construction of small personnel boats for the US navy. Pressure bags and vacuum injection were the manufacturing methods of choice at this time and were required to deal with the high pressure curing resins. With the development of low pressure, room temperature curing resins, hand lay-up became a popular manufacturing method and lead to a ‘boom’ in the use of GRP in boat construction. The success of composite materials in the small craft field can be attributed to a number of factors including [6]:

1. Competitive first cost: particularly where a number of hulls are to be built from the same design.
2. Lower labour skill level compared to the that required for traditional wooden hulls
3. Low maintenance finish to hull resulting from the seamless and leak-proof qualities of GRP.
4. Low cost of repair
5. Ability to produce complex shapes for hydrodynamic or aesthetic purposes.

Between 1955 and the 1980’s the number of boats constructed from GRP had grown from 4 to 80 percent [7, 8]. A historical view on composite materials can be found in Appendix I.

2.2.1.1 Naval applications

Between 1945 and 1965, the number of marine applications of composite materials grew rapidly. In 1951 the US Navy built a 15.5m Mine Counter Measure Vessel (MCMV) using a honeycomb sandwich structure [9]. Although this was not a success due to water absorption and poor construction quality it was the first real move away from wooden MCMV's. Other applications during this time included: 9.5m patrol boats used on the rivers during the Vietnam war; Sonar domes, fairwaters, fins and non-pressure hull casings for submarines and masts, radomes, piping, crew shelters, hatch covers and deck houses for surface war ships.

The late 1960's and early 1970's saw both the US Navy and Royal Navy producing 100 percent glass reinforced plastic MCMV's. The first being the HMS Wilton of the Royal Navy at 46.6m long and 450 tonnes full-load displacement. The success of HMS Wilton led to the rapid expansion of the use of composite materials for MCMV's and since the 1980's more than 200 all-composite MCMV's have been built, many over 50m long and 600 tonnes full-load displacement. It should be emphasised that the design of these vessels was driven by the requirement for non-metallic hull-envelopes to avoid the detonation of magnetic mines. This requirement evolved due to a reduction in expertise in the construction of wooden vessels previously used for minhunting. However, specific expertise was developed in the construction of large vessels using GRP.

One major driver towards the use of composite materials for naval (and commercial) applications is the stiffness property advantages that it provides. In steel ships large stress concentrations can be found at the corners and connections between the superstructures and the deck [6]. This can result in fatigue cracking of the deck and surrounding areas. The use of composite materials in this application can provide relief from this phenomena due to the differences in stiffness between the steel and the GRP superstructure. The reduced stiffness of the GRP reduces the stresses transferred through the deck and connection during global hull-bending. This reduces stress concentration and hence reduces the possibility of fatigue cracking of the deck.

2.2.1.2 Commercial applications

There are numerous possible applications for composite materials in the commercial marine industry. However, there are increasing restrictions to their use mainly regarding fire safety. A number of solutions to the problem of fire have been found. However, they involve insulating the composite material, which has the effect of compromising the weight advantage that composite materials afford.

2.2.1.3 Recreational applications

Probably the most active area for composite construction is in marine pleasure craft. Mass production of small, medium and relatively large sailing and motor yachts in GRP have lead to a reduction in material cost. In addition to material costs, development in construction techniques and material types has led to a reduction in labour input and turnover for each hull.

The high performance racing yacht industry is often where major development of the use of composite materials, for example composite masts were once only used in high performance racing yachts. However, in recent years the technology has matured and the confidence in their performance has allowed their application to production blue water cruisers. Yachts in the racing field usually have high material and fabrication costs as speciality material combinations and fabrication methods are employed. Combinations of carbon, aramid and glass reinforcement can often be found, bound in relatively expensive epoxy resin systems. The designs of these yachts commonly take risks beyond what is acceptable in the other marine fields. Durability is sometimes sacrificed for minimum weight in an effort to outperform the competition. Incidents such as the structural collapse and sinking of Australia's entry (AUS 35) to the 1995 America's Cup after only 21 races [10] prove that racing yachts are built to the limit of the materials in an effort to gain fractions of a knot of boat speed. This type of construction stretches the technological limits and both failure and success provide valuable spin-off technologies in design methodology and material limitations that can be applied to lower-performance composite application.

Although it has been shown that the use of composite materials for the construction of marine vehicles is an active engineering sector it should be noted that composite material application does have limitations. Large composite constructions are ideal if manufactured from a single mould, however, in some cases this is not possible. The Royal Navy mine hunter hulls are constructed from one laminate but decks and bulkheads need to be attached in a secondary process. This involves joints and can consist of a mechanical fastening, an adhesive bond or a combination of the two. Similarly, large ships greater than 100 metres have not yet been built entirely from composite materials. This is primarily due to economic reasons. In reality only a small number of vessels would be constructed in each class of ship. The construction of moulds and the quantity of materials involved would make this uneconomical. In addition there is also limited expertise in the construction of very large vessels in terms of the present manufacturing and design technology. However, the benefits that composite materials bring to an engineering structure make it an excellent candidate for construction. Understanding the design and fabrication of structural connections for the application of composite materials to weight critical areas of a vessel is vital.

In the 1980's and 1990's a number of studies were conducted on the performance of steel/composite ship superstructures under nuclear air blast conditions [11, 12]. The hybrid deckhouse consisted of GRP panels bolted to a steel internal frame system. The results suggest that under moderate blast loadings the hybrid structure will experience smaller displacements due to the rigidity of the steel frames. However, under extreme blast conditions the GRP structure is destroyed but the hybrid structure remains intact. The GRP structure is destroyed due to the excessive strains in the GRP stiffeners. However, the hybrid structure is able to plastically deform due to the ductile nature of the steel framing. Although this is an early application of composites to the production of superstructures, the work conducted does not deal with the connection of the GRP superstructure to the deck. In addition, Chalmers [13] discusses in detail the use of composite materials in marine vehicles. One application being the superstructure, again however, the subject of the connection between the steel and FRP is highlighted as an area for future research to ensure that it is durable in the marine environment and capable of withstanding fire.

2.3. STRUCTURAL CONNECTIONS

As discussed, joints are essential in the construction of large composite structures and for the application of composites in weight critical areas of traditionally constructed structures. There are two main methods of jointing used in the composite industry. Firstly there is the mechanical fastening which has been used extensively in metallic constructions and until the advent of welding was the fastening of choice. Mechanical fastenings for metallic structures can still be found extensively in the civil and aerospace industries. Metallic marine construction uses welding nearly exclusively for the construction of steel and aluminium ships. The use of mechanical fastenings for composite joints has been thoroughly investigated [14, 15]. The main disadvantages to consider with regard to mechanical fastening in composite materials are:

- Fretting of the composite materials, particularly under cyclic loading
- Fibre discontinuity caused by the drilling of holes in the laminate
- Possible micro-cracking of the laminate during the drilling process

The second process used for the jointing of composite materials, and the process which is discussed throughout the presented research, involves the adhesive bonding of the components.

In recent years the application of adhesives as a structural jointing mechanism has become more accepted within engineering design. Adhesives are being applied in industries that include aerospace, marine and automotive. Most engineering structures consist of a number of component pieces that are connected to provide a load path between components. Joints can be assembled in a variety of ways including bolting, riveting, welding or adhesive bonding. Bolted or riveted joints can only achieve a maximum tensile strength of 50 percent of the weakest adherend due to the stress concentrations located at the holes. However, adhesively bonded joints can achieve in excess of 80 percent of the tensile strength of the weakest adherend using just a simple shear joint configuration [16].

It could be said that the weakest part of any structure will be its joints, regardless of whether a mechanical fastening or adhesive bond is used. Furthermore, a weight penalty may be incurred, as the joints may require additional material to compensate for a reduction in stiffness or strength in the region of the joint.

Compared to other techniques adhesive bonding can provide economic and performance advantages [17] to the structural engineer including;

- The ability to join dissimilar materials, especially in harsh environments where, for example, dissimilar metals may cause galvanic corrosion if in direct contact. The use of adhesives provides an insulating layer between these materials;
- The ability to join thin sheet material efficiently and without distortion;
- The final product is aesthetically pleasing as there is no distortion of the joint surfaces as found with spot welding;

- Reduced cost due to relatively unskilled labour input. The adhesive dispensing process can be fully automated insuring repeatability;
- Flexibility of design allows novel joint concepts to be used with a wider range of materials.

However, as with any engineering process there are some disadvantages [17] including;

- Time involved in achieving 100 percent joint strength, especially if cold cure adhesives are used;
- Long term extreme load durability is relatively undocumented;
- Designing of the jointed area is intensive and may require optimisation for each load condition;
- There is a limit to the upper service temperature of adhesives and this is dependant on the adhesive used;
- Non-destructive evaluation of joints is limited in comparison to alternative mechanical jointing techniques.
- Poor performance under dynamic loading such as blast

There are a large number of studies in the literature which discuss the use of adhesive joints for applications where the bond is made between similar and dissimilar materials. The advantages discussed above refer to the non-distortive nature of adhesive joints. This is particularly advantageous when bonding thin metallic sheets such as those found in the aerospace industry. Welding of such thin plates can lead to substantial distortions which may require remedial work, which is both time consuming and labour intensive. The application of adhesive bonding of thin plates removes the distortions due to heat and hence expensive remedial work [18].

In structures that contain weight critical components there is often a desire to use dissimilar metallic materials to achieve a specific weight characteristic. One common combination specifically in the cruise liner industry is aluminium superstructures or upper decks attached to a mild steel main hull envelope [19]. The use of an adhesive bond provides not only the joint but also the insulation between the two materials, which when in contact can result in an electrolytic reaction causing corrosion of one or both metals.

One of the most obvious applications of adhesive bonding is in the connection between non-metallic, non-weldable materials, such as FRP. There has been extensive research into the design of adhesive joints for use in the composite industry [20-25].

2.3.1 HYBRID CONNECTIONS

Metal-to-composite joints are most readily found in the aerospace industry for the attachment of lightweight composite components to metallic sub-structures. Initially, the use of the metal-to-composite joint was restricted to composite repair patches for metallic structures.

A number of research programmes have investigated the use of such patches in terms of fatigue life and compared them to traditional riveted/bolted aluminium patches. Ong and Shen [26] investigated the patch repair of aluminium honeycomb panels using carbon and boron reinforced patches. The aim of the work was to demonstrate that the use of a composite patch would provide superior fatigue characteristics than a more standard riveted aluminium patch. It was found that the fatigue life was increased three fold. Tay et al. [27], also investigated the use of boron reinforced patches for cracks near holes in aluminium structures. This research also found an increased fatigue life and reduced rate of crack growth using composite patches rather than more traditional aluminium patches. Naboulsi and Mall [28] characterised crack growth rate in aluminium panels with bonded composite patches. And developed a numerical tool for either predicting the fatigue life of a composite patch, or alternatively, for designing a patch repair for extended fatigue life.

The use of metal-to-composite connections began expanding into other industrial sectors and as the use of composites as a structural material became more accepted, increased applications were being found.

In composite structures it is often required that a connection to a metallic component is a feasible application. Therefore, integration of any composite components with the rest of the structure is a critical part of the design process. Sasdelli et al. [29] investigated the use of metallic inserts in composite materials for attachment purposes. Resin transfer moulded (RTM) parts containing metallic inserts for connection showed comparable or superior mechanical performance compared to current steel parts. In addition to the mechanical performance, it was found that the use of composites reduced part weight. However, a number of issues were highlighted for further work prior to full acceptance of such component parts, including performance during and after environmental exposure and long-term performance.

The use of joints between metals and composites has expanded to provide substantial proportions of some structures to be made from composite materials. One reason for this move is an effort to reduce overall weight. One such application is the manufacture of composite outer shell structures for train carriages. Shin et al. [30] investigated adhesively bonded lap-joints for composite-steel shell structures for high-speed trains. The use of composites in such applications aids the demand for increased speeds. This research investigated the joint between the upper composite car body and the steel chassis. The joints used were lap joints of both single and double configuration. The joints were loaded to represent an internal pressure force within the carriage. This simulated the train passing through a tunnel at high-speed. It was found that a single-lap joint with the composite as the inner lap produced the best results. However, this research investigated only the joint strength in terms of a pressure vessel and did not include global bending or twisting of the carriage.

The majority of research carried out on metal-to-composite connections has been on secondary process joints. This involves the manufacture of a composite structure and subsequent adhesive bonding to the metallic structure. There is increasing interest in producing joints by the co-curing method. This is similar to placing inserts into composite materials [29]. Co-curing involves the making of the joint while consolidating the composite material. The adhesive used in the joint is excess resin from the consolidation. Instead of the secondary process being the adhesive bonding, the joint is made using traditional and well-established welding techniques to attach the hybrid component to a metallic structure. Shin and Lee [31] investigated the tensile load bearing capacity of co-cured double lap joints using steel and pre-preg carbon fibre reinforced epoxy components to be joined (adherends). Pre-preg carbon is a composite material, which in its uncured state consists of the fibres being pre-impregnated with resin. The material is then heated under vacuum to consolidate the laminate. The resulting composite material is of high quality with high fibre volume fraction, which will increase the Young's modulus.

The use of metal-to-composite joints has extended into the marine field as a novel method of incorporating lightweight GRP superstructures to steel hulls. The advantages of using such technology are most apparent in naval vessels. Warships are required to function in a wide variety of sea states. Even in the worst sea states they are expected to operate effectively as platforms for numerous instruments and weapons. For this reason seakeeping is an important aspect in the design of a warship hull. One way of improving seakeeping ability is to reduce the vessel's centre of gravity without increasing vessel weight. Structures such as masts, superstructures and even internal non-strength decks and bulkheads can contribute to weight aloft. Replacement of such structures using composite materials could provide substantial savings in weight and increase seakeeping ability and vessel stability.

Hildebrand and Hentinen [32] investigated solutions to joints between large FRP-sandwich and metal structures. Four joints are considered in this work, but the most relevant with respect to the presented research and most thoroughly discussed is the over-laminated joint (Figure 2.1). This consists of an aluminium or steel section that is laminated into an FRP-sandwich panel. Experimental static compression and bending tests were carried out in addition to numerical analyses. The static strength was found to be adequate compared to the strength of the sandwich panel. All four joint concepts were deemed to be feasible. The composite panels, with associated metallic inserts, would be welded to the steel deck. Problems associated with heating during the welding process could be avoided by locating the adhesive bond a reasonable distance from the weld. The comparison of a bolted joint with the overlaminated joint highlighted the bonded joint as being superior in terms of static strength but also in terms of cost during joining by as much as 50%.

Le Lan et al. [33] also investigated joints between sandwich panels and metal structures. Their application was the connection between a warship's steel hull and sandwich composite superstructure components. Two possible assemblies were considered: internal non-load bearing structures and external load bearing structures. The internal solution was to use a bolted connection but the external connection was a co-cured joint where a steel insert was located in a FRP sandwich. A number of mechanical, functional, industrial and economic criteria were expected of the new joint design. Static, fatigue, thermal ageing and blast tests were carried out and the joint was found to perform well. However, details of the test results are not presented in this reference. At the time of publishing two complete superstructure assemblies had been built and a third was under construction. It was found that the manufacturing of the composite structure was more expensive than a metal alternative, but in terms of through life cost and the technological advantage, the composite superstructure was more beneficial than metal.

Wright et al. [34] investigated FRP-steel connections for structural transverse bulkheads in ship structures. In contrast to the joint configuration used by Le Lan et al. [33] the joint configuration in this work bonded the steel to the laminate and is described as an optimised 'tuning fork' connection. The 83m VT-designed corvette was used to examine the feasibility of using large FRP sandwich panels as major bulkheads. Three bulkheads were chosen for the investigation, a collision bulkhead and two bulkheads bounding the machinery space near amidships. The composite bulkheads were designed to satisfy the same criteria as their metallic counterparts. Finite element analysis was used to assess the composite bulkhead performance and it was found that 8 mm skins on a 50 mm balsawood core would satisfy the design criteria. Static and fatigue tests were carried out on the 'tuning fork' joint and it was found that satisfactory connections could be designed to ensure structural integrity. Numerical strength predictions were in good agreement with the experimental results and indicated that relatively simple maximum shear stress failure criteria can be used for strength prediction of the joint.

Clifford et al. [2] also investigated a steel-to-composite joint for structural connections between a steel hull and a composite superstructure. The geometry of the specimens were similar to that of Le Lan et al. [33] and were tested as cantilever beams with a point load applied to the composite end of the joint. Two approaches were taken to improve the design of the original joint by altering the termination position of the steel and by changing the material used at the steel/sandwich core interface. Extensive numerical modelling was carried out using a fracture mechanics approach. Experimental values of interfacial fracture toughness were obtained from four-point bend delamination tests. The base design exhibited a sudden loss in stiffness under flexural loading. However, the relatively simple modifications provided a significant increase in performance. The properties of the steel/FRP interface were found to be critical in the performance of co-cured joints.

The available literature previously described shows that there is some research being carried out on the use of metal-to-composite joints, but the volume of reseach available on these joints is far from significant. Further areas need to be addressed before such joints can be fully recognised. Two such areas of research that should be addressed before complete acceptance to full-scale manufacture are:

- fatigue life characterisation,
- durability of steel/GRP bond after environmental ageing.

These two topics are essential in deciding the suitability of hybrid connections for application in the marine environment.

2.4. SHORT-TERM LIMIT STATE – DAMAGE

The analysis of adhesive joints has been on going for a large number of years and has become a highly complex task with the advent of orthotropic adherend materials and developments in adhesive technology. In general the most studied joint is the single lap joint. The main reasons for this are its simplicity and it being the basis for many joint designs employed in practise. Perhaps the most obvious place to begin is with closed-form solutions developed to analyse adhesive joint stresses and stress concentrations in single lap joints.

Volkerson [35] was the first person to study the stresses arising from the differential straining of the adherends in the bonded single lap joint. This must be accounted for as the adhesive is not subjected to a uniform shear strain, as would occur if the adherends were rigid and were not subjected to strain themselves. Volkerson's analysis assumes that the adhesive deforms in shear while the adherend only deforms in tension. However, two important factors are excluded from this analysis. In a single lap joint the applied forces will not be co-linear if applied to the central axis of the adherends. This subjects the joint to a bending moment in addition to the axial force. In addition, the bending moment will cause the joint to rotate due to the axial force. This leads to a geometrically non-linear problem.

Goland and Reissner [36] took account of the bending moment in the joint caused by the eccentric loading by including a bending moment factor and a rotation factor. These two factors are not independent of each other but the bending moment factor is regarded as the dominant term. The bending moment factor depends on the geometry of the joint, the elastic properties of the adherends and the stress on the adherends. For an undeformed adherend the bending moment factor is equal to one and as the joint bends under axial load it tends towards zero. However, it rarely goes below approximately 0.35. Goland and Reissner [36] considered two cases, firstly where the adhesive layer is thin and is of similar elastic properties to the adherends and secondly where the elastic properties of the adhesive are considerably different than the adherend. In the first case it was found that the tensile (tearing) stress, σ_{yy}, is very high at the edge of the joint and all stresses decrease with increasing bending (decreasing *k*). In the second case it was found the tensile (tearing) stress is present however the shear stress concentration is twice as high as that obtained from Volkerson's analysis [35].

These classical works were limited due to the peel and shear stress being assumed constant through the thickness of the adhesive. In addition the shear stress was assumed to be at a maximum at the end of the adhesive overlap. However, due to the end face of the adhesive being a free surface there can be no shear stress on it and thus, the law of complementary shears states that the shear stress at the joint end must be zero.

Allman [37] presented a solution which resulted in the correct zero shear stress at the ends of the adhesive joint, and a formulation for the peel stress distribution along the adhesive overlap. The Allman solution uses the Golland and Reissner [36] term, *k*, for the rotation of the joint due to eccentric loading. For flexible adherends or high applied loads this term approaches a value of 0.26, conversely for stiff adherends or low applied loads the value of *k* approaches 1.0. For typical single lap joints with isotropic materials a value for *k* of 0.35 is suitable.

The majority of analyses consider the adhesives and the adherend behaving elastically. However, most modern adhesives usually exhibit an elastic-plastic behaviour. Hart-Smith [17] used closed-form solutions, incorporating iterative solutions for more complicated joints. It was shown that the inclusion of the plastic behaviour of the adhesives when loaded in shear reduced the shear stress concentrations substantially, however the tensile (tearing) stress, σ_{yy}, was still significant. Hart-Smiths [17] work concentrated on GRP and carbon fibre reinforced plastic (CFRP) adherends and due to the low inter-laminar strength of such adherends it was recommended that primary structures should not be joined with single lap joints unless attached to a moment resistant support to resist the effects of the eccentric loading.

The above analyses concentrate on closed-form solutions. However, with the advent of more affordable computing power, the use of more complex analysis tools have become more dominant in this field. Finite Element Analysis (FEA) is now the tool of choice for the analysis not just of adhesive joints but of any structure subjected to loading, whether thermal or structural. The extent of literature regarding the FEA of adhesive joints and composite materials is vast and will not be covered here. However, the current research does use specific FEA tools which will be reviewed later in this chapter.

A large number of studies into the progressive damage modelling of composites can be found in the literature. The majority of these are associated with in-plane loading of composite laminates with particular interest in defects such as notches and holes.

One possible reason for the large number of studies into damage progression modelling of composite laminates containing holes is the use of mechanical fastenings. Mechanical fastening of composite materials is commonly undertaken as a ‘belt and braces’ approach to the connection of components. The addition of a bolt or other similar fastening can serve as a redundant means to prevent structural collapse. However, it is well known that a hole in metallic structures results in stress concentrations around the hole. This is exaggerated in composite materials as holes result in fibre discontinuity and it is the fibres which carry the majority of the load. Due to fibre discontinuity at the hole, the load is transferred from the discontinuous fibres to the continuous fibres adjacent to the holes. This results in further stressing of the surrounding composite material. There are a large number of experimental studies looking at the effect of stacking sequence, geometric properties and lateral clamping pressure across the mechanically fastened joint between composite components [38-41].

Camanho and Matthews [14] describe a large number of investigations into predicting damage propagation prior to laminate failure in mechanically fastened joints in FRP. Some of these are described here.

Chang and Lessard [42] investigated laminated composite plates containing holes subjected to only in-plane compressive loads. As this study was only interested in the in-plane compression failure of the laminate, geometric buckling or out of plane deformations were not considered. This assumption allows the reduction of the problem to that of two-dimensional plane stress. Four failure modes are used in this study:

1. matrix tensile cracking,

2. matrix compression,
3. fibre-matrix shearing,
4. fibre Buckling.

However, these failure modes were developed for use with unidirectionaly reinforced composites. Chang and Lessard [42] extended the failure criteria used by Chang and Chang [43] to include the fibre buckling and fibre-matrix shearing failures. The failure criteria used by Chang and Chang [43] was based on the work by Hashin [44]. No out-of-plane failure criteria, i.e. delamination failure, were included in this analysis. The effects of ply orientation, ply clustering and geometry on the strength and response of laminated composite plates containing a hole were also studied. Good agreement between the numerical and experimental work was observed.

Dano *et al.* [15] investigated the effect of including all the essential mechanical aspects of mechanically fastened joints, namely a full contact finite element model that includes friction and bolt clearance, non-linear shear behaviour, large deformation theory and property degradation. The paper concentrates on the influence of failure criteria and the inclusion of both geometric and shear non-linearities.

Gamble *et al.* [45] investigated the growth of damage in carbon fibre composite materials. The method involved constructing a finite element model of the specimen or component. The material properties for each ply and any known defects were defined. The load was added incrementally and stresses and strains calculated. The model was examined for areas of damage and if found suitable material property degradation was applied. Two damage criteria are discussed in this study, stress-based and strain-based. The stress-based criterion used was a modified Hill criterion [46].

All of the above references describe the damage propagation modelling of composite materials subjected to in-plane loading. In comparison there have been relatively few studies that have looked at the damage propagation prediction of composite laminates subjected to out-of-plane loading. Some of the few investigations are discussed below.

Kim et al. [47] investigated progressive failure of laminated beams using a beam finite element with Layer-wise Constant Shear (BLCS). This finite element allows the accurate computation of the stresses within each layer. A linear elastic behaviour is assumed and any damaged layer in the system is replaced with a degraded homogeneous layer. Maximum stress and Tsai-Wu failure criteria are used. Degradation factors are used to alter the stiffness of the elements once failure has occurred. A parametric study on the effects of various degradation factors was carried out and provides guidelines for their appropriate selection. Good correlation between experiment and predicted results was found for two distinct beams, a graphite/epoxy and a glulam reinforced with GRP.

Padhi et al. [48] investigated the ultimate collapse of laminated composite panels under transverse loading. A number of commonly used failure criteria such as Tsai-Wu and Tsai-Hill are used to predict failure mechanisms. The analysis is non-linear in that the material properties are degraded with the onset of damage and the model is geometrically non-linear to account for the large deformations present with such a loading regime. It was found that the predictions correlated well with experimental data for panels of differing aspect ratios.

The literature reviewed thus far has concentrated on the analysis and prediction of failure within the composite laminate by testing the laminate itself. It is appropriate at this stage to extend this review to include realistic structures such as joints between composite laminates. There are relatively few such studies in the literature, one of which is by Minnetyan and Chamis [49]. They investigated the progressive damage of a composite double lap joint and composite stiffened panel. In both studies the behaviour of the adhesive and the laminate were tracked separately. The adhesive layer is described as a single ply layer with zero fibre content. The finite element program defines the layers of adhesive and laminate separately and uses tying equations to ensure continuity of surface displacements between two contacting layers. If any location within the adhesive layer fails the corresponding node and tying equation are eliminated. The double lap joint was tested with two adhesive thickness', one corresponding to one ply layer (0.132 mm) and one corresponding to two ply thickness' (0.264 mm). The work concluded that the use of established composite mechanics and finite element modules to assess and track damage initiation and growth can be used to predict the influence of adhesive thickness on the durability of adhesively bonded composite structures. It was found that the double lap joint durability was not sensitive to adhesive thickness when loaded in tension. However, in compression the thicker adhesive delays the damage progression.

Feih *et al.* [50] use FEA analysis, appropriate failure criteria and material property degradation models to investigate the damage evolution of CFRP peel joints. This work uses the Hashin failure criteria for the composite material. For the adhesive, failure is assumed to occur when the maximum tensile strain is reached. In the experiment, initial failure occurs in the adhesive fillet propagating into the first ply. Numerically however, the initial failure occurs in the first ply with failure occurring in the adhesive fillet at a larger displacement. This may occur due to an underestimate of the adhesive failure criteria. As was mentioned, only the maximum tensile strain is considered. This is essentially a non-interactive failure criterion. By employing an interactive criterion, failure could be predicted in the position observed in experiment due to the combination of tensile and shear strains.

Feih *et al.* [51] examine the effects of different material degradation models on the progressive failure of an isotropic plate with a drilled hole. The degradation applied was to reduce the Young's modulus by 20 percent after Von Mises yielding criteria. Four methods of applying the degradation were studied:

Method 1:	Stabilised integration point degradation
Method 2:	Stabilised homogeneous element degradation
Method 3:	One-by-one integration point degradation
Method 4:	One-by-one homogenous element degradation

Method 1 is the simplest of the 4 methods. The material properties are degraded locally at the integration points. This method does have a problem with regard to 'healing' effects. This effect occurs if the integration point information is stored in an array that is only updated after each load increment. Within each load increment there may be a number of equilibrium iterations. Convergence of the equilibrium iterations relies on the failed integration points remaining failed until equilibrium is reached. This phenomena is seen as a 'jumping' effect where integration points exhibit alternating failure within an element in subsequent iterations. Storing the current integration point states for each equilibrium iteration and using this to update the increment integration point array once convergence has been achieved can avoid the 'jumping' or 'healing' effect.

Method 2 also avoids the jumping or healing effect by degrading the element properties by reducing the integration point properties simultaneously. The average of the integration point values indicates failure. However, a current element damage array is required to prevent healing of previously failed elements.

By using either method 1 or 2 the result shows a degree of increment-size dependency. If the number of increments used to solve the problem is changed the prediction of damage may also differ. It was found that this effect had a greater impact when high mesh densities were used. It was found that by minimising the failure to one element per iteration of every load increment a more stable failure path is achieved. However, this can only be applied to the first iteration of each load step as this criteria requires knowledge of the iteration number. This may lead to more than one element failure occurring in iterations subsequent to the first.

Methods 3 and 4 avoid this problem by only allowing one integration point/element to fail per iteration. The failure values for the model are stored in an array and only the integration point/element with the largest value is deemed to have failed. Increment reduction is therefore no longer necessary, as these methods are completely stable.

2.5. LONG TERM PERFORMANCE – FATIGUE AND AGEING

The ageing of composite materials is an area of research that is generating a growing interest. Due to the performance advantages of FRP they are gaining wider use in both commercial and military applications. As the technology behind composite construction and processing increases and application becomes more wide spread, the material performance challenges increase correspondingly. One such challenge is the performance of composite materials after exposure to high temperature and moisture content environments, the marine industry being one such environment. For a small craft the water temperature can range from extremes of cold to relatively warm dependant on global location. In addition, saltwater spray, ballast tanks, wastewater tanks and bilge water on larger craft can all contribute to the environmental ageing process.

Ageing of composite materials can be said to occur in two forms;

1. Chemical: This is non-reversible ageing. Chemical changes occur within the composite matrix due to exposure to a humid environment, elevated temperature and stress. Changes can include continued curing of the resin (polymerisation),

hydrolysis of the resin, internal stress induced by water absorption causing fibre/matrix bond rupture.

2. Physical: This is a reversible process; by heating the material above its glass transition temperature the thermodynamic equilibrium is restored. The water molecules are removed from the resin matrix by this process.

In general the absorption of water into the matrix material causes the material to swell. This increases the distance between the chains of polymeric molecules, reducing the bonding forces within the structure resulting in a softer more ductile polymer matrix [52].

Moisture can be absorbed into a polymeric material via a number of channels either along the polymer chains or between the polymer chains [53]. The former method results in a more rapid ingress of moisture as less energy is required for the water molecules to penetrate the material. An analytical model can in most cases, describe the rate at which moisture is absorbed by a polymer. The rate of absorption is initially high; there is a slowing of the absorption rate as the saturation point is reached.

The application of the standard equations to moisture diffusion is clearly defined by Shen and Springer [54] where the expressions for the moisture distribution and moisture content as a function of time in both one dimensional homogeneous and composite materials exposed to humid air or water are presented. Test procedures are described for determining experimental values of moisture content and the diffusivity of composite materials. The experimental data is used to validate the numerical predictions of moisture content and distribution.

Kotsikos et al. [55] used diffusion coefficients for isophthalic polyester resin to model the degradation of mechanical material properties after ageing in water at elevated temperature. The work concluded that the material properties were adversely affected by the exposure. NMR imaging analysis highlighted that water penetrates through the fibre/resin interface. The concentration of water at the interface of the fibre and the resins was three times that of the bulk resin. Water appears to penetrate the polyester resin much further than predicted by Fick’s law via a combination of diffusion and wicking along the fibre reinforcement interface.

Springer [56] provides a comprehensive review of the literature regarding the effects on the performance of epoxy matrix composite materials. The study includes subjects such as absorption and desorption characteristics of single and multi-layered composite materials under steady and transient ambients. In addition, the author also looked at literature relating to the changes on mechanical performance. It was found, for example, that moisture content had a negligible effect on the tensile strength of laminates of 0-degree or 45-degree plies, however, there was a considerable loss (between 60-90 percent) of tensile strength in 90-degree laminates. A similar trend is true of elastic modulus of the laminates examined. One likely explanation is the tensile strength of the 90-degree laminates is dependent on the performance of the resin whereas the 45 and 0-degree laminates are more fibre dependent. Since the study in Ref. [56], further knowledge has been gained on the effect of moisture on the resin properties and would explain the considerable loss in mechanical properties of the 90-degree laminates.

Literature post-1979 extends the knowledge of the effects of moisture in a number of subject areas including material properties, the influence of new resin/fibre systems, modelling of moisture diffusion and detection of moisture.

Vauthier et al. [57] investigated the effect of hygrothermal ageing on glass-epoxy composite on fatigue performance. Two means of assessment were chosen, firstly by physio-chemical changes induced by water absorption and secondly, a mechanical approach coupling the effects between environment and fatigue. Damage mapping was carried out microscopically to relate the changes in fatigue properties to the distribution of fibre strength after ageing. The specimens were immersed in distilled water at 60°C for approximately 1 year.

Static tests were carried out in a three point bending configuration at 2 mm/min and the tensile surface scanned for fibre breakage using a microscope attached to a camera at each strain step. Fatigue tests were also carried out in the three-point bend configuration, a failure criterion of a ten percent loss in stiffness was selected, as final breakage is not usually observed in bend tests. The ten percent failure criterion suggested was selected to given favourable test duration. A larger value could have been chosen but would have only influenced the time required to complete each test and not the validity of the results.

It was found that the hygrothermal ageing substantially reduced the endurance properties of the composite during fatigue loading. This was related to a decrease in fibre strength. It was found that the increased pH levels especially at the matrix/fibre interface probably caused the decrease in endurance. It was implied that the pH increase might be due to the leaching of the unreacted curing agent remaining within the composite.

2.5.1 AGEING IN BONDED STRUCTURES

Although the diffusion in composites is an integral part of the current research the experimental specimens developed consist of an adhesively bonded joint. The process of diffusion into bonded structures can be said to be more complex than with bulk materials as there are an increased number of locations for moisture absorption. In a joint between two steel substrates, for example, there are two possible routes for moisture ingress – firstly through the adhesive material itself and secondly through the interface between the adhesive and the substrate. By introducing a semi-permeable substrate, such as composite material, a third ingress path through the substrate must be considered.

2.5.2 ACCELERATED AGEING

Ageing of composite structures is a long and time-consuming job if carried out at service temperatures and humidity. In reality, this method of ageing is unacceptable. In order to speed up the ageing process a number of accelerated ageing procedures have been developed. The most commonly found methods are, high humidity air, immersion in liquid and thermal ageing. Standard humidity ageing processes are usually carried out at constant humidity associated with the required moisture concentration. This reduces the ageing time considerably from thousands of days to hundreds of days. Determining when full moisture saturation of the composite occurs depends on a large number of factors including the diffusion coefficient of the material being aged and the ageing conditions. With prior knowledge of the diffusion coefficient and the conditions that the structure is being subjected to, a prediction of the saturation point can be approximated. The saturation point can also be determined experimentally by observing the moisture up-take of the composite during the ageing process. Saturation can be said to occur when the material absorbs no further moisture.

Criscioli et al. [58] investigated ways of further reducing the ageing process for composite materials. The method involves exposing the specimen to 100 percent humidity for a period of time, t_c. After this time the humidity is reduced to a value corresponding to the required moisture concentration and is achieved at time, t_t. The problem lies in the selection of the change-over time t_c and must be chosen so that the moisture concentration is correct at every point within the structure and the desired moisture concentration is obtained in the shortest possible time, t_t. Equations for the calculation of t_c are derived. Solution of the equations is carried out using specialised software however the equations are summarised using dimensionless parameters. A sample problem was analysed and a value of change over temperature t_c was found. The results were verified with experimental coupons. In addition, the coupons were also subjected to normal ageing conditions. The mechanical properties of the coupons using both ageing processes were compared and it was found that both processes produced similar properties. This sample problem showed that the new ageing method produced aged specimens in a considerably shorter time (approximately 21 percent faster).

2.6. DESIGN OPTIMISATION

With the development of new materials, such as FRP, for the construction of ship structures, the requirement for structural connections for the construction of large vessels regardless of the material being used and the emphasis on short term and long term behaviour characterisation of structures for use in the marine industry has placed a high level of importance on efficient design. In the context of the present research efficient design is defined as the most efficient solution to meet the design requirements, for example low resistance for hull-form design or maximum pay load capacity for a given displacement. The present research concentrates on detailed design rather than global design issues. However, the methods of optimisation for both global and detailed design problems are the same.

Optimisation methods come in many forms, however the choice of method depends greatly on the problem being optimised. Secant or Newton-Raphson methods [59] are efficient ways of finding minimum or maximum values of a one-dimensional function and hill-climbing methods can be used to find minimum or maximum values of multi-dimensional problem. However, engineering design problems such as joint design or hull-form design often consist of large discrete, non-linear and often discontinuous design spaces. In this case more complex optimisation techniques such as evolutionary algorithms can be applied. This method of optimisation is based on the traditional Darwinian theory of “survival of the fittest” found in nature. Competition in nature for finite resources results in the fittest individuals dominating over the weaker ones.

Genetic algorithms (GAs) form one of the evolutionary optimisation techniques and is inspired by natural selection and genetics. The method is very general and is capable of being applied to a wide variety of problems. However, its use in the optimisation of engineering problems is not as widespread as one may expect. The use of genetic algorithms began in the 1960’s by John Holland on the subject of cellular automation. This is a discrete model studied in mathematics and theoretical biology and consists of an infinite, regular grid of cells (similar to a page of graph paper). A typical example is that each cell can have two possible states, black and white, and has 8 neighbours (those cells touching it) therefore there are 512 possible patterns for the cell and its neighbours. The most common reference to cellular automaton is the “game of life” invented by John Horton Conway. Games such as this form the building blocks for what is now called genetic algorithms. Fogel [60] describes simulated evolutionary optimisation in terms of genetic algorithms, evolution strategies and evolutionary programming and provides a detailed review of simulated evolutionary techniques and identifies that it will form an important method of solution to real world problems but its advancement will come from “careful observation and abstraction of the natural process of evolution”.

Four main steps can be used to define evolutionary optimisation methods:

1. A number or population of guesses of the solution to the problem;
2. A way of judging the quality of each individual in the population;
3. A method of mixing the fragments of the better solutions to form a new population;
4. A mutation operator to ensure diversity of the population.

The question remains why use a genetic algorithm to solve a particular problem rather than more traditional methods? One of the most common reasons is that an exhaustive search of the problem may require calculations that may take many years to complete. In this case there is good reason to use GAs as a method of efficiently searching a large problem. There are relatively few examples in the literature of the use of GAs to solve particular design problems.

Day and Doctors [61], used evolutionary algorithms to assess the hydrodynamic performance of ship hull forms. The hull forms are described by a fixed number of variables based on mathematical curves. The variables are given a number of limitations to ensure realistic hull forms are created. The variables are then chosen at random to generate an initial population. Hydrodynamic resistance prediction based on the Michell integral [62] was used to assess each individual of the population. Selection was based on minimum resistance and "breeding" was carried out using crossover and mutations to create the new generation. The work showed that the use of GAs provided a robust and rapid first principles technique to assess the design space for minimum resistance hull forms.

Genetic algorithms were used along with a gradient method which used a truncated Newton algorithm [63] and a direct search approach to investigate two problems, a two-dimensional diffuser and a drag minimisation problem of a fixed area body in flow which can be defined by two and four variables respectively [64]. For the diffuser the goal was to maximise the static pressure recovery coefficient and for the drag minimisation the goal was minimum drag coefficient. In both tests it was found that the more traditional direct approaches of Newton and the direct search produced results in fewer evaluations than with GAs. However, it is agreed by the authors that the GA would be more suited to a large problem that contained a number of local optima in the design space. Neither of the problems examined in this work contained local optima. This is highlighted by the better optimum solution found in the higher dimensional problem of drag minimisation by the GA.

A number of other investigations have utilised genetic algorithms for the design of various engineering structures including, minimum weight design of composite plates and stiffened panels [65], Design of steel structures in tall buildings [66] and design for operation of large container ships [67]. These references are specifically concerned with design. However, their application is to a very large component, i.e. a building, ship or entire system. In the present research the genetic algorithm will be applied to the design of a specific component of the system, the joint between the hangar and deck of a naval vessel.

2.7. DISCUSSION

Table 2.1 shows a table of references associated with the present research. The squares shaded in grey indicate the subject areas to be examined in this thesis. Cells that do not contain any references highlight subject areas that either do not have published information or not covered by the present literature review. Figure 2.1 shows that overall there has been relatively little research conducted on hybrid connections experimentally. One area of high importance is the fatigue life characterisation of the joint between the composite material and the steel. The literature also highlighted that there are few references on the numerical simulation of hybrid joints either involving stress analysis or optimisation of joint design. These two areas either combined or individually would provide the structural engineer with valuable information for the effective design of hybrid connections. In addition, although hygrothermal ageing of composite materials is a relatively mature subject, the influence of the moisture environment on the performance of the composite-steel interface is not well documented.

The literature has shown that there is a move away from traditional materials for marine constructions and this is particularly obvious in the recreational industry where only the largest of luxury sail and motor yachts are being constructed in steel and aluminium. In addition, advanced materials such as FRP are being used in larger marine vehicles. This increases the requirement for structural connections between components. In addition to large marine structures that are built entirely of composite materials, there is an increasing demand for lightweight components on large steel structures. This has resulted in the desire to use hybrid steel-to-composite connections. Although it has been shown that there are a number of existing applications of this jointing technique, there is little known about the long-term behaviour of such connections particularly under fatigue and hygrothermally aged conditions. In addition, the design of components and connections between components incorporating advanced materials is based somewhat on equivalence to traditional materials, with slight modifications to incorporate the advanced material. However, the joints are not necessarily designed efficiently for purpose. Evolutionary optimisation techniques have been shown to be applicable to large and some component design problems but their usage is not widespread.

Based on the literature reviewed in this chapter the strength and durability of metal-to-composite joints is a subject that needs to be addressed to better understand the mechanisms involved in their performance and ultimately failure. The present research will address this initially through experimental evaluation of static and fatigue performance under axial and bending loads. This will complement some previous research areas where similar work has already been highlighted in Table 2.1. However, the understanding of the performance of the hybrid connection in the marine environment is important to the successful design of such structural connections. This will be addressed through axial and bending tests on aged structures and provide information previously not covered in the literature to the designer. In addition, progressive damage modelling will be applied to the hybrid joint under static loading in an attempt to understand the way in which failure occurs in hybrid connections. The design of hybrid structural connections is also an important factor in the efficient design of advanced marine vehicles and this will be addressed by undertaking a parametric study of joint design variables and formal optimisation using genetic algorithms. The latter three subject areas, i.e. hygrothermal ageing, progressive damage modelling and optimisation will be addressed in the present thesis and provide a reference to fill some of the blank grey cells in Table 2.1.

Table 2.1 Reference matrix

	Progressive Damage	Lap Joints	3-D connections	Hybrid Connections	Marine Structures
Static Axial loading	[49]		[34]	[29-31, 34, 68]	[34]
Static Bending	[48]		[1, 2, 69]	[1, 2]	[2, 18, 69, 70]
Fatigue Testing			[34]	[28, 34]	[34]
Numerical Modelling			[2, 34]	[2, 30, 34, 71]	[2, 34]
Progressive Damage	[14, 38-41]		[49, 69]		[69, 70]
Optimisation					[61, 67, 72]
Hygrothermal Ageing		[73]	[73, 74]		[53]
Hybrid Connections				[29, 68]	[19, 33]

Chapter 3

Materials and manufacturing

3.1. INTRODUCTION

The aim of this chapter is to introduce the philosophy behind the use of a hybrid joint and define the materials and the manufacturing methods employed in the present research. The La Fayette class frigates of the French Navy incorporate a composite helicopter hanger attached to the steel hull using a hybrid connection (see Figure 3.1). The present research uses this joint described by Le Lan et al. [33] as the concept or base design. Figure 3.1 shows schematically how such a joint could be applied to the hanger structure. The base design for the present research was agreed upon by a selection of European navy representatives and hereafter will be referred to as the Hybrid Structural Connection or HSC. The geometry and materials used in the HSC are shown in Figure 3.2. The hybrid joint is a double lap joint of steel and GRP, the composite end being of GRP sandwich configuration. The joint is asymmetric in geometry to ensure a smooth outer surface of the helicopter hangar.

One underlying philosophy behind the design of any naval vessel is that it must remain an effective fighting platform in a wide range of weather, sea and operational conditions. Stability is the key to achieving this objective as it is the stability of the ship that dictates the motion of the vessel while operating in a seaway or conducting a manoeuvre. An important factor in achieving particular stability characteristics is the position of the centre of gravity of the vessel. The longitudinal position will directly affect the pitch characteristics and correspondingly the vertical position mainly influences the roll characteristics of the vessel. For very narrow fighting vessels such as the La Fayette class frigate it is the roll degree of freedom that is the predominant ship motion. Therefore, the position of the vertical centre of gravity is most important. In order to have 'high' stability, weight should be located as low as possible in the ship structure, which can be achieved by removing weight aloft. One possible way of achieving this is to construct the upper sections of the vessel using a lightweight material. To an extent this has been achieved in the past through the use of high tensile steel and aluminium to replace mild steel upper decks and superstructures [19]. With the rapid development of composite and bonding technologies the use of FRP is also becoming a viable option.

Structures that can take advantage of the use of lightweight material construction would ideally be located above the main weather deck. This ensures structural integrity of the hull envelope by using well-established steel construction methods with well-established performance characteristics for hostile (military) environments. Areas such as the superstructure, communication masts and helicopter hangers could be constructed from composite material. In order to incorporate the use of lightweight materials a method of providing a structural load carrying connection between the steel and composite must be established. Although there could be a number of methods employed the joint examined in the present research has been designed specifically for naval applications and is currently in service in the French navy.

The superstructure of a ship can be designed in two ways; to contribute to the global longitudinal stiffness of the hull girder or not. In the first instance the superstructure to deck connection must be rigid, the superstructure should be as long as possible, be the full width of the deck and contain internal longitudinal stiffening. If however, the superstructure is not contributing to the global stiffness of the hull then its structural role reduces to that of withstanding own weight issues, green seas or in the case of naval vessels air blast and launch loads from ordinance etc. This is only possible if the superstructure is short compared to he length of the ship and does not contain longitudinal stiffening. For long superstructures the cyclic wave-induced hull girder bending transfers stress through deformation of the superstructure. This can cause stress raisers particularly at the ends of the structure at the connection with the deck [6]. One effective way of avoiding this issue is to introduce a low modulus material in the superstructure. FRP is an obvious choice as it has a similar strength to mild steel but a fraction of the stiffness. The use of a hybrid connection would allow the attachment of a composite superstructure to a traditionally constructed ship which would benefit from reduced stress concentrations. In addition, the hybrid connection located at the interface between the hull and the superstructure would allow the plastic deformation of the superstructure is a similar manner to that shown in Ref. [11].

The hybrid joint is the key joint for attaching the lightweight superstructure or component to the steel hull. In addition to the strength and durability of the joint, there are a number of other requirements that the European navy representatives stipulated that the design must embrace:

- Manufacturing cost. Composite materials are already deemed more costly than steel. Therefore savings must be made through innovative use of the composite for construction. The use of adhesives, for example, can reduce distortion due to welding and hence reduce the cost of reworking distorted panels etc.
- Surface finish. Important for commercial craft in terms of asthetics and equally important if not more so in naval applications where smooth surfaces are of benefit in terms of radar signature.
- Minimum post assembly fitting work. Should be limited to fire insulation at most.
- Inspection, maintenance and repair.

Based on these requirements a number of proposals were put forward by European navy design groups with the HSC being chosen as the most suitable for this particular application.

The HSC is composed of essentially a double lap joint, which compared to the single-lap joint, has been shown to produce a more efficient connection due mainly to its symmetry when loaded in tension or compression, resulting in a planar load path and the increased bond area [23]. The steel insert protrudes from the double lap joint (Figure 3.2) to provide a location for traditional welding of the composite hangar wall to a steel deck (Figure 3.1). The use of welding as the method of attaching the composite hangar to the steel ship allows the manufacture of the composite material at a specialist manufacturing facility and transportation to the shipyard for attachment to the ship. This reduces the requirement for specialist composite manufacturing labour skills at shipyard level. The method of manufacture of the composite panels will be discussed later in this chapter.

The HSC, as presented here, represents a full-scale joint that could be used as the superstructure/hull connection on a vessel. However, it is the interface between the steel and the GRP that will be transferring service loads from hull to the superstructure. Therefore it is important to characterise the strength and durability of this aspect of the connection to better understand the HSC as a whole.

A simple double-lap representation of the hybrid joint was also developed for the present research and hereafter will be referred to as the Double Lap Hybrid Connection (DLHC). The geometry and materials used in the DLHC are shown in Figure 3.3. The DLHC was designed to represent just the connection between the steel and the GRP of the HSC joint. There are a number of reasons for testing this generic hybrid connection.

The HSC is deemed to be a full scale representation of a hybrid joint and incorporates part of the composite superstructure in the form of a balsawood sandwich. In the current configuration the HSC joint is asymmetrical and this leads to load path eccentricity when subjected to axial loading. In terms of a generic hybrid connection, such load eccentricity is felt to be an unnecessary complication. In addition, one aim of the present research is to examine the effect environmental exposure has on the strength and durability of the hybrid connection. In the HSC the balsawood is exposed at the specimen edges. By immersing the HSC in water a considerable amount of water would be absorbed by the balsawood resulting in substantial losses in structural integrity and it is not the aim of the present research to examine the effect of moisture on the balsawood. Therefore, the DLHC was designed to provide information on the structural performance of hybrid connections using a well-known and relatively simple configuration, the double lap joint.

3.2. MANUFACTURING METHOD – RESIN INFUSION

Resin infusion is a closed mould laminate manufacturing method [75]. The resin is allowed to infuse into the dry reinforcement by the application of a vacuum. The resin is drawn through the fibres helping to minimise the amount of air entrapped in the laminate and encouraging a high fibre volume fraction by efficient resin dispersion for full fibre saturation. However, despite the process producing a superior laminate to open mould techniques, infusion requires significantly more operator skill and involves a large number of non-reusable consumables, making the process considerably more expensive. However, in contrast to hand lay-up methods the resin is enclosed within the mould and with careful ventilation will not breach any health and safety regulations with regards to occupational health or volatile emissions in the workplace.

Table 3.1 identifies some of the advantages and disadvantages of the resin infusion method for laminate manufacture highlighting the major disadvantage of cost [75]. However, the resulting laminate from the resin infusion process compared to a similar laminate manufactured using a hand lay-up technique will be significantly superior, albeit with an increased amount of laminator skill. Table 3.2 details the basic steps involved in the resin infusion process and describes the importance of each of the steps.

Although the resin infusion process is a room temperature technique, the properties of the resulting laminate can be further improved by post-curing. For this reason all specimens, both HSC and DLHC, were post-cured at 60°C for 12 hours.

Table 3.1 Advantages and Disadvantages of Resin infusion over hand lay-up [75]

Process	Resin Infusion	Hand Lay-up
Advantages	• Closed mould system allowing for controlled emissions • Low void content laminate • High fibre volume fraction • Preparation carried out with dry materials	• Relatively cheap process • Low labour skills
Disadvantages	• Expensive non-reusable consumables • Relatively skilled labour	• Uncontrolled emissions • Low fibre volume fraction • Uncontrolled resin distribution • Time constraints based on resin gel time

Table 3.2 Step by step resin infusion process

Step	Description
1	Prepare mould surface by applying suitable release agent
2	Lay-up composite laminate/joint/component, peel ply and distribution mesh
3	Mask mould area with vacuum bag sealing (tacky) tape
4	Fix into position the resin inlet and vacuum outlet tubing and seal into place
5	Lay-up vacuum bag and ensure good seal with tacky tape
6	Clamp resin inlet port and evacuate vacuum bag to ensure there are no leaks in the bag
7	Mix resin and allow resin to be drawn into the laminate through the resin inlet port
8	Once resin gels, clamp resin inlet and keep under vacuum for at least 4 hours
9	After 24 hours, remove vacuum bag, distribution mesh and peel ply

3.3. MATERIALS

In terms of material content the DLHC is a later generation of hybrid connection; the materials used for the HSC projects were gradually replaced with those that were either more readily available or of superior mechanical properties.

For the HSC, the steel insert is marine grade structural mild steel known as ST52 (or 50D). Compared to more common shipbuilding grades of mild steel ST52 has an elevated yield strength of 355 MPa. The reinforcement used in the GRP laminate is manufactured by Chomarat and is described as an E-glass 3x1 twill, balanced woven roving with a weight of 780g/m^2 and is designated Chomarat 800 S4 (111A). This material has excellent drape-ability, important for the manufacture of non-planar geometries. The resin in which the reinforcement is bound is a state-of-the-art vinylester resin, DOW Derakane 411-45 manufactured by Dow Chemicals. Vinylester resin was chosen for its resistance to moisture ingress [76] and its viscosity is lower than polyester resins making it particularly suitable for the resin infusion process.

In the manufacture of the DLHC, the steel insert material remained the same but the GRP laminate materials changed. The reinforcement used for the DLHC was a tri-axial stitched E-glass fabric manufactured by DeVold. The use of stitched rather than woven reinforcement removes crimp in the fibres, resulting in a stiffer laminate. The resin is manufactured by Reichhold and is designated Norpol Dion 9500-501. This is a rubber modified vinylester resin. Table 3.3 provides a detailed list of each of the materials and some of the major material properties.

3.4. SURFACE PREPARATION

The European navy consortium considered the surface preparation of the steel was a very important aspect of the manufacturing process. It is generally accepted for the application of naval paint that shot blasting of the steel is the most suitable surface preparation technique. Once shot blasting was carried out there was a small time lag before the steel was wiped with acetone to remove grit-blasting debris, the acetone was allowed to evaporate and the steel was primed with the infusion resin within 4 hours of the grit blasting (accepted UK MoD requirement for painting). The priming resin prevents an oxide layer from forming on the freshly exposed steel surface, which may influence the strength of the joint. The steel was shot blasted to SA2.5 standard in accordance with BS EN ISO 8501-1:2001, using chilled iron grit, G24. Once the steel surface preparation was complete, the specimens were infused according to the method outlined in Table 3.2.

Table 3.3 Materials for HSC and DLHC specimens

Joint	Material	Manufacturer	Product code	Description	Comments
HSC	**Steel**	N/A	ST52 (50D)		Higher than normal yield strength
	Balsa	Baltek	AL600/10 CK-100	128kg/m^3 balsa cubes bound together by a mesh	Elastic Mod perp to grain – 89.6 (MPa) Elastic Mod parallel to grain – 5295 (MPa)
	Glass	Chomorat	800S4 (111A)	3x1 Twill woven roving E-glass	UK Mod Specific material
	Resin	Dow Chemicals	C411-45	Vinyl-resin	Elastic Mod. – 3600 (MPa) Shear strength on steel – 17200 (MPa)
DLHC	**Steel**	N/A	ST52 (50D)		Higher than normal yield strength
	Glass	DeVold		0/+45/-45 stitched tri-axial E-glass	
	Resin	Reichhold	Norpol Dion 9500-501	Rubber Modified Vinyl-ester	Elastic Mod. – 3600 (MPa)

3.5. TEST SPECIMEN ARRANGEMENT

Both the HSC and DLHC joints were manufactured in a similar process. An important aspect of experimental test specimen manufacture is to eliminate as many variables between specimens as possible. In order to achieve this for the HSC and DLHC joints a method where batches of specimens are manufactured simultaneously was employed. In general this is achieved in composite materials by manufacturing a large panel and cutting the smaller specimens from it. This way the properties of the composite material should be uniform as it was all made simultaneously. However, this is not possible with the HSC and DLHC joints as they contain steel. Cutting of steel using conventional mechanical methods results in the generation of heat. If, as in the case of the HSC and DLHC, the joint was located between the steel and GRP, the heat generated due to the process of cutting the steel would result in damage to the GRP and reduce the performance of the joint. In order to prevent damage an alternative method of cutting smaller specimens from a larger panel needed to be employed.

Machining the steel prior to the manufacture of the specimens allowed gaps to be located to facilitate cutting of specimens without the tool coming into contact with the steel. The use of laser cutting technology allowed the manufacture of accurate steel plates containing the steel required for each specimen. Figure 3.4 shows the steel plates used for the DLHC specimens. The additional steel, located top and bottom of each plate, was removed after the GRP joint had been manufactured without risk of damaging the GRP/steel joint as it is sufficiently far from the cutting region. A water-cooled diamond impregnated circular saw was then employed to separate the individual specimens running along the gaps between the steel. In the DLHC as shown in Figure 3.2, holes were pre-drilled in the steel to allow drilling only of GRP prior to mounting the specimen in the test machine.

Chapter 4

Experimental techniques

4.1. INTRODUCTION

The aim of this chapter is to outline the principles used and to describe the experimental test set-ups used in the following chapters. Two specimens are examined in the present study and are fully described in Chapter 3, namely the HSC (Hybrid Structural Connection) and DLHC (Double Lap Hybrid Connection).

4.2. TESTING FACILITIES

All of the experimental testing was carried out in the Transport Systems Research Laboratory (TSRL) in the School of Engineering Sciences at the University of Southampton, the majority of which took place using the FORTRESS structural testing rig. In addition an Instron 8802 test machine with a 100 kN load cell was used to conduct some static tests.

4.2.1 FORTRESS

FORTRESS was developed as a multi-axial test facility in the early 1990’s specifically for testing large marine composite structures. In its present configuration a maximum of 209 kN can be generated using the current hydraulic pressure output connected to a hydraulic ram with a rod diameter of 110 mm. Load is acquired via an Instron 250 kN dynamic load cell and position via a displacement transducer attached between the rig and the load cell. An Instron 8800 controller and associated software can control the loading of the test structure in either load or position control (i.e. in kN/min or mm/min). The controller is capable of producing linear and bilinear ramps of either load or displacement. In addition a sine, triangular or square wave function can be produced to perform fatigue tests. The control software can be used to acquire load, position and time data at a maximum frequency of 500Hz. In addition to the INSTRON data acquisition software, an 8-channel analogue to digital conversion card is used with the Wolfson Unit[†] software TURBO AD. This data acquisition system can acquire from the INSTRON test equipment and can also acquire data from additional sensors such as displacement transducers, temperature sensors, strain gauges, etc.

Incorporated within FORTRESS is an environmental chamber (FEARLESS) which allows specimens to be loaded while in a hot, humid environment. The chamber is capable of producing temperatures of 120°C and a relative humidity of 95 percent. Load can be transferred through the walls of the chamber by the use of stainless connecting rods. An adaptable specimen mounting and the load transfer system were developed specifically for testing of both the HSC and DLHC joints. Figure 4.1 shows a schematic representation of the test rig, specimen arrangement and the various fixtures used for each test.

The FORTRESS/FEARLESS testing facility was used to carry out the axial static strength, fatigue life and axial residual strength tests of both the HSC and DLHC joints.

4.2.1.1 FORTRESS parameters

A short study was made of the rig and its behaviour using the test fittings associated with both the DLHC and HSC configurations. The study involved instrumenting a solid steel bar with strain gauges and tested in FORTRESS using the fittings associated with the testing of the hybrid connections. The strain bar was loaded to a predetermined level and the displacement was acquired from the control transducer and from a transducer spanning the specimen. In addition, the signal from the strain gauges was acquired. Figure 4.1 shows schematically the position of the displacement transducers and strain gauges. From the strain gauges the displacement of the steel specimen was obtained. The difference between

---

[†] Wolfson Unit for Marine Technology and Industrial Hydrodynamics

the three displacements, control, span and strain, provides information on the flexibility of the rig, test specimen fixtures and specimen respectively. Figure 4.2 shows the difference between the control and span transducers, the relationship between these two curves is almost linear with respect to load. Therefore, it can be said that the relationship between the rig movement and applied load can be described as linear.

Based on the results obtained it is estimated that the rig has a stiffness of approximately 20 kN/mm and the immediate fixtures have a stiffness of 160 kN/mm. The strain bar has a stiffness of approximately 3000 kN/mm. The values obtained from the rig flexibility tests are applied most importantly to the numerical modelling for the definition of the boundary conditions and their application is described in detail in Chapter 7. However, the rig stiffness is important with respect to the experimental results and the determination of the global stiffness of the joint rather than the global stiffness of the joint plus the test rig. Due to the configuration, construction and size of FORTRESS and the magnitude of the applied loads it is inevitable that there will be some deformation of the rig and its fittings while subjected to possible loads in excess of 18 tonnes. Account of this movement must be made not only for the analysis of the experimental results but also for the numerical simulation in terms of boundary conditions. This became a factor when the HSC and DLHC were tested as the failure loads were in excess 100 kN and 160 kN respectively. For example, this resulted in rig movement in excess of 10 mm when testing the DLHC to failure.

4.2.2 INSTRON 100 KN TEST MACHINE (INSTRON A)

A standard servo-hydraulic 100 kN Instron test frame was used to perform a small number of tests either for material characterisation or for residual strength purposes. An Instron 8800 controller controls the actuator and data is acquired via a Strawberry Tree Data Shuttle and stored using the DasyLab suite of software. Out-of-plane static and residual strength tests were carried out using this test equipment.

4.3. TESTING OF THE DLHC AND HSC CONFIGURATIONS

The aim of this test programme was to investigate the performance characteristics of both a generic hybrid connection (DLHC) and a representative structural hybrid connection (HSC) between steel and GRP substrates. An extensive programme of performance characteristic testing has been carried out on the DLHC involving static and fatigue testing. In addition, a programme of environmental ageing has been undertaken to determine the change in performance of the joint after exposure to moisture. The HSC has been characterised in terms of its compressive strength and fatigue life under various compressive fatigue load amplitudes. In addition, the HSC was examined to assess its residual strength, both in-plane and out-of-plane, after compressive cyclic loading. The following sections will describe the different phases of each joint's test programme.

4.3.1 STATIC AND FATIGUE TESTING

This phase of both the DLHC and HSC test programmes was undertaken in the FORTRESS test facility for axial tests and in Instron A for out of plane tests. Figures 4.3 and 4.4 show the test set-up for the DLHC and HSC specimens respectively for axial tests. The static tests were conducted in position control to observe any stress relief caused by joint damage during loading. The rate of loading for the static testing was 1 mm/min. Load and ram displacement were obtained for the HSC and additionally span displacement was acquired for the DLHC. The results were presented in the form of load-displacement curves.

Fatigue testing was conducted in the same configuration as that used for the static testing. However, the tests were carried out in load control to a percentage of the ultimate failure load of the specimen as found from the static tests.

In addition to the axial testing, 4-point static bend tests were conducted on the DLHC using Instron A. Figure 4.5 shows the test set-up for this phase of the testing.

4.3.1.1 Loading conditions for hybrid connections

The aim of this section is to justify the loading conditions applied to both the HSC and DLHC. In the present research three loading scenarios are used. For the HSC the axial load is compressive and the bending loads are applied using a 4-point bend test. For the DLHC the axial load is tensile and the bending load is a 4-point bend test.

The HSC has been previously defined as a likely candidate for a full-scale structural connection and therefore the envisaged loading on such a joint should be considered with respect to its location and function onboard a naval vessel. The location of such a joint was described in Chapter 3 as being suitable for naval superstructures particularly helicopter hanger structures. These are most often found on the after deck of naval platforms.

It is assumed that the helicopter hangar structure does not contribute to the global bending strength of the hull girder due to its length being considerably smaller than the overall length of the hull, and is decoupled from the hull girder due to the differences in elastic modulus of the materials used for the hull (steel) and hangar (GRP) as discussed in Chapter 3. Therefore only forces induced by the structures own weight and accelerations due to motion are considered significant. With the vessel at rest and in calm water, the joint will experience only a compressive force equal to the apportioned weight of the hangar structure and any ancillary equipment mounted on it. The generation of tensile forces on the other hand, whilst unlikely, are not inconceivable. When the vessel is underway and is sailing in seas rather than calm water, it will experience motions in all six degrees of freedom. These motions translate to the connection between the hull of the vessel and the hangar superstructure. Assuming the hangar is located on the after-deck of the ship, for the connection to experience a tensile load or at most a relief of the compression loading due to the hangar's structural weight, the aft end of the ship needs to experience one negative g for weightlessness or greater for tensile load. This scenario would be possible if the aft end of the ship was in free fall from coming off the back of a wave but in reality this would be highly unusual.

It is feasible that either the port or starboard side of the structure would be subjected to one or more negative g's during roll. The size of the tensile force would be related to the position of the neutral axis of the hangar structure and the roll rate but again it is highly unlikely that one negative g will be experienced in reality and only a combination of roll and heave may in extreme circumstances produce enough acceleration to cause the structure to be weightless.

From the discussion of realistic loading scenarios described above, the most likely force to be encountered by the HSC is therefore compressive and to this end the testing of the strength and durability of the HSC has been carried out in compression. Although this is the loading condition assumed in the present research it should be noted that depending on the configuration of the superstructure it may contribute to the global hull stiffness and therefore be subjected to stress transfer from the hull. This may change the loading condition. However, this is not considered in the present research.

For the DLHC it would have been advantageous if the specimen were also tested in compression, as this would keep the loading scenarios consistent. However, due to the test facility (FORTRESS) containing the environmental chamber (FEARLESS), load had to be transferred through the wall of the chamber via a stainless steel connecting rod 30 mm in diameter. Loading this system in compression would have resulted in the buckling of the connecting rod. Therefore all static and fatigue tests on the DLHC are in tension. Due to the DLHC being a symmetric joint the difference between tensile and compressive properties, provided that buckling did not occur in compression, would produce similar results.

Both the HSC and DLHC specimens were tested in 4-point bending as this load situation would represent an externally applied force. It is known that this test set-up will result in zero transverse shear across the joint between the rollers, however this joint represents a thin skin commonly found in marine structures, and assumed not to contribute to the shear strength of the structure, the surrounding support structure, transverse framing, will provide the transverse shear carrying capability.

4.3.1.2 Boundary conditions for HSC

The final boundary conditions used for the static and fatigue testing of the HSC were decided upon after the response of the specimen to compressive loading. Due to the HSC specimen's asymmetry the compressive load path will be eccentric. This will influence the response of the joint by inducing a lateral deflection of the specimen under compression. Although due to the load path eccentricity this is the expected response of the joint, in full-scale application it is unlikely. The HSC, as described in Chapter 3, is designed for application to a helicopter hangar structure. It can be expected that such a structure will incorporate an internal transverse framing system. This internal structure should prevent lateral bending of the joint. Therefore it is deemed unacceptable to allow such deflections in the experimental study. The effect of the lateral deflection on ultimate joint strength is examined in Chapter 6.

In order to prevent lateral deflection experimentally, a system of anti-bending guides were designed and consisted of a set of rollers mounted perpendicular to the specimen plane. These were rigidly attached to the test machine and are shown in the HSC set-up in Figure 4.4. A check was made to obtain the lateral stiffness of the anti-bending guide system by the use of a dial gauge while a specimen was loaded. A small amount of lateral deflection was observed. This small amount of lateral deflection is expected to have an influence on the global axial stiffness of the specimen under compressive load compared to a fully rigid structure. The anti-bending guides were found to have a stiffness of 2 mm at an axial load of 100 kN. This was measured using a dial gauge on the specimen measuring lateral deflection.

It is expected that although the anti-bending guide system provides a realistic reduction in the lateral bending of the specimen while under compressive load, its presence may influence the damage mechanisms within the joint. However, in order to realistically constrain the specimen it is felt that the presence of the anti-bending guides is more beneficial than any influence it may have on the progression of damage.

4.3.1.3 Boundary conditions for the DLHC

The DLHC specimen was tested in axial tension and 4-point bending. For the axial tests the specimen was clamped at either end in a similar manner to the HSC. No anti-bending guides were required due to the tensile loading. The 4-point bending configuration is shown in Figure 4.5.

4.3.1.4 Fatigue data analysis

Data was acquired at regular intervals (in most long term tests after every 100 cycles) during each fatigue test. The data was analysed via a FORTRAN routine, which calculated the stiffness, using a linear least squares fitting procedure, and the area within the hysteresis loop, using the trapezium rule. It was felt that due to the density of the data acquired, approximately 100Hz, the trapezium rule provides sufficient accuracy and is an extremely robust and easy to apply method for data with varying interval values.

The area within the hysteresis loop can be equated with the energy lost by the test system [77]. If there were no loop, i.e. the loading and unloading of the test system against displacement follows the same line, the system could be described as perfectly elastic (Hooke's Law) – the energy input into the system during loading is exactly the same as the energy output by the system during unloading. However, if, while testing a specimen, a loop began to form after a given number of cycles, this can be defined as energy being dissipated by the system. If the loading and unloading part of the system is said to be initially ‘perfect’, then any resulting energy dissipation over time must be originating from the specimen itself, provided that the loading and unloading of the specimen is purely adiabatic. Therefore, a change or development of energy dissipation can be considered a sign of damage within the specimen [77].

In the case of the present study, it is known from the rig stiffness tests, described in Section 2.1.1, that the testing system is not ‘perfect’. This will therefore lead to the generation of a hysteresis loop as energy is dissipated in the form of rig movement. Therefore, during testing the change in energy dissipation (area inside the hysteresis loop) is monitored as an indication of specimen damage due to fatigue cycling, assuming no failure in the test rig.

Both the energy dissipation and the stiffness are plotted against number of cycles to help to identify when damage due to cyclic loading occurs.

4.3.2 ENVIRONMENTAL AGEING

The DLHC specimens are subjected to an environmental ageing programme to determine the change in performance, if any, of the hybrid connection due to moisture ingress. Environmental ageing can be conducted in a number of ways, for example, by exposure to cyclic temperature loading, exposure to a wet environment or to a combination of hot and wet conditions. These tests can be carried out either with or without load and the load can be applied statically or dynamically. The facilities in the TSRL allow for any of these scenarios. However, consideration must be given to the length of time required for each test and the environment that the full-scale structure will encounter during its life.

The hybrid joints being examined in the present study are designed for use in the marine environment. This is usually associated with moisture, with possible variations in temperature depending on the location of the vessel, i.e. the Gulf – hot and humid; North Atlantic – cold and wet. However, the common factor with both locations is moisture.

In order to undertake the most realistic study into the effects of moisture on a hybrid joint, the connection would ideally be fitted to an operating vessel and tested at regular intervals throughout its operating life to determine its residual strength. However, this is unfeasible. In order to make research viable, the ingress of moisture must be accelerated. However, the mechanisms of accelerated ageing and natural ageing can be different and the correlation between time under accelerated ageing and time under natural ageing is not clear. The main reason is because of a lack in naturally aged specimens of reasonable quality. The artificial methods used to age composite materials commonly involve elevated temperature and complete immersion in water.

In the present research, the experimental test specimens were immersed in water at 40°C. The temperature was chosen so as not to cause any adverse effects due to close proximity of ageing temperature to the glass transition temperature of the resin, which as discussed in Chapter 2 leads to excessive plasticization of the resin matrix. However, the temperature was sufficient to accelerate the ageing process. Immersion provides a true 100 percent humidity situation that in reality is unlikely but experimentally should result in efficient accelerated ageing [53]. During immersion there is a very high concentration of penetrant due to the nature of a liquid, in addition there is hydrostatic pressure acting on the specimen. To create a 100 percent humid environment without immersion is very difficult. Earl [53] conducted experimental studies that compared immersion and non-immersion ageing techniques with respect to moisture content. It was found that more water penetration was found through immersion and therefore this method of accelerated ageing was chosen for the present research as a worst-case scenario.

It can be assumed that the full-scale structure would be subjected to moisture in the form of a salt-water solution whereas the present ageing is conducted in distilled water. Again, this is considered a worst-case scenario. The concentration of H_20 molecules in salt-water will be less due to the mineral content of the liquid. The distillation process removes the minerals from the liquid resulting in a liquid with a higher concentration of H_20 molecules. Therefore, it assumed that the distilled water will diffuse more easily into the resin matrix material than a saline solution due to differences in concentration. More penetration of moisture, in addition to the elevated temperature, will further accelerate the ageing process. Conversely, a salt-water solution will have a more corrosive effect on any exposed steel surfaces. However, this is not the ageing mechanism that is to be investigated. The mode of moisture ingress into the steel/GRP interface should be through the GRP. Therefore the distilled water method should provide the worse case scenario.

Careful consideration must be given to the way in which moisture is absorbed by the experimental specimen and that this relates to how moisture could penetrate the structure at full-scale. It should be noted that it is not the influence of moisture on the composite material or steel that is of importance in the present research, but the impact of moisture on the joint itself. If, for example, the DLHC specimen shown in Figure 3.3 of Chapter 3 was placed in an immersion bath, moisture could penetrate the joint from a number of directions:

- From the outside surface of the joint, i.e. passing through the thickness of the laminate;
- From the interface of the laminate and the steel on the surface of the specimen;
- From the edges of the specimen.

Of the three moisture ingress directions only the first two are possible in the full-scale structure, as these are the only surfaces exposed to the environment. The third direction is a function of the specimen geometry used in the present experimental programme. In the full-scale structure, the edges of the joint would not be exposed, as the joint would consist of a large panel of which the specimens examined here are small sections. Therefore, in terms of realistic moisture ingress the third direction described above must be eliminated in order that the experiments are as realistic to full scale as possible.

In the present research this was overcome by manufacturing the specimens in panels of three. This ensured that the test specimens for a single test configuration were manufactured identically. At the edges of the panels a sacrificial edge coupon was also manufactured. It is assumed that the sacrificial edge will absorb moisture through its exposed edge and therefore not penetrate into the test specimen edges, the results in Chapter 6 confirm this by having a small (<5%) experimental scatter between specimens from the same panel. Figure 3.3 in Chapter 3 shows the layout of the test specimen panel.

The objective of the ageing process was to determine the extent of degradation, if any, moisture had on the joint strength or durability. Once the specimens had been suitably aged they were subjected to static and fatigue testing in exactly the same manner as with the unaged specimens described in Section 4.3.1. In the case of the fatigue tests it was important not to allow moisture to escape from the specimen during testing, especially as fatigue tests can last for a considerable length of time. This was conducted using absorbent wrapping around the specimens and associated fixtures that were soaked in water and wrapped in plastic. During the fatigue tests additional water was added to maintain the moisture content in the hybrid joint.

4.3.3 RESIDUAL STRENGTH TESTING

Residual strength tests allow the evaluation of remaining strength in a structure after a given life cycle. In the present research the hybrid joint has been subjected to in-plane fatigue cycling to induce a crack up to a pre-determined length, representing a portion of the structure's life. The joint was then tested in 4-point bending with end conditions exhibiting a high degree of fixity (approaching fully encastred) as shown in Figure 4.6. The fully encastred end conditions are assumed to represent the attachment of the joint to the weather deck of the vessel at the steel end and the position of a stiffener at the composite end. The 4-point bending tests were carried out using the INSTRON A test machine, described in Section 2.2. Due to limited specimen numbers a single static test was carried out on an un-fatigued specimen to set a baseline by which residual strength could be measured. This result was confirmed by tests conducted by other European navy partners. The specimen length was 700 mm and 100 mm of each end were encastred. The loading rollers were located 100 mm either side of the steel/balsa interface.

The fatigue cracks were grown and monitored by an automated system. A resistance wire was placed at the desired position of the crack front. A small voltage was applied to the wire and the voltage monitored by the Instron control system. Once the crack reached the required length the resistance wire broke resulting in a loss in voltage, the Instron controller then shut down the hydraulic power ending the test. This monitoring process worked well and produced four distinctly different crack lengths. The results of the residual strength tests were compared with the static baseline test.

4.4. MATERIAL CHARACTERISATION AND VALIDATION EXPERIMENTS

Material characterisation tests were conducted on the GRP and glue materials. These tests were performed to verify the data supplied by the manufacturers with respect to the resin and to establish the tensile strength of the GRP laminate, critical to the failure criteria and correct implementation of the elasticity matrix for the GRP in the numerical models.

4.4.1 TENSILE RESIN TESTS

Four moulds were manufactured for the casting of Norpol Dion 9500-501 vinyl-ester resin samples for tensile tests. The moulds were created using a British Standard steel test specimen as a template and were cast using a silicone-based rubber moulding compound. The silicone moulding compound was chosen due to its ease of use being a cold curing material. The resulting moulds can be used at temperatures up to 70ºC which is greater than the heat expected from the exothermic reaction of the resin cure cycle. In addition, the silicone compound allows for easy removal of the resin casting and its durability allows it to be repeatedly used. Figure 4.7 shows the moulds used for the resin casting.

The resin was mixed with the appropriate catalyst as per the manufacturers instructions. Any foaming of the resin/catalyst mixture was allowed to subside. The resin was not degassed under vacuum as it was felt that this would provide an over ideal material property for the resin that would not be representative of the resin as found in both the DLHC and HSC[†]. The resin was then poured carefully into the moulds to prevent any additional air entrapment. Three castings were made from the same batch of catalysed resin. The castings were allowed to cure for 24 hours. As with the DLHC and HSC the resin castings were post cured at 60°C for 12 hours. The resin specimens were tested in tension to failure; an extensometer was used to measure strain. The results obtained are presented in Table 4.1. A typical stress-strain plot is given in Figure 4.8. The resin response has a large linear region to the stress-strain plot with a small amount of non-linearity just before maximum stress. In a number of the experiments there was a further increase in strain post maximum stress indicating a continuing absorption of energy to cause complete rupture. This is an important aspect to the numerical modelling in terms of the post initial failure material degradation model as discussed in Chapter 5

.

Table 4.1 Results of resin bulk tests

Specimen	Young's Mod (MPa)	Failure Load (N)	CSA (mm^2)	Ultimate strength (MPa)
1	2774.9	1484.9	31.53	47.1
2	2780.5	1791.9	32.08	55.9
3	2775.6	1692.9	30.54	55.4
4	2804.1	1662.6	30.48	54.6
Average	2783.8	1658.1	31.16	53.25
Coef. Of Var (%)	0.5	7.7	2.5	7.8

4.4.2 RESIN FRACTURE TOUGHNESS TESTS

Double cantilever beam (DCB) tests were conducted to obtain the Mode I fracture toughness (G_{IC}) for the resin material Norpol Dion 9500-501. In order to obtain correct values of fracture toughness, the two substrates used for a DCB specimen must have the same flexural stiffness. As the hybrid connection has dissimilar materials the flexural stiffness of the substrates is not equal. To ensure cohesive failure two GRP substrates were used to obtain the fracture toughness of the resin. It could not be guaranteed that cohesive failure would occur if steel specimens were used and the facilities for the replication of the surface preparation of the steel were not available. Pre-cured laminates of glass-reinforced vinyl-ester were manufactured using the resin infusion technique for the DCB tests.

The DCB specimens were manufactured by bonding two GRP substrates with a nominal width of 25 mm and nominal thickness of 4 mm using the resin system. As with the HSC and DLHC the bondline thickness is very small, therefore no adhesive bondline thickness spacers were used. The resultant specimens had an average bondline thickness of 0.18 mm, which compared relatively well with the approximate bondline thickness of the HSC and DLHC specimens. A Teflon insert was placed at the end of the bondline to act as a crack pre-starter. Aluminium blocks were bonded to the ends of the DCB specimens containing the Teflon strips to enable loading. The specimens were loaded in tension at a rate of 1.0 mm/min. The tests were conducted according to BS 7991 'Determination of the Mode I adhesive fracture energy G_{IC} of structure adhesives using double cantilever beam (DCB) and tapered double cantilever beam (TDCB) specimens'. The specimens manufactured

---

[†] For infused laminates the resin is initially held at room pressure, any entrapped air caused by over vigorous mixing or by the foaming reaction would be drawn into the laminate and may not be totally dissipated due to

corresponded to the '*type a*' specimens as described in the above standard. The principal dimensions for the specimens are given in Table 4.2. The average fracture energy obtained was 241.8 J/m^2 (7.8 % coefficient of variation).

Table 4.2 DCB test specimen dimensions

Dimension	**Value**	**Units**
Length	290	mm
Width	25	mm
Substrate thickness	4	mm
Adhesive thickness	0.2	mm
End block height	10	mm
End block length	25	mm
Loading rate	1	mm/min

4.4.3 GRP STIFFNESS TESTS

Two GRP laminates were manufactured using the two different E-glass reinforcements found in the DLHC and HSC. The first laminate representing the HSC contained the 3x1 twill woven roving. The second laminate, representing the DLHC contained the tri-axial cloth. Both panels were manufactured using the resin infusion method. Both panels were cut to provide tensile specimens of the dimensions 250x50 mm lengths. The thicknesses of the two panels varied slightly and were measured as 3.5 mm for the woven roving and 4.9 mm for the tri-axial. The specimens were tested in the Instron A test machine described in Chapter 4. As with the resin tests, strain was measured via the use of an extensometer. The average result for Young's modulus provided a value of 20.6 GPa for the woven roving and 19.7 GPa for the tri-axial cloth. These values can be said to be typical for GRP laminates [6].

---

the vacuum surrounding the laminate.

Chapter 5

Simulation and optimisation methods

5.1. INTRODUCTION

This chapter deals with the methods that are employed in the present research associated with numerical simulation and formal optimisation of the hybrid connections. In Chapter 2, progressive damage was highlighted as a short-term limit state method of detecting and monitoring damage in a structure. The method by which this technique is applied to the hybrid connections is explained in the first instance. This technique as described in Chapter 2 can be divided into three main areas. The numerical simulation of the joint using finite element analysis (FEA), the detection of damage within the numerical simulation and the degradation of material properties to reflect the damage detected. The final part of this chapter is the description of the methods used for the parametric study and formal optimisation of the hybrid connection. This section will describe the simulation used, the reasoning behind the level of simulation chosen, the method of encoding the joint variables, the “breeding” of the population, the method of obtaining the selection variables and the implementation of the selection criteria.

5.2. DAMAGE PROGRESSION OF HYBRID CONNECTIONS

Catastrophic failure of a composite material rarely occurs at the load corresponding to initial or first-ply failure. The structure ultimately fails due to the propagation of local failures as the applied load increases. Initial failure of a layer can be predicted using an appropriate failure criterion or first-ply failure theory. The subsequent catastrophic failure prediction requires the understanding of the accumulation of all failure modes and failure propagation. Progressive failure analysis has been the focus of a number of research studies, Ochoa and Reddy [78] provide a review of progressive failure analysis. Failure within a composite laminate is often caused by one of three failure modes, fibre breakage, matrix cracking, fibre/matrix shear or through delamination [78].

Progressive Damage Modelling (PDM) is a numerical tool for predicting the failure of a material in a methodical and iterative process whereby FEA is employed to produce a stress state at a known load step. The results of the FEA are examined with respect to a failure criterion. If failure is deemed to have occurred then a material degradation model is applied. The FEA analysis is carried out again to re-establish equilibrium and if no further failure occurs then the load is increased to the next load step. Figure 5.1 shows a typical progressive damage analysis methodology. The typical method is made up of 4 main parts:

1. FEA to establish equilibrium;
2. A failure criterion is applied to ascertain if failure has occurred;
3. A material degradation procedure to propagate damage and estimate a reduction in local material properties;
4. Re-establishment of equilibrium after material property modifications.

In the following sections parts 2 and 3 of the PDM will be discussed with respect to the hybrid connections examined in the present research.

5.2.1 FAILURE ANALYSIS

Mention of failure criteria for use with composite materials commonly refers to now classic theories such as Tsai-Hill, Tsai-Wu, Hoffman etc. A world-wide study on failure modelling where the commonly used failure criteria were compared to experimental results was conducted in 2002 [79]. These failure analysis tools are specific to composite or orthotropic materials where failure may occur in the fibre, matrix or the fibre-matrix interface. In the context of adhesively bonded composite joints, there is an additional scenario where failure could occur in the isotropic adhesive layer. In this instance more simplified criteria for isotropic materials could be used.

5.2.1.1 Failure in isotropic materials

It is convenient to begin the discussion of failure criteria by first examining an isotropic material. This is defined as a material that has mechanical properties that are independent of the plane examined. Due to this characteristic the concept of principal stresses and strains can be used to define failure. Knowledge of the tensile, compressive and shear strengths of an isotropic material can be used to completely define its strength. Most commonly the stresses associated with an isotropic layer can be defined by the orthogonal direct stresses σ_x and σ_y and the associated shear stress σ_{xy}. These stresses can then be resolved into the two principal stresses σ_1 and σ_2, the major and minor principal stress respectively using the transformations defined by Equations 5.1 and 5.2.

$$\sigma_1 = \frac{\sigma_x + \sigma_y}{2} + \sqrt{\left(\frac{\sigma_x - \sigma_y}{2}\right)^2 + \tau_{xy}^2} \tag{5.1}$$

$$\sigma_2 = \frac{\sigma_x + \sigma_y}{2} - \sqrt{\left(\frac{\sigma_x - \sigma_y}{2}\right)^2 + \tau_{xy}^2} \tag{5.2}$$

The maximum shear stress is then found using the two principal stresses σ_1 and σ_2 and the maximum shear stress acting at 45° to the plane of the major principal stress σ_1. Correspondingly the strains, principal direct strains and the maximum shear strains can be found in a similar manner. Due to the ply being isotropic, the planes of principal stresses and maximum shear stress coincide with the planes of principal strains and maximum shear strain. With knowledge of the above mentioned stresses and strains a number of failure criteria commonly used for isotropic materials can be examined.

Two failure criteria are commonly used to predict the failure of ductile isotropic materials, the maximum shear stress criterion and the Von Mises Criterion.

The maximum shear stress criterion is sometimes referred to as Tresca's or Guest's criterion [80] and is applied mainly to ductile materials. In two-dimensional stress, the maximum shear stress is related to the difference in the two principal stresses, σ_1 and σ_2. Therefore the criterion requires the principal stress difference, along with the principal stresses themselves, to be less than the yield shear stress (τ_y):

$$\left.\begin{aligned}|\sigma_1| &\leq \tau_y \\ |\sigma_2| &\leq \tau_y \\ |\sigma_1-\sigma_2| &\leq \tau_y\end{aligned}\right\} \tag{5.3}$$

Graphically, the maximum shear stress criterion requires that the two principal stresses be within the dotted line presented in Figure 5.2.

The Von Mises Criterion (VMC), also referred to as the maximum distortion energy criterion [80] is also used to estimate the yield point of ductile materials. The VMC states that failure occurs when the energy of distortion reaches the same energy for yield or failure in uniaxial tension (σ_y). Mathematically this is expressed as:

$$\frac{1}{2}\left[(\sigma_1-\sigma_2)^2+(\sigma_2-\sigma_3)^2+(\sigma_3-\sigma_1)^2\right] \leq \sigma_y{}^2 \tag{5.4}$$

In the cases of the plane stress $\sigma_3=0$ and the Von Mises criterion reduces to:

$$\sigma_1{}^2-\sigma_1\sigma_2+\sigma_2{}^2 \leq \sigma_y{}^2 \tag{5.5}$$

This equation represents a principal stress ellipse. Figure 5.2 shows that the principal stresses required for Von Mises criterion must fall within the solid line ellipse. It is also shown that the Maximum shear stress criterion (dotted line) is more conservative than Von Mises as it falls within the VMC ellipse.

5.2.1.2 Failure in a non-isotropic material

Non-isotropic materials can either be orthotropic or anisotropic. The former is defined as a material that has at least two orthogonal planes of symmetry, where material properties are independent of direction in each plane. An anisotropic material, in contrast, has no planes of symmetry. In general, composite materials fall into the orthotropic category if the laminate is symmetrically balanced. This may not always be the case but within the context of the present research, composite materials are assumed to be orthotropic.

In general, overall structural damage in composite materials may include individual ply damage and also through-thickness fracture of the composite laminate. In order to assess the damage or failure in a composite material the various damage mechanisms are simulated by the evaluation of the individual ply failure modes and associated degradation of laminate properties. The type of damage growth and the sequence of damage progression depends on the composite structure, loading, material properties, and hygrothermal environment [49]. Because of the non-isotropic (orthotropic) nature of composite lamina, the failure criteria have to include and identify the various failure mechanisms that may occur, including matrix cracking, fibre breakage or fibre-matrix shear.

The catastrophic failure of a composite material rarely occurs due to initial or first ply failure. It is more likely that ultimate failure occurs due to an accumulation of local damage as load is increased and the progression of further damage through the material. The initial failure can be detected by using an appropriate failure criterion. As discussed above, fibre reinforced materials can fail due to fibre breakage, matrix cracking or by delamination of the layers. Most failure criteria are based on the stress state within the material. Failure criteria for composite materials can be divided into two distinct groups: namely, interactive and non-interactive criteria.

A non-interactive criterion is defined as one that does not have any interactions between the stress or strain components. These criteria examine the individual stress or strain components and compare them directly with the corresponding material allowable strength values. The maximum shear stress criterion, described in Section 5.4.1.1, falls into this category. The failure surfaces for these criteria are rectangular in stress and strain space.

An interactive failure criterion is one, which involves some interaction between the stress and strain components. Interactive theories fall into three main categories: polynomial theories, direct mode determining theories and strain energy theories. Polynomial theories describe the failure surface using a polynomial function. The direct mode determining theories are usually polynomial in nature but use separate equations to describe each mode of failure. Finally, the strain energy theories are based on local strain energy levels determined during non-linear analyses, the Von Mises failure criterion falls into this category but is also a polynomial function.

One of the most general polynomial failure criteria for composite materials is the tensor polynomial criterion proposed by Tsai-Wu [81]. The criterion is expressed in tensor notation as:

$$F_i\sigma_i + F_{ij}\sigma_i\sigma_j + F_{ijk}\sigma_i\sigma_j\sigma_k \geq 1 \qquad i,j,k = 1,....,6 \tag{5.6}$$

where F_i, F_{ij} and F_{ijk} are components of the lamina strength tensors in the principal material axes. The usual stress notation is used except $\sigma_4=\tau_{23}$, $\sigma_5=\tau_{13}$ and $\sigma_6=\tau_{12}$. However, the third order tensor F_{ijk} is usually ignored from a practical standpoint due to the large number of material constants required. This reduces the general polynomial criterion to a general quadratic criterion given by:

$$F_i\sigma_i + F_{ij}\sigma_i\sigma_j \geq 1 \qquad\qquad i,j = 1,....,6 \qquad\qquad (5.7)$$

Based on this general quadratic criterion there are various alternatives, which differ in the way that the tensor stress components (F_{ijk}) are determined, some of the most commonly used criteria include Tsai-Hill [46, 82], Azzi-Tsai [83] and Hoffman [84]. The failure surfaces of all of these quadratic criteria are elliptical in shape. Although all of these criteria will predict the initiation of failure none of them state explicitly what the failure mode is or how the composite fails.

The direct mode determination criteria have the advantage of predicting failure and describing the failure mode occurring during loading. Hashin [44] proposed a quadratic failure criterion in piecewise form based on material strengths. Two failure modes are present, fibre failure and matrix failure. In fibre failure it is the fibres, which break in tension or buckle in compression. In matrix failure, matrix cracking occurs.

Although the use of non-isotropic failure criteria provide a well established method of detecting not only failure but the form of failure in composite materials, their application must be carefully considered. In the present research failure criteria are applied to what is essentially an adhesive joint between a GRP substrate and a steel substrate. The experimental tests showed (Chapter 6) that in most cases the failure of these joints occurred in the adhesive layer. The only damage caused to the composite material occurred post-failure of the joint. This implies that the uses of the more complex non-isotropic failure criteria are not required as failure occurs in the isotropic adhesive layer. Therefore, the present research applies only the interactive Von Mises failure criterion in the PDM analysis of the hybrid connections.

5.2.2 POST-INITIAL FAILURE MATERIAL DEGRADATION

The initial failure of composites or adhesives rarely results in instant catastrophic failure. Closed-form solutions for adhesive joints, for example, predict joint failure occurring when the stress in any region of the joint exceeds the corresponding material property, (non-interactive failure criteria) [23]. This is not a realistic simulation of how many materials fail. In steel, for example, initial failure can be defined as the transition from the elastic region to the plastic region of the stress strain curve (yield strength). However, the material can withstand further deformation and load before complete rupture of the material. Some brittle materials, glass for example, may fail instantaneously after initial failure. However, in a large majority of materials, although initial failure may have occurred, structural integrity may still be present providing a prolonged load carrying life beyond initial failure. From the point of initial failure to final failure it could be said that there is a progressive reduction in stress-carrying capability for an increasing strain [45].

Based on this assumption, it is felt that the ‘standard’ material degradation models used most regularly with interactive failure criteria, which present instantaneous reduction in elastic material properties, do not accurately represent the response of the majority of structural materials. However, there may be a number of purely brittle materials but these are not considered present in either the DLHC or HSC.

Figure 5.3 shows a schematic representation of a number of material degradation models. The instantaneous model has already been discussed and deemed be a poor representation of the present material response due to results obtained from resin characterisation tests from Chapter 4 revealing that failure does not occur instantly. Therefore the instantaneous model will be disregarded in the present study. The constant stress model represents an elastic-purely plastic material. Once initial failure has occurred the material becomes purely plastic, with no increase or decrease in stress with increasing strain. This is the method commonly found in the non-isotropic polynomial criteria where, depending on the failure type, specific elastic modulus values are reduced to a near zero state [48]. Between the instantaneous and elastic-purely plastic models there could be an infinite number of possible functions. This would require not only a reduction in the stiffness of the material but also a reduction in the stress present in the failed element. This can be represented as a negative elastic modulus. This will result in a number of issues including numerical instability during the non-linear solution of the finite element model. The choice of the stress reduction function will depend on the behaviour of the material post-initial failure and can only be obtained through an experimental testing programme. Information used for the materials degradation model were obtained from the material characterisation experiments outlined in Chapter 4.

5.2.3 IMPLEMENTATION OF THE PDM TECHNIQUES

The failure criteria and property degradation model are implemented using user subroutines written in FORTRAN that can be linked into the FEA software ABAQUS, information and file format details on these subroutines can be found in the ABAQUS documentation[†]. Two of the subroutines that can be used in the implementation of damage progression analysis are USDFLD and UMAT. The former is used to perform calculations on the stress and strain state of the numerical model and to output field variables to indicate failure. The latter, UMAT, is used to implement user defined material properties, and hence resultant strain levels based on the material properties and the stress levels within the numerical model. Both subroutines can be programmed with the appropriate failure criteria to alter material properties and indicate the failure of any element. In order to incorporate both the non-linear material properties and the damage progression model the UMAT subroutine was used within the analysis.

5.3. DESIGN OPTIMISATION METHOLOGY

The present research has used experimental and numerical techniques to analyse the static, fatigue and aged performance of a typical hybrid connection. However, it was described in Chapter 3 that the design of the HSC, the full-scale hybrid connection, was performed outside of the present research. This section aims to outline the method that was used to investigate whether there is a better design of the hybrid connection based on two main goals, increased structural performance and reduced weight.

There are a number of techniques that can be used to obtain optimum solutions to a given problem and the selection of the method is dependent on the problem to be solved. Such techniques include Secant and Newton-Raphson methods often used to obtain minima and maxima of single dimension problems, hill-climbing methods for multi-dimensional problems and evolutionary algorithms that are used for non-linear, discrete and often discontinuous problems. In the present research the design space of the hybrid connection could fall into the latter category and is the method implemented. Regardless of the

---

[†] ABAQUS Inc., Rising Sun Mills, 166 Valley Street, Providence, RI 02909-2499, USA

evolutionary method used there are a number of discrete steps involved in the search for an optimal solution.

- Input generation
- Encoding
- “breeding”
- Selection

5.3.1 INPUT GENERATION

The first step in any numerical optimisation method is to describe the object mathematically. In the present research a joint design is being analysed, the principal dimensions of the joint are used as the main information to describe and define the joint in mathematical space. The joint design being analysed in this study is the HSC configuration as it is representative of a real structural connection.

A number of parameters are assumed to be constant throughout the analysis, these are:

- Overall joint length – 700 mm
- Material properties of GRP, steel and Balsa core
- Length of steel beyond the GRP/steel overlap used for attachment of superstructure to the deck of the ship – 110 mm (minimum permitted value due to heat transfer during welding)

The joint can now be described by seven variables:

1. Adhesive thickness
2. Steel thickness
3. Core thickness
4. GRP skin thickness
5. Steel/GRP bond length
6. Taper zone length

7. Adhesive Young's modulus

Knowledge of these geometric parameters allowed the definition of the HSC specimen and formed the basis of a finite element model, the geometry defining the location of the key points of the joint. A FORTRAN programme was developed to create a finite element model of the joint. A number of important considerations were addressed at this stage. Firstly, it is known that FEA mesh density is important for the accurate modelling of resultant stresses and global response. This was incorporated into the programme by ensuring that the mesh density was constant. Secondly, the location and magnitude of the applied load and boundary conditions were kept constant. These two points ensured that the results were directly comparable. Finally, the mesh aspect ratio was kept within the limits (1:20) of the software to ensure accurate results. The solution to the finite element analysis can be used to obtain information on the joint configuration being analysed and form the basis of the selection methods. The inputs of the basic geometric values mentioned above are provided from within the genetic algorithm.

5.3.2 GENETIC ALGORITHM IMPLEMENTATION

The genetic algorithm methodology is shown in Figure 5.4. The first step involved the physical model definition described in Section 5.3.1. The design space was then constrained by limiting the range in which the geometric variables can be altered. This can be conducted using two methods. Firstly, the range of the variables can be chosen based on realistic and practically achievable geometries, i.e bondlines greater than 20 mm or GRP skin thicknesses less than 1 mm are not practical. This will result in a relatively large design space. Secondly, a technique such as the parametric study from the previous section, can limit the design space to explore only the range of variables that will give favourable results. In the present research the latter of the two methods was implemented and will be discussed in Chapter 8.

Once the design space was established a random number of individuals was created to produce the initial population by randomly selecting a value for each design variable. This process is repeated to achieve the required initial population. The random input variables were then processed to generate finite element models from which solutions were obtained. Information obtained from the FEA and elsewhere was used to form a fitness criteria for each individual in the population, which will be discussed in detail in Section 5.3.3. Based on the results of the fitness analysis the best individuals are selected to create the new generation. “Breeding” of the chosen individuals requires that each individual’s variables be encoded so that they form a genetic code, analogous to nature’s genome. Binary numbers are often used to achieve this.

The first stage in the “breeding” process is crossover. This is a process whereby two genetic codes (individual joints) are combined to create a new code (new individual). The philosophy is that the new individual may be better than the two individuals used to create it if the new individual takes the best characteristics of each. There are a number of ways in which crossover can be completed. In the present research a single point crossover is conducted. Consider the following binary strings, which represent two individuals, which have been selected for crossover. The symbol ‘|’ is used to indicate the randomly chosen crossover point.

Individual 1: 11001|010

Individual 2: 00100|111

After interchanging the individuals codes at the crossover point two new individuals are created.

New individual 1: 11001111

New individual 2: 00100010

If the genetic algorithm was allowed to run using only crossover as the “breeding” parameter it could be possible for the population to stagnate at a local optimum. Mutation is used to introduce new individuals into the population to prevent this occurring. Again there are a number of ways in which this can be conducted. In the present research a relatively simple ‘flip bit’ method is used. This method is only valid if the individuals are encoded into binary numbers. At a randomly chosen location in the binary code a single bit of information is flipped from being a 1 to a 0 or vice versa, thus creating a new individual. Mutation occurs during the genetic process according to a user-definable mutation probability. Low values will prevent the search turning into a primitive random search.

Once the new population has been created through crossover and mutation the binary representation of the individual is decoded into a physical joint. If the genetic algorithm has completed the user-defined number of generations or certain convergence criteria are met then the process can be stopped. However, if the algorithm is to continue then the evaluation and selection stages are completed once more and a new generation created.

5.3.3 SELECTION CRITERIA

The selection criteria or measure of fitness ensures that joints with favourable attributes are carried forward into the next generation of the genetic algorithm. The method of obtaining a suitable fitness criterion can be complex. This is particularly true if there is more than one objective to the problem, commonly referred to as multi-objective functions. In the present research a single main objective function was used. However, as the optimisation of the main objective occurred a reduction in the fitness of the secondary functions was prevented. This simplified the problem by eliminating the true multi-objective nature of the problem but monitors the secondary objectives as an important feature of the joint design.

Chapter 6

Strength and durability characterisation of steel-composite connections

6.1. INTRODUCTION

The aim of this chapter is to develop an understanding of hybrid steel-to-composite joints for use in marine structures under static and cyclic loading. Currently there is little knowledge on the behaviour of such joints and this information is required by the structural engineer to better understand the performance of such joints during the service life of the structure. The joints used in the fatigue life characterisation, the DLHC and HSC, are described in Chapter 4. The former joint can be described as a generic hybrid connection and a good understanding of the loading mechanisms and failure modes will help in the design of more complex structural connections, such as the HSC, which is a representation of a full-scale hybrid connection.

Firstly, the HSC configuration is examined in both the static compressive loading and compressive fatigue loading. This characterises the performance of the HSC joint and provides an insight into its failure modes and loads. Secondly, the unaged base-line characteristics of the DLHC configuration are obtained through static and fatigue in tension and bending. This information will be compared to the hygrothermally-aged performance. Finally, the residual strength of the HSC joint after compressive fatigue loading is assessed.

6.2. STRENGTH AND FATIGUE CHARACTERISTICS OF THE 'HSC' JOINT

6.2.1 STATIC TESTING

The first phase of characterising the fatigue life of any material or joint configuration is to obtain the ultimate strength of the material/joint. This will identify the maximum load amplitude for the fatigue test phase. For the static testing of the HSC, two boundary conditions were examined; with and without anti-bending guides, as described in Chapter 4.

The first static tests were carried out without the use of anti-bending guides. Under compressive loading, it was observed that there was a large lateral deflection in the region of the steel-balsa interface caused by the load path eccentricity of the joint design. It was felt that such deflections were unrealistic for the application proposed for the hybrid joint. When used as the external skin of a helicopter hangar, internal frames and stiffeners would support the joint region. As mentioned earlier this would prevent the excessive lateral bending observed in the experiments. A similar axially compressive static test was carried out with the anti-bending guides, described in Chapter 4, in place. This significantly reduced the out-of-plane bending caused by the eccentric load path and provided a more realistic response to the compressive load. The position of the anti-bending fixture and hence the internal framing within the helicopter hanger structure will also have a marked influence on the response of the hybrid joint. Figures 6.1a and 6.1b show a numerical simulation (with exaggerated displacement scaling) of the joint and its response to compressive loading with the anti-bending guides located in two positions. A detailed discussion on the use of anti-bending guides is given in Chapter 4 with the main reasons being the accurate representation of the boundary conditions of the specimen as would be found in a realistic application. The results are presented in detail in section 6.2.1.2.

6.2.1.1 Failure mode

It is known that any axially loaded joint will develop high stress concentrations at the ends of the jointed region [23]. In the current research, an additional stress concentration will be present due to load eccentricity and subsequent internal bending (global bending has already been removed by the anti-bending guides). Thus, it is assumed that the most highly stressed region of the joint should be located at the steel/balsa interface and in particular on the flat side. It is in this region that the initial crack was observed. The anti-bending guides prevent bending in the lateral direction of the flat side of the hybrid joint. Due to this constraint there was some subsequent lateral bending in the opposite direction in the region of the balsawood taper. This caused some shearing failure of the balsawood core near to the end of the taper, which introduced some additional stress concentrations at the crack tips. Ultimately the failure of the balsawood in shear caused de-bonding of the balsa and the GRP.

Once initial failure had occurred, the crack propagated along the steel/GRP interface on the flat side. It is expected that the cause of the initial crack is due to peel forces resulting from the load path eccentricity. This crack extended due to Mode I crack opening until the anti-bending guides are approached. From this point on the crack extended due to Mode II shearing of the adhesive layer. Figure 6.2 shows an annotated picture of a failed specimen.

In some cases, as the crack propagated beyond the second anti-bending guide, structural collapse appeared to be dictated by buckling failure of the GRP skin between the anti-bending rollers. Figure 6.3 shows the matrix whitening and subsequent fibre breakage in this location. In this figure the crack front is also visible as being significantly beyond the second anti-bending guide location.

A series of Euler buckling calculations were conducted to determine the critical buckling load of the de-bonded skin. The material properties of the laminate are given in Chapter 4 and the geometric properties assume it is a 4 mm x 100 mm column (equivalent to the skin thickness and the specimen width respectively), assuming that the de-bonded skin is treated as simply supported, a critical buckling load of -22 kN is obtained. This load value is considerably less than the load being applied to the system at the time of failure. In addition, if the skin is treated as fully encastred at either end then the critical buckling load is -88 kN. Whilst neither of these buckling calculations is physically representative due to the gross approximation in applied boundary conditions, it is reasonable to assume that the determined values bound the physical case. The load level applied to the joint at the time where the crack extends beyond the anti-bending guide is higher than either Euler critical bending loads. Therefore as the crack extends to beyond the anti-bending guides it can be expected that the now unsupported skin would immediately destabilise.

The joint appears to fail entirely cohesively. There is no apparent delamination of the GRP laminate before the onset of full structural collapse and there is only some minor damage to the balsawood core. The majority of failure occurs within the adhesive layer between the steel and the GRP leaving resin residue on both surfaces.

The use of a grit-blasted surface preparation appears to have a positive influence on the failure mode of the joint. The presence of resin on both surfaces of the failed components indicates that the resin has had good mechanical and chemical adhesion to the steel surface and the resulting failure is a function of the shear and peel strength of the resin itself. Therefore, it can be assumed that an increase in properties of the resin in terms of shear and peel strength characteristics would result in a higher resistance to failure providing the mechanical and chemical connection between the resin and steel remains equal.

6.2.1.2 Results

The results obtained from the static testing are shown in Figure 6.4. From the graph it is clear to see that the use of the anti-bending guides has a marked influence on both the stiffness and ultimate failure load of the HSC, the ultimate strength is increased by over 200 percent by the use of the guides. This result is expected, as the large lateral deflection observed in tests without anti-bending guides would result in a large increase in the magnitude of the stress concentration.

From Figure 6.4, there is a decrease in stiffness of the joint at a load of just over -60 kN. It is assumed that this corresponds to the lateral deflection of the taper region and hence the onset of damage within the joint. The crack appears to extend between -60 kN and ultimate failure and Figure 6.4 suggests that the crack growth is steady as stiffness remains constant. Ultimate failure of the joint occurs at a load of -108 kN.

In order to account for possible experimental error and scatter, not measurable experimentally due to limited specimen numbers, a nominal ultimate compressive strength (UCS_{nom}) of -100 kN is used for the remainder of the fatigue and residual strength work on the HSC. The -100 kN UCS_{nom} provides a conservative limit for maximum cyclic load levels and equates to an expected experimental scatter of 8 percent.

6.2.2 FATIGUE LIFE CHARACTERISATION

6.2.2.1 Data analysis

Load and displacement data was acquired every 100th cycle and stored for analysis. This data was used to investigate any stiffness degradation over the specimen life. Fitting a straight line to the hysteresis loop of the load-deflection curve and obtaining the gradient provided the stiffness of the joint. The results are plotted against number of cycles. In addition, the area inside the hysteresis loop is calculated. A change in this area with number of cycles indicates a release of energy due to damage within the structure [77] assuming no rig damage. More detail with respect to the data analysis can be found in Chapter 4.

6.2.2.2 Compression-compression (17-34 percent UCS_{nom}, specimen 12a)

Specimen 12a was tested in a compression-compression cycle between approximately 17 and 34 percent of its UCS_{nom}, corresponding to -17.2 kN to -34.4 kN. The test was carried out at a frequency of 1 Hz to ensure that the correct load levels were being reached and to limit the effect of thermal stress caused by rapid deformation. After 10^6 cycles the test was stopped. Figure 6.5 shows that there is very little variation in the stiffness of the specimen or energy released by the system. In addition, after 10^6 cycles there was no visual indication of damage. Based on these results it could be assumed that there is no damage within the structure and so its residual strength should be similar to the static compressive strength.

6.2.2.3 Compression-compression (34-69 percent UCS_{nom}, specimen 12b)

In an attempt to induce failure of the hybrid joint before 10^6 cycles the mean load was increased. Specimen 12b was tested in a compression-compression cycle at a mean load level of approximately 52 percent of UCS_{nom} with a load amplitude of approximately 17 percent at a fatigue rate of 2Hz. The frequency was increased from 1Hz to 2Hz as the actuator had no difficulty in reaching the prescribed loads in time and no change in temperature was observed in the specimen during cycling. This specimen showed no visible signs of damage after nearly 1.3×10^6 cycles. The acquired data from the test was analysed for specimen stiffness degradation and energy release. Figure 6.6 shows the results of the analysis. The two peaks in the stiffness plot are caused by tightening the rig during the test when the rig bolts began to work themselves loose. The stiffness plot indicates that there is very little if any loss in stiffness of the specimen. Based on the results obtained from the first two fatigue tests (specimens 12a and 12b) it could be assumed that if there is no loss in stiffness or increase in energy release, both indicative of damage, then it can be assumed that there will be little drop in residual strength.

6.2.2.4 Zero-compression (0-86 percent UCS_{nom}, specimen 13a)

The fatigue tests carried out on Specimen 12b (mean load equal to 52 percent of UCS_{nom} and a load amplitude equal to 17 percent of UCS_{nom}) did not produce failure therefore it was decided to test a specimen with the load amplitude increased to 43 percent of UCS_{nom} and the mean load reduced slightly. The results were again analysed for loss in stiffness and plotted in Figure 6.7. It is apparent from this plot that there is a loss in stiffness and a corresponding increase in energy release. Both of these results indicate damage within the joint, which is verified by failure occurring after 1700 cycles.

6.2.2.5 Zero-compression (0-69 percent UCS_{nom}, specimen 14a)

Specimen 14a was tested at a load range of between 0 kN and –68.8 kN (or 0-69 percent UCS_{nom}). Complete failure occurred after 80264 cycles. The results were again analysed for loss in stiffness and energy dissipation in the system. It was observed that at approximately 50,000 cycles that a small area of debonding occurred at the interface of the steel and GRP on the tapered side of the specimen. The crack grew progressively with increasing numbers of cycles. Figure 6.8 indicates a loss in stiffness just below 50,000 cycles corresponding to the appearance of the debond. Unusually the stiffness of the specimen appears to increase between the point of initial failure and the next observed debond growth at 63,000 cycles. However from this point to failure there is a steady loss in stiffness as the crack grew. Similarly, there is a corresponding increase in energy dissipation as energy is used to propagate the crack towards failure.

6.2.2.6 Zero-compression (0-60 percent UCS_{nom}, specimen 14b, 15a)

Two specimens were tested at cycling load levels from 0 kN to -60.2 kN. Specimen 14b failed after 187153 cycles but on removal of the specimen from the test rig, one of the four mounting bolts on the composite end of the specimen was found to have failed. This failure might have led to an increase in the lateral deflection of the specimen and subsequently a premature failure of the hybrid joint due to increased peel stresses at the interface between the steel and GRP on the flat side. A second test was therefore carried out on specimen 15a, the results of which are shown in Figure 6.9. Specimen 15a failed after 561700 cycles.

6.2.2.7 Zero-compression (0-51 percent UCS_{nom}, specimen 13b)

Specimen 13b was tested at a load level cycling from 0 kN to -51.6 kN. On visual inspection, after 3548500 cycles the specimen appeared to be virtually undamaged, with perhaps the slightest of matrix cracking in the overlaminate radius on the tapered side and slight whitening apparent on the flat side of the specimen between the GRP skin and the steel (indicative of debonding). The stiffness degradation and energy release plots are given in Figure 6.10 and reflect the fact that whilst the specimen appears to be relatively undamaged, there are progressive failure mechanisms at work. Despite this it seems that with these prescribed boundary conditions and load levels, the specimen is operating at, or close to, the endurance limit.

6.2.2.8 Zero-compression (0-77 percent UCS_{nom}, specimen 15b, 16a)

Two specimens were tested at cycling load levels from 0 kN to –77.4 kN. Specimen 15b failed after 30880 cycles and specimen 16a after 11018 cycles, the results of which are shown in Figures 6.11 and 6.12 respectively. The failure of both specimens was a result of complete debonding of the GRP from the steel on the flat side of the specimen.

6.2.2.9 Fatigue life curve

The tests performed to produce the fatigue life curve are shown in Table 6.1. This test matrix became evolutionary in nature as it became apparent that some of the tests were not suitable to this joint configuration. For example, the performance of the joint at low load amplitudes (below 25 percent UCS_{nom}) and relatively high mean load has been shown to be operating under the endurance limit and hence low load amplitude tests were replaced. Figure 6.13 shows the fatigue life curve of the hybrid joint in terms of load amplitude (P_a) and number of cycles ($\log_{10}N$).

Table 6.1 Fatigue life test matrix

Test	Result	Comment
17-34% UCS_{nom}	N/a	No Failure, increase mean load
34-69% UCS_{nom}	N/a	No Failure, increase load amp
0-86% UCS_{nom}	1700	Failure
0-77% UCS_{nom}	20949	Failure
0-69% UCS_{nom}	101432	Failure
0-60% UCS_{nom}	374427	Failure
0-51% UCS_{nom}	3548500	No Failure, approaching endurance limit

A representation of the whole life of the joint may be described by a number of discrete functions. Figure 6.13 shows a discrete logarithmic function representing the experimental data without consideration of the static test case. The level of correlation between the chosen logarithmic function and the experimental data is high, with a *variance accounted for* value, VAC or R^2, equal to 0.95. A more appropriate and useful function to represent the data would be continuous in nature. A Weibull cumulative density function, W(N), commonly used to describe the fatigue behaviour of composite structures [85, 86] is therefore also presented in Figure 6.13. The Weibull function is defined from the UCS and is fitted using the *shape, β*, and *scale, η*, parameters as described in Equation 6.1. These parameters are selected so as to provide a minimum value of error through the least squares approach. The correlation between the experimental data and the function used to fit the data is very good with an R^2 value also equal to 0.95, validating the use of the Weibull function to describe the as-determined fatigue life of the hybrid joint. It must be noted that the function is based upon a fatigue load endurance limit of 25 percent of UCS_{nom} at this load level the specimen exceeded 3.5 million cycles but did not fail. A refinement of the endurance limit may produce a slightly different curve.

$$W(N) = UCS - \left(UCS \cdot e^{-\left(\frac{N}{\eta}\right)^{\beta}} \right) \qquad (6.1)$$

The curve obtained from the present study is typical of those obtained from fatigue characterisation of composite materials [85]. The goodness of fit of the Weibull cumulative density function provides confidence in predicting the joint life and the corresponding probability density function can predict the probability of failure for any given load amplitude under the prescribed boundary conditions.

6.3. STRENGTH AND FATIGUE LIFE OF THE DLHC

The aim of the ultimate strength tests of the DLHC is to identify the failure mode and location of initial failure. In addition, the static tests will provide the maximum load amplitude possible for the fatigue testing. The ultimate strength of the DLHC will be used as a base to which the hygrothermally aged specimens can be compared.

The experimental test methods used to characterise the performance of a hybrid joint have been described in detail in Chapter 4. The DLHC was tested in axial tension and 4-point bending.

6.3.1 SPECIMEN CONFIGURATION

The strength and fatigue tests for the DLHC were conducted on specimens having two GRP laminate configurations. The difference between the two was the introduction of an additional interface layer between the tri-axial cloth and the primed steel surface on a number of specimens (for more information on specimen manufacture see Chapter 3). The additional reinforcement layer consists of a light chopped strand mat (CSM) layer. The reason behind the inclusion of this layer was to increase the resin rich layer at the interface of the steel and GRP laminate. During the resin infusion manufacturing process (Chapter 3) the resin which forms the bond between the GRP and the steel is very thin (approximately 0.3 mm). It was suggested that by increasing the thickness of the resin layer at the interface an increase in joint performance could be achieved. A number of static and fatigue specimens were manufactured without the CSM layer and the remainder with the CSM interface.

6.3.2 STATIC TESTING

Both the specimens, with and without the CSM interface layer, were tested in both axial tension and 4-point bending to destruction. Load, span deflection and control deflection were acquired for the axial tests and load and roller deflection acquired for the 4-point bend tests. Details of the test set-up for both axial and bending tests can be found in Chapter 4. Due to the high loads expected during the destructive testing of the axial specimens no visual observations of the specimen failure were conducted due to safety issues.

6.3.2.1 Axial tension results

Figures 6.14 and 6.15 show the load-deflection curves for the DLHC specimen manufactured with and without the CSM respectively. The specimens containing the CSM failed at a greater average load of -180 kN than the -171 kN obtained from the specimens that did not contain the CSM interface layer. Table 6.1 provides some statistical information on failure loads and specimen stiffness during the experiments calculated from Figures 6.14 and 6.15. The increased failure load of the specimen containing the CSM layer could be due to the CSM layer artificially increasing the adhesive layer thickness. The CSM material results in a GRP lamina that has a lower fibre volume fraction than the rest of the laminate. By increasing the adhesive thickness it can be shown using closed-form solutions that the Von Mises stress concentration can be dramatically reduced compared to very thin adhesive layers. This will be discussed in more detail in Chapter 8 and the results can be seen in Figure 8.3. The adhesive layer is known to be very thin when no CSM is present (0.3 mm) and by introducing the CSM layer the bond thickness may approach 1 mm. This would significantly reduce the von Mises stress concentration resulting in a higher load at which failure would be initiated. However, Table 6.2 does highlight that the CSM layer produced a range of results with a higher coefficient of variation than those without the CSM. It was observed that some of the CSM fibres at the internal end of the joint were highly stressed, noticeable due to the excessive matrix whitening. This was the reason for the failure, in some cases, to switch from the interface between the steel and CSM and the CSM and the tri-axial cloth. This resulted in the increased experimental scatter for the CSM specimens.

Table 6.2 Results from the DLHC static tests

	Failure Load (kN)	
	No CSM	**CSM**
Specimen 1	-170.3	-169.7
Specimen 2	-165.4	-184.7
Specimen 3	-177.9	-184.2
Average	-171.2	-179.5
Coeff. Of Var (%)	3.7	4.8

Numerical regression was conducted to examine the rate of change of stiffness with respect to increasing deflection. Figure 6.16 directly compares two of the typical load-deflection curves, specimen 3 from each of the tests. Only between 10 percent and 90 percent of the ultimate failure load is presented to minimise any possible errors during the regression. Data located outside of this load range can influence the regression and result in a poor level of fitness. At the lower end (i.e. below 10 percent) there maybe slack in the experimental test fixtures being taken up resulting in an uncharacteristic curve shape. Similarly at levels above 90 percent (i.e. just before failure) there may be some unusual curve characteristics due to, for example, a material entering the plastic phase prior to failure. By applying a limited range of data for the regression analysis, the procedure can be made more robust reducing the possible introduction of errors.

A polynomial regression line with an R^2 value in excess of 0.99 was applied to the data in order to conduct a numerical differentiation to obtain the stiffness of the load deflection plots with respect to increasing deflection. Figure 6.17 shows the relationship between stiffness and deflection for the load-deflection curves given in Figure 6.16. It can be seen that there is a more rapid loss in stiffness in the specimen without the CSM layer. However, there is a larger proportion of the curve with constant stiffness with the CSM layer than without the CSM layer. As both specimens approach their ultimate failure load there is an increase in the non-linearity of the load-deflection curves.

It is assumed that a large stress concentration will develop at the ends of the GRP overlap as is often found in adhesive lap joints [23]. In addition, due to the small balsawood section between the two steel inserts of the DLHC causing internal bending, there may be some additional stress concentration near the internal end of the steel insert at the balsa/steel interface. However, it is expected that the initial crack occurred at the end of the overlap and progressed along the joint to a point where insufficient bond area remained and the joint failed due to shear. Based on a failure load of -180 kN this equates to a critical bond length of 52 mm, just over half of the joint length. Therefore, a crack length exceeding 48 mm in length would be expected to result in complete failure of the bond. This simple calculation assumes that failure occurs in the adhesive and is based on the shear strength of the adhesive. It also assumes that the specimen remains perfectly in plane. As was discussed earlier this may not be the case with the possibility of some internal bending at the centre of the joint where the balsawood section is located. If failure occurs in the laminate the inter-laminar shear strength could be used to assess the critical crack length.

The failure modes of the DLHC specimen with and without the CSM layer are shown pictorially in Figure 6.18a and 6.18b respectively. The specimen containing the CSM layer

(Figure 6.18a) shows failure occurring in both the interface between the steel and CSM and between the CSM and the tri-axial cloth. However, in terms of the present research, the CSM layer is not deemed to be a part of the adhesive system as its presence is to increase the resin volume fraction at the interface between the steel and GRP. Figure 6.18b shows the failure surfaces of the specimen without the CSM layer. Failure occurred only at the interface between the steel and tri-axial layers. In addition, this specimens failure load was lower than that obtained from the specimen in figure 6.18a. Figure 6.18 highlights that there is better adhesion between the GRP and steel when the CSM layer is present (Figure 6.18a).

6.3.2.2 4-point bending results

Figures 6.19 and 6.20 show the load-deflection results from the 4-point bend tests on the specimens without and with the CSM layer respectively. In Figure 6.19 a significant experimental scatter of over 14 percent is present in the ultimate failure load results. This compares to a coefficient of variation of only 2.5 percent for the specimens that do not contain the CSM layer (Figure 6.19). However, on average, failure load is 38 percent higher with the CSM interface layer.

The failure of both the specimens with and without the CSM layer always occurred on the lower face (tensile face) of the specimen. Figures 6.21 and 6.22 show the failed specimens without and with the CSM interface respectively. From Figure 6.22 it is clear that failure occurred within the CSM interface layer, as there were random fibres present on both the steel and GRP surfaces. In contrast the specimen with no CSM layer failed at the steel/GRP interface cohesively in a similar manner to both the HSC and DLHC axial tests. It is assumed that the introduction of the CSM layer at the interface between the steel and GRP will result in a layer that has a relatively high resin volume fraction compared to the remainder of the GRP laminate. This is the equivalent of increasing the adhesive thickness. This change in the joint configuration is known to result in a reduction in Von Mises stress concentration in the joint under axial tension and bending as discussed in Section 6.3.2.1.

6.3.3 FATIGUE TESTING

One of the aims of this research was to investigate the fatigue performance of the DLHC as a baseline for the hygrothermally aged specimens. In order to achieve this the fatigue performance of the unaged DLHC must be defined for specific load levels based on the results of the static testing. A fatigue load range of -17.95 kN to -107.7 kN, equivalent to 10% to 60% of the ultimate tensile strength (UTS) of the DLHC specimens was examined as a load which would induce failure but provide a relatively large number of cycles to failure. Three specimens were tested at this load range at a frequency of 1 Hz. The results are given in Table 6.3. The value of the coefficient of variation shows that the results obtained from the fatigue tests are unacceptable due to the extremely large experimental scatter. The level of experimental scatter is surprising as all three specimens were manufactured simultaneously in panel form as described in Chapter 3.

Table 6.3 Number of cycles to failure of DLHC for 10% to 60% of UTS

Number of cycles to failure				
Spec 1	**Spec 2**	**Spec 3**	**Average**	**Coef. of Var.**
16188	128527	65113	69942.6	80.5

Figure 6.23 shows the stiffness loss of specimens 2 and 3 for the DLHC tested at 10% to 60% of the UTS. Specimen 1 is ignored in this discussion due to a poor quality of data obtained during the test. The results show little difference in initial stiffness however specimen 3 does show the same level of stiffness degradation near to failure. Therefore the stiffness degradation plots do not reveal the reason for the experimental scatter. Limited experimental specimens prevent further investigation of the experimental scatter by further testing. The failure surfaces of the fatigue specimens were examined visually in an attempt to understand why the fatigue tests result in such large experimental scatter, particularly for specimens that were manufactured simultaneously. Figures 6.24a and 6.24b show the failure surfaces of specimen 2 and 3 respectively. The figures show the surface of the GRP that debonded from the steel and balsawood remains at the top of each picture indicate that this was the centre of the joint. The first noticeable difference in the failure surfaces is the amount of de-lamination between the CSM layer and the tri-axial cloth at the centre of the joint. Figure 6.24a corresponds to the specimen with the highest number of cycles to failure and this failure surface shows the largest amount of de-lamination. Also noticeable in the failure surfaces is the presence of matrix whitening around the random fibres at the end of the de-lamination. This may be one reason why the de-lamination did not continue along the CSM/tri-axial cloth interface. If the failure crack jumped to the steel/GRP interface

earlier in Specimen 2 (Figure 6.24b) as indicated by the smaller de-lamination zone this may have resulted in premature failure. The results of the fatigue tests in this section of the present research are an area that requires considerable further research. The stacking sequence and the introduction of the CSM layer at the interface could have a significant influence on the repeatability of the fatigue tests. Due to limited experimental specimens such an investigation cannot be considered in the present research.

6.4. RESIDUAL STRENGTH CHARACTERISATION OF HSC

Residual strength tests allow the evaluation of remaining strength in a structure after a given life cycle. In the present research the hybrid joint has been subjected to in-plane fatigue cycling to induce a crack up to a pre-determined length, representing a portion of the structures life. Full details of the experimental set-up and procedure can be found in Chapter 4.

6.4.1 FATIGUE CONDITIONING OF THE HSC

A fatigue cycle that produced damage in a reasonable time scale was chosen to condition the residual strength specimens. The fatigue cycle chosen was 0-69 percent of the UCS_{nom}, equivalent to a load amplitude of -34.4 kN at a frequency of 1Hz. The test set-up used was identical to that used in the fatigue life characterisation in Section 6.2.2. The method of obtaining specific crack lengths in the investigation of residual strength was conducted by the use of a resistance wire approach described in detail in Chapter 4.

6.4.2 RESIDUAL STRENGTH TEST RESULTS

The crack lengths and corresponding residual strength results obtained from the out-of-plane residual strength tests are presented in Table 6.4. A graph of initial joint stiffness against crack length is shown in Figure 6.25. From this figure there appears to be a trend of stiffness reduction with increasing crack length. Figure 6.26 shows the full load displacement plot for specimen 22a (50 mm crack length). There are a number of points of stress relief in this graph and these correspond to the specific failures within the joint (description of the events in Figure 6.26 are given in Table 6.5). The out-of-plane failure of the hybrid joint is shown graphically in Figure 6.27. The results presented in Table 6.4 indicate that residual strength remains at 100 percent regardless of the length of the fatigue cracks investigated. However, due to the joint being fully encastred, the steel near the end clamp yields. This causes a peel stress at the steel end of the GRP overlap on the flat side and begins a debond at this interface. If the fatigue crack and the crack induced from the peel stress at the steel end met, resulting in a complete debond of the GRP/steel interface on the flat side, the stiffness and hence the ultimate strength of the joint may be reduced. However, with the fatigue crack tip being sufficiently far away from the end of the overlap, and limitations in the experimental test rig, the two cracks did not converge hence the joints all fail due to a debond between the GRP and balsa on the taper.

Table 6.4 Out-of-plane residual strength test results

Specimen No.	Crack length	Failure Load (kN)	Mid-Span Displacement
23a	0	11.4	14.1
22a	50	11.4	12.0
20a	75	11.3	16.0
19b	115	12.7	20.7
23b	145	11.1	13.7

Table 6.5 Events recorded during residual test

Event	Observation	Load (kN)	Disp. (mm)
0 to A	Tip of balsa within the taper begins to make cracking sounds as load is increased. The GRP begins to debond from the steel on the taper side at the centre of the joint	0-11.4	0-12.0
A to B	Once the crack on the taper side (steel/GRP interface) exceeds a critical length, load is released as the GRP/Balsa interface parts along the length of the taper on the taper side	11.4-7.9	12.0-12.7
B to C	The remaining balsa outside the taper region is put under stress as the load rises	7.9-10.1	12.7-19.9
C to D	The GRP/balsa interface parts along the entire length of the interface on the taper side	10.1-6.9	19.9-22.3
D to E	Load rises over a large increase of displacement as the existing fatigue crack is opened and increased by a further 10 mm	6.9-10.3	23.3-46.2

It is expected that the loading applied to the residual strength specimens will result in an in-plane shear stress in the adhesive layers caused mainly by the differences in elastic modulus. As discussed in Chapter 4, the specimen is not expected to withstand transverse shear stress due to external loading. This would be taken by the internal stiffening of the structure a common scenario in thin walled structures. The 4-point bend test represents this, as there is zero transverse shear stress present between the rollers. Therefore, the extension of the crack due to bending is assumed to be due to the in-plane shear due to material property differences.

6.5. INFLUENCE OF HYGROTHERMAL AGEING ON PERFORMANCE

The aim of this section is to investigate the effect, if any, moisture has on the performance, both statically and dynamically, of the DLHC. It is commonly agreed that the influence of moisture can have a dramatic effect on the mechanical performance of GRP as discussed in Chapter 2. In the present research it is the performance not only of the GRP but also the interface of the connection between the steel and GRP substrates. Although there has been relatively little work conducted on the correlation between accelerated and natural ageing, the influence of moisture on the performance of steel to composite joints is unknown.

As discussed in Chapter 4, the DLHC specimens used for the hygrothermal ageing can be described as a worst-case situation. Other than the vinylester resin layer present due to the infusion manufacturing process, there is no protective coating applied to either the steel or the GRP. This in terms of realistic ships structures is very unlikely. However, by obtaining results with structures in this bare state, a level of safety is automatically incorporated into the results as the real structure would be more resistant to the ingress of moisture due to primers and external paints.

Specimens were subjected to immersion in distilled water at 40ºC and removed at intervals to assess their static performance. The results of this provide information on any degradation in global response. Based on the results of the static tests a series of fatigue tests are conducted to assess any change in the dynamic global response of the DLHC due to accelerated ageing.

6.5.1 STATIC TESTING

Axial and bending static tests were conducted on aged specimens at intervals during the accelerated ageing process described in Chapter 4. The method of testing was exactly the same as that used for the unaged specimens. All aged specimens contained the CSM interface layer. The results of the axial static tests are presented in Table 6.6. The coefficients of variation of both the failure load and displacement results were good resulting in a high level of confidence in the results. The change in failure load with increasing immersion time was relatively small. This indicated that there was little degradation of the interface between the GRP and the steel. Failure of the unaged specimens containing the CSM interface layer, as discussed in Section 6.4, occurred between the CSM and the Tri-axial cloth. The first observation after 5544 hours of immersion was that the failure location had moved and was now solely between the steel and GRP. Figures 6.28a and 6.28b show the comparison between the unaged and aged failure surfaces respectively.

Table 6.6 Results of the static tests on aged DLHC specimens

Panel	Hours immersion	Spec 1	Spec 2	Spec 3	Average	Coef. of Var (%)	% change
					Failure Load (kN)		
20	0	169.70	184.75	184.20	178.36	4.75	0
3	5544	169.69	169.10	170.17	169.66	0.32	-4.88
11	11592	154.66	153.32	162.83	156.93	3.28	-12.01
12	14280	-	163.55	169.39	166.47	2.48	-6.67
28	18936	-	152.83	142.54	147.69	4.93	-17.20
					Failure Displacement (mm)		
20	0	9.75	11.62	11.69	11.02	10.01	0
3	5544	10.05	10.55	10.31	10.30	2.42	-6.48
11	11592	9.33	9.41	9.98	9.57	3.74	-13.11
12	14280	-	9.34	9.73	9.53	2.92	-13.49
28	18936	-	7.39	6.92	7.16	4.63	-35.03

A comparison was made between the load deflection curves of the unaged, 5544 hours and 11492 hours aged specimens to determine if there was any significant difference between the response of the specimens. The plots are shown in Figure 6.29. Within the groups of unaged and aged specimens there is consistency of slope and overall shape of the load deflection curves. However, when comparing the unaged and aged curves there is a marked difference between their shapes. The point at which the curves become non-linear is lower for the aged specimens. However, the stiffness of the specimens less than -100 kN is very similar. This may be an indication the failure paths are different as highlighted in Figure 6.28.

From Table 6.6 the major change due to the accelerated ageing process was in the failure displacement. Figure 6.30 shows the comparison between percentage change in failure load and percentage change in failure displacement with increasing hours of immersion. This figure shows that although there is a small loss (17%) in failure load after over two years of accelerated ageing (18936 hours) the largest change was a loss of over 35% in failure displacement. This result is somewhat surprising as it is expected that during hygrothermal ageing there is a plasticization of the resin resulting in a more ductile material and hence greater strain to failure.

In addition to the axial static tests 4-point bending tests were also conducted on the aged specimens. The results are presented in Table 6.7 and shown graphically in Figure 6.31. From Figure 6.31 there is no change in the slope of the load-deflection curve after ageing and Table 6.7 shows that there is no loss in failure load. The unaged specimens show a higher coefficient of variation. However, unlike the axial tests the failure mode was the same for unaged and aged specimen with failure occurring in the CSM layer as shown in Figure 6.32.

Table 6.7 Results for 4-point bend tests of aged and unaged DLHC specimens

	Failure Load (kN)				
Condition	**Spec 1**	**Spec 2**	**Spec 3**	**Average**	**Coef. of Var. (%)**
Unaged	-25.34	-19.90	-19.69	-21.64	14.81
Aged (18936 hrs)	-22.94	-21.99	-22.13	-22.35	2.31

All of the static testing revealed that there is little effect on performance after the joints exposure to hygrothermal ageing. To identify if this was a global issue a number of tensile specimens were cut from both unaged and specimens aged for 18936 hours. The tensile specimens were tested to destruction to obtain both ultimate failure load and material stiffness. The specimens were approximately 100 mm long and 15 mm wide with a nominal thickness of 4 mm. The specimens do not conform to a tensile standard due to the material available from the specimens. The results obtained are presented in Table 6.8. The results clearly show that there is no difference in the stiffness of the material after more than 2 years of hygrothermal ageing. This would explain why there is little loss in global stiffness of the hybrid connection and relatively little change in the ultimate failure load of the joint.

Table 6.8 does suggest that there is a change in the ultimate failure load of the material after ageing. However, this is not the case. The specimens all failed in the test grips due to the specimens being prismatic. The results indicate that the failure loads have a considerable experimental scatter and this is caused by the differing failures that did occur. In some cases the specimen surface sheared and in others the test grips created cracks that resulted in premature failure. Little knowledge can be gained from the results obtained. In order to obtain data on the ultimate strength of the test specimens a modification to the test set-up is required to eliminate premature failure in the hydraulic test grips.

Table 6.8 Failure load and Young's modulus of aged and unaged composite material

Specimen	Failure load (kN)	Young's Modulus (MPa)
1	19.58	19742
2	15.05	19239
3	16.64	19185
4	14.63	19014
5	12.43	20075
Average	15.66	19451
CoV (%)	16.95	2.27

Generally, results of the aged material tests are particularly important for numerical simulation as this provides information for the modelling of material degradation due to moisture ingress. However, this study has shown that for the specimens tests there is no change in the material properties and therefore degradation modelling is not required.

6.5.2 FATIGUE TESTING

As discussed in Section 6.3 the fatigue data obtained from the unaged specimens had a considerable amount of experimental scatter (i.e. in excess of 80%). Although this work cannot be used to assess the fatigue performance of the DLHC specimen, aged specimens were examined after 18936 hours of immersion and the results are presented in Table 6.9. The results indicate that on average the aged specimens result in a lower number of fatigue cycles to failure. But as with the unaged specimens in Section 6.3 the coefficient of variation is extremely high being in excess of 81 percent. This again leads to the conclusion there is no confidence in the fatigue results for this joint configuration. Further investigations into the failure mechanisms of this joint configuration are required to better understand why the fatigue results have such experimental variation.

Table 6.9 Number of cycles to failure of DLHC for 10% to 60% of UTS, aged and unaged

	Number of cycles to failure				
Condition	**Spec 1**	**Spec 2**	**Spec 3**	**Average**	**Coef. of Var. (%)**
Unaged	16188	128527	65113	69942.67	80.5
Aged (18936 hrs)	5708	19380	4812	9966.67	81.92

6.6. DISCUSSION

Four main strength characteristics have been addressed in this chapter namely the static strength of hybrid connections, the durability of hybrid connections subject to cyclic loading, the residual strength of a hybrid connection subjected to cyclic loading and finally the influence of hygrothermal ageing on static performance. These are the areas in which new knowledge has been gained from the work conducted in this chapter to complement information already in the public domain.

Previous studies have concentrated on the out-of-plane static loading of the hybrid connections [1, 2] however, very little is understood about the in-plane performance. The present research has clearly identified, for the HSC joint configuration, the way in which the joint fails through experimental testing under static axial load and also under fatigue cycling.

The static tests revealed that the response of the hybrid connections, both the DLHC and the HSC, is predominantly linear. There is only a relatively small portion of the load-deflection curves that exhibit non-linear behaviour just before ultimate failure. This is consistent with the failure mode of the majority of both HSC and DLHC joints failing due to shear failure of the adhesive, which is known to be a relatively brittle material. In addition, it has been shown that the use of grit-blasting as a surface preparation for steel prior to adhesive bonding provides an ideal surface to promote cohesive failure of the joint. There is slightly more non-linearity observed in the HSC specimens due to the more complex geometry and mixture of materials which have influenced the failure mechanisms. Overall it has been found that the static performance of the joints are consistent and produced results for the HSC and DLHC of -108 kN and -180 kN respectively which can be considered greater than in-service loads.

Taken into context, if the specimens were part of the panels used to construct a helicopter hanger for a Duke Class Type 23 Frigate, the weight of the structure if constructed from composite would weigh 47 tonnes [87] which is a 60% reduction in weight from an equivalent steel superstructure. This corresponds well to the advantages quoted by Dow [12] who stated a 60% reduction in weight with an all GRP superstructure or a 40% reduction for a steel framed GRP superstructure. The footprint of the helicopter hanger, estimated from scaling a photograph, for the jointed region where the hanger is attached to the deck, is 68 linear metres (based on the fact that the hanger only has joints with the deck on three of the four sides). Therefore, based on the weight of the composite hanger structure, approximately 0.4 metres of HSC joint could support the entire structural weight without failure (while the ship was at rest).

Using the total jointed footprint and the total weight of the composite hanger, the load per 100 mm of jointed length (equivalent to one experimental specimen) is -0.07 tonnes (or -0.67 kN). This is only 0.63 percent of the total load carrying capacity of a 100 mm wide section of HSC. This accounts for the joint carrying only the weight of the hanger while the ship is at rest. Taking into account the motion of the ship, and based on human performance limitations for personnel where a maximum vertical acceleration of 0.4g is recommended [88], the force applied to the 100 mm wide section of hanger joint increases to just under -1 kN. Therefore it can be assumed that from these basic calculations that the strength of the HSC joint in a typical helicopter hanger application has a large residual load carrying capability both when the ship is at rest and while underway.

The results of the static strength tests obtained from the present research and the simplified calculations described above imply that the joint is suitable for a typical helicopter hanger application. In addition, the low force applied to a 100 mm section of the hanger suggests that under cyclic loading the fatigue performance of the joint will be well under the fatigue endurance limit found during the fatigue life characterisation of the HSC specimen. However, there are many loading scenarios that should also be considered but are beyond the scope of this research. Blast for example produces rapid dynamic loading that may result in premature failure. Consideration must be given to these loading regimes during the design phase of naval structures.

It has been demonstrated that the fatigue life of the HSC can be closely represented using a statistical function such as the Weibull Cumulative Density Function (WCDF) for the prescribed boundary conditions. Due to this function’s statistical nature, it can also be used to generate a probability density function. Due to the excellent agreement of the WCDF to the experimental data obtained, the use of the corresponding probability density function can be used with confidence in the prediction of fatigue life for any given load amplitude. The fatigue tests conducted on the DLHC resulted in large experimental scatter. This is not desirable as the fatigue life for the load level examined cannot be determined with any confidence. A number of factors could have had an impact on this result including the introduction of the CSM layer at the interface. This material is random in nature and it appeared from visual inspection of the failure surface that the CSM layer may have contributed to the failure. This may have introduced a random element into the fatigue results for the DLHC. This is an area that requires further detailed investigation.

The residual strength results provided confirmation that regardless of the damage produced in the joint during the present research there was no significant loss in out-of-plane residual strength. This is an important result as the worst case studied resulted in a debond of 60 percent of the overlap length with no loss in ultimate failure load. With the residual strength being 100 percent with the extent of damage investigated the operator of the vessel can be confident that damage incurred during service that produces considerable debonds in the hybrid joint will not affect structural integrity and does not require immediate remedial attention. This could be extremely important if the ship is operating in remote foreign waters, where allied repair yards may not be accessible.

Finally the influence of hygrothermal ageing was examined. Under static axial and bending loads it was found that hygrothermal ageing did not have a degrading effect of performance. This is especially true for 4-point bending tests where there was no change in the performance of unaged specimen and those aged for 18936 hours (2 years) at 40ºC. In the axial tests a small drop in failure load is experienced however some of this is possibly due to a change in the failure mode where the crack forms between the CSM and tri-axial layers for unaged specimens and between the CSM and steel for aged specimens. It was shown that there is a change in the load level at which the joint becomes non-linear and this is most likely due to the change in position of the failure crack. Material characterisation tests in the form of tensile tests were conducted on unaged and aged material to assess the change in properties of the GRP after hygrothermal ageing. It was found that there was no change in material stiffness. This result shows that indeed moisture has had little effect on the performance of the hybrid connection as there has been no influence on the materials in the hybrid connection.

Chapter 7

Numerical simulation of hybrid joints

7.1. INTRODUCTION

The aim of this Chapter is to create numerical models of the hybrid connections and model their failure through the use of progressive damage methodologies as discussed in Chapter 5. The results from the experiments in Chapter 6 will be used to validate the numerical model in terms of both material characterisation and global response. The validation procedure will then allow the stress distribution, failure mechanisms and damage progression to be examined in detail to aid the design of the hybrid joint. The methods used to predict the stress field within the hybrid joint and predict the failure and damage progression are outlined in detail in Chapter 5.

7.2. JOINT GEOMETRIES AND BOUNDARY CONDITIONS

The geometry of the joints used in this study were created so as to accurately represent numerically those used experimentally in Chapter 6. Similarly, the boundary conditions have been represented in a similar manner. Two joints are simulated, the double lap hybrid connection (DLHC) and the hybrid structural connection (HSC), shown in Figure 7.1. Figure 7.2 shows the boundary conditions applied to each of the connections.

During the experimental study of the rig characteristics carried out in Chapter 4, it was found that due to the high applied forces required and the size and configuration of the test rig, a significant amount of the test rig movement was observed and subsequently measured. In order to accurately represent the stiffness behaviour of the joint it is important that this rig movement is included in the numerical model boundary conditions. The results of the rig flexibility tests carried out in Chapter 4 indicated that the relationship between rig displacement and load was approximately linear. Therefore the flexible boundary conditions can be represented by the use of linear spring elements in place of fixed boundary conditions, COMBIN14 and SPRING2 are the elements used in ANSYS and ABAQUS respectively. The stiffness of the springs is defined using the results obtained from Chapter 4.

In addition to rig movement, there is also some lateral deflection of the HSC configuration caused by the eccentric compressive loading of the joint. It is assumed that this is not representative of how the structural joint would behave under full-scale application. It has been discussed in Chapter 3 that the HSC could represent the joint between the steel hull of a ship and the helicopter hanger located on the weather deck. In this application it can be said that transverse frames would support the hybrid connection and adjoining superstructure internally. This additional structure would prevent lateral bending of the joint region.

In the experimental and numerical studies, an additional boundary condition, referred to as the anti-bending guide, is applied to the HSC configuration. This device prevents lateral bending of the joint under compressive loading. However, due to the stiffness of the anti-bending guide system not all of the lateral deflection was eliminated. This is a result of the global stiffness of the anti-bending guide itself. The amount of lateral force generated through compressive loading of the HSC is considerable and thus some lateral deflection is inevitable. This has also been represented using spring boundary conditions that allow approximately 2 mm deflection at 100 kN axial load (see Chapter 4).

7.3. NON-LINEARITY

7.3.1 GEOMETRIC

In purely geometric non-linearity problems the relationship between stress and strain is assumed to be linear. Non-linearity occurs due to both non-linear strain-displacement relations and from finite changes in geometry; therefore encompassing large strain and displacement problems. Equation 7.1 gives the formulation of the stress in an element that is made up of the stiffness matrix [*D*], the strain-displacement matrix [*B*] and the displacement matrix $\{u\}$.

$$\{\sigma\} = [D][B]\{u\} \tag{7.1}$$

Geometric non-linearity occurs in the strain-displacement matrix. At any instance in time, i.e. for small strains, the strain-displacement relationship can be assumed to be linear. In order to calculate the strain-displacement matrix for a further instance in time the following relationship is used.

$$[B]_{new} = [B]_{old}[T]_{new} \tag{7.2}$$

Where $[B]_{\mathrm{new}}$ is the new strain-displacement matrix, $[B]_{\mathrm{old}}$ is the old strain-displacement matrix and $[T]_{\mathrm{new}}$ is the transformation matrix relating the old element coordinates to the new element coordinates. For large displacements the direction cosines in the transformation matrix become functions of the displacement state as well as of the initial geometry, so non-linearities are introduced into the equilibrium equations.

7.3.2 DISCUSSION

In the present research experimental tests were conducted on the resin system in order to obtain both tensile and fracture toughness properties (details in Chapter 4). The tensile tests revealed that the resin is almost linear in response with small degree of non-linearity close to ultimate failure. The fracture toughness highlighted the amount of energy required to cause complete rupture of the material. These material properties provide the information required to implement the material non-linearity model into the numerical study. Geometric non-linearity was assessed during the numerical investigation and although in most cases inclusion of geometric non-linearity did not influence the results it was included to ensure accurate results for all cases. This however has a significant influence on computational efficiency. A comparison was made between the global response of the joint and the levels of stress present in the adhesive layer at a particular location to determine if a geometric non-linear method was required. The results showed that there was a less than 1 percent difference in the global stiffness response between linear and geometrically non-linear computation at the displacement at which the Von Mises stress criterion is exceeded in the adhesive, indicating the initiation of failure. However, there is considerable difference in the stress distribution along the lower steel/GRP interface near the centre of the joint, i.e. the location of highest stress concentration. The linear result shows an increase in Von Mises stress of over 10 percent and hence premature failure compared to a non-linear analysis. In order that the point of initial failure and any subsequent failure is not predicted prematurely a geometrically non-linear approach is adopted throughout the numerical analysis.

7.4. MODEL GENERATION AND LOAD APPLICATION

In general the ANSYS suite of FEA software was used for mesh generation. Stress analysis was then either conducted using the ANSYS solver or alternatively and in the case of the progressive damage modelling the ABAQUS solver.

Both the HSC and DLHC hybrid connections were represented using 2-dimensional 8-noded quadrilateral elements under plane stress with thickness. The elements used were Plane82 and CPS8 for ANSYS and ABAQUS respectively. A 2-D model was chosen due to computational savings and the assumption that the stress is distributed uniformly throughout the width of the joint. The computational savings become more apparent once the progressive damage modelling is implemented.

A plane stress with thickness approach was chosen against a plane strain method for a number of reasons highlighted by an analysis conducted to investigate the difference between the two theories for the geometry of the specimen examined in the present research. Firstly, a plane strain analysis was conducted to confirm the expected zero strain in the out-of plane direction. Five further plane stress analyses were conducted each having a different specimen width value, 1, 10, 100, 500, 1000 mm, where 1 mm represents a purely plane stress analysis. Figure 7.3 shows the out-of plane strain with respect to specimen width. It is known that when the specimen width is infinity, i.e. a plane strain situation, the out-of-plane strain is zero. Therefore, as the specimen width increases the curve of plane stress in Figure 7.3 will tend towards zero. The result obtained at 100 mm (equivalent to that used in the present research) shows a substantial level of out-of-plane strain. Therefore, the plane strain approximations would only be applicable if the width of the specimen was substantially larger (i.e. > 1000 mm) than that used in the present research.

With increasing specimen width, the consequences of neglecting out-of-plane stress becomes increasingly detrimental to the calculation of in-plane stresses due to Poisson effects. For example, this effect can be readily seen by substantially increasing the width of the specimen to 1000 mm. In this instance the global response is significantly affected and a plane strain analysis would be desirable. However, the current research specimen is only 100 mm wide and therefore the influence of zero out-of-plane stress on global response is felt to be insubstantial.

The specimens used in this study are divided into material areas. For the DLHC there are three areas representing the steel, GRP and glueline. The HSC has 4 areas, steel, GRP, glueline and balsawood. The material properties for the material areas were either obtained experimentally or from manufacturers data. The GRP and glueline material properties were obtained experimentally and the results were discussed in Chapter 4.

7.4.1 MESH DENSITY CONVERGENCE

A small convergence study was conducted to assess the sensitivity of joint global stiffness by changes in mesh density. Initially, a simple model was constructed with a minimum of elements in order to satisfy the element size criteria of the FEA software. The number of elements was increased to a point where the maximum number of nodes allowed by the software was exceeded. The method used to conduct this was to change the number of elements through the thickness of each of the areas of the joint. Care was taken not to exceed the element aspect ratio of 1:20 in non-critical areas and 1:5 in areas of most interest. An applied displacement of 1 mm was used for the convergence study. The results of the study are shown in Table 7.1 for a total rig deflection of 160 kN/mm. It is clear to see from the results that mesh density has little or no effect on the resultant forces on the model. There are a number of possible reasons for this result. Firstly the simple nature of the joint geometry may make its sensitivity to mesh density minimal. Alternatively the lack of apparent sensitivity to mesh density may be caused by the software's criteria for element aspect ratio. The element size is controlled mainly by the elements in the adhesive layer. In this region two or three elements are used to represent a 0.3 mm adhesive thickness. In order to satisfy the aspect ratio criteria the resulting mesh is very dense. Therefore, it could be said that the minimum mesh density examined is beyond the sensitivity threshold and therefore suitable for this analysis in terms of providing the correct global stiffness. Conversely, by satisfying the aspect ratio criteria, taking into account that the resin thickness is so small (0.3 mm), the number of elements in the model is very high. Historically this may have been a problem but due to the rapid increase in computing power now available, the large model still produces a solution in a matter of seconds.

Table 7.1 Mesh Convergence results

Run Number	Node Count	Resultant Force (kN)	Maximum Von Mises Stress (MPa)
1	6059	-34.8	60.711
2	8071	-34.812	62.068
3	10641	-34.813	62.078
4	13501	-35.078	67.384
5	16194	-35.091	68.997
6	19417	-35.087	69.718
7	24877	-35.114	70.07
8	27351	-35.125	70.086

Although the effect of mesh density appears to have little effect on the response of the model, the progressive damage model will rely on sufficient mesh density to accurately predict the rate of growth of any damage with in the joint. A very coarse mesh will result in accelerated damage growth due to large elements failing, a fine mesh will, although more computationally expensive, allow the rate of damage growth to be represented accurately.

7.4.2 LOAD APPLICATION

Load was applied to both the DLHC and HSC in a similar manner to that in the experimental tests. A displacement was applied to the nodes located at the steel end of the specimen, in incremental steps. A total displacement of 4.5 mm was applied to the HSC joint. This value is representative of the failure displacement of the joint experimentally. The reaction force due to the displacement is output for each step. In addition, stress data for the adhesive layer was analysed to determine whether elements had exceeded their failure limits.

In order to undertake a progressive damage model (PDM) node and element data from ANSYS were output processed in a custom-written FORTRAN routine to convert the format of the node and element files into those used by the ABAQUS suite of FEA software. The loading of both the ANSYS and ABAQUS models was conducted in the same way. A comparison of the global response and the magnitude and location of the maximum Von Mises stress confirm that the models were identical.

7.4.3 SENSITIVITY ANALYSIS OF NUMERICAL MODEL TO DISPLACEMENT INCREMENT SIZE

When using a non-linear model it is required that an initial displacement step is specified to begin the analysis procedure. The ABAQUS input file provides an initial increment value; the software will examine the rate of convergence and alter the increment size correspondingly to increase the efficiency of obtaining equilibrium. Similarly, during displacement steps where poor convergence rate is observed the software will reduce the increment size in an attempt to establish equilibrium. However, it was noticed that changing the value of initial increment size had an influence on the global response of the model.

In order to investigate the influence of the initial increment size on global response the increment was decreased from 100 percent of the required global displacement to 0.001 percent systematically. The results are shown in Figure 7.4. As the displacement increment size becomes smaller there is a corresponding increase in the resultant global load on the model. The most extensive region of resultant load stability occurs between 100 percent and 0.25 percent of the total required global displacement. Therefore initial load increments less than 0.25 percent of the total load were avoided in order to reduce the artificial loading of the model.

7.5. SIMULATION OF A HYBRID STRUCTURAL CONNECTION

7.5.1 NON-LINEAR FINITE ELEMENT MODELLING

A non-linear analysis was conducted to assess the correlation between initial experimental and numerical stiffness of the joint. The joint was subjected to a total displacement of 4.5 mm resulting in a global reaction load of -142 kN giving a global joint stiffness of -31.56 kN/mm. The standard Newton-Raphson method was the solution method used. In comparison, the experimental results provide a global stiffness of -33.06 kN/mm. However, good correlation between experimental and numerical stiffness is only achieved in the linear region of the curve to approximately -65 kN. Figure 7.5 shows the plot of the load deflection curves obtained from the experiment and numerical model. There is a clear point of divergence between the results at a deflection of approximately 2.0 mm. Based on this result it was felt that a non-linear material model would take into account the loss in global stiffness of the joint at higher deflections and in addition a damage modelling approach would account for element failure during increased displacement application and hence influence the global response non-linearity in the numerical results.

The aim of the numerical model is to provide a better understanding of the failure mechanisms of the hybrid connection. The experimental testing highlighted that failure occurred initially at the centre of the joint at the end of the steel insert on the flat surface of the specimen (see Figure 6.2). The failure then proceeded along the flat side of the joint at the interface between the steel and the GRP from the centre of the joint outwards. With this knowledge an examination of the numerical model was conducted.

The first step in the numerical analysis was to apply a displacement that resulted in a Von Mises nodal stress exceeding 50MPa (Von Mises failure criterion) in the adhesive material. Four stresses were examined during this phase, S_x, S_y, S_{xy} and S_{vm}, where the x-axis runs along the specimen and the y-axis runs through the thickness of the specimen as shown in Figure 7.1. Figure 7.6 is a close up of the centre of the joint showing the ends of the balsawood and steel inserts and associated glueline and GRP. Based on the experimental results there are two areas of interest. Adhesive area 1 where it was observed that the failure crack proceeded experimentally and secondly Adhesive area 2 which is expected to be a location of relatively high stress concentration. Figure 7.7 shows a plot of the Von Mises stress located in the adhesive layer. Note that the location of the highest stress is at the end of the steel on the lower interface, the same location as the initial failure observed experimentally. At a compressive displacement of 0.72 mm it is shown that the Von Mises failure criterion has been exceeded at this location.

Figure 7.8 shows the four stress components in the adhesive layer at the interface between the steel and GRP in Adhesive area 1 for the first 10 mm of the interface as indicated in Figure 7.6. It can be seen that the Von Mises stress is in excess of 50 MPa and therefore indicating the initiation of failure. The other three stress components, S_x, S_y, S_{xy}, were used to determine which component of stress provided the greatest contribution to the failure. At the point of maximum stress concentration there were equal levels of both compressive stress in the x-direction (S_x) and shear stress (S_{xy}). Of these two components the shear stress was going to have the greatest influence on the failure, as the shear strength of the adhesive is 17.2 MPa (Table 3.3), which is lower than that of the 50 MPa tensile strength. In addition, in the calculation of Von Mises stress the largest influence is from shear stress, therefore, in the current loading condition it can be said that shear failure was the predominant mode of failure. However, there are a number of issues associated with this conclusion. Firstly, the end of the steel is modelled as a perfect corner. This is unlikely in reality and will result in a numerical singularity at this point. This may result in an artificially high stress. This is somewhat highlighted by the rapid drop in compressive stress in the x-direction as one moves away from the end of the steel. There is also a reduction in the shear stress but this is smaller in magnitude. This could imply that failure is being predicted prematurely due to a numerical singularity at the sharp end of the steel. However, it is known that initial experimental failure did occur at this point.

As a simple example of how the progressive damage model is applied the elements that exceed the Von Mises stress had their stiffness properties reduced to 1.0 MPa ($\approx 2.7 \times 10^{-4}$ of initial stiffness). Figure 7.9 shows the three elements that had their properties modified all located around the lower, inner corner of the steel insert. The resultant plot of Von Mises stress in adhesive areas 1 and 2 after element modification is shown in Figure 7.10 and indicates that the stress has been re-distributed to the elements surrounding the modified elements. The levels of stress concentration for the same displacement have increased due to the re-distribution. This implies that further elements would need to be removed until none of the elements exceed the Von Mises stress criterion. Manually this is a very user intensive exercise; progressive damage modelling is an automated method of reducing the properties of the failed elements.

Examining the stress field in the GRP as shown in Figure 7.11 the Von Mises stress is considerably lower (≈67 MPa) than the tensile yield stress of a typical GRP woven roving laminate (250 MPa). This indicates that there are no failures within the GRP laminate. However, this could be a gross underestimation where non-isotropic materials are concerned. As discussed earlier the Von Mises failure criterion is used mainly with isotropic materials. However, the stress coupling in laminated non-isotropic materials is more complex and the failure criteria are usually based on quadratic functions with separation of the different failure modes of fibre, matrix and fibre-matrix failure as discussed in Chapter 5. Tsai-Wu [81] created one of the many now classical failure theories for composite materials and the theory is described in Chapter 5. The Tsai-Wu failure criterion values were calculated for the GRP to assess whether failure would occur within this material. The displacement that is known to cause failure in the adhesive is 0.72 mm, at this load level the GRP failure criterion is less than the Tsai-Wu failure criterion of 1 at

0.142. This is well below the threshold of failure in the GRP laminate. If the displacement exceeds 1.5 mm then failure of the GRP would occur. However, this is unlikely as the progressive failure of the adhesive, which occurred experimentally and was modelled numerically, changes the stress field present in the GRP. Therefore, due to the adhesive failing before the GRP, the re-distribution of the stress due to the failed adhesive elements would result in a re-distribution of the stress in the GRP, which may never reach the Tsai-Wu criterion. This would result in the observed purely cohesive failure.

7.5.2 PROGRESSIVE DAMAGE MODELLING

The details of the method used for the progressive damage modelling are given in Chapter 5 and shown schematically in Figure 5.1. In brief the load/displacement is applied incrementally to the structure. At each increment the stress field in the structure is obtained. The stress field is then examined for instances of the Von Mises failure criterion having been exceeded. If failure has been detected the properties of the failed element/integration point are reduced accordingly. The incremental step is recalculated and the stress field examined again, if no failure is detected the next incremental load/displacement step is calculated.

The failure criterion used in this study is Von Mises failure criterion for isotropic materials. This criterion was chosen as the experimental tests showed that failure only occurred in the adhesive layer, which is an isotropic material. Therefore only the adhesive is examined for failure. The degradation of the material properties once failure is detected was based on experimental tests conducted on the adhesive material. As discussed in Section 5.2.2 the material degradation model is not that used in the previous work conducted on this subject (see Chapter 2). The stress in the failed elements is reduced, resulting in a negative Young’s modulus for the material.

7.5.2.1 Progressive damage modelling results

The progressive damage model is a method of predicting failure within the joint to better understand the path of failure and to predict the load-displacement response of the structure. As described in Chapter 5 previous work [48] on damage modelling simulates failure by reducing the *stiffness* of elements or integration points within the numerical model. In the present research a *stress* reduction model is used to reduce the *stress* present in the failed locations. The results obtained from the numerical model are given in Figure 7.12. This graph shows the experimental load-deflection curve compared with a finite element result and three non-linear results based on damage progression.

The non-linear results have used the three differing stress reduction models as shown in Figure 7.13. The stress reduction models used in this phase were based on the tensile strength results described in Section 4.4. The tensile tests did not capture many data points after the maximum load point. Therefore an estimation of the shape of the post initial failure curve was assumed, the three assumptions are shown in Figure 7.13.

The progressive damage model was run with each of the three material degradation models. As discussed in Section 7.5.1, there is a clear point of divergence between the predicted linear response and experimental observation at 2 mm deflection. The non-linear PDM successfully identifies this point of divergence for all three stress reduction models.

Furthermore, beyond a global displacement of 2 mm the correlation between the presented non-linear numerical results and the experimental result, depending on the choice of post-failure material function (see Figure 7.13), represents a compromise between excellent prediction of failure load with excellent prediction of failure strain.

The progressive damage model clearly indicates the path of failure in the joint as the stresses in the adhesive layer combine to exceed the failure criterion. Figure 7.14 shows the position of the first point of failure of the joint. Its location is at the interface of the steel, balsawood and GRP on the flat side of the hybrid joint. It is in this location that the first experimentally observed crack occurs, subsequently leading to the GRP/steel debond. In the case of the experimentally tested specimens, subsequent increased loading led to crack propagation along the flat side in the steel/GRP interface. Figure 7.15 shows the result obtained from the progressive damage model as a series of snapshots for increasing displacement. Note that when the first integration point in an element exceeds the Von Mises criterion the displacement is less than 1.0 mm. This is considerably earlier than the displacement at which non-linearity occurs in the load deflection curves. However, it is envisaged that it is the collective failure of integration points that results in a loss in global stiffness of the joint. In contrast to what was assumed to have occurred in the experimental testing, failure in the adhesive layer occurs along both the upper and lower adhesive interfaces simultaneously. Experimentally the non-linearity in the load-deflection curve occurs at approximately 2 mm deflection. Figures 7.15 (c) and (d) span this deflection and exhibit a crack of approximately 20 mm in length on both adhesive interfaces. Figure 7.15 (e) shows that at 3.39 mm deflection a substantial crack had developed. The crack also began to propagate into the interface between the GRP and balsawood.

The material degradation models used thus far are based on an assumption of how the material behaves post initial failure based on the tensile tests conducted in Chapter 4. The approximation involved the consideration of a negative stiffness to ensure a reduction in stress that resulted in zero stress in any failed element when maximum displacement of the model had reached 4.5 mm (Section 7.4.2). However, this assumes that the elemental stress is zero when the global displacement of the specimen is 4.5 mm. In order to increase the accuracy of the prediction of the non-linear behaviour of the joint a better description of the material property degradation curve post-maximum stress should be used.

It could be considered that the area under a stress-strain curve from zero stress to initial failure is the energy required to cause initial failure. If there is further load carrying capability after initial failure then the area under the stress-strain curve from initial failure to complete failure is the energy required to cause complete failure. This latter area could be considered the fracture energy G_{IC} of the material. This assumption was also considered by De Moura et al. [89] to obtain the relative failure displacement and good correlation between experiment and the model was achieved. This methodology was used in the present research in an attempt to improve the prediction of the non-linear load-deflection curve. The fracture toughness energy values were obtained from double cantilever beam tests as described in Chapter 4. The results showed that the area under the curve was very small and this resulted in a very steep negative stiffness post-maximum stress. When applied to the numerical model this resulted in a large degree of numerical instability, despite efforts to control the numerical stability through the implementation of viscous damping variables the model would not converge. Initial failure load prediction and the on set of non-linearity remain unchanged using the GIc method. However, further research is required on controlling numerical stability with highly negative material stiffness values. The progressive damage modelling approach has been shown to accurately predict the point at which non-linearity occurs and broad assumptions regarding the shape of the post-maximum stress curve resulted in good correlation with experimental results. The new approach of using fracture toughness values could result in further improvement in the load-displacement prediction when the numerical issues are resolved.

7.6. DISCUSSION

This chapter has examined the numerical simulation of hybrid connections using non-linear finite element analysis and progressive damage analysis. The aim is to develop a method whereby the performance of the joint can be predicted and the knowledge used to aid the design of more efficient hybrid connections.

A numerical model of the hybrid connection was developed which accurately defined the boundary conditions present in the experimental testing. The result of the FEA analysis showed excellent convergence with the linear portion of the experimental joint response. This provided confidence in the validity of the simulation.

A progressive damage methodology was developed for predicting the progression of failure in adhesive connections. The majority of present work with progressive damage modelling concentrates on failure within the composite material [43, 47, 48, 70]. The present work employed a new stress reduction method of failing elements in order to simulate failure within the physical joint. This is contrary to the material degradation models used in the analysis of progressive failure in composites where stiffness is reduced [48]. In addition, a new method of incorporating fracture energy of the adhesive into the progressive model has been developed and a method of applying the method explored.

The information obtained from this chapter will be essential for future structural engineers to examine hybrid joint designs and be able to predict the way in which failure will develop and progress.

Chapter 8

Parametric and optimisation studies of a hybrid joint

8.1. INTRODUCTION

The aim of this chapter is to take the HSC design as tested in previous chapters and use this as the baseline design and hence baseline performance of the hybrid connection. Closed form solutions are used to look at basic joint parameters such as overlap length and adhesive thickness and assess how sensitive the performance is to changes in these variables. A parametric study is then conducted which systematically changes individual joint parameters to assess their influence on joint performance. The method by which joint performance is evaluated is discussed in relation to lessons learnt in previous chapters. The results of this study provide a guide on how to combine individual changes to the joint variables to obtain a combined improvement to the performance of the joint. Finally, a genetic algorithm is used to search the whole design space for an optimal solution keeping in mind that an improvement on the performance of the baseline joint is required.

8.2. JOINT VARIABLE SENSITIVITY ANALYSIS

In order to better understand the influence of certain geometric and material property variables on the performance of a joint, closed form solutions can be employed. Work on the calculation of shear and peel stresses in single and double lap joints and the use of closed form solutions has been on going for many years. In 1938, when Volkersen [35] conducted the first major study in this field, the use of finite element analysis was non existent. In 1943, Courant [90] utilized the Ritz method of numerical analysis and minimisation of variational calculus to obtain approximate solutions to vibration systems. Turner et al. [91] later produced a paper that centred on the stiffness and deflection of complex structures. These were the first works to focus on the use of finite element analysis. However, in the 1970's the use of FEA was limited to large mainframe computers such as in the aeronautics and nuclear industries.

At the time of Volkersen's work [35], closed form solutions were the most commonly used way of understanding the development of stress in an adhesive joint. Further studies have been based on this initial work in order to improve the solution and to account for geometric rotations e.g. Golland and Reissner [36]. These classical works were limited due to the peel and shear stress being assumed constant through the thickness of the adhesive. In addition, the shear stress was assumed to be maximum at the end of the adhesive overlap. However, due to the end face of the adhesive being a free surface there can be no shear stress on it, thus the law of complementary shear states that the shear stress at the joint end must be zero.

Allman [37] presented a solution which resulted in the correct zero shear stress at the ends of the adhesive joint, and a formulation for the peel stress distribution along the adhesive overlap. The Allman solution uses the Golland and Reissner [36] term, *k*, for the rotation of the joint due to eccentric loading. For flexible adherends or high applied loads this term approaches a value of 0.26, conversely for stiff adherends or low applied loads the value of *k* approaches 1.0. For typical single lap joints with isotropic materials a value for *k* of 0.35 is suitable [37].

For validation purposes a single lap joint was modelled in both the closed form solution by Allman and in the finite element software ANSYS. The joint has the basic dimensions and applied loads defined in Table 8.1 including the shear and tensile strengths of the adhesive. Figures 8.1 and 8.2 show the comparison between the finite element analysis results and the Allman result for both the shear and peel stress respectively. The FEA and Allman results show good correlation in both shear and peel stress. However, it can be seen in Figure 8.1 that the Allman closed form solution underestimates the maximum shear stress by nearly 13 percent. However at the centre of the joint the shear stress calculated by Allman is just over

8 percent larger. In the peel stress (Figure 8.2) the closed form solution produces a larger peel stress both at the centre of the joint and at the end of the overlap. From 50-100 percent of the distance from the centre of the joint the Allman theory predicts a more rapid rise to maximum peel stress than the FEA solution. Although there is some discrepancy between the Allman and FEA results it is felt that the closed form solution will provide a useful first look at the sensitivity of some geometric and material parameters of simple joint configuration to enable an educated decision on the variables to be investigated in the more detailed FEA parametric study.

Table 8.1 Example joint parameters

Joint parameter	Dimension	Units
Overlap length	50	mm
Joint Width	50	mm
Adherend Thickness	6	mm
Adhesive Thickness	3	mm
Applied Load	25	kN
Adherend Young’s Mod.	209000	MPa
Adhesive Young’s Mod.	2000	MPa
Adhesive Tensile Strength	50	MPa
Adhesive Shear Strength	17	MPa

Using the Allman closed form solution a number of variables can be changed relatively quickly to better understand the stresses present in the adhesive layer. In joints containing isotropic materials such as steel and aluminium the majority of failure is observed in the adhesive layer. In composite materials this is not always the case, however there is evidence in hybrid steel/composite connections, published by the present author (See Appendix II), that failure occurs in the adhesive layer [92]. Three joint parameters are investigated in this section namely:

1. Adhesive thickness
2. Joint overlap length
3. Adhesive Young’s modulus

8.2.1 ADHESIVE THICKNESS

The range of adhesive thicknesses investigated was from 0.1 mm to 7 mm and the results are presented in Figure 8.3. This figure shows that the influence of adhesive thickness on the shear stress in the adhesive layer is negligible, however the peel stress at very low adhesive thicknesses (0.1 mm) is approaching the tensile strength of the adhesive (50 MPa) at an applied load of 25 kN. However, the Von Mises stress is a better indication of failure in isotropic materials, e.g. the adhesive. Von Mises stress is calculated from the equation:

$$\sigma_{VM} = \sqrt{\sigma_1^{\ 2} + \sigma_2^{\ 2} - \sigma_1\sigma_2}\ , \tag{8.1}$$

where σ_1 and σ_2 are the principal stresses. This equation can be decomposed to obtain the Von Mises stress in terms of the direct stresses σ_x, σ_y and σ_{xy} by the relationship:

$$\sigma_{VM} = \sqrt{\sigma_x^{\ 2} + \sigma_y^{\ 2} - \sigma_x\sigma_y + 3\sigma_{xy}^{\ 2}} \tag{8.2}$$

In this case the Von Mises stress is very close to the tensile strength of the adhesive and therefore it could be assumed that the adhesive would fail just above this load level. As the adhesive thickness increases by a factor of 10 (1 mm thick adhesive layer) the Von Mises stress reduces to only 57 percent of the tensile strength of the adhesive. At a thickness of 7 mm reduces slightly further to less than 50 percent of the tensile strength.

Figure 8.4 shows the change in distribution of shear stress from the centre of the joint to the end of the adhesive. In all joint configurations the distribution of shear stress either side of the centre of the joint is symmetrical. This figure shows that the distribution remains relatively unchanged with increasing adhesive thickness. At the centre of the joint there is a slightly higher level of shear stress with thicker adhesive layers but a correspondingly lower maximum value. This implies that for thicker adhesive layers the shear stress is carried more evenly along the joint length with a much lower stress concentration at the ends.

The change in the distribution of peel stress in the adhesive layer with changing adhesive thickness is shown in Figure 8.5. The distribution of peel stress in adhesive layers that are very thin are significantly different to those in thicker adhesive layers. For thicker layers the rate of change of peel stress distribution is much less and more gradual. This will ultimately lead to lower stress concentrations.

8.2.2 JOINT OVERLAP LENGTH

Overlap length for the single lap joint was increased from 10 mm to 120 mm and the results in terms of maximum shear, peel and Von Mises stresses are presented in Figure 8.6. If Von Mises stress is considered the criterion for adhesive failure then it is clear from Figure 8.6 that with an overlap length less than 20 mm the maximum Von Mises stress of 50 MPa is exceeded. In comparison to the variation in adhesive thickness, from Section 8.2.1, the magnitude of shear stress is higher and the influence of the overlap length on the shear stress is markedly greater. The trend in peel stress is similar for both adhesive thickness and overlap length variation.

The distribution of shear stress from the centre of the joint to the end of the overlap for varying overlap lengths is presented in Figure 8.7. It is clear that the shear stress in the adhesive layer is constant to about 80 percent of the distance from the joint centre to the end of the adhesive. However, it is also shown that the shear stress present at the centre of the joint decreases with increasing overlap length and these values correspond well to the theoretical predicted values obtained from the equation:

$$\tau_{xy} = \frac{P}{a} \tag{8.3}$$

where τ_{xy} is the shear stress, P is the applied load and a is the bond area of the joint. The shear stress distribution curves for the changes in overlap length look relatively constant from 0 to 80 percent of the overlap length. This is deceiving as the scale of the graphs is controlled by the relatively high shear stress present in the 10 mm overlap length result. All of the curves with an overlap length greater than 20 mm exhibit a curve shape similar to that found in Figure 8.4.

The peel stress distribution curves, shown in Figure 8.8, exhibit a dramatic change in shape with varying overlap length. The result containing an overlap length of 10 mm produce a 2nd order polynomial shape. As the overlap length increases the order of the polynomial describing the curve increases, 4th order for 30 and 50 mm and 6th order for 100 mm. This is mainly due to the 10 mm joint being subjected to large amounts of peel stress along its whole overlap length. As the overlap length increases the peel stress is concentrated more at the end of the joint. If only the last 10 mm of each overlap length were analysed all would exhibit a 2nd order polynomial distribution. As the overlap length increases a larger length of the joint is subjected either to less or even negative peel stress.

8.2.3 ADHESIVE YOUNG’S MODULUS

For the analysis of the sensitivity of stress to adhesive Young’s modulus the basic joint had the configuration provided in Table 8.1. A number of adhesives from various manufacturers were used to obtain a realistic range of Young’s modulus values for a range of adhesive types. In this study a range from 1000 MPa to 3000 MPa was examined. The adhesive at the lower end of the range (1000 MPa) is a two part toughened methacrylate adhesive with high shear strength properties and gap filling ability. The higher end of the range (3200 MPa) corresponds to epoxy and vinylester resin systems with lower shear strengths but high stiffness, these adhesives may be less suitable for gap filling applications greater than 1 mm.

In this analysis the only parameter changed systematically is the Young's modulus value. However, for the Allman solution, the shear modulus of the adhesive is required. This has been estimated using the relationship:

$$G = \frac{E}{2(1+v)} \tag{8.4}$$

where G is the shear modulus of the adhesive, E is the Young's modulus of the adhesive and v is the Poisson's ratio of the adhesive, assumed in all cases to be 0.35.

The change in shear, peel and Von Mises stress is shown in Figure 8.9, which shows that changes in the adhesive Young's modulus has little influence on the maximum shear stress. In addition the Von Mises stress throughout this range of Young's modulus at this load level does not result in failure of the adhesive. However, if a very thin adhesive layer was used in this study the influence of the Young's modulus may have been more marked.

Figures 8.10 and 8.11 show the distribution of shear and peel stress respectively. The peel stress graph (Figure 8.11) shows the most influence to changes in adhesive Young's modulus, however, the shape of the curve is very similar with the peel stress at the centre of the joint being the same regardless of the modulus value. At the end of the joint overlap the peel stress increases with increasing Young's modulus.

8.2.4 DISCUSSION

Three areas were examined to assess the changes in shear and peel stress, namely: adhesive thickness, overlap length and adhesive Young's modulus. By conducting this analysis the sensitivity of each of these geometric or material changes can be judged as a function of the development of stresses that could ultimately lead to failure. Overall the most sensitive changes were to adhesive overlap length. This however, is expected as it directly related to the effective bond area of the joint. Shorter bond lengths result is smaller bond areas and hence higher stresses. Using the information obtained from varying the bond length of the joint considered in this example phase, a minimum bond length can be specified. The next most sensitive parameter was the adhesive thickness, this is a very important parameter and mainly controls the level of peel stress present in the joint. The least sensitive parameter studied is the adhesive Young’s modulus. However, it is not clear form this study the importance of the relationship between adhesive thickness and Young’s modulus. This study has shown that the joint is sensitive to changes in adhesive thickness, overlap length and adhesive Young’s modulus. However, due to the eccentricity of the HSC joint the geometry of the joint is more complex and cannot be represented using closed form solutions. In addition, the variables that could be changed in the HSC are also much greater, variables such as taper length, GRP skin thickness and core thickness could have a significant influence on the performance of the joint. A finite element model of the joint must be created in a manner that allows the easy variation of the principal joint variables in a quick and efficient manner.

8.3. FINITE ELEMENT PARAMETRIC STUDY

The closed form solutions used in Section 3 provide a useful tool to investigate the effect of individual joint parameters on the stresses in a simple easily defined joint configuration. The HSC joint modelled experimentally and numerically in this research is a more complex joint, which cannot be represented simply using closed form solutions. However, the closed form solutions do represent portions of the HSC joint and so any lessons learnt from the closed form solutions can be used to identify the sensitivity of particular geometric parameters.

It is important that the model used in the parametric study is easily varied to account for changes in the principal joint dimensions and material properties. In order to achieve this the joint was defined by a number of geometric dimensions that provided enough information to describe the joint. The method used to achieve this is described in detail in Chapter 5.

As discussed in Chapter 7 the mesh density of the HSC joints is dictated by the element shape criteria within the finite element software and the thickness of the adhesive, which always contains a minimum of two elements through its thickness. The mesh density for each joint variation is kept constant by ensuring that the element lengths and thicknesses are a function of the appropriate principal joint dimension.

Each model had the same applied load of -10 kN (compression) applied to the steel end of the specimen. The specimen was constrained in a similar manner to that described in Chapter 7 including the anti-bending guides. However, spring boundary conditions were not applied due to the excessive computation time involved in their creation. Although this will have an effect on the realistic response of the specimen the comparison of the results to the baseline geometry and any increase/decrease in performance due to the geometric changes will still be valid.

8.3.1 PERFORMANCE CRITERIA

A number of joint performance objectives should be considered when analysing the results. It is known that failure of the hybrid connections, examined in the present research, occurs in the adhesive layer which is isotropic and therefore can be described using Von Mises failure criteria. As described in Chapter 5, examining the Von Mises stress in the adhesive layer assesses failure in isotropic materials. For each parametric variation the maximum instance of Von Mises stress forms the first output variable of the analysis. Due to the configuration of the joint and the results from Chapters 6 and 8, maximum Von Mises stress is located at the interface between the balsawood core and the steel on the flat side of the specimen. The design driver behind the use of composite materials on ships as discussed in Chapter 3 is the reduction of weight and hence increased stability. Therefore the weight of the hybrid joint must be considered as an important design feature. Finally, joint stiffness can be considered as important, however, careful consideration should be given to this as in some instances this is not a desirable design attribute, i.e. during blast loading. Based on these three output variables judgement can be made as to the performance of each individual joint. The calculation of the weight required only the input variables to the ANSYS routine and the densities of the materials within the joint (Table 8.2).

Table 8.2 Densities of materials used for weight calculation

Material	Density
Steel	7833kg/m^3
GRP	1813kg/m^3
Adhesive	1210kg/m^3
Balsawood	128kg/m^3

In order to assess the performance of each parametric variation a suitable baseline joint was selected as Chapters 6 and 7 have provided a good understanding of the performance of this joint configuration. The mesh density of the model was reduced by increasing the thickness of the adhesive from 0.3 mm to 0.5 mm. Chapter 5 showed that the mesh density is dependent on the adhesive thickness and a reduction in mesh density reduces computation time for each parametric variation. Table 8.3 also provides the maximum Von Mises stress, global stiffness and weight of the baseline joint to which every parametric variation is compared.

Table 8.3 Baseline HSC joint dimensions and performance properties

Joint Variable	Value
Adhesive Thickness	0.5 mm
GRP Skin Thickness	4.0 mm
Balsawood Core Thickness	38.0 mm
Steel Thickness	6.0 mm
Adhesive Young's Modulus	2000 MPa
GRP/steel Bond Length	240 mm
Taper Length	120 mm
Maximum Von Mises Stress	12.79 MPa
Global Stiffness	49500 N/mm
Weight	2.97 kg

8.3.2 ADHESIVE THICKNESS

The closed form solutions highlighted that changes in adhesive thickness had little impact on the shear stress in the joint however there was a significant impact of peel stress development. As the adhesive layer became thicker the levels of peel stress and hence Von Mises stress reduced. A similar trend is observed from the finite element study and shown in Figure 8.12. This plot shows that the maximum Von Mises stress in the adhesive decreases with increasing adhesive thickness. By increasing the thickness by a factor of two the reduction in maximum Von Mises stress is of the order of 17.5 percent. Doubling the adhesive thickness again reduces the stress by a further 14 percent. Beyond a thickness of 2 mm the reduction in stress becomes less. In addition, the increasing adhesive thickness increases the global stiffness of the joint by over 5.5 percent with an adhesive thickness increase to 2 mm. If the adhesive layer is increased by a factor of 4 on both adhesive layers, this could amount to a sufficient increase in the second moment of area to provide an increase in bending stiffness therefore preventing lateral deflection and increasing axial global stiffness. Unsurprisingly the influence of the adhesive thickness on weight is negligible as the quantity of adhesive is extremely small.

The peel stress distribution along the adhesive layer (Figure 8.13) on the flat side of the specimen shows relatively little change with increasing adhesive thickness. This is somewhat surprising as the influence of the adhesive thickness on peel stress in the closed form solutions was significant. In contrast the influence of adhesive thickness on the distribution of shear stress (Figure 8.14) is marked. The peaks of shear stress lie at the interface between the steel and balsawood core and as the adhesive thickness increases there is a marked decrease in the peak of shear stress at this point.

By increasing the adhesive thickness to between 2 and 3 mm the largest gains in terms of stiffness and strength are attained with a decrease in maximum stress in the adhesive of between 32 and 38 percent and an increase in stiffness of between 5 and 10 percent with little increase in weight.

8.3.3 CORE THICKNESS

An increase in the core thickness of the sandwich panel is going to have a number of effects on the joint response to load. Firstly, as the core thickness increases the load eccentricity of the joint is going to increase. This is most likely to have a detrimental effect on the stresses in the adhesive as increased force is applied to the anti-bending guides due to lateral bending of the joint in compression. The increased thickness is also going to influence the lateral stiffness of the sandwich section, however, as the core thickness has increased for a fixed taper length, the angle of the taper will be much larger. The load bearing material longitudinally in the GRP sandwich is the GRP skin. This is no longer in-plane with the applied load. This should therefore result in decreased stiffness. These points are confirmed by the results presented in Figure 8.15. This figure shows that by increasing the core thickness to 60 mm for example there is an increase in maximum Von Mises stress of over 12.5 percent and a decrease in global stiffness of just over 10 percent. In addition, there is an increase in weight of over 3 percent. All of these factors suggest that increasing the core thickness for in-plane loading will not benefit the performance of the joint.

8.3.4 SKIN THICKNESS

As the GRP skins are relatively dense, any increase in the volume of the skins will incur a weight penalty. However, this may be balanced by the increase in mechanical performance through increased stiffness preventing lateral bending of the specimen due to eccentric loading, and hence reduced stress in the adhesive. Figure 8.16 shows the results for increasing GRP skin thickness. By increasing the skin thickness by 2 mm to 6 mm there is a 40 percent increase in stiffness and a 16 percent decrease in maximum Von Mises stress in the adhesive. However, there is a weight increase of 20 percent. It is assumed that the objective of the joint design is the minimisation of weight therefore an increase in skin thickness may not be a valid option. However, the benefits in terms of stiffness and maximum stress make the increase a viable option.

Figures 8.17 and 8.18 show the distribution along the adhesive layer of shear and peel stress respectively. There is very little variation between the 4 and 6 mm GRP skins except at the peaks where the 4 mm results show higher instances of both peel and shear stress.

8.3.5 GRP/STEEL BONDLINE LENGTH

During the experimental phase of the present research it was observed that the failure of the HSC specimen was initiated at the steel/GRP/balsa interface on the flat side of the specimen. The crack then propagated along the GRP/steel interface towards the steel end. Final failure occurred due to a loss in bond area to a point whereby the applied load caused shear failure of the adhesive. It was observed that the initial failure was due to Mode I crack opening. Reducing the bond length between the steel and the GRP could result in a more rapid failure in terms of fatigue, as the crack will have less distance to travel to reach the point of shear failure. However, as the failure is due to shear, the static performance may not be affected provided that the intact bond area is greater that the critical shear failure bond area.

Figure 8.19 shows the results of changing the bondline length. As the bond length decreases there is a small increase in the maximum Von Mises stress in the adhesive (< 7 percent) this is greatly overshadowed by the dramatic reduction in weight with over 14 percent decrease for a 100 mm loss in bondline length. However, there is a significant reduction in the stiffness of the joint also (> 22 percent).

There is one overriding factor behind the loss in stiffness. As the bond length decreases and the remaining input dimensions of the joint remain constant, including the overall joint length, the only dimension that will change is the length of the GRP sandwich at the composite end. This is shown clearly in Figure 8.20, which shows a short bondline length (8.20a) compared to a long bondline length (8.20b). The lateral deflection at the taper in Figure 8.20a is twice that of 8.20b and this will inevitably lead to an increase in global stiffness.

8.3.6 TAPER LENGTH

Changing the taper length as an individual parameter will most likely result in similar results to those found from varying the bondline length. As the taper length decreases the stiffness will reduce correspondingly due the to GRP sandwich length increasing. However. Figure 8.21 shows that as the taper length decreases there is a significant increase in the maximum Von Mises stress in the adhesive. This is most likely due to the angle of the taper also increasing which increases the eccentricity of the joint in a similar manner to changing the core thickness. When the transition between the thin steel end of the joint and the thicker GRP sandwich end takes place over a shorter length the internal moment is greater producing a larger stress on the adhesive.

The response of the sandwich section of the joint under compression with a long taper is shown in Figure 8.22a, and with a short taper in Figure 8.22b. The displacement has been exaggerated in both images for visual purposes. The slope of the flat side of the specimen at a greater distance from the steel end is significantly different in both specimens. This influences the position of the maximum shear stress concentration along the adhesive layer. Figure 8.23 shows the shear stress distribution and how it moves from approximately 220 mm from the end of the steel/GRP overlap for specimens with a long taper (180 mm taper) compared to nearly 260 mm for the specimen with a taper length of 80 mm.

8.3.7 TAPER LENGTH TO BOND LENGTH RATIO

In light of the results obtained for individual bond length (Section 8.3.4) and taper length (Section 8.3.5), both being influenced by the increased GRP sandwich length with decreasing taper/bond length, it was considered appropriate to keep the length of the sandwich section constant. In order to do so the total length of the taper and the bond length must also be kept constant. The ratio of taper length to bond length was then varied and ensured that the results were truly comparable.

Figure 8.24 shows the results of this analysis. The baseline design has a bond length to taper ratio of 2 (bond length =240 mm, Taper = 120 mm). Increasing the bond length (decreasing the taper length) has a negative effect on both the stress and weight of the joint, with little increase in stiffness. However, by reducing the length of the bondline or increasing the taper length there are weight advantages to be made. For example if the bond length to taper ratio is equal to 1.0 then there is a decrease in weight and stress of 11 and 12 percent respectively with only a 10 percent loss in stiffness.

The distribution of shear and peel stress along the bondline is also influenced by the ratio of bond length against taper length. Figures 8.25 and 8.26 show the distribution of shear and peel stress respectively. The peaks of both shear and peel stress occur at the interface between the balsawood core and steel, these are located at 180 mm and 240 mm for the bond length ratios of 1 and 2 respectively. The shorter bond length (ratio = 1) has a higher instance of peel stress located at the balsa/steel interface but a lower shear stress. This is most likely due to a shallow taper angle, and hence reduced bending stiffness of the tapered section, resulting in increased bending moment of the sandwich interface. This in turn creates the peel stress in the adhesive layer on the flat side of the specimen.

8.3.8 STEEL THICKNESS

The most dramatic influence the steel thickness has on the performance of the joint is weight. Figure 8.27 shows the weight, maximum Von Mises stress and the global stiffness of the joints examined. Reducing the thickness of the steel from the baseline of 6 mm does not change the stress and reduces the stiffness. Increasing the thickness by 4 mm increases the stiffness by only 8 percent but increases weight by 40 percent. This result indicates that increasing the thickness of the steel will have no performance benefits. However, a reduction in steel thickness, while reducing the stiffness only slightly, will result in a significant reduction in weight.

8.3.9 COMPARISON OF RESULTS

The previous sections have investigated the performance effects of changing the geometric design variables for the HSC joint. Each investigation highlighted how by changing a single design variable the performance of the joint was improved. The following recommendations of changes to joint geometry were obtained:

- Increase adhesive thickness to between 2 and 3 mm to improve both strength and stiffness
- No change or possibly a slight reduction in core thickness
- Increase in skin thickness by 2 mm to 6 mm for both strength and stiffness
- Increasing the taper length to increase joint strength
- Decrease steel thickness to reduce weight

Figure 8.28-8.30 present this information graphically in terms of strength, stiffness and weight respectively. Figure 8.28 shows the percentage change in maximum Von Mises stress compared to the baseline joint of the five geometric changes mentioned above. Adhesive thickness has the greatest influence on the stress present. When the five changes are combined into a single joint and re-analysed the performance is further improved. A similar trend is seen in Figure 8.29, which shows the stiffness change from the baseline design for the five geometric changes and also the combined change. In this case the sum of the individual percentage changes equals the hybrid percentage change. The increase in the skin thickness increases the weight by 20 percent against the baseline design (Figure 8.30). However, by reducing the steel thickness by 1 mm, which has little effect on either the strength or stiffness, the weight increase due to the skin thickness is counteracted. Both the change in taper length and core thickness reduce the weight of the joint but their influence is relatively small. When combined, the result is also a summation of the individual geometric changes.

This result is very positive, as the change in just five geometric variables has had a substantial influence on the joint performance, particularly the maximum Von Mises Stress in the adhesive. Almost a 50 percent reduction in stress has been obtained and this will improve not only the fatigue life but also the static strength of the joint by delaying the point at which adhesive failure occurs. In principle, the geometric changes recommended here are feasible, however, the control of the adhesive thickness would need to be addressed for the resin infusion process.

8.4. OPTIMISATION SOLUTUON

The result obtained from the parametric study provides a joint that has a 50 percent reduction in maximum Von Mises stress, a 50 percent increase in stiffness for a weight penalty of only 7.5 percent. This can be considered to be an excellent result for a method which looks only at 5 individual parameters and combines them to form a final joint design. Although, the result is very positive, it is still feasible that in the design space further improvements could be made. Optimisation methods could be used to efficiently search the design space for a more optimal result than that presented from the parametric study. The optimisation method chosen is evolutionary in nature and is commonly referred to as a genetic algorithm (GA). This methodology is described in detail in Chapter 5.

8.4.1 DETERMINATION OF THE GENETIC ALGORITHM PARAMETERS

There are a number of parameters associated with any GA analysis. These include the probabilities of mutation and crossover, both of which influence the “breeding” of the surviving individuals into the next generation. The size of the generation and the size of the selected group from the generation also influence the speed and efficiency of the genetic algorithm. The objective is to reduce the number of individuals analysed to increase the speed at which the optimal solution is obtained. The present research uses a case study to conduct this analysis and determine suitable values for the probabilities and to better understand the influence of the size of selection and population on the speed of convergence.

The case study joint is a double lap joint as shown in Figure 8.31. Table 8.4 provides the limits and resolution of the joint input variables and therefore defines the size of the design space. Due to the size of the design space an exhaustive search of the space is feasible and therefore the optimum solution will be known. The results provided two individuals each having the same value of fitness and therefore both were deemed optimum solutions. Therefore the following analyses were conducted to assess the speed at which both optimum individuals were found. As this process is comparative in nature this will not influence the trends present in the results.

Table 8.4 Limits and resolution of case study double lap joint variables

Joint Variable	Min Value	Max Value	Resolution	No. of Increments
Adhesive Thickness	1.0 mm	3.0 mm	0.1 mm	21
Adherend Thickness	7.0 mm	13.0 mm	1.0 mm	7
Overlap Length	110 mm	130 mm	1.0 mm	21
Adhesive Young's Modulus	Data base containing 15 values			15
Adherend Young's Modulus	209 GPa	-		1

The genetic algorithm code and the multi-objective function of weight, cost, maximum Von Mises stress and stiffness which uses a ranking method were developed in-house. The present author developed the interface between the GA and fitness evaluation modules with the ANSYS numerical modelling. The total algorithm can then be run and the algorithm parameters changed to see what influence they have on the number of individual calculations/generations required to obtain the known optimum solution.

Firstly, an understanding of what influence the population size had on the speed of convergence to the optimum solutions was conducted. The population size was varied from 20 to 10000 individuals and they were all selected for "breeding" to create the next generation. Only the top three individuals were carried directly through to the next generation. This ensures the survival of the previous best individuals, as it is not guaranteed that better individuals will be created in the next generation. This is the elitism policy. The results are presented in Figure 8.32, which shows the number of generations required to obtain the top two optimum solutions against the size of the population. There is a trend that increasing the population size increases the number of calculations to obtain the optimum solutions. This indicates that the population size should be smaller and the number of generations examined increased to increase the efficiency of the algorithm.

Figure 8.33 shows the results of changing the selection size from 50 to 500 for a population of 500 individuals in each generation. The results show that the optimum solution is again found most quickly if a small proportion of the population is selected for "breeding". This implies that only the best individuals are used in the "breeding" process and therefore increases the chance of further improvement of the next generation as a whole.

For the crossover probability study the population size was set at 100, the selection size set to 50 and the mutation probability was set at 0.03. The results are presented in Figure 8.34.

Lower values of crossover probability result in higher numbers of generations being required and hence more individual calculations. There is a plateau of individual calculations when the probability exceeds 0.4 extending to 0.9. This implies that any value of crossover probability in this region will provide the optimum solutions in a similar number of calculations. By selecting a value of crossover probability of 0.4 more than 50 percent of the selected individuals from the population will survive into the next generation with only 40 percent being modified through crossover. This provides a good balance between already good individuals and the possibility of creating another good individual. Having a crossover probability that is too large in a very large design space would result in more of a random search method, reducing the algorithms efficiency.

In the mutation probability analysis the crossover probability was set at 0.4. The results are given in Figure 8.35. In this case a mutation probability of 0.03 results in the fewest required calculations to obtain the top two solutions. As the mutation probability increases beyond 0.1 there is a rapid increase in the required number of generations. This is often referred to as an increase in population disturbance as the mutation probability is external to the population rather than an internal population trait.

The results of the GA parameter analysis suggest that a small generation population and small selection group size result in the most efficient search of the design space. The "breeding" probabilities of crossover and mutation should be set at 0.4 and 0.03 respectively. However, the value of these may be influenced by the problem being investigated and also the size of the design space. However, for the remainder of the work the parameters used for the optimisation of the HSC are given in Table 8.5.

Table 8.5 Genetic algorithm parameters

Parameter	**Value**
Design space size	26,900,000
Population size	50
Selection group size	15
Number of generations	30
Elitism policy	Top 3
Crossover probability	0.4
Mutation probability	0.03
Number of repeated runs	20

8.4.2 OPTIMISATION OF THE HSC JOINT

The same input parameters were used for the physical representation of the HSC joint for the optimisation as for the parametric study in Section 8.3. The results of the parametric study were used to define the extent of the design space for the HSC joint and the limits and resolution of the joint input parameters are given in Table 8.6. This information provides the number of calculations required if an exhaustive search was conducted. In the present study in excess of 26.9 million calculations are required to examine each and every possible individual. On an Intel Pentium 4 desktop personal computer with a 3.0 GHz processor and 2.0 GB of RAM it would take approximately 4 years to complete this investigation. Table 8.5 provides the Genetic Algorithm parameters.

Table 8.6 Limits and resolution of joint input variable

Joint Variable	**Min Value**	**Max Value**	**Resolution**	**No. of Increments**
Adhesive Thickness	1.0 mm	2.5 mm	0.05 mm	31
GRP Skin Thickness	3.0 mm	7.0 mm	0.5 mm	9
Balsawood Core Thickness	20 mm	50 mm	1.0 mm	31
Steel Thickness	2.0 mm	8.0 mm	0.1 mm	61
Adhesive Young's Modulus	2000 MPa	-	-	1
Bond Length	240 mm	-	-	1
Taper Length	100 mm	200 mm	2.0 mm	51

The analysis of the HSC was conducted in three stages based on the three objective functions of this joint: the weight, the maximum Von Mises stress in the adhesive and the global stiffness. As stated in Chapter 5 the selection criteria for this study is not a true multi-objective function; a single objective function is examined individually, for example weight. However, the maximum Von Mises stress in the adhesive and the global stiffness of the joint are also monitored and any individual that exhibits a reduction in performance of these secondary objectives is given a zero fitness value and will be "bred" out of the population. This ensures that only improvements on the base joint are achieved. The same base joint is used in this study as in the parametric study and the input variables are given in Table 8.3.

The first objective function that the joint is optimised for is minimum weight. As stated earlier there will be no loss in performance in terms of either maximum Von Mises stress in the adhesive or global stiffness. The GA parameters are given in Table 8.5 and 20 repeated runs are made to examine the repeatability and to remove the possibility of optimising to a local optimum. Figure 8.36 shows the progression of the GA by plotting the fitness value against the number of generations for each of the 20 repeated runs. The shape of the plot is typical of an optimisation solution and shows that although the initial populations are randomly generated there is a final focus on the global optimum solution after 30 generations. Figure 8.37 shows the results of the optimisation in terms of percentage change from the baseline joint. Also in the comparison are the results obtained from the parametric study. It is known that individual variable changes and the combination of changes resulted in an improvement to the performance of the joint in terms of increased global stiffness and decreased Von Mises stress in the adhesive. However, this method of improving the joint performance is not optimal. One core objective of the use of the hybrid connection is its weight-reducing attribute. The Genetic Algorithm was used to minimise the weight of the joint without sacrificing the stiffness and stress properties. This methodology resulted in a joint that was 38 percent lighter than the base design and also provided a 55 percent reduction in the Von Mises stress. This can be considered a significant improvement on performance regardless of the relatively small improvement in global stiffness of only 2.5 percent. In addition to being a significant improvement over the base design there is also an improvement over the parametric studies joint, particularly with respect to weight but also in reduction of Von Miss stress. However, the global stiffness improvement is sacrificed.

A similar result is obtained when the GA is used to minimise Von Mises stress in the adhesive. Figure 8.38 shows the progression of the GA for a total of 20 runs, a similar shape plot is achieved as in the minimisation of weight. The percentage change in performance of the joint with minimum Von Mises Stress in the adhesive is given in Figure 8.39. Although with the objective being to minimise stress, there is only a further 4% reduction in Von Mises stress compared to the results for minimisation of weight (Figure 8.37). However, there is a significant improvement in global stiffness over the base design of 39 percent. This is not quite at the level of the parametric study. The improvement in weight is less than that obtained by minimising weight. Over all this optimisation has resulted in the greatest combined improvement over the base design.

Maximising the global stiffness of the joint resulted in a joint with improved stress and stiffness properties compared to the parametric study (Figure 8.40). However, there was very little improvement in the weight (2 percent).

The optimisation study showed that further improvements could be made to the hybrid connection in terms of the weight, stress and stiffness. However, it is the designer that must consider which performance characteristics are most important and consider the results in favour of those parameters. In the present research it has been suggested from the outset that weight is a critical design feature. In addition, it is known from the experimental and numerical studies that the Von Mises stress in the adhesive is critical in the failure of the adhesive, which results in the ultimate failure of the joint. Therefore, it is felt that it is these two performance characteristics that should be used to assess the results of the optimisation. Based on this assumption the minimisation of weight produces the most significant improvements to the joint design (Figure 8.37).

8.5. DISCUSSION

The aim of this chapter was to investigate the HSC joint using genetic algorithm optimisation to improve the performance characteristics of the hybrid connection and also reduce the weight of the joint. Very little work has been conducted on the optimisation of bonded connections and in particular hybrid connections as discussed in Chapter 2. The work presented here provides an important tool for the structural engineer to optimise a structural connection for the loading conditions that it is likely to encounter in-service. The genetic algorithm has been shown to be an efficient method of creating evaluating and selecting design configurations and could prove to be invaluable in the search for the ideal structural connection.

Three numerical methods were employed to investigate the influence on performance of a hybrid connection’s geometric variables. The first took the classical approach of Allman [37] and the use of closed form solutions to predict the shear, peel and Von Mises stress distribution in a double lap joint. The lap joint used was representative of the DLHC. The results highlighted that apart from the overlap length, which is related to the effective bond area, the most sensitive variable investigated was the adhesive thickness. Very thin adhesive layers result in a rapid rise in Von Mises stress and is therefore considered, in light of the results in Chapter 7, an undesirable result. However, this agrees with the use of CSM as an interface layer to increase the bondline thickness in the DLHC joints in Chapter 6.

The second approach involved the parametric variation of individual joint variables within the finite element method. Three performance criteria were examined, the weight, the Von

Mises stress in the adhesive and the global stiffness. This work formed the basis of a set of design curves that were used to define the geometric boundaries of the joint's design space for a formal optimisation study.

The final part was a formal optimisation of the HSC joint with design goals of weight, Von Mises stress and global stiffness. The results showed that the optimisation of such structural connections is possible and the results indicate that substantial gains could be made in terms of weight reduction and minimisation of the failure inducing Von Mises stress.

Chapter 9

Conclusions

9.1. DISCUSSION

Firstly, experimental testing of the full-scale steel-composite joint (HSC), developed for use in the construction of naval superstructures and in particular a helicopter hangar, was conducted. It was identified that the joints compressive strength was dictated by the provision of local stiffening of the joint through internal framing within the helicopter to prevent lateral deflection of the joint. However, the failure load achieved with out-of-plane deflection reduced was far in excess of the loads that the structure would see during normal service conditions. Secondly, the fatigue life characterisation identified an endurance limit at approximately 60% of the ultimate compressive load. A statistical function was used to define the curve and a good level of correlation was achieved. This provided good confidence in the results of the fatigue life characterisation. The endurance limit of the connection was considerably higher than the anticipated in-service load levels, therefore it can be stated that the joint would not be subjected to load levels, during normal service, that would induce fatigue failure before $3.5\text{x}10^6$ cycles.

The fatigue cycles were used to create fatigue damage within the specimens. The specimens were then subjected to bending loads. It was found that there was no loss in joint stiffness or residual strength for the range of damages investigated.

Thirdly, the hygrothermal ageing of the generic connection under accelerated ageing conditions for two years showed a relatively small drop in failure load under static loading. This result provided confidence in the environmental durability of the steel-to-composite connection. The lack of performance degradation is a very positive result. A study was conducted to assess if there was any performance degradation within the hybrid connections composite material. This study also showed no loss in material Young's modulus after two years of accelerated ageing. This was a surprising result as the joint used in the present research considered as a worst-case scenario as there is no paint or primer applied to the joint to prevent absorption of moisture through the GRP. However, there is a trend of diminishing failure load and particularly displacement.

Although experimental testing can provide a physical result regarding the structures performance, numerical techniques can be employed to further enhance the understanding of how a structure behaves under load. Fourthly, the present research examines the hybrid connection using FEA and developed a model that produced results of a high confidence level and excellent correlation to the experimental results. The model included the non-rigid boundary conditions present in the experiments and successfully predicted the linear response of the HSC. A progressive damage methodology was developed which examined and progressed failure within the adhesive layer. In the literature [48] progressive damage methods commonly apply a stiffness reduction method to modify the material properties after initial failure. However, in the present study an alternative method is proposed whereby the stress in the failed element is reduced. This provides results with excellent correlation to the experimental results in the non-linear region of the joint response. The method accurately predicted the displacement and load point where the response became non-linear. Although the correlation of the numerical and experimental results was good there was still an over prediction of either the failure load or failure displacement. An alternative method of predicting the material degradation model was proposed whereby the fracture toughness energy, obtained experimentally, could be used to provide the stress reduction model. Although the method is promising there are issues regarding numerical stability. However, the prediction of non-linear response and maximum load are predicted with the same accuracy with this method.

The results of the numerical modelling provided an accurate model of the steel-composite connection. Finally, this model was used to assess the influence of changes in geometric variables associated with the joint on performance. Increased performance was gauged by a reduction in weight of the hybrid connection, a reduction in the maximum Von Mises stress in the adhesive (indication of initial failure) and an increase in global stiffness. All the geometric variations made were compared to the baseline joint configuration tested in the experimental phase. It was found that a substantial reduction in Von Mises stress and an increase in global stiffness were possible with little gain in the connection's weight. Although this provided a number of design curves for the joint based on individual geometric characteristics however further improvement could be made through a more formal examination of the design space. Genetic algorithms were used and the results showed that further improvement was indeed possible. A substantial reduction in the joint weight could be achieved with an equivalent improvement as in the parametric study for Von Mises stress and global stiffness. This study identified that genetic algorithms could be used to optimise the geometry of the joint to improve structural performance. They could form part of the range of tools available to structural engineers for the development of structural connections.

Overall the present research has provided valuable information that can be used by the naval architect to better understand the application of steel-composite joints in a marine structure. The results presented in this thesis when viewed alongside the previously available literature on hybrid connection show that there is an increasing level of knowledge in the joints application. It is now feasible that the application of hybrid connections can be designed with more confidence due to the lessons learnt and the tools developed by the present research.

9.2. SPECIFIC CONTRIBUTIONS TO THE SUBJECT

The aim of this thesis was to develop an understanding in areas of the field of hybrid connections that are not currently addressed in the open literature. In particular the mechanisms of failure in the current hybrid steel to composite connections were investigated and used to look at the performance improvements of the author's proposed new generation joint design. The four areas in which this thesis uniquely contributes to the subject of steel-composite joints are:

- In-plane static and fatigue performance of hybrid connections
- Accelerated ageing of hybrid connections

- Progressive damage modelling of hybrid connections
- Optimisation of a hybrid connection

The present research identifies the static and fatigue characteristics of the hybrid connection to provide information on how the connection behaves under axial loading. The results identified the location of initial failure under static loading. In addition, a statistical function was used to correctly represent the fatigue characterisation curve.

A long-term accelerated ageing program to investigate moistures influence on the hybrid connection found that the in-plane tensile performance of the joint was unaffected by the accelerated ageing process. This is an important result for the application of hybrid connections to marine vessels.

The present research also investigated the behaviour of the HSC joint providing information vital to the understanding of the mechanisms of stress distribution within the joint and the progression of failure. The progressive damage modelling used a new method of defining the degradation of the material properties post-maximum stress. In addition the model for the degradation was based on a new method of incorporating fracture toughness energy as the variable to describe the mathematical function of property degradation.

Genetic algorithms, were used to investigate the design space of the HSC joint and provided a number of possible improvements to the performance of the joint through geometric changes alone. The main objective of the study was reduced joint weight. The present research highlighted the importance of optimisation as a tool for the structural engineer in an area where little research has been conducted. A large step change in performance in terms of weight was achieved through the use of this optimisation technique.

Chapter 10

Further work

The present research has highlighted a number of areas that require further research. These can be divided into four main areas:

1. Fatigue life characterisation of the generic steel-composite joint
2. Further hygrothermal ageing studies
3. Numerical instability of the progressive damage model for negative Young's moduli
4. Validation of the optimisation study through an experimental programme

The fatigue life characterisation of the generic steel-to-composite connection was inconclusive. This was due to the experimental scatter obtained from the tests conducted. There was no physical evidence to determine a reason for this scatter. A further study of fatigue life with smaller scale specimens that require lower loads and less specialist test equipment may reveal why the scatter occurred. Lessons learnt from the small-scale tests may provide a solution to the large scale testing.

The hygrothermal ageing results indicated a small loss in performance after 2 years of accelerated ageing. This was unexpected. One reason put forward was the anodic reaction of the steel preventing the corrosion of the more protected interface between the steel and GRP. The influence of the anodic reaction on the corrosion of the interface between the steel and GRP should be investigated on a smaller scale. Coatings, such as those found on naval vessels should help to inhibit the corrosion of the steel away from the connection this may help to promote the corrosion at the interface and therefore judge the reduction in joint performance based on corrosion at the interface alone. However, further research would be required to verify this assumption.

The numerical modelling incorporating the progressive damage modelling requires further work to successfully link the fracture energy values for the adhesive, which can be obtained experimentally, to the property degradation model. In addition, the subsequent large negative Young's modulus results in numerical instability in the equilibrium calculations within the finite element code. Careful implementation of this within the user-defined subroutines should provide a better correlation with the experimental results.

Finally, the optimisation study revealed that a joint with lower Von Mises stress in the adhesive and greater global stiffness with a lower overall weight is possible. However, this study is quite simplified and experimental validation of this result would provide further information and improve the prediction by the optimisation method. In addition, further work involving a multi-objective function for the selection process could provide a better optimal solution as a larger number of outputs from the analysis could be used in the assessment process.

References

1. **Cao, J. and Grenestedt, J.L.**, "Test of a redesigned glass-fibre reinforced vinyl ester to steel joint for use between a naval GRP superstructure and a steel hull," *Composite Structures*, **60**:439-445, 2003.

2. **Clifford, S.M., Manger, C.I.C., and Clyne, T.W.**, "Characterisation of a glass-fibre reinforced vinylester to steel joint for use between a naval GRP superstructure and a steel hull," *Composite Structures*, **57**(1-4):59-66, 2002.

3. **Melograna, J.D. and Grenestedt, J.L.**, "Adhesion to stainless steel to fibre reinforced vinyl ester composite," *Journal of Composite Technology Research*, **24**(4):254-260, 2002.

4. **Melograna, J.D. and Grenestedt, J.L.**, "Improving joints between composites and steel using perforations," *Composites Part A*, **A33**:1253-1261, 2002.

5. **Ho, B.S.**, "An archaeological study of Glamis: The role of a 19th-century iron barque", *Master of Science*, Florida State University, USA, 2004.

6. **Smith, C.S.**, "Design of Marine Structures in Composite Materials", Elsevier Applied Science, UK, 1990.

7. **Anon**. "80.5% GRP at London Boat Show". *Reinforced Plastics* 16(1). 1972.

8. **Anon**. "Boat Show '81". *Reinforced Plastics* 25(2). 1981.

9. **Spaulding, K.B.** "A History of the Construction of Fibreglass boats for the Navy". *Bureau of Ships Journal* 15(2-11). 1996.

10. "32nd America's Cup Official Website". http://www.americascup.com . 2006. 30-3-2006.

11. **Smith, C.S. and Murphy, P.**, "Response of hybrid GRP/steel superstructures to blast loading - theory and experiment", *Advances in Marine Structures - 2, Dunfermline, Scotland, UK*, Elsevier Applied Science, pp392-415, 1991.

12. **Dow, R.S.** "Experimental and theoretical response prediction of steel-stiffned glass-reinforced plastic ship deckhouse subject to blast loading". *Marine Structures* 7(2-5), 399-416. 1994.

13. **Chalmers, D.W.** "The potential for the use of composite materials in marine structures". *Marine Structures* 7(2-5), 441-456. 1994.

14. **Camanho, P.P. and Matthews, F.L.**, "Stress analysis and strength prediction of mechanically fastened joints in FRP: a review," *Composites Part A*, **28A**:529-547, 1997.

15. **Dano, M.-L., Gendron, G., and Picard, A.**, "Stress and failure analysis of mechanically fastened joints in composite laminates," *Composite Structures*, **50**:287-296, 2000.

16. **Hart-Smith, F.L.**, In: *Joining Fibre Reinforced Plastics*, F.L. Mathews, ed.,Elsevier, 1987.

17. **Hart-Smith, F.L.**, In: *Developments in adhesives - 2*, A.J. Kinloch, ed.,Applied Science Publishers, 1981.

18. **Hashim, S.A., Winkle, I.E., and Cowling, M.J.**, "A Structural Role for Adhesives in Shipbuilding," *Naval Architect*,203-220, 1990.

19. **Bacicchi, G. and Nevierov, A.**, "Use of alternative structural materials in the superstructures of cruise vessels", *International Conference on Ship and Shipping Research (NAV2000) XIII Congress*, Venice, Italy, pp10.2.1-10.2.12, 2000.

20. **Matthews, F.L., Kilty, P.F., and Godwin, E.W.**, "A review of the strength of joints in fibre-reinforced plastics: Part 2. Adhesively bonded joints," *Composites*, **13**(1):29-37, 1982.

21. **Tsai, M.Y., Morton, J., and Matthews, F.L.**, "Experimental and Numerical studies of a laminated composite single-lap adhesive joint," *Journal of Composite Materials*, **29**(9):1154-1275, 1995.

22. **Vinson, J.R.**, "Adhesive bonding of polymer composites," *Polymer Engineering and Science*, **29**:1325-1331, 1989.

23. **Adams, R.D., Comyn, J., and Wake, W.C.**, "Structural Adhesive Joints in Engineering", 2nd ed.,Chapman & Hall, London, 1997.

24. **Lang, T.P. and Mallick, P.K.**, "Effect of spew fillet geometry on stresses in single lap adhesive joints," *International Journal of Adhesion and Adhesives*, **18**:167-177, 1998.

25. **Chamis, C.C. and Murthy, P.L.N.**, "Simplified procedures for designing adhesively bonded composite joints," *Journal of Reinfored Plastics and Composites*, **10**:29-41, 1991.

26. **Ong, C.L. and Shen, S.B.**, "Some Results on Metal and Composite Patch Reinforcement of Aluminium Honeycomb Panel," *Theoretical and Applied Fracture Mechanics*, **16**(2):145-153, 1991.

27. **Tay, T.E., Chau, F.S., and Er, C.J.**, "Bonded boron-epoxy composite repair and reinforcement of cracked aluminium structures," *Composite Structures*, **34**(3):339-347, 1996.

28. **Naboulsi, S. and Mall, S.**, "Characterisation of fatigue crack growth in aluminium panels with a bonded composite patch," *Composite Structures*, **37**(3/4):321-334, 1997.

29. **Sasdelli, M., Karbhari, V.M., and Gillespie, J.W.Jr.**, "On the use of metal inserts for attachment of composite components to structural assemblies - a review," *International Journal of Vehicle Design*, **14**(4):353-369, 1993.

30. **Shin, K.C., Kim, Y.G., Lee, D.G., and Choi, J.M.**, "Adhesively bonded lap-joints for the composite-steel shell structure of high-speed vehicles," *Composite Structures*, **38**(1-4):215-227, 1997.

31. **Shin, K.C. and Lee, J.J.**, "Tensile load-bearing capacity of co-cured double lap joints," *Journal of Adhesion Science and Technology*, **14**(12):1539-1556, 2000.

32. **Hildebrand, M. and Hentinen, M.**, "Efficient solutions for joints between large FRP-sandwich and metal structures", *Proceedings of the 19th SAMPE Europe International Conference*, Paris, France, 1998.

33. **Le Lan, J.Y., Parneix, P., and Gueguen, P.L.**, "Composite material superstructures", *International Conference on Nautical Construction with Composite Materials*, Paris, France, 1992.

34. **Wright, P.N.H., Wu, Y., and Gibson, A.G.**, "Fibre reinforced composite-steel connections for transverse ship bulkheads," *Plastics, Rubber and Composites*, **29**(10):549-557, 2000.

35. **Volkerson, O.**, "Die niektraftverteiling in zugbeansprunchten mit konstanten laschenquerscritten," *Luftfahrforsch*, **15**:41-47, 1938.

36. **Golland, M. and Reissner, E.**, "Stresses in cemented joints," *Journal of Applied Mechanics*, **11**:A17, 1944.

37. **Allman, D.J.**, "A theory for elastic stresses in adhesive bonded lap joints," *Quarterly Journal of Mechanics and Applied Mathematics*, **30**(4):415-436, 1977.

38. **Collings, T.A.**, "The strength of bolted joints in multi-directional CFRP laminates," *Composites*, **8**:43-54, 1982.

39. **Collings, T.A.**, "On the bearing strength of CFRP laminates," *Composites*, **13**:241-252, 1987.

40. **Hamada, H., Kazushi, H., and Maekawa, Z.-I.**, "Effects of stacking sequence on mechanically fastened joint strength in quasi-isotropic carbon-epoxy laminates," *Journal of Composite Technology Research*, **17**(3):249-259, 1995.

41. **Quinn, W.J. and Matthews, F.L.**, "The effect of clamping pressure on bolt bearing loads in glass fibre-reinforcement plastics," *Journal of Composite Materials*, **11**:139-145, 1987.

42. **Chang, F.-K. and Lessard, L.B.**, "Damage tolerance of laminated composites containing an open hole and subjected to compressive loadings: Part I - Analysis," *Journal of Composite Materials*, **25**:2-43, 1991.

43. **Chang, F.-K. and Chang, K.-Y.**, "A progressive damage model for laminated composites containing stress concentrations," *Journal of Composite Materials*, **21**:834-855, 1987.

44. **Hashin, Z.**, "Failure criteria for unidirectional fibre composites," *Journal of Applied Mechanics*, **47**:329-334, 1980.

45. **Gamble, K., Pilling, M., and Wilson, A.**, "An automated finite element analysis of the initiation and growth of damage in carbon-fibre composite materials," *Composite Structures*, **32**:265-274, 1995.

46. **Hill, R.**, "A theory of the yielding and plastic flow of anisotropic metals," *Proccedings of the Royal Society, Series A*, **193**, 1948.

47. **Kim, Y., Davalos, J.F., and Barbero, E.J.**, "Progressive failure analysis of laminated composite beams," *Journal of Composite Materials*, **30**(5):536-560, 1996.

48. **Padhi, G.S., Shenoi, R.A., Moy, S.S., and Hawkins, G.L.**, "Progressive failure and ultimate collapse of laminated composite plates in bending," *Composite Structures*, **40**(3-4):277-291, 1998.

49. **Minnetyan, L. and Chamis, C.C.**, "Progressive fracture of adhesively bonded composite structures," *Theoretical and Applied Fracture Mechanics*, **31**:75-84, 1999.

50. **Feih, S., Shercliff, H.R., and McGrath, G.**, "Optimisation of peel joint geometries in CFRP laminates under static loading with regard to first and final failure", *Proceedings of the International Conference on Composite Materials (ICCM13)*, Brighton, UK, 2000.

51. **Feih, S., Shercliff, H.R., and McGrath, G.**, "3-D progressive damage modelling for adhesively bonded composite peel joints: Implementation in a UMAT and related computational issues", *Proceedings of the ABAQUS users conference*, Warrington, UK, 2000.

52. **Levy, R.L., Fanter, D.L., and Sommers, C.J.**, "Spectroscopic evidence for mechanochemical effects of moisture in epoxy resins," *Journal of Applied Polymeric Science*, **24**:1643-1664, 1979.

53. **Earl, J.S.**, "The influence of hygrothermal ageing on polymeric composite sandwich materials and structures", *Doctor of Philosophy Thesis*, University of Southampton, 2001.

54. **Shen, C.H. and Springer, G.S.**, "Moisture absorption and desorption of composite materials," *Journal of Composite Materials*, **10**:2-20, 1976.

55. **Kotsikos, G., Morris, K., and Mawella, J.**, "Durabilty assessment of marine composites", *10th CF/DRDC Meeting on Naval Applications of Materials Technology, 13-15 May 2003*, Defence R&D Canada, 2003.

56. **Springer, G.S.**, "Environmental effects on epoxy matrix composites", *Composite Materials: testing and Design (Fifth Conference)*, American Society for Testing and Materials, pp291-312, 1979.

57. **Vauthier, E., Chateauminois, A., and Bailliez, T.**, "Hygrothermal ageing and durability of unidirectional glass-epoxy composites", *10th International Conference on Composite Materials (ICCM10)*, 6 pp185-192, 1995.

58. **Criscioli, P.R., Lee, W.I., Peterson, D.G., and Springer, G.S.**, "Accelerated environmental testing of composites," *Journal of Composite Materials*, **21**:225-242, 1987.

59. **Gerald, C.F. and Wheatley, P.O.**, "Applied numerical methods", Addison-Wesley Publishing Co., London, 1984.

60. **Fogel, D.B.** "An introduction to simulated evolutionary optimization". *IEEE Transactions on Neural Networks* 5(1), 3-14. 1994.

61. **Day, A.H. and Doctors, L.J.**, "The survival of the fittest - evolutionary tools for hydrodynamic design of ship hull form," *Trans. of the Royal Institution of Naval Architects*, **142 Part C**:182-197, 2000.

62. **Michell, J.H.**, "The resistance of a ship," *Philosophical Magazine*, **45**(5):106-123, 1898.

63. **Nash, S.G.** "Newton-type minimisation via the lanczos method". *SIAM Journal on Numerical Analysis* 21(4), 770-778. 1984.

64. **Clayton, R.P. and Martinez-Botas, R.F.** "Application of generic algorithms in aerodynamic optimisation design procedures". *The Aeronautical Journal* 108(1090), 611-620. 2004.

65. **Kang, J.-H. and Kim, C.-G.** "Minimum weight design of compressively loaded composite plates and stiffened panels for postbuckling strength by genetic algorithm". *Composite Structures* 69, 239-246. 2005.

66. **Kicinger, R., Arciszewski, T., and DeJong, K.** "Evolutionary design of steel structures in tall buildings". *Journal of Computing in Civil Engineering* 19(3), 223-238. 2005.

67. **Hearn, G.E., Wright, P.N.H., and Welsh, M.**, "Design for optimal operation of large container ships", *Proc. of the Intl. Conf. on Design and Operation of Container Ships*, Royal Institution of Naval Architects, 1999.

68. **Melograna, J.D., Grenestedt, J.L., and Maroun, W.J.**, "Adhesive tongue-and-grove joints between thin carbon fiber laminates and steel," *Composites Part A*, **34**(2):119-124, 2003.

69. **Blake, J.I.R., Shenoi, R.A., House, J., and Turton, T.** "Strength modelling in stiffened FRP structures with viscoelastic inserts for ocean structures". *Ocean Engineering* 29, 849-869. 2002.

70. **Blake, J.I.R., Shenoi, R.A., House, J., and Turton, T.** "Progressive damage analysis of tee joints with visco-elastic inserts". *Composites Part A* 32A, 641-653. 2001.

71. **Cheuk, P.T., Tong, L., Wang, C.H., Baker, A., and Chalkley, P.**, "Fatigue crack growth in adhesively bonded composite-metal double-lap joints," *Composite Structures*, **57**(1-4):109-115, 2002.

72. **Pashias, C., Turnock, S.R., and Abu-Sharkh, S.M.**, "Design optimization of a bi-directional integrated thruster", *Proc. of Propellers/Shafting 2003 Symposium*, SNAME(13), pp1-13, 2003.

73. **Ashcroft, I.A., Digby, R.P., and Shaw, S.J.**, "The effect of environment on the performance of bonded composite joints", Professional Engineering Publishing, London, UK, pp73-85, 1999.

74. **Crocombee, A.D.** "Durability modelling concepts and tools for cohesive environmental degredation of bonded structures". *International Journal of Adhesion and Adhesives* 17, 229-238. 1997.

75. **Williams, C., Summerscales, J., and Grove, S.**, "Resin infusion under flexible tooling (RIFT): a review," *Composites Part A*, **27**(7):517-524, 1996.

76. "Crystic Composites Handbook", Scott Bader Company Ltd., 2003.

77. **Shenoi, R.A., Read, P.J.C.L., and Hawkins, G.L.**, "Fatigue failure mechanisms in fibre-reinforced plastic laminated tee joints," *International Journal of Fatigue*, **7**(6):415-426, 1995.

78. **Ochoa, O. and Reddy, J.N.**, "Finite element analysis of composite laminates", Kluwer Academic Publishers, Dordrecht, The Netherlands, 1992.

79. "World wide failure exercise on failure prediction in composites". *Composites Science and Technology* 62(12-13), 1479-1797. 2002.

80. **Benham, P.P. and Crawford, R.J.**, "Mechanics of engineering materials", Longman Scientific & Technical, UK, 1987.

81. **Tsai, S.W. and Wu, E.M.**, "A general theory of strength for anisotropic materials," *Journal of Composite Materials*, **5**:58-80, 1971.

82. **Tsai, S. W.**"Strength characteristics of composite materials", NASA CR-224, NASA, 1965,

83. **Azzi, V.D. and Tsai, S.W.**, "Anisotropic strength of composites," *Experimental Mechanics*, **September**:283-288, 1965.

84. **Hoffman, O.**, "The brittle strength of orthotropic materials," *Journal of Composite Materials*, **1**:200-206, 1967.

85. **Burman, M. and Zenkert, D.**, "Fatigue of foam core sandwich - 1: undamaged specimens," *International Journal of Fatigue*, **19**(7):551-561, 1997.

86. **Lee, J., Harris, B., Almond, D.P., and Hammett, F.**, "Fibre composite fatigue - life determination," *Composites Part A*, **28A**:5-15, 1997.

87. **Kapadia, A**"Weight and cost comparison of base design structure toa given steel structure", Technical Report VT-2.3-C3-IP3.0, EUCLID RTP 3.21, 2002,

88. **ABCD Working Group on Human Perfomance at Sea**, "Generating and using human performance simulation data to guide designers and operators of navy ships: Two large multinational programmes", *International Conference on Seakeeping and Weather*, London, UK, 1995.

89. **de Moura, M.F.S.F., Goncalves, J.P.M., Marques, A.T., and de Castro, P.M.S.T.** "Prediction of compressive strength of carbon-epoxy laminates containing delamination by using a mixing-mode damage model". *Composite Structures* 50, 151-157. 2000.

90. **Courant, R.**, "Variational methods for the solution of problems of equilibrium and vibrations," *Bulletin of the American Mathematical Society*, **49**:1-23, 1943.

91. **Turner, M.J., Clough, R.W., Martin, W.C., and Topp, L.J.**, "Stiffness and deflection analysis of complex structures," *Journal of Aeronautical Sciences*, **23**:805-824, 1956.

92. **Boyd, S.W., Blake, J.I.R., Shenoi, R.A., and Kapadia, A.**, "Integrity of hybrid steel-to-composite joints for marine application," *Journal of Engineering for the Maritime Environment, Proceedings of the Institution of Mechanical Engineers, Part M*, **218**(M4):235-245, 2004.

93. **Smith, C.S. and Monks, A.H.**, "Design of High Performance Hulls in Fibre-Reinforced Plastics", *Symposium on small fast warships and security vessels*, The Royal Institiution of Naval Architects, London, UK, 1982.

Illustrations

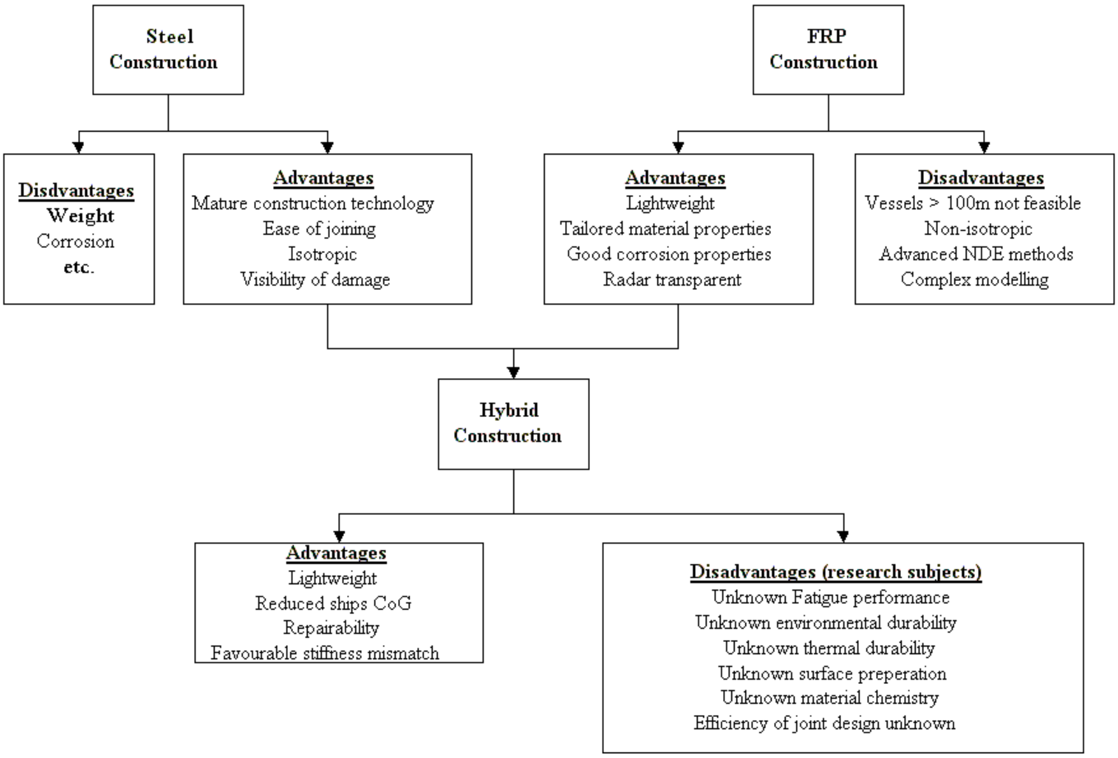

Figure 1.1 Advantages and disadvantages of Steel, GRP and hybrid construction

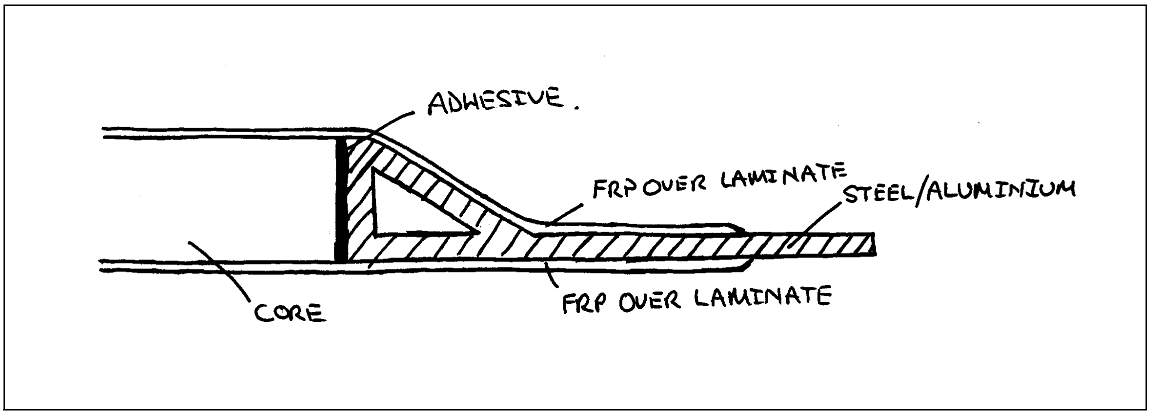

Figure 2.1 Over-laminated joint from Hildebrand and Heintinen [27]

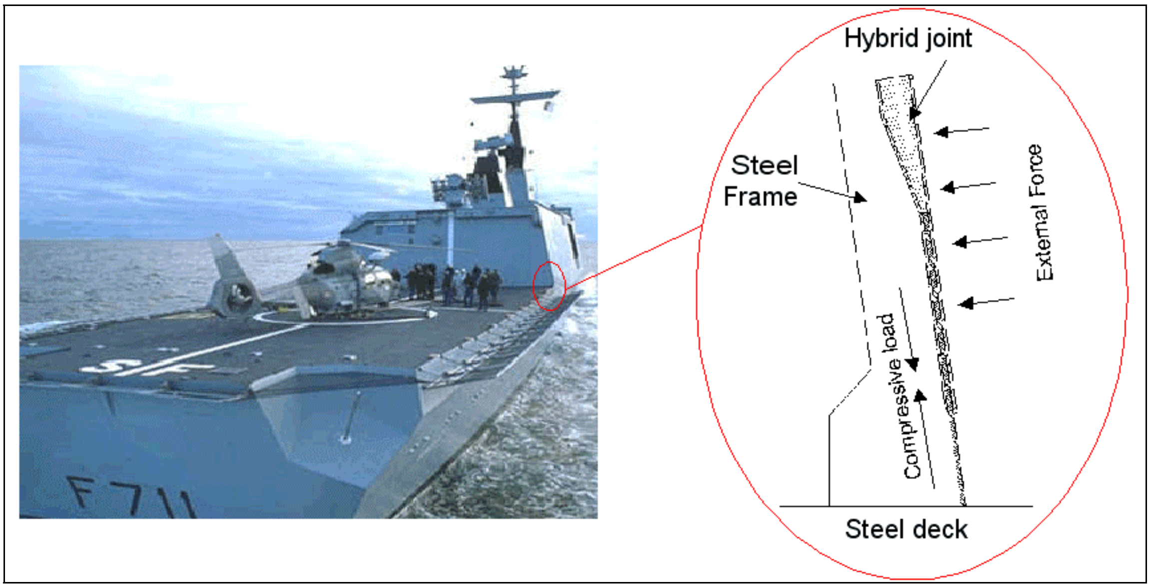

Figure 3.1 Typical location for a hybrid joint on a naval vessel (courtesy of DCN)

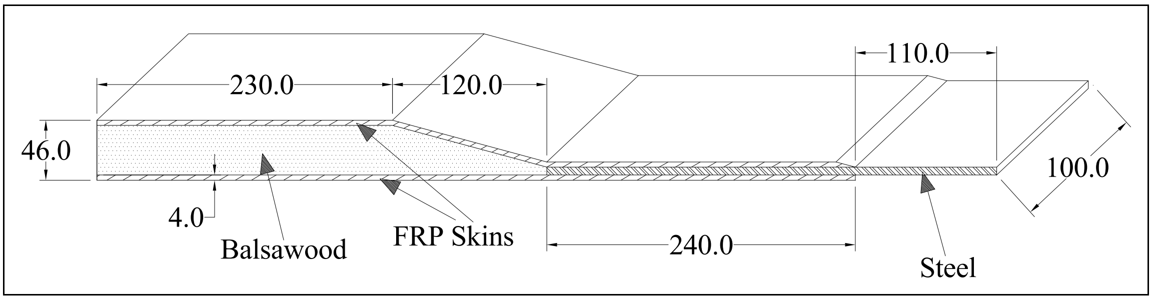

Figure 3.2 Schematic representation of HSC specimen (mm)

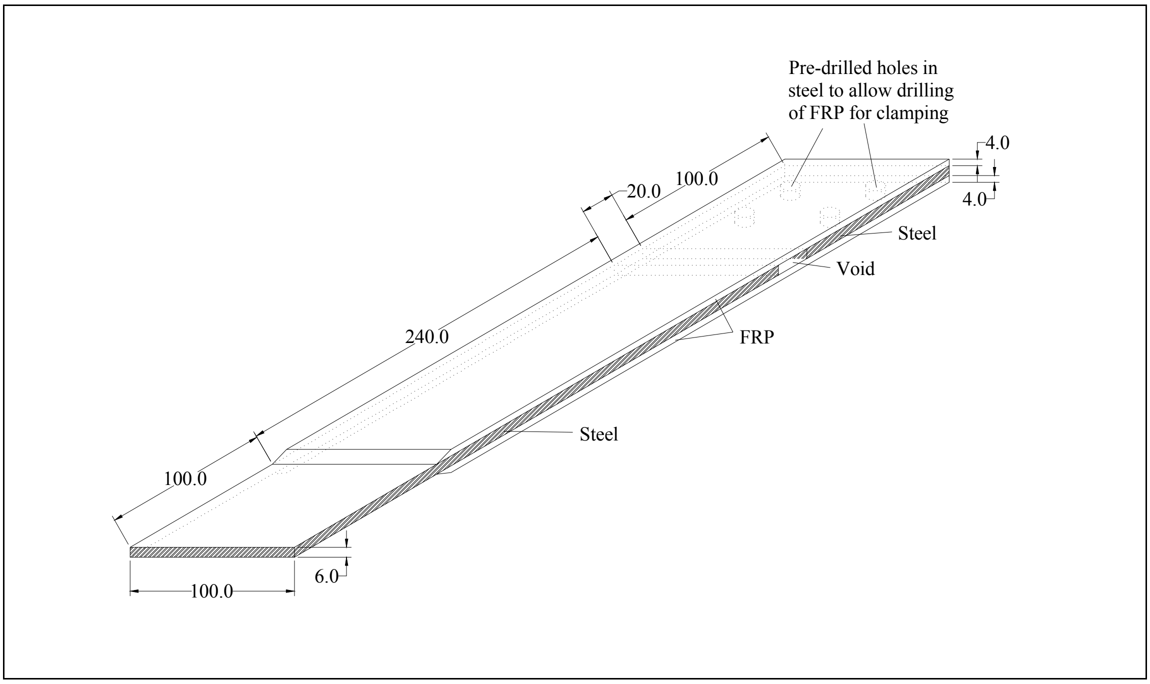

Figure 3.3 Schematic representation of the DLHC specimen (mm)

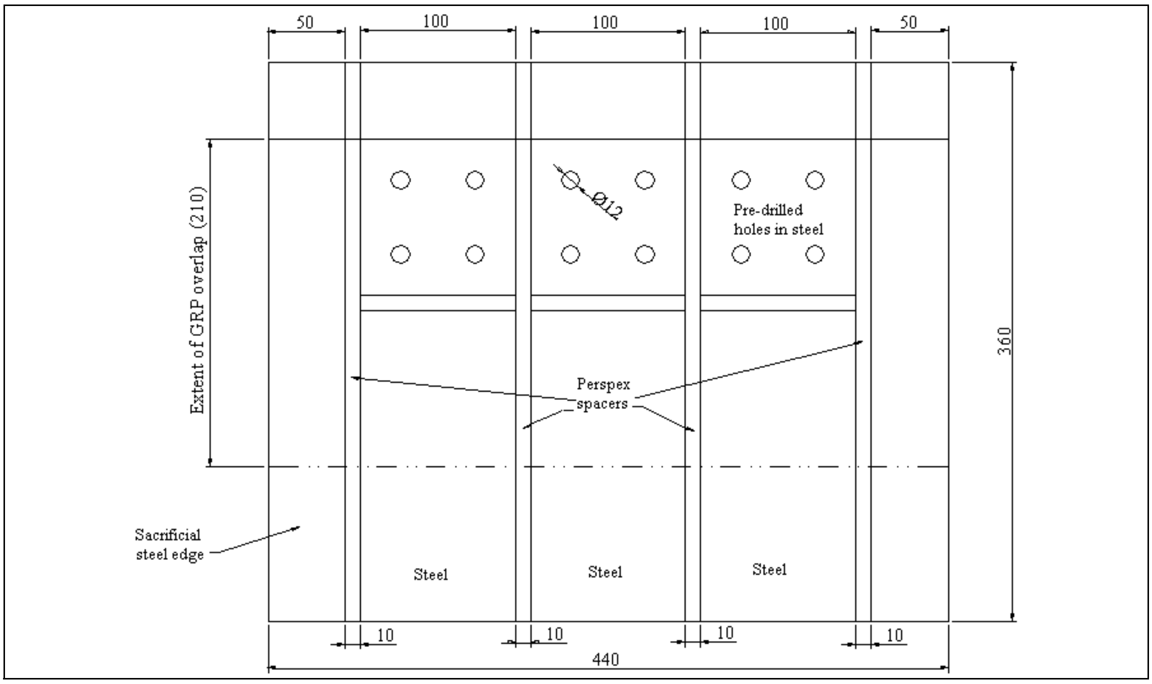

Figure 3.4 Lay up steel for DLHC specimens (mm)

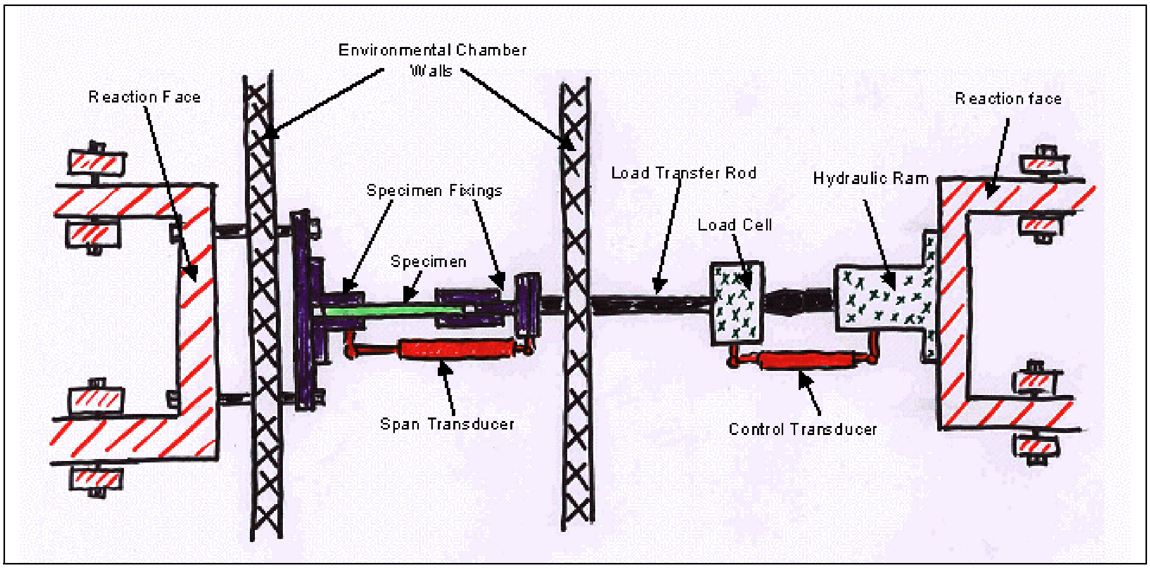

Figure 4.1 Schematic representation of FORTRESS testing rig

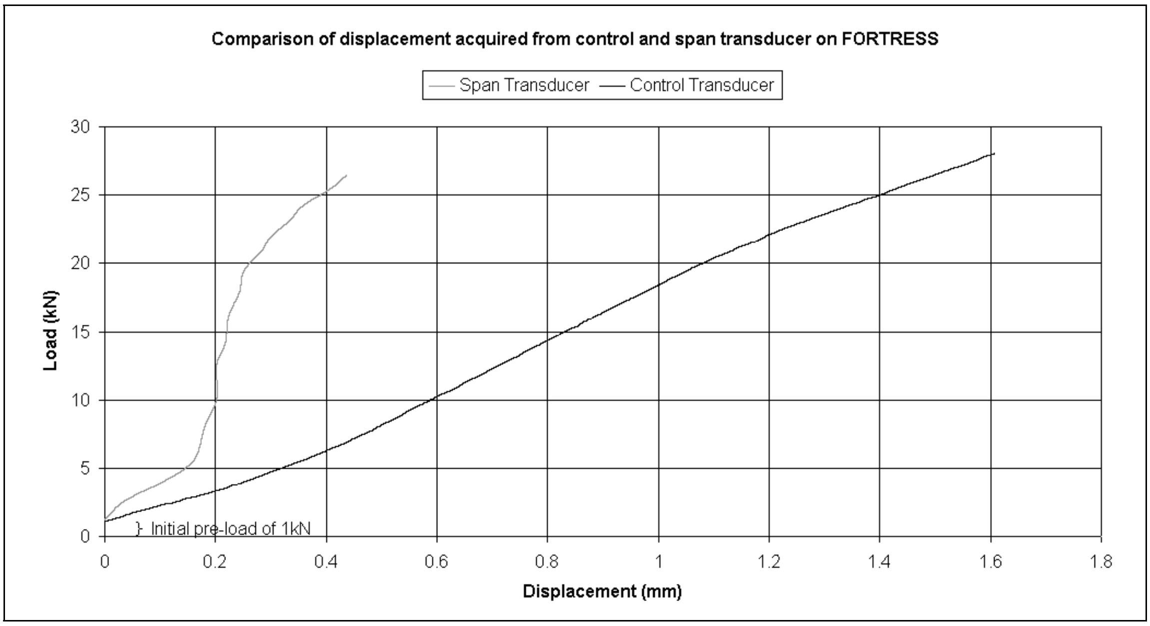

Figure 4.2 Control and span transducer differences for FORTRESS

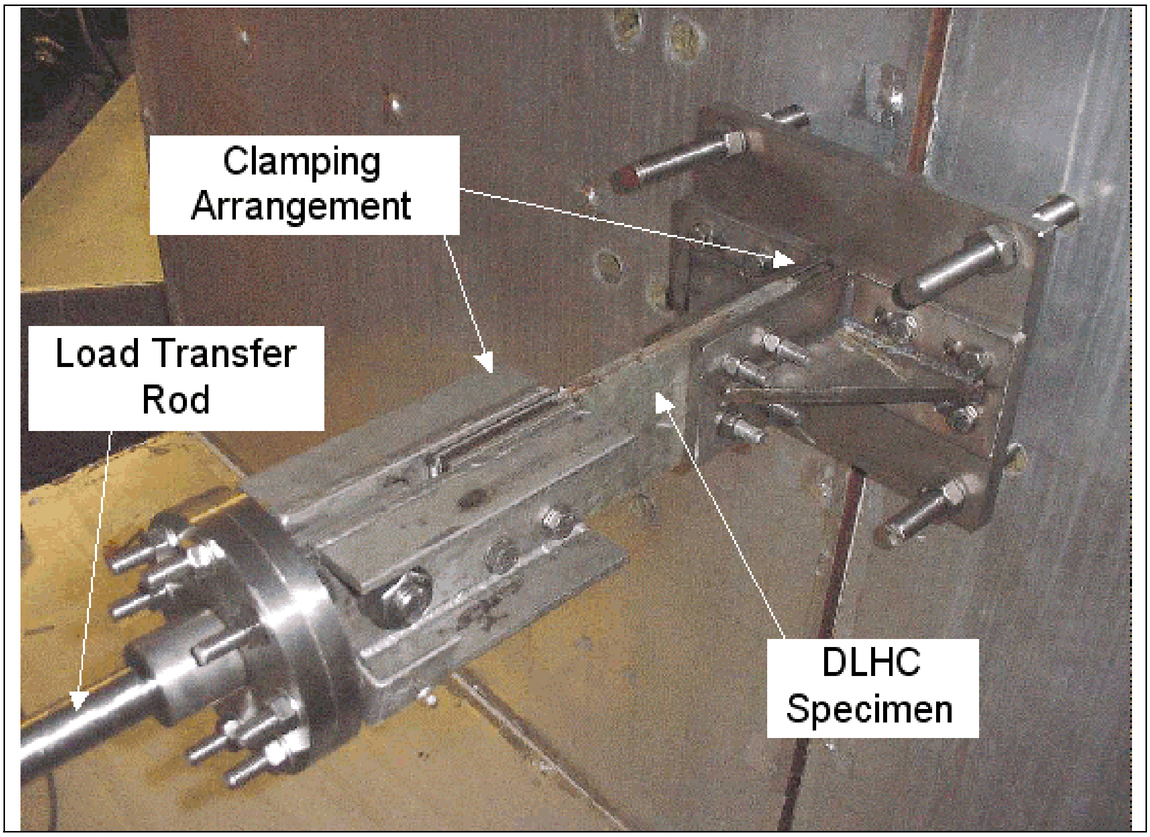

Figure 4.3 Experimental test set up for DLHC specimen

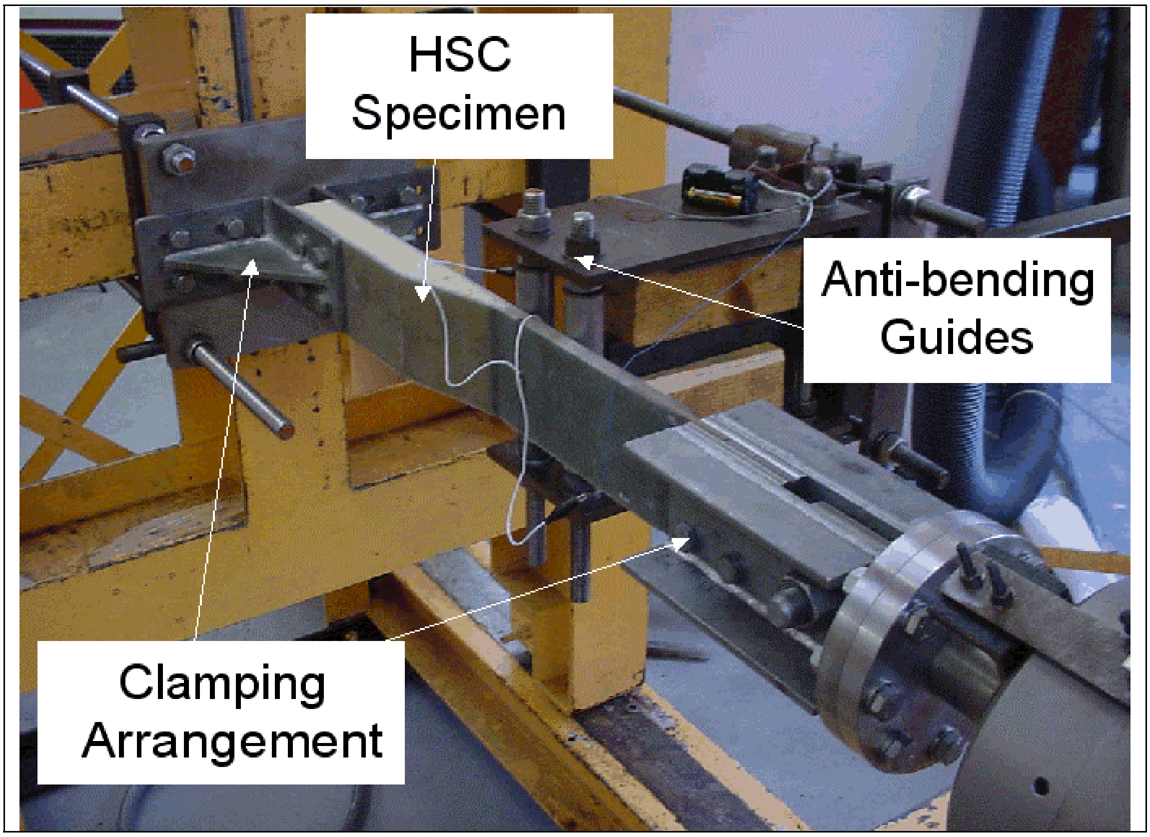

Figure 4.4 Experimental test set up for HSC specimen

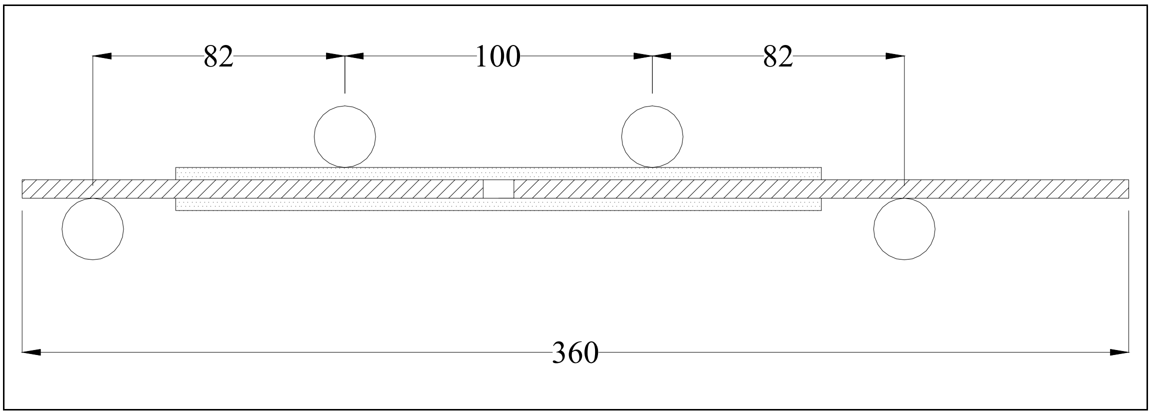

Figure 4.5 Schematic of test setup for bending tests of DLHC (mm)

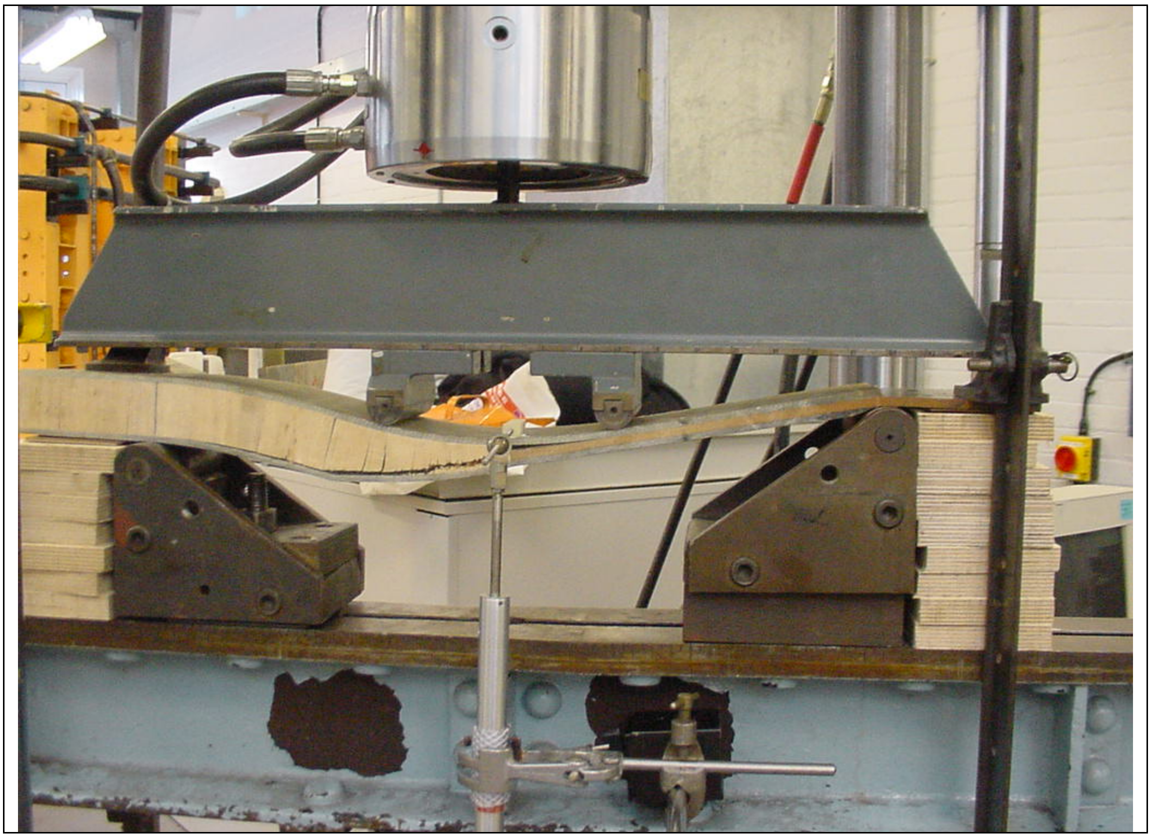

Figure 4.6 Experimental test setup for HSC bending tests

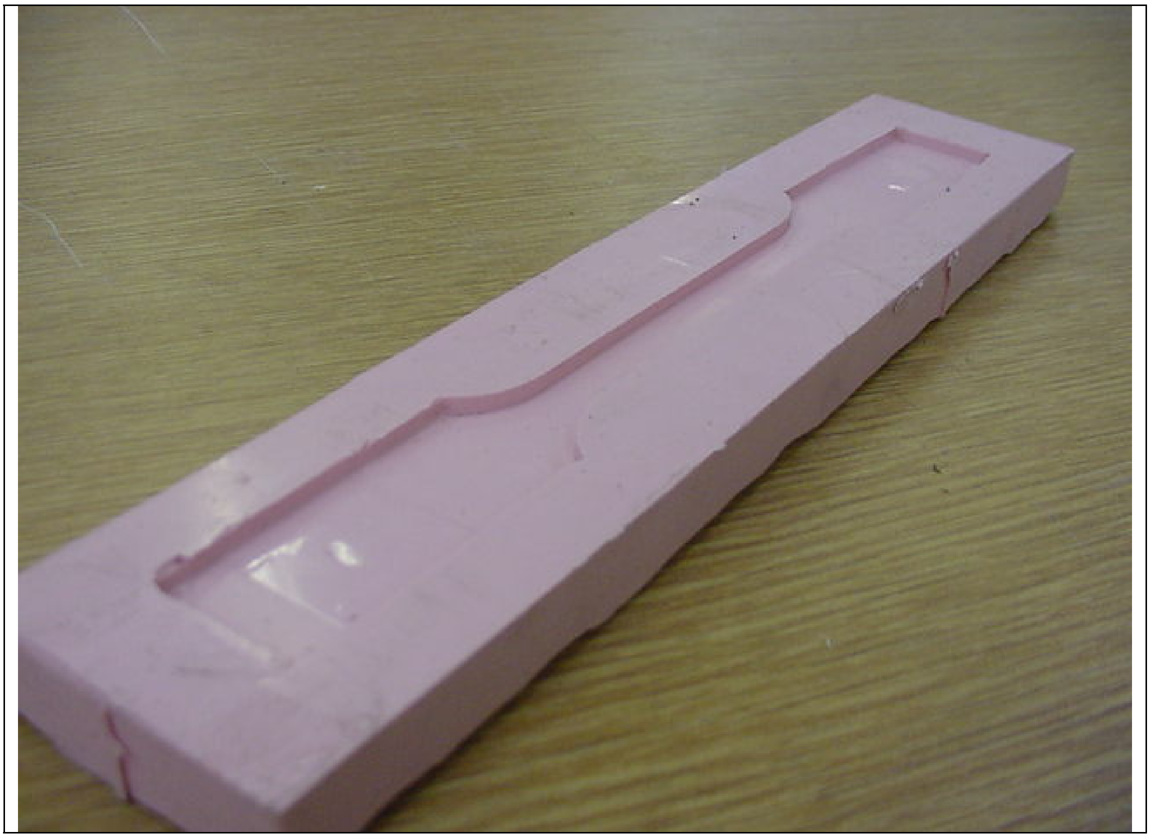

Figure 4.7 Mould for producing resin castings from steel BS template

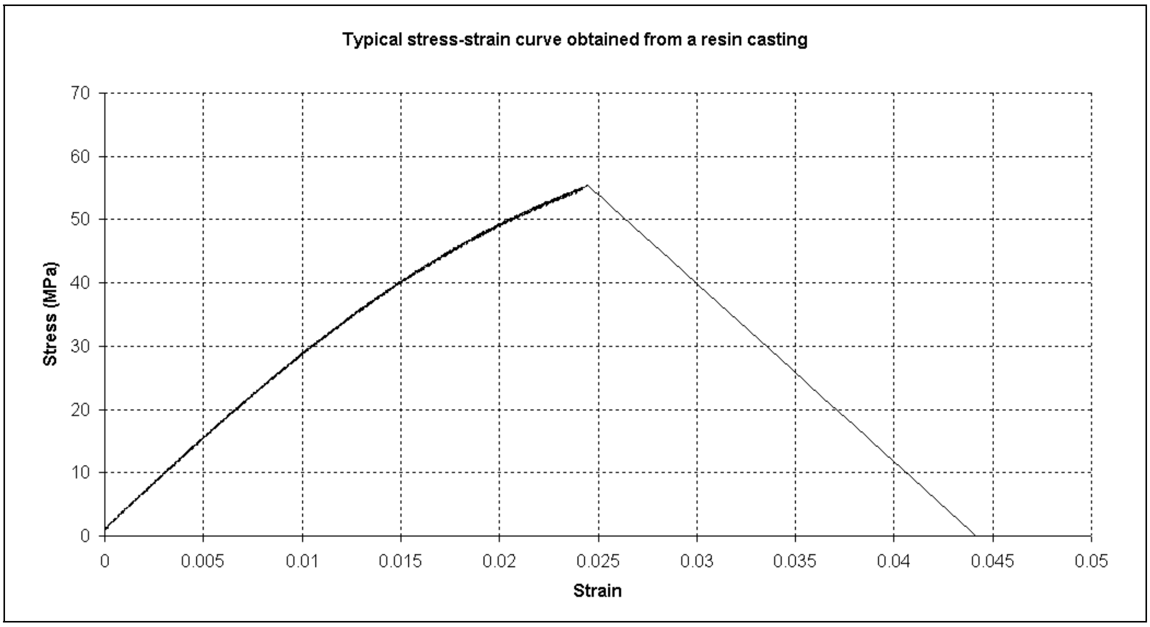

Figure 4.8 Typical stress-strain curve for resin casting in tension

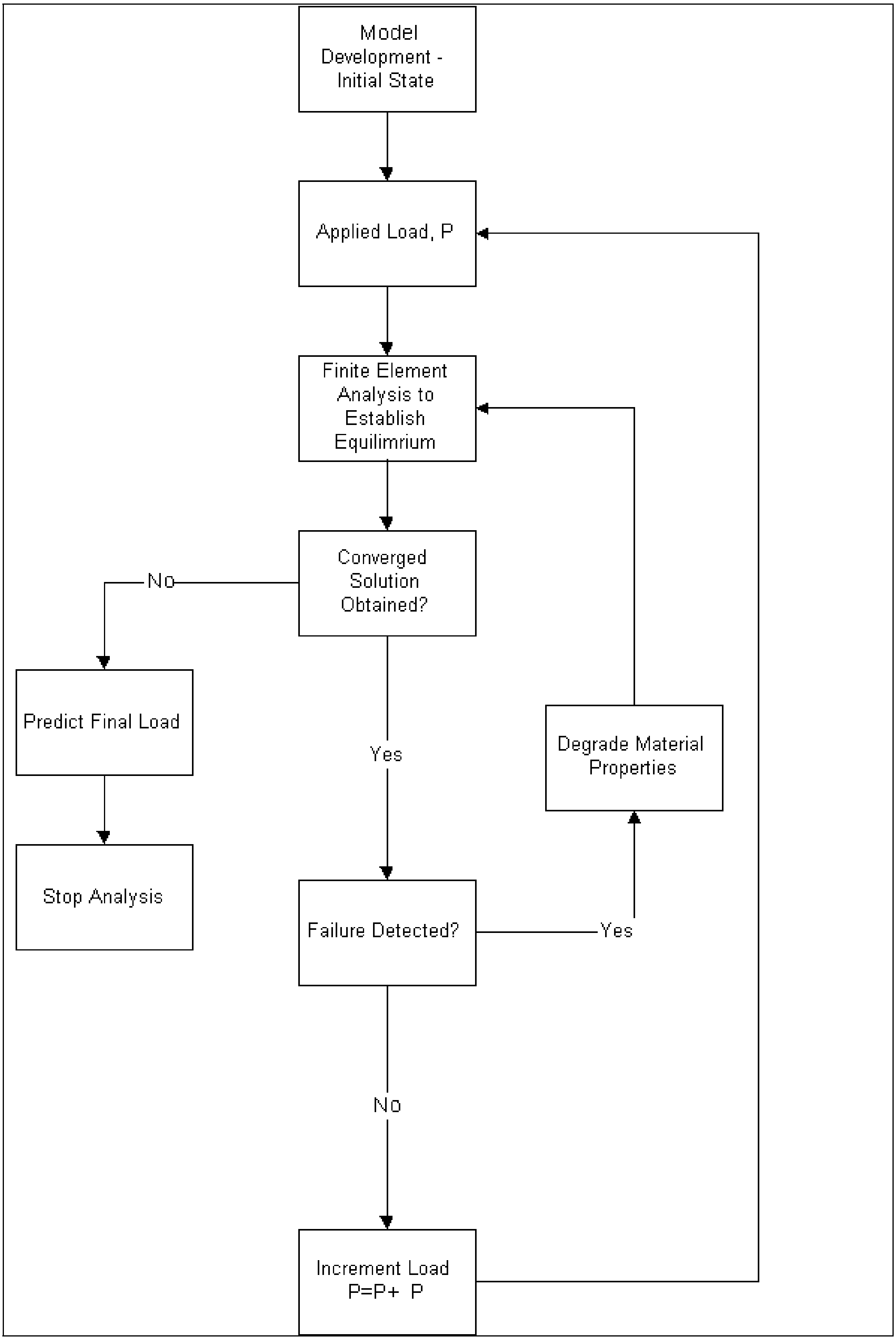

Figure 5.1 Progressive damage methodology

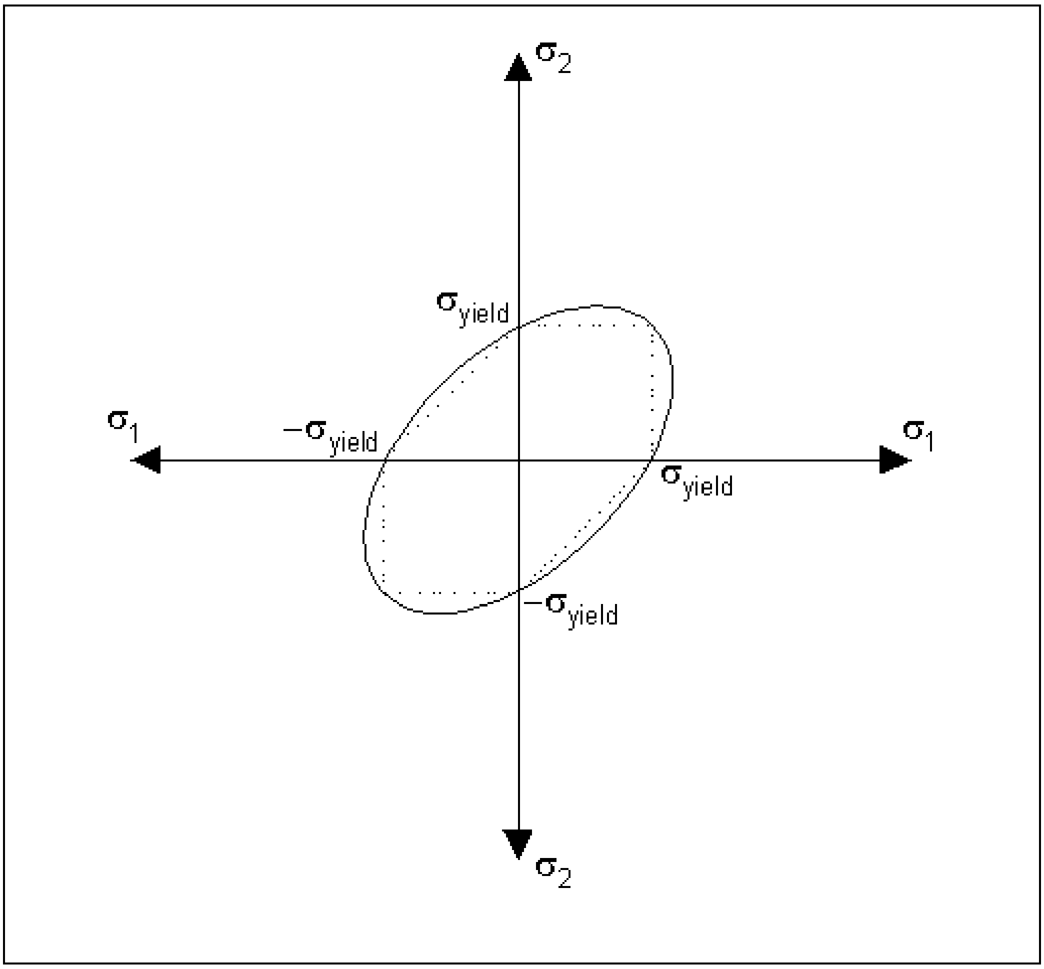

Figure 5.2 Maximum shear and Von Mises criteria

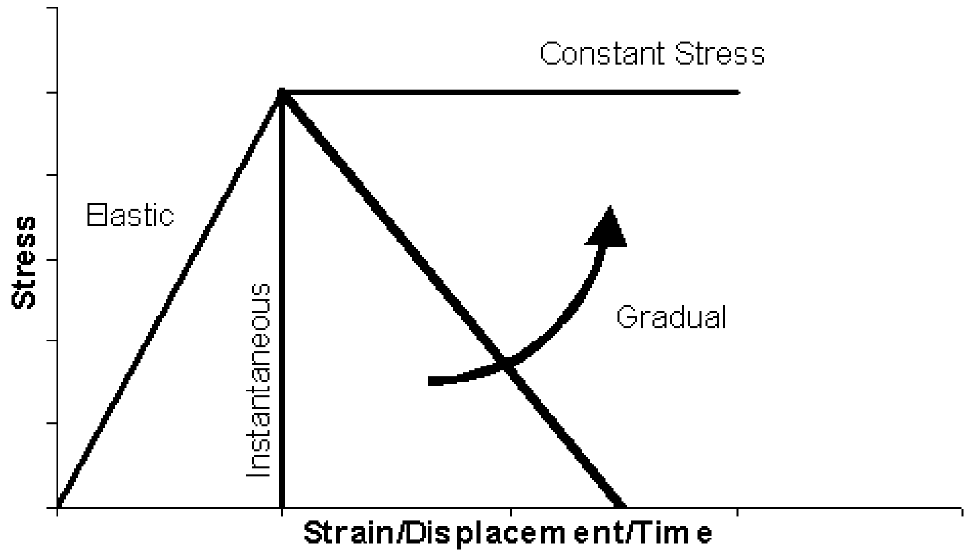

Figure 5.3 Schematic of material degradation post initial failure

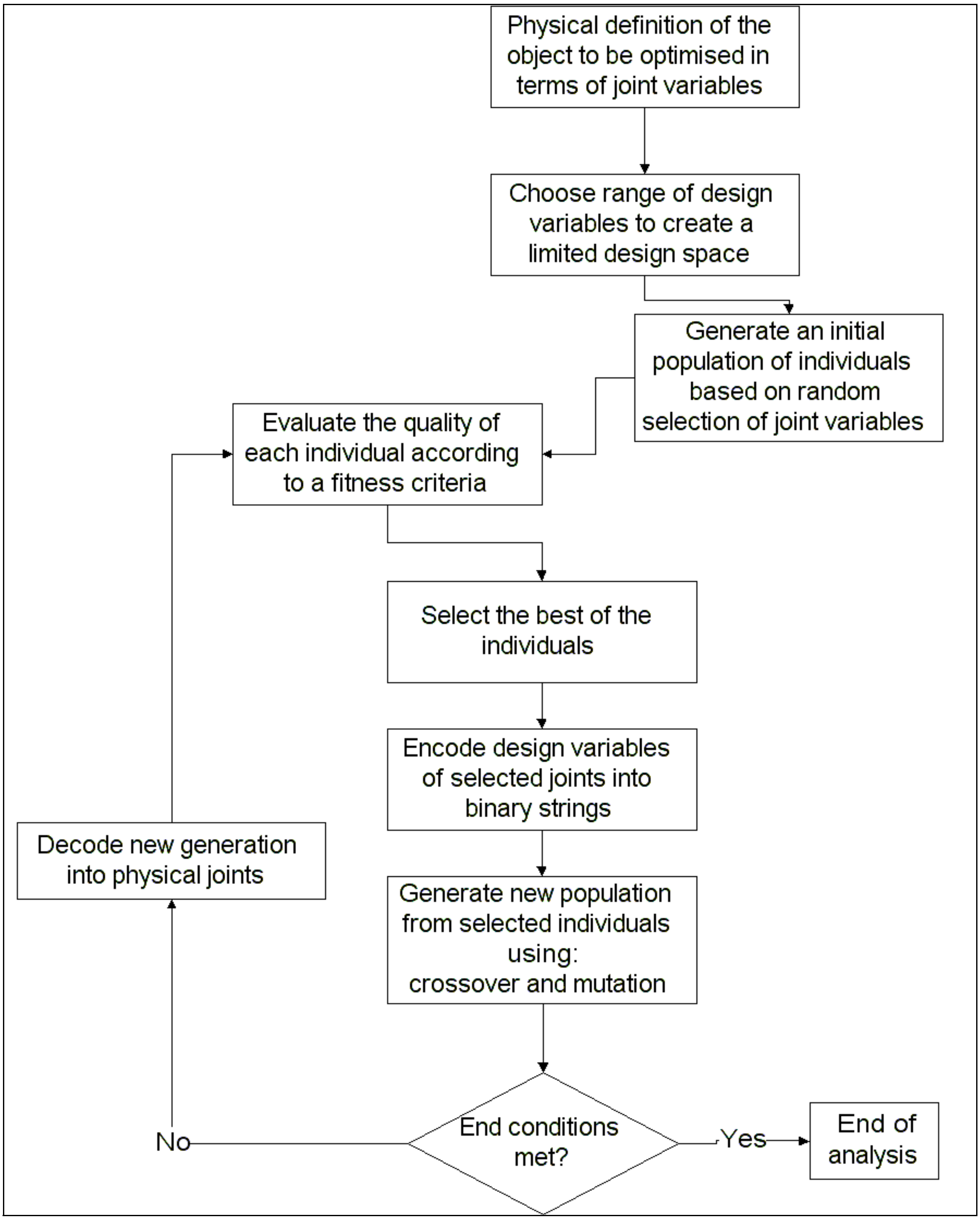

Figure 5.4 Genetic algorithm methodology

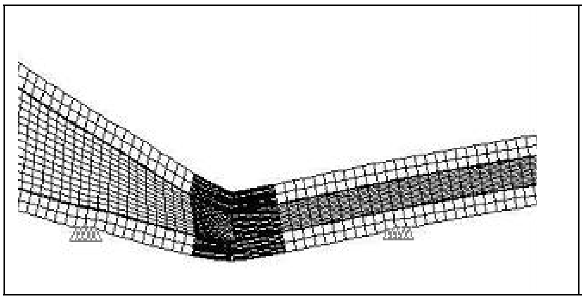

Figure 6.1a Numerical simulation of HSC with anti-bending guides straddling the balsa/steel interface

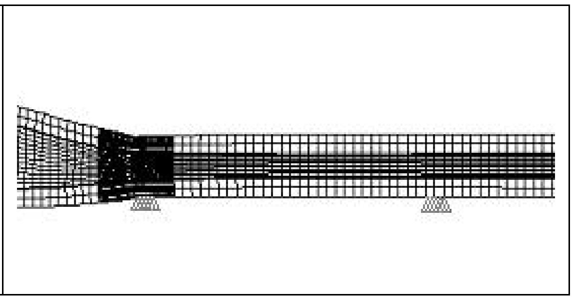

Figure 6.1b Numerical simulation of HSC with anti-bending guides supporting only the steel

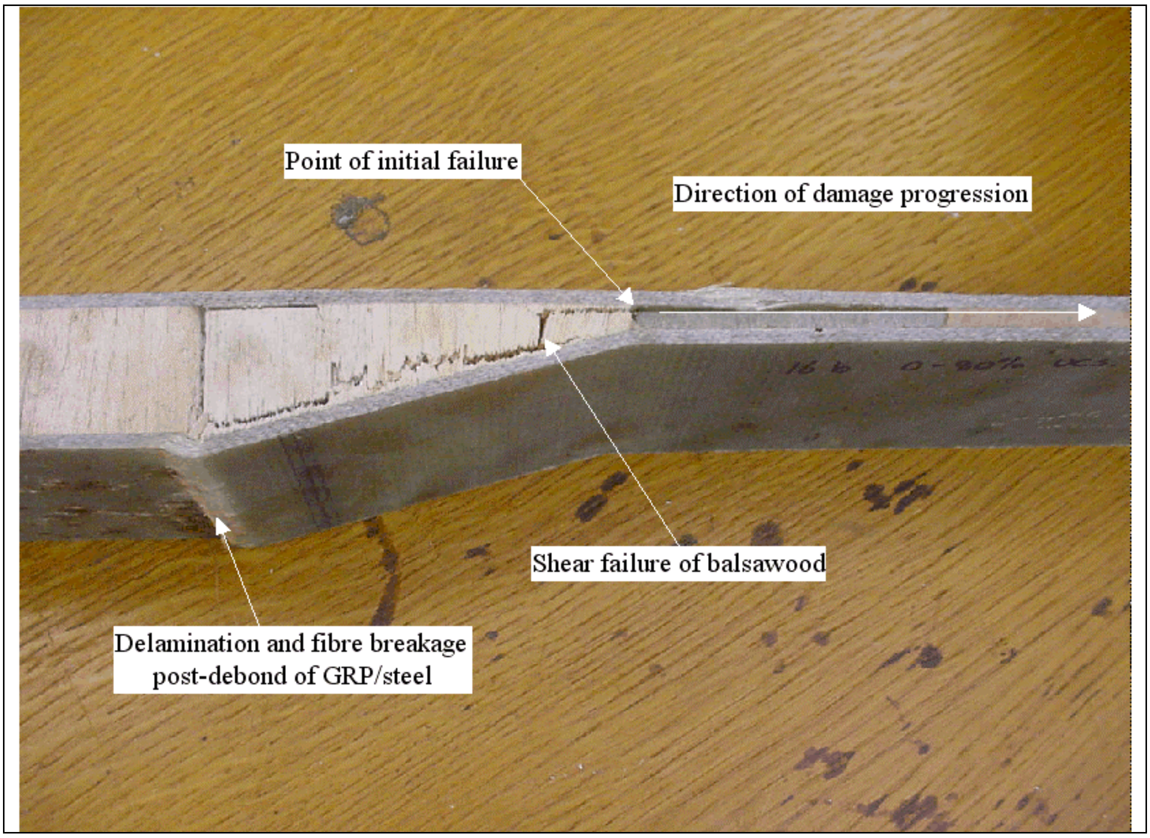

Figure 6.2 Annotated picture of HSC specimen compressive failure

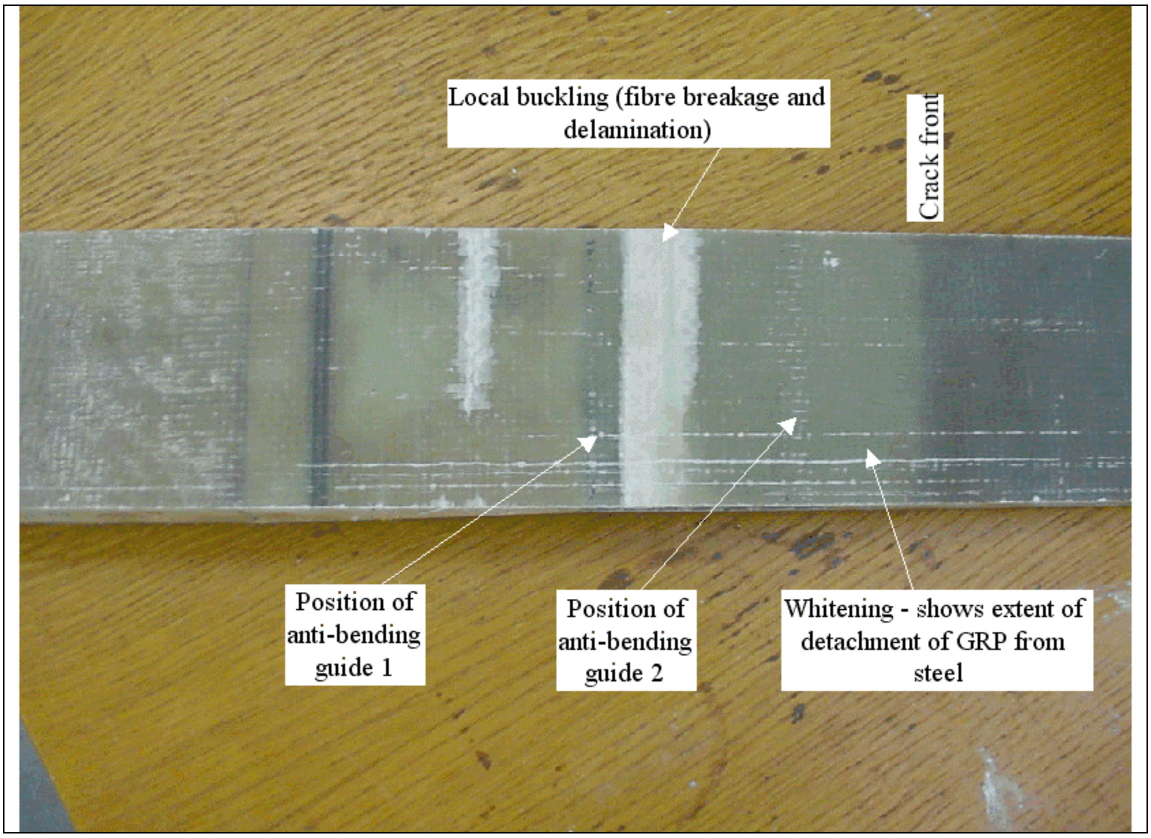

Figure 6.3 Matrix whitening due to skin buckling during compressive static test of HSC – external face of joint (see figure 3.1)

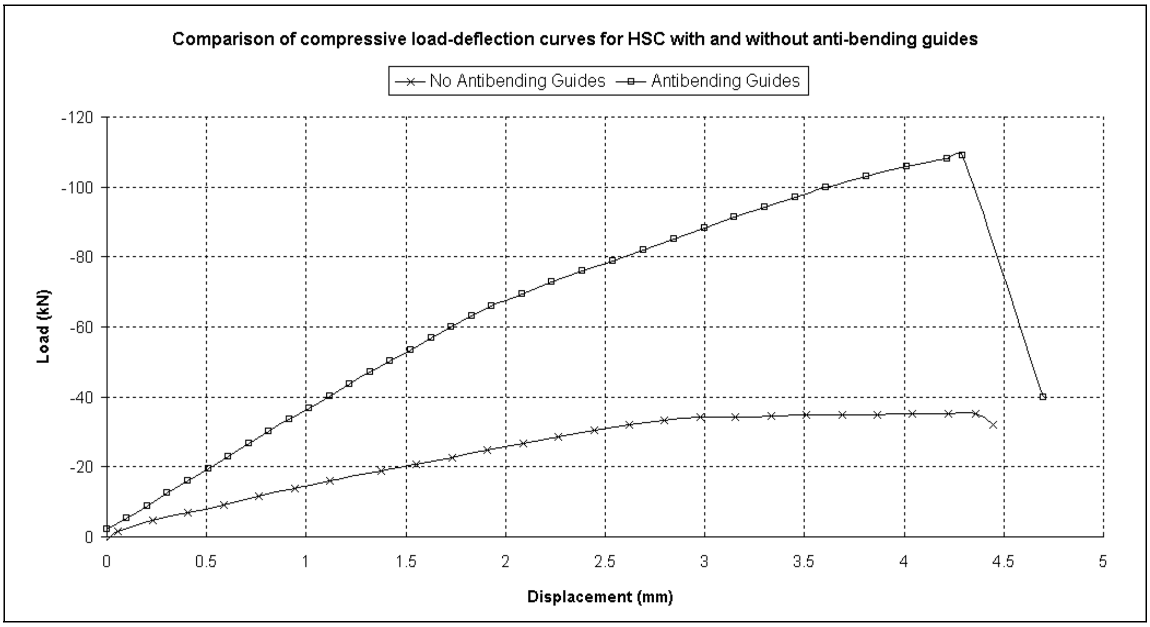

Figure 6.4 Axially compressive static test results for HSC with and without anti-bending guides

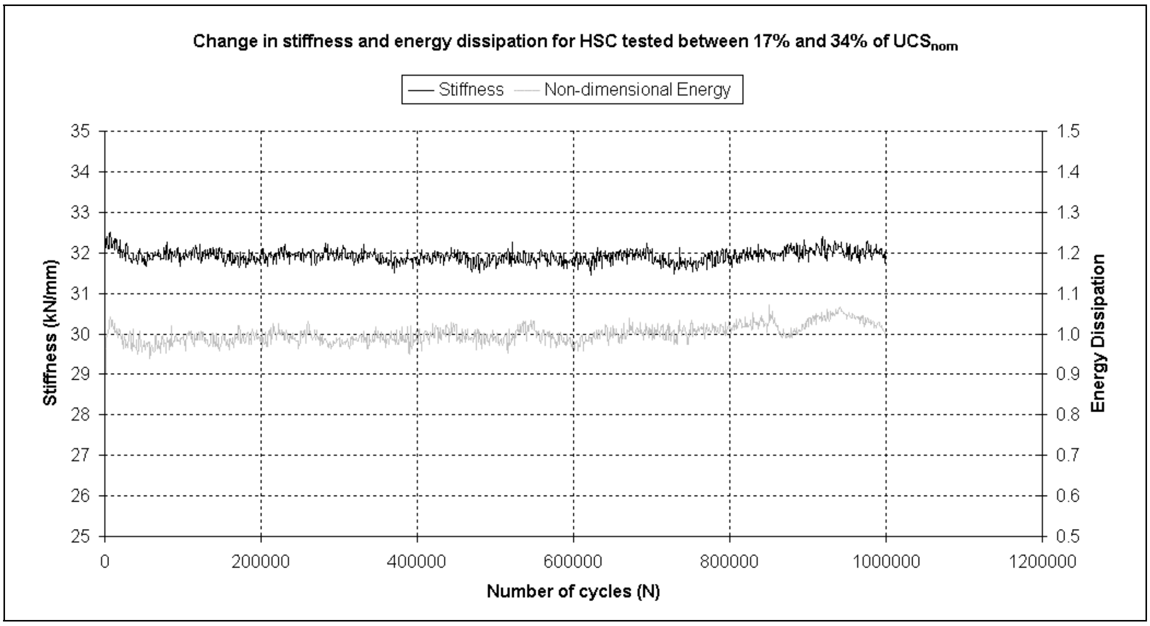

Figure 6.5 Change in HSC stiffness and energy dissipation for 17%-34% UCS$_{nom}$

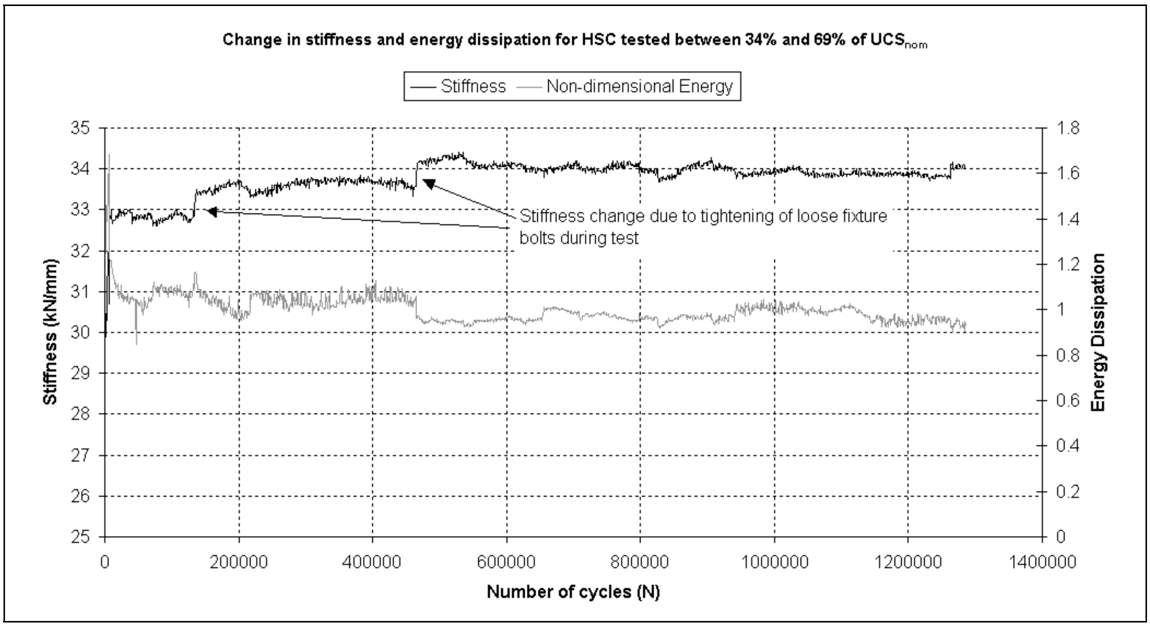

Figure 6.6 Change in HSC stiffness and energy dissipation for 34%-69% UCS$_{nom}$

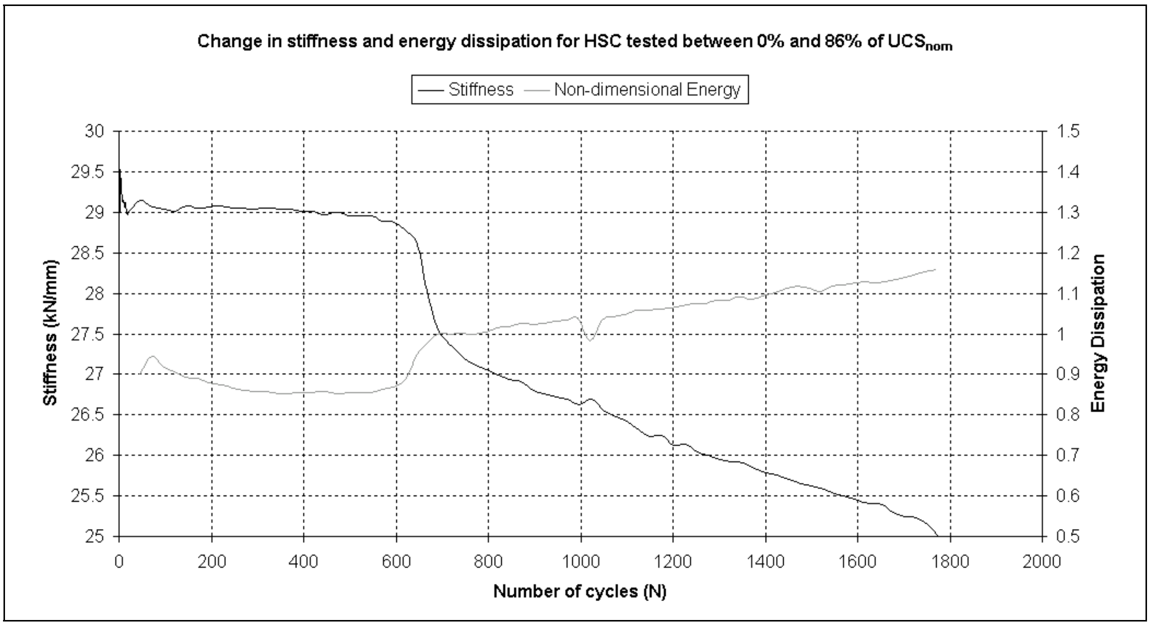

Figure 6.7 Change in HSC stiffness and energy dissipation for 0%-86% UCS_{nom}

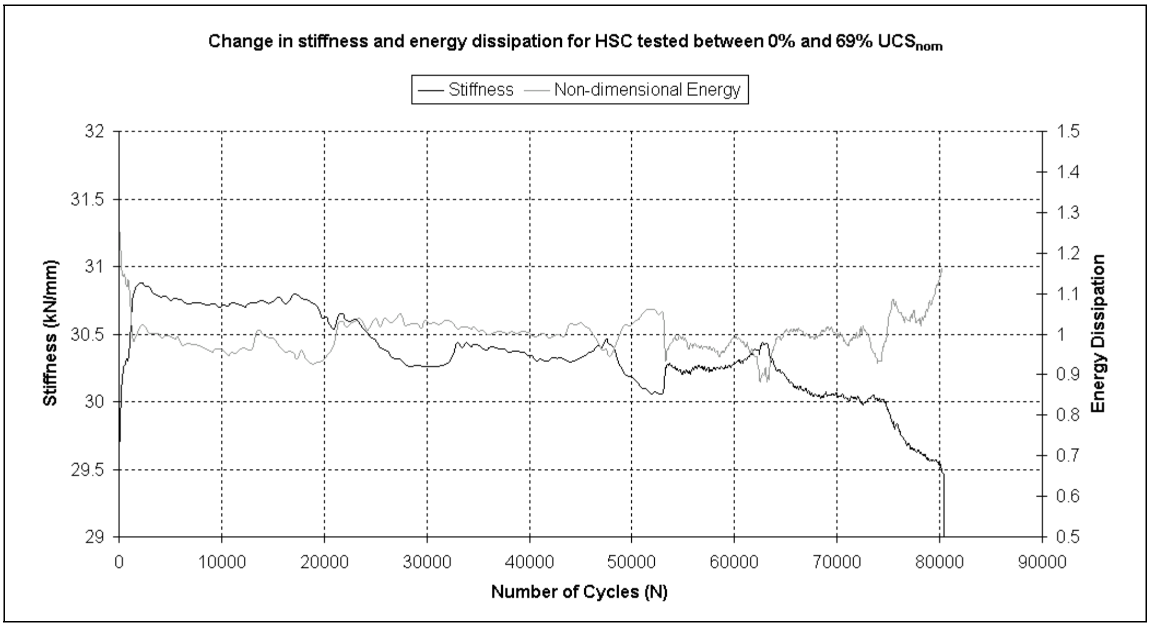

Figure 6.8 Change in HSC stiffness and energy dissipation for 0%-69% UCS_{nom}

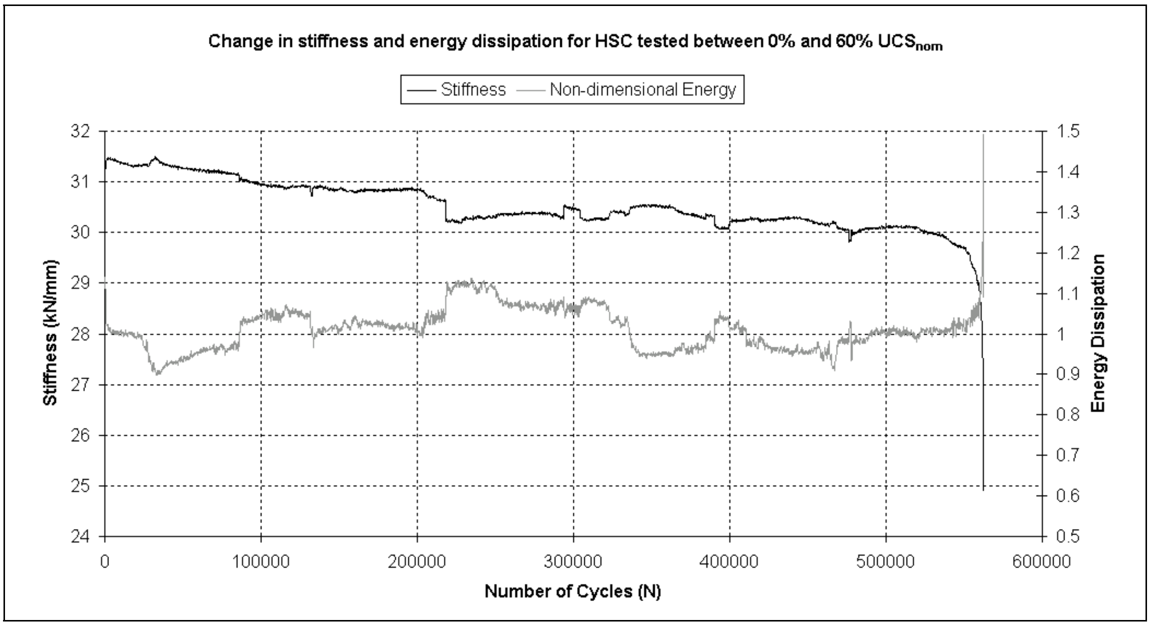

Figure 6.9 Change in HSC stiffness and energy dissipation for 0%-60% UCS$_{nom}$

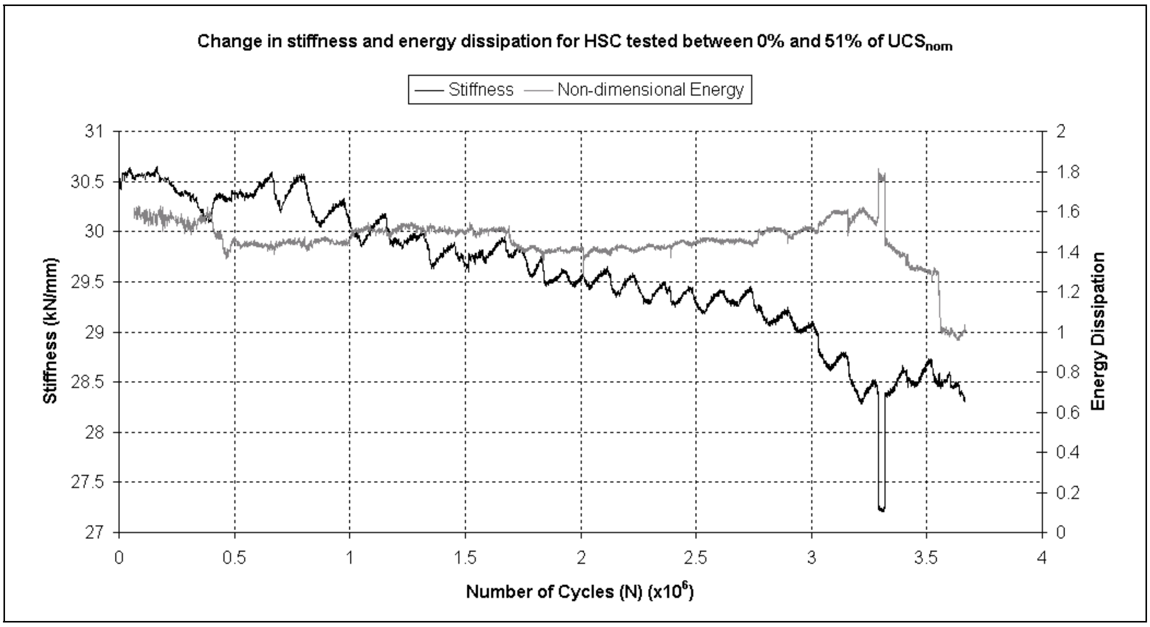

Figure 6.10 Change in HSC stiffness and energy dissipation for 0%-51% UCS$_{nom}$

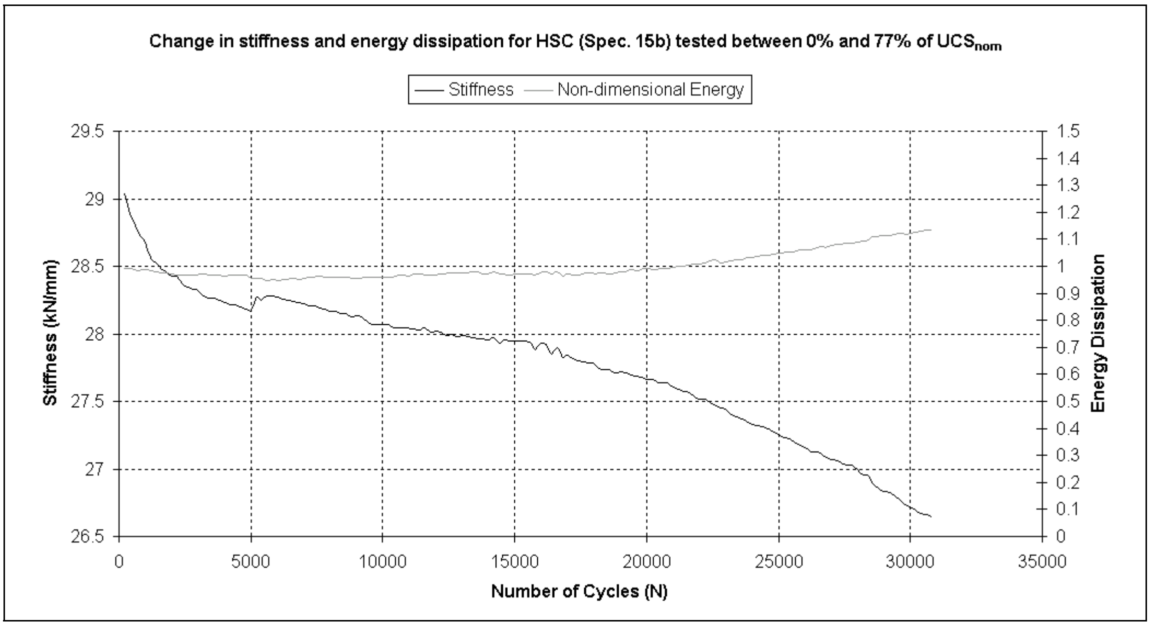

Figure 6.11 Change in HSC stiffness and energy dissipation for 0%-77% UCS$_{nom}$, specimen 15b

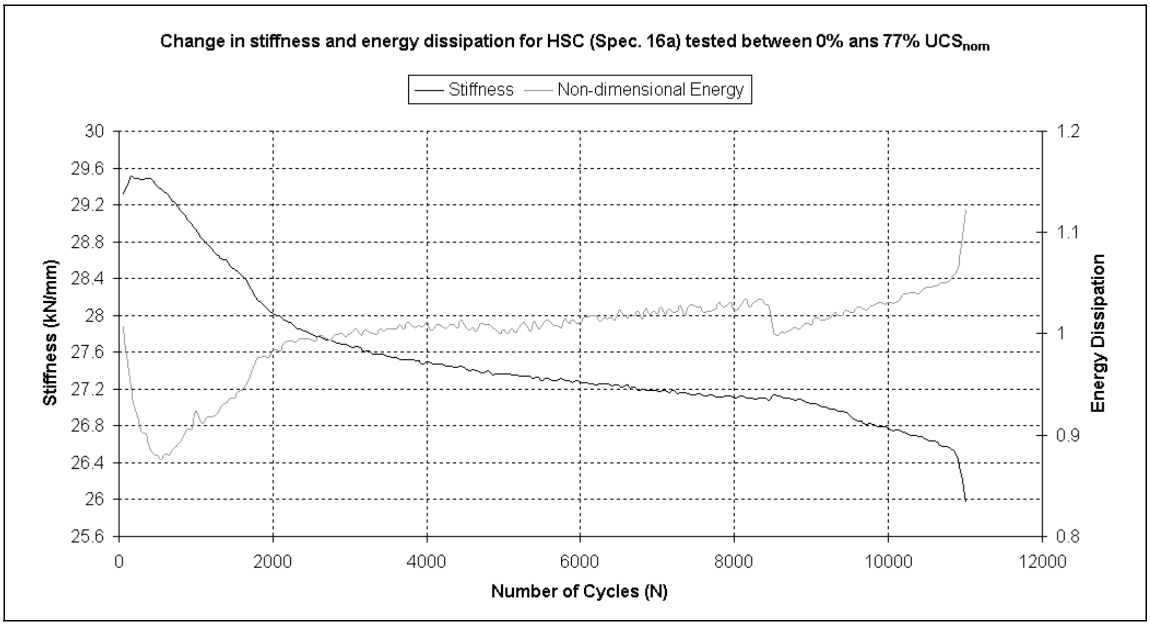

Figure 6.12 Change in HSC stiffness and energy dissipation for 0%-77% UCS$_{nom}$, specimen 16a

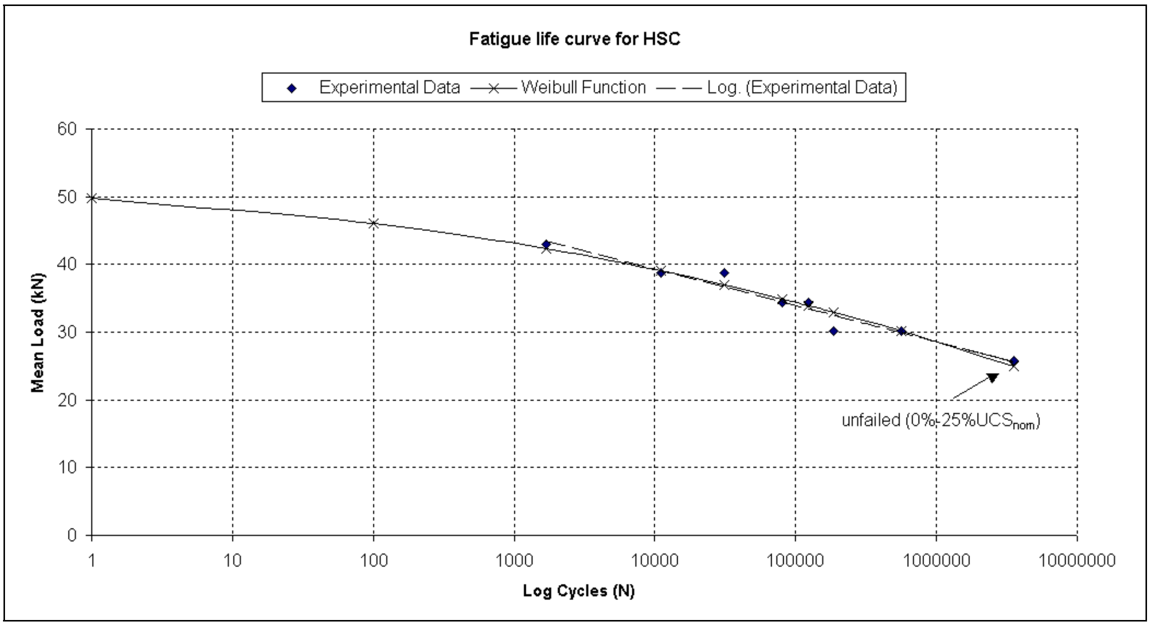

Figure 6.13 Fatigue life curve for HSC joint

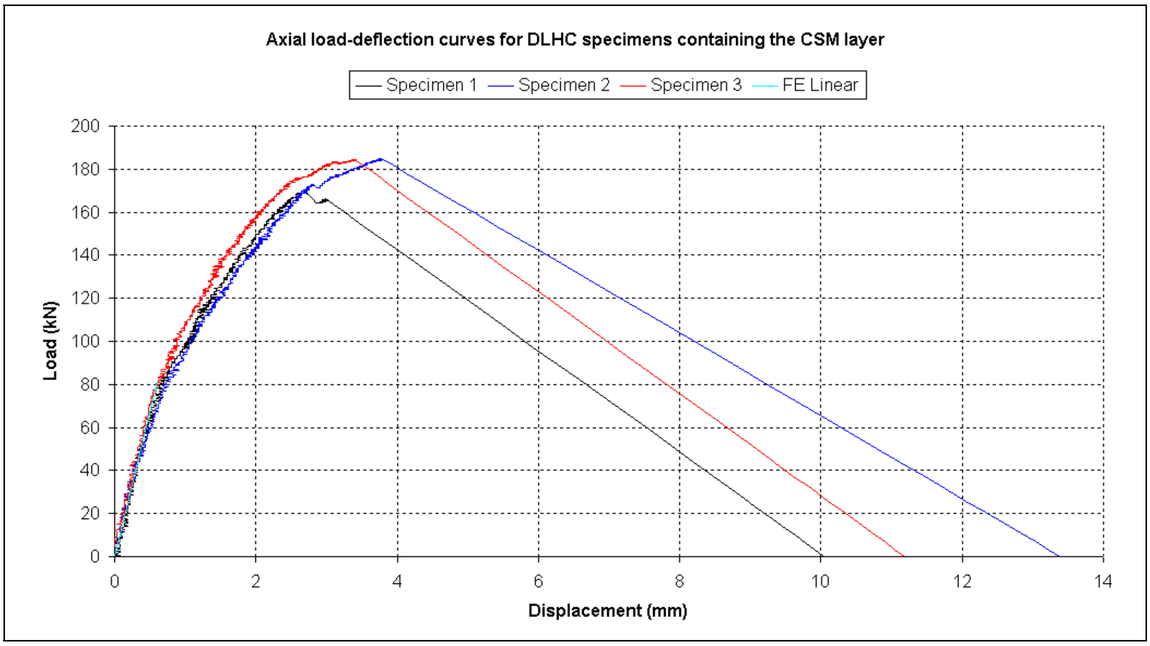

Figure 6.14 Static test results for DLHC with CSM interface

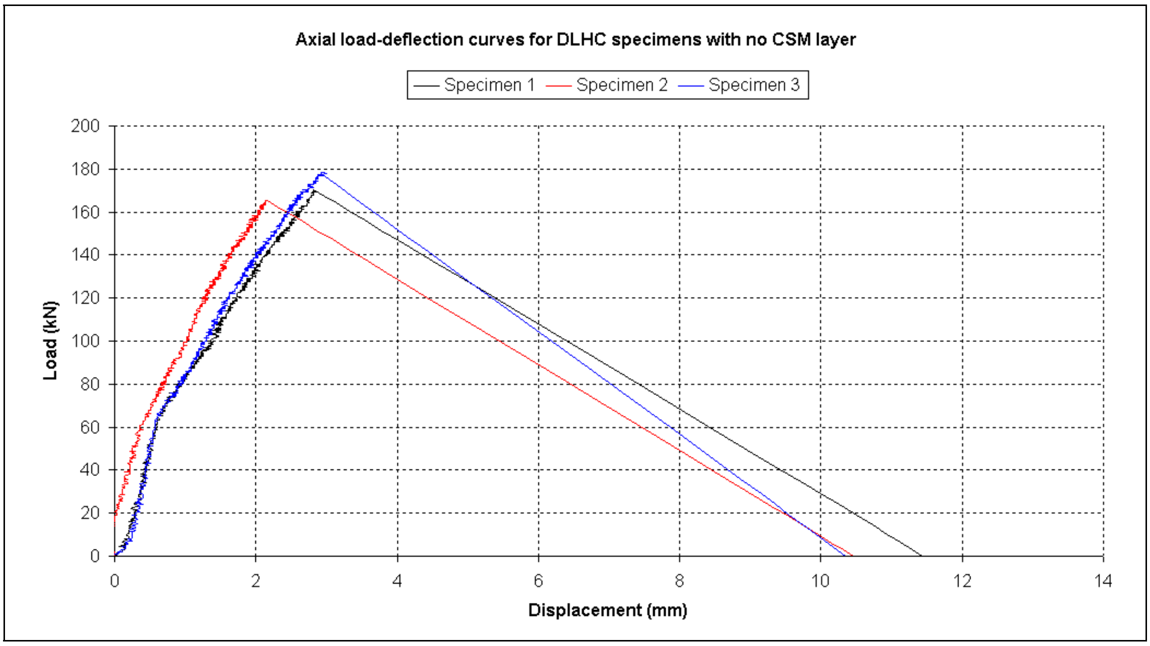

Figure 6.15 Static test results for DLHC without CSM interface

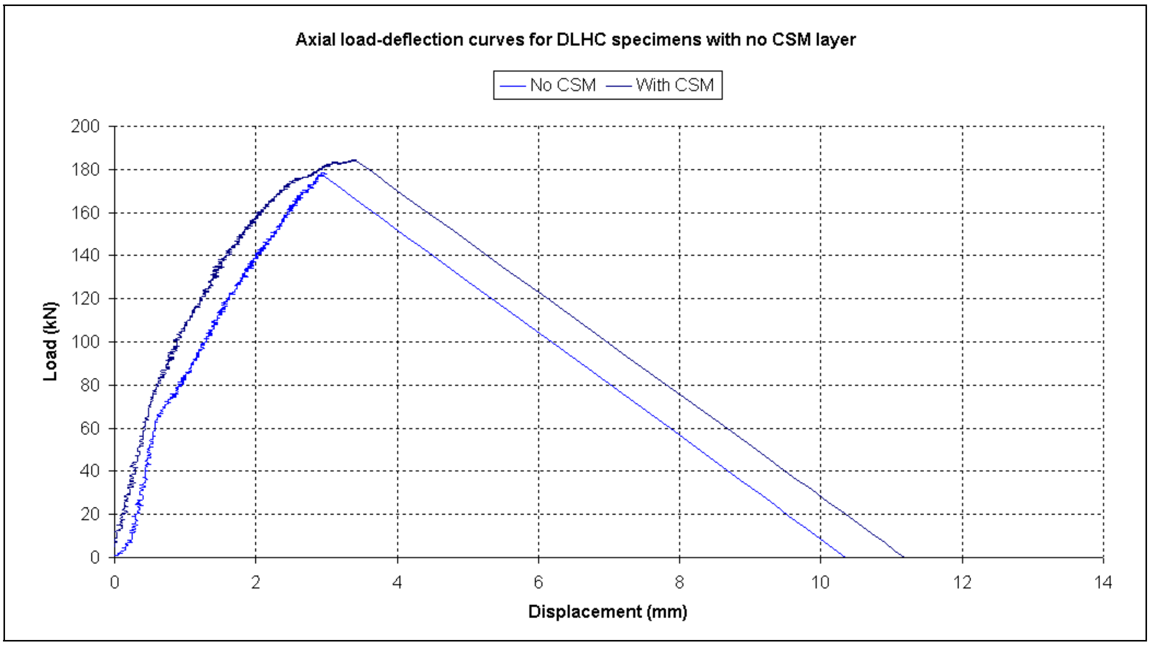

Figure 6.16 Comparison of load-deflection for the two DLHC lay-ups

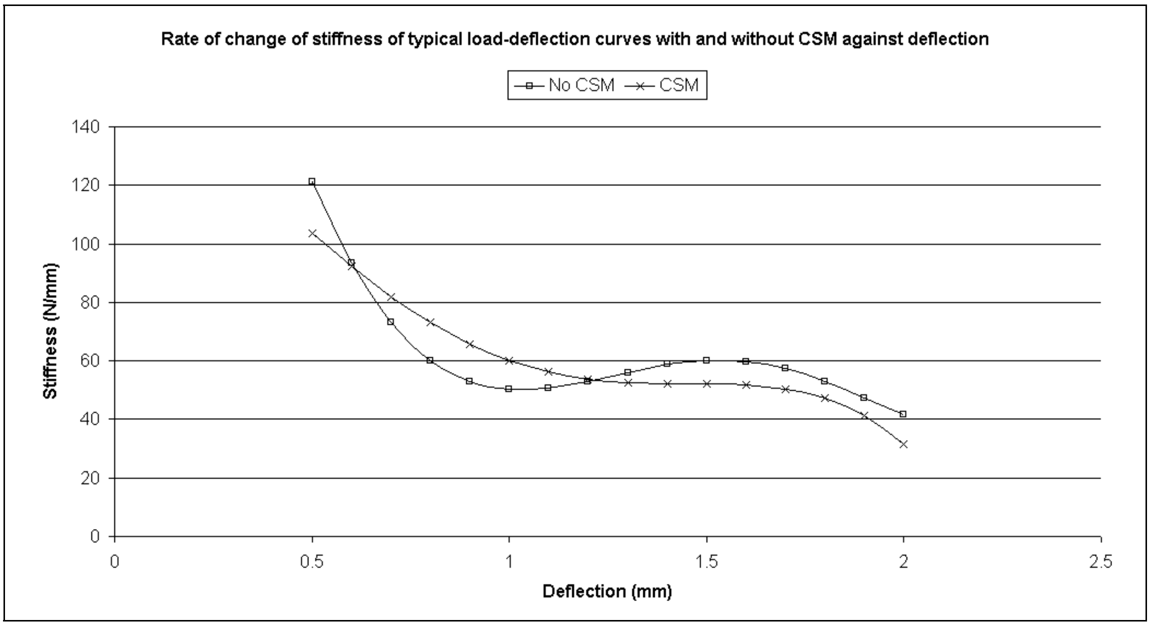

Figure 6.17 Comparison of stiffness against deflection

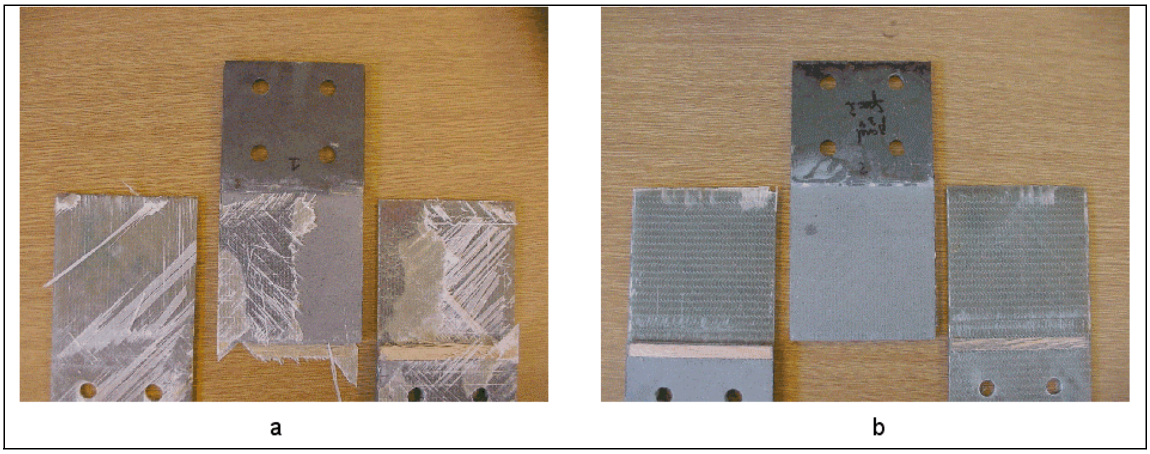

Figure 6.18 Pictorial comparison of failure surfaces with (a) and without (b) CSM layer

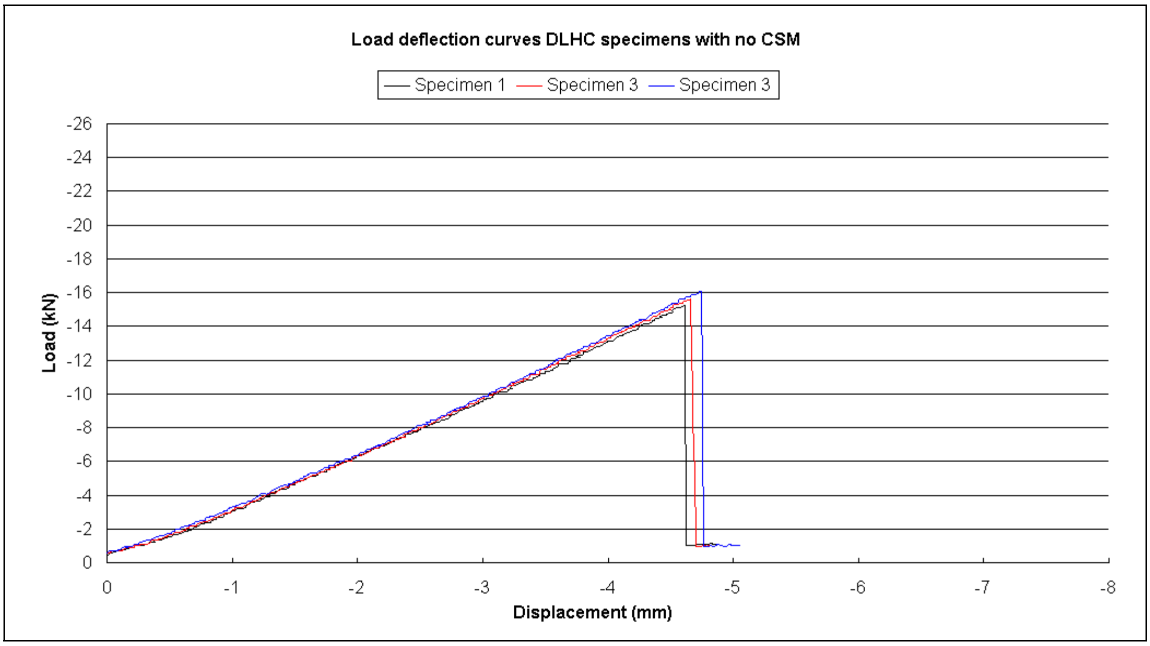

Figure 6.19 Load-deflection curves for 4-point bend of DLHC without CSM

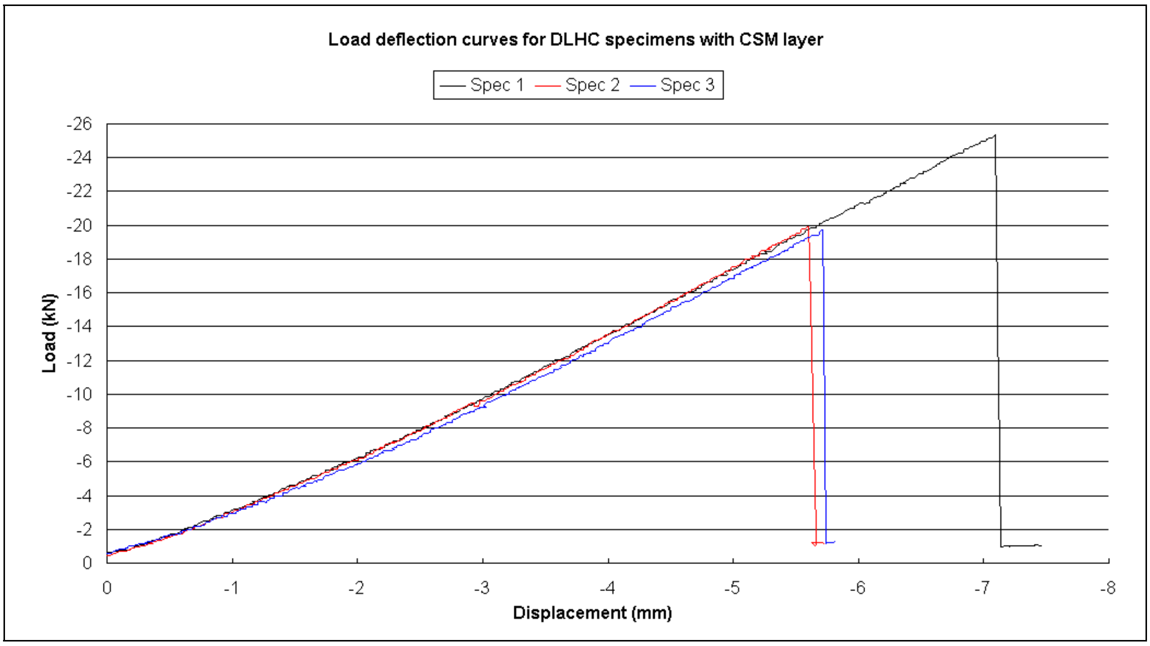

Figure 6.20 load-deflection curves for 4-point bend of DLHC with CSM

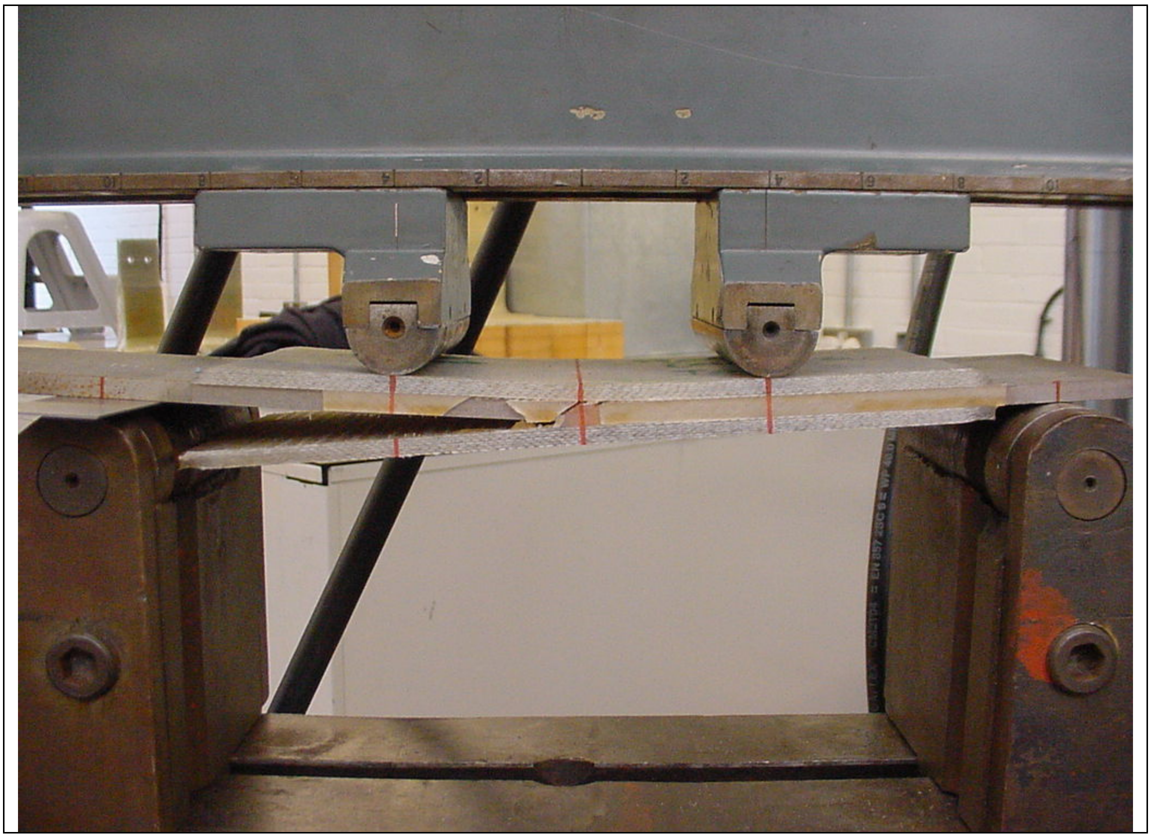

Figure 6.21 Failure of DLHC in 4-point bend without CSM

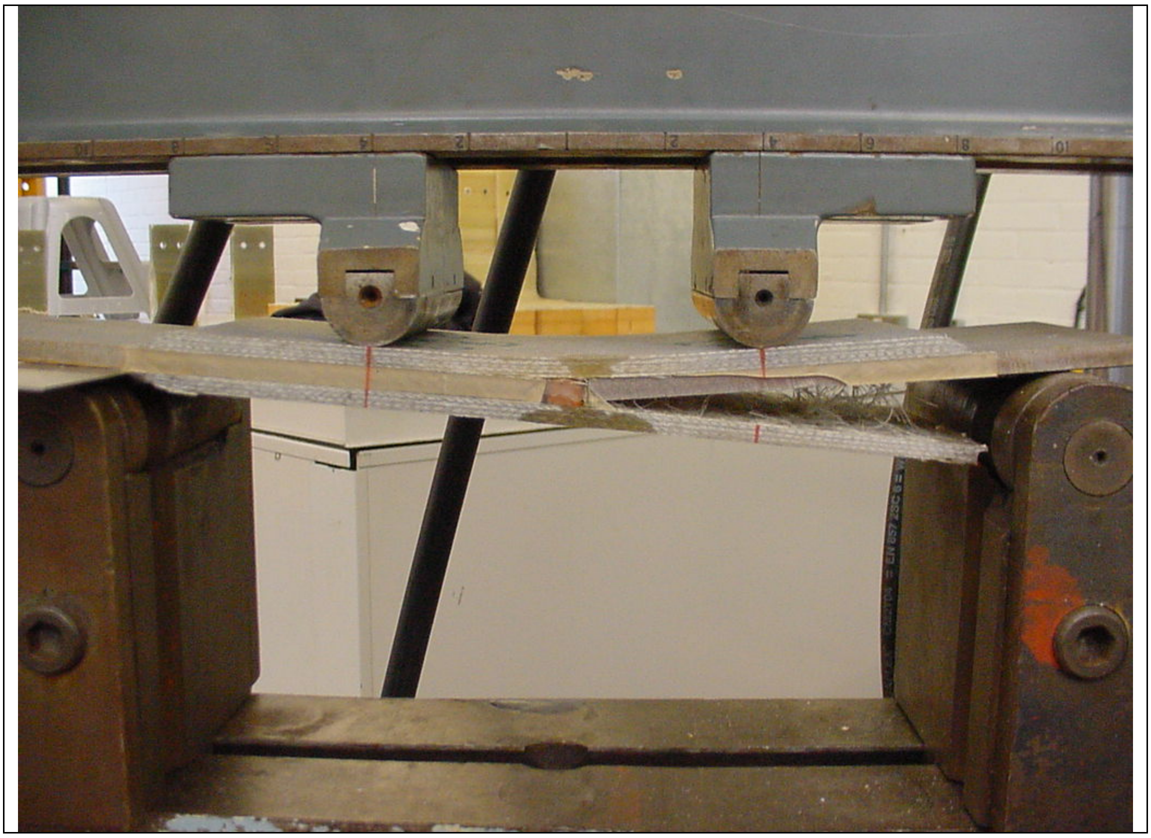

Figure 6.22 failure of DLHC in 4-point bend with CSM

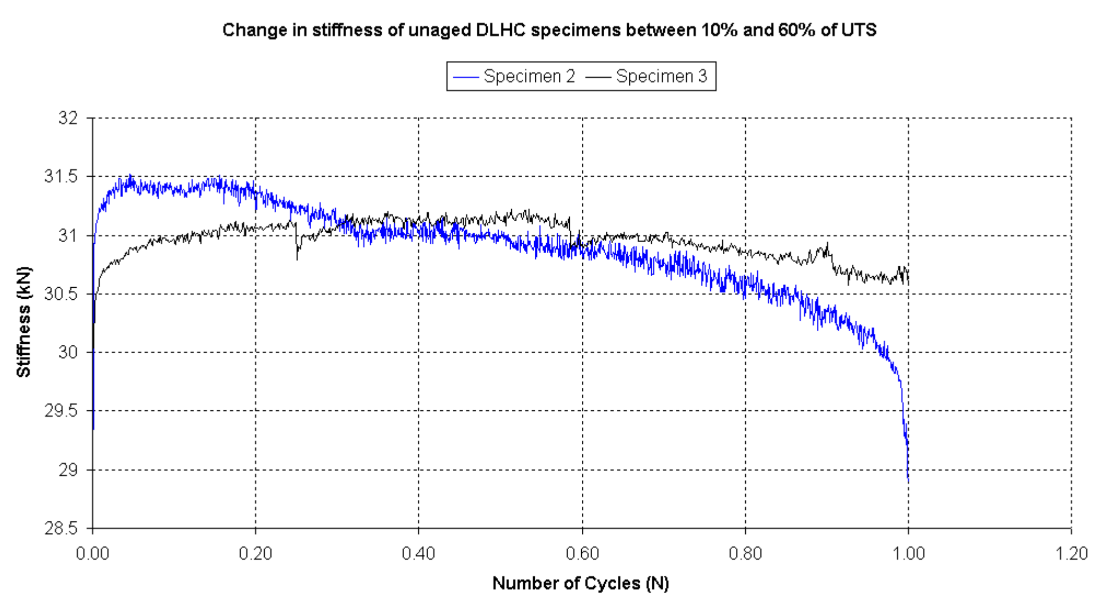

Figure 6.23 Comparison in stiffness change for DLHC in fatigue between 10% and 60% of UTS

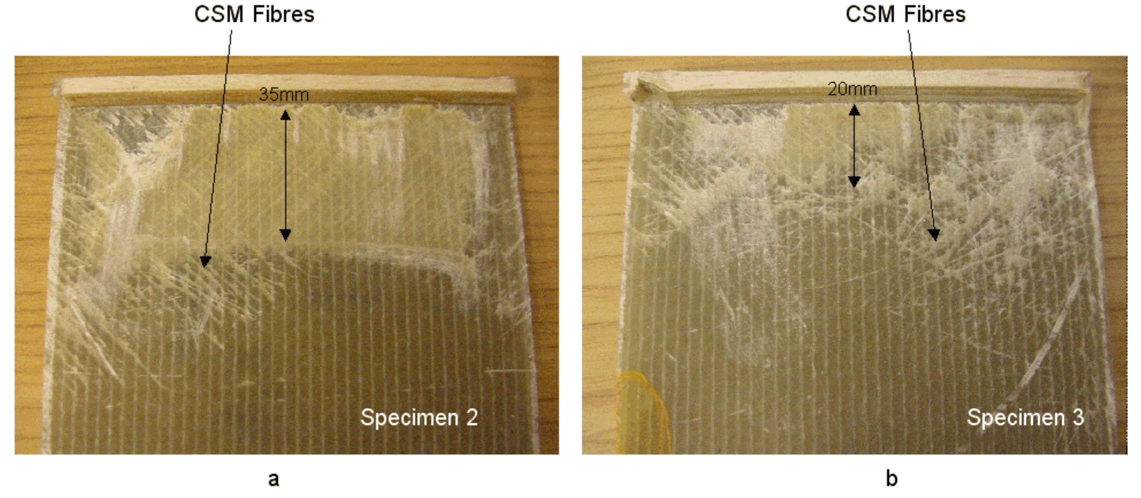

Figure 6.24 Fatigue failure surfaces of aged DLHC specimens

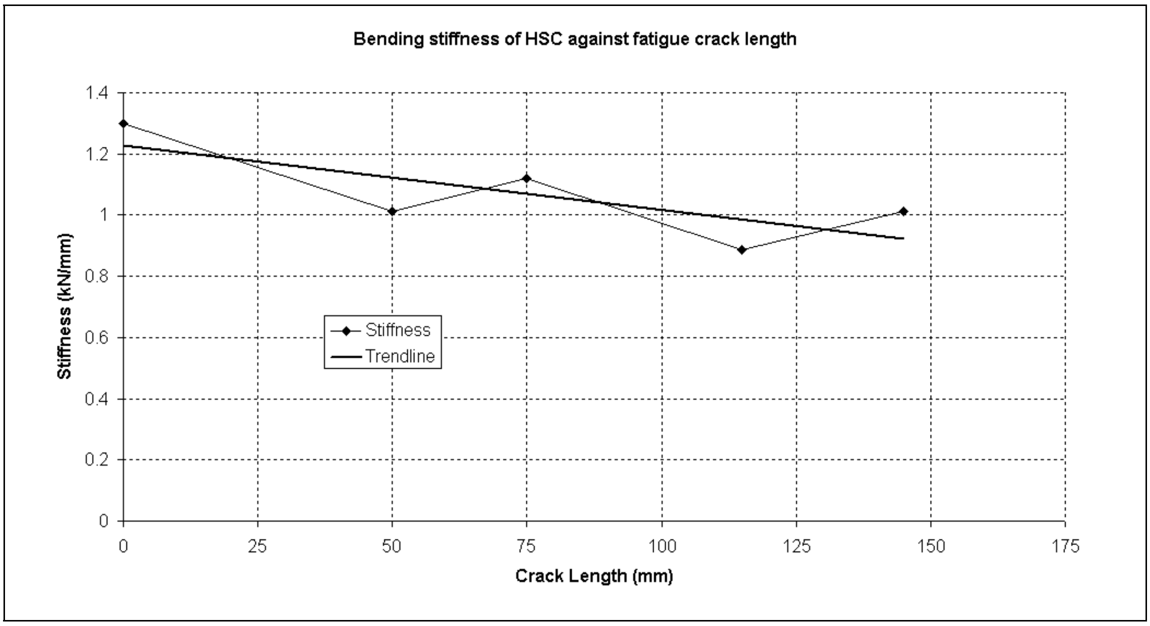

Figure 6.25 Change in HSC bending stiffness with increasing fatigue crack length

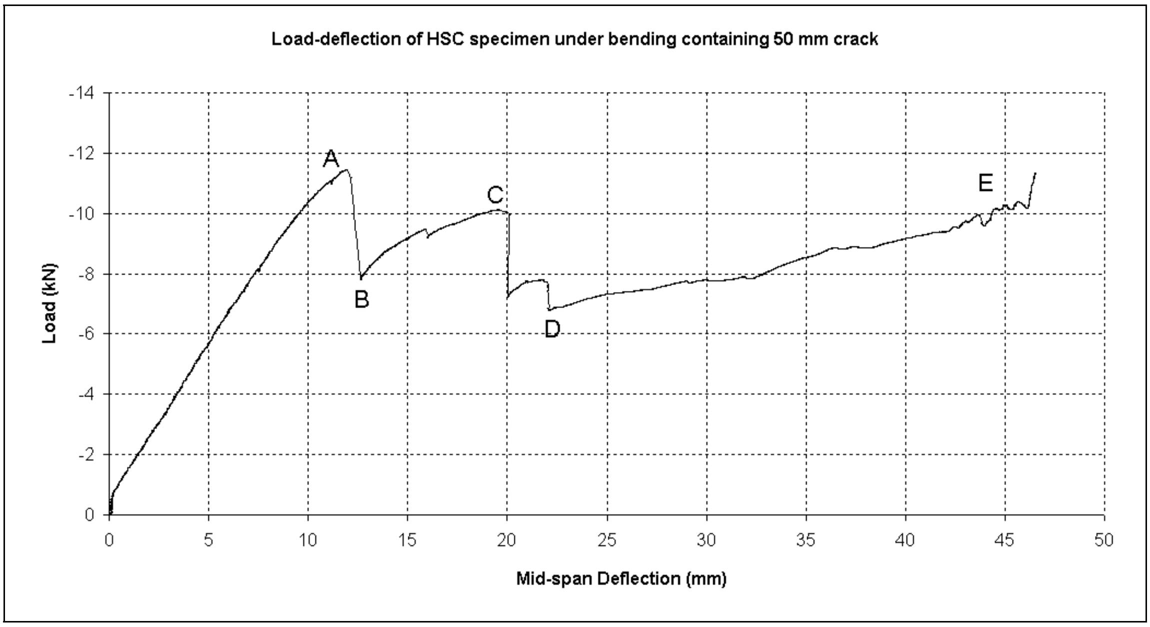

Figure 6.26 Load-displacement plot for out-of-plane residual strength test, 50mm fatigue crack (see Table 6.4 for A-E information)

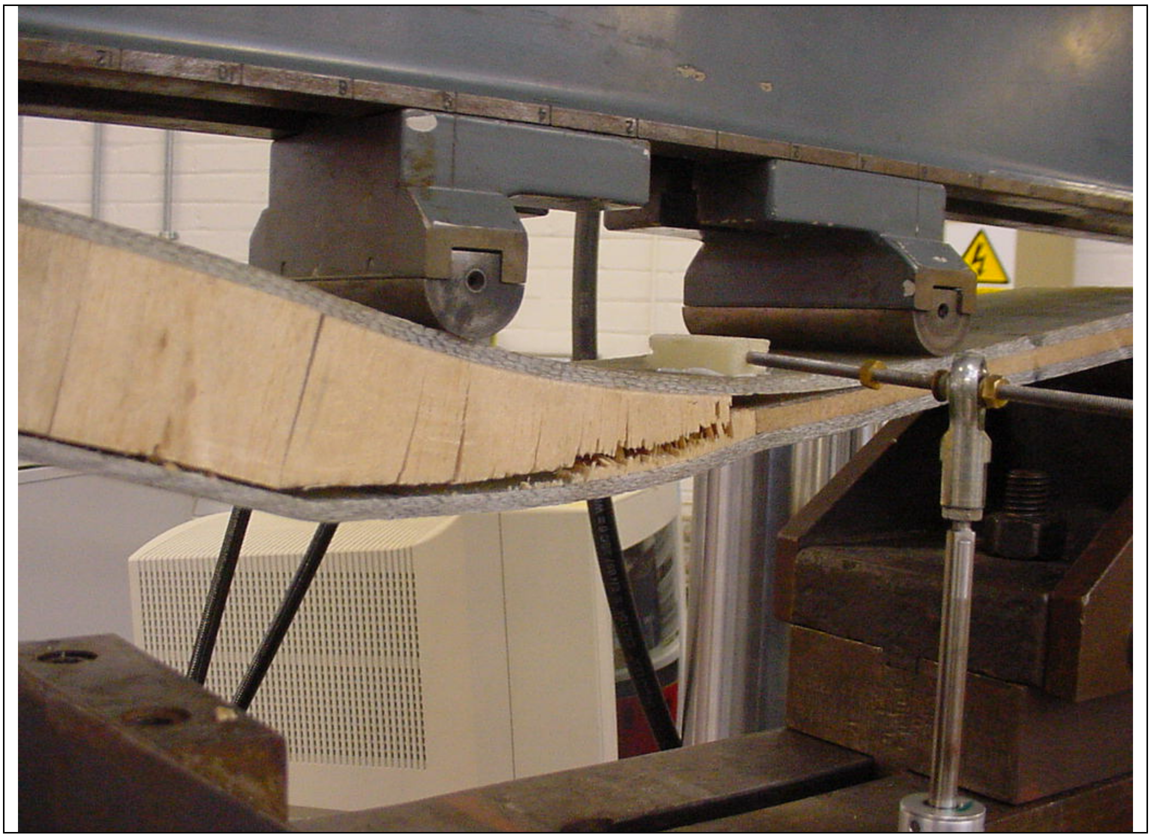

Figure 6.27 Failure of HSC joint in 4-point bending

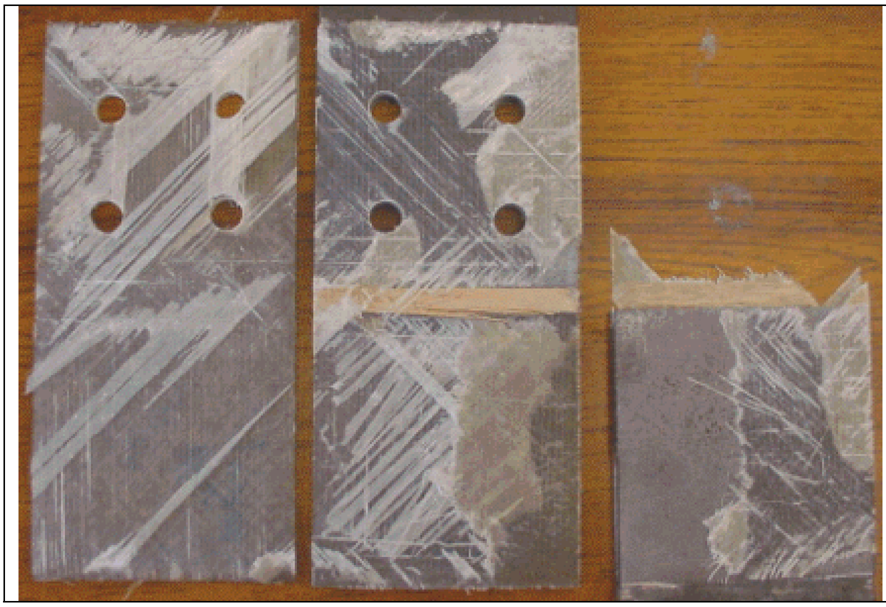

Figure 6.28a Failure surface of tensile DLHC specimen, unaged

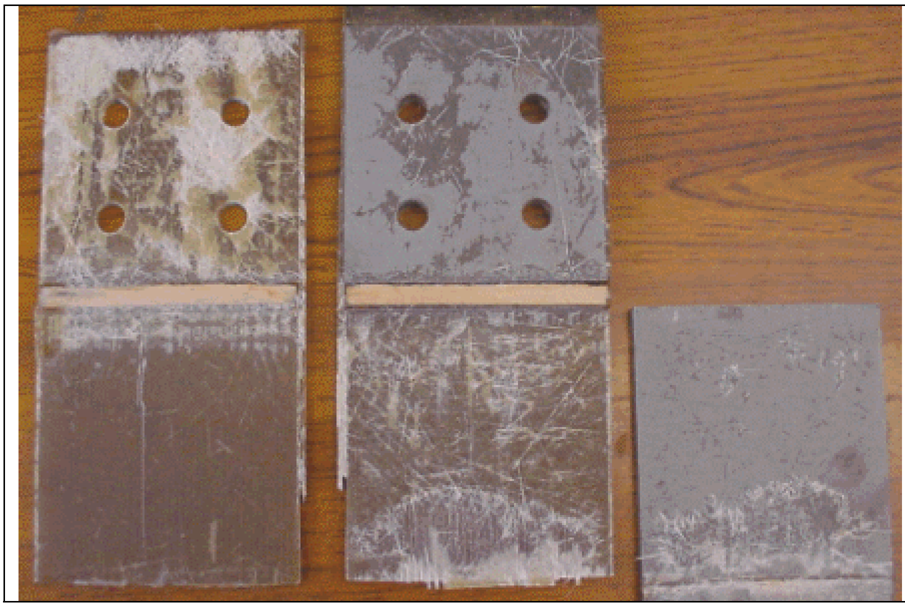

Figure 6.28b Failure surface of tensile DLHC specimen, aged

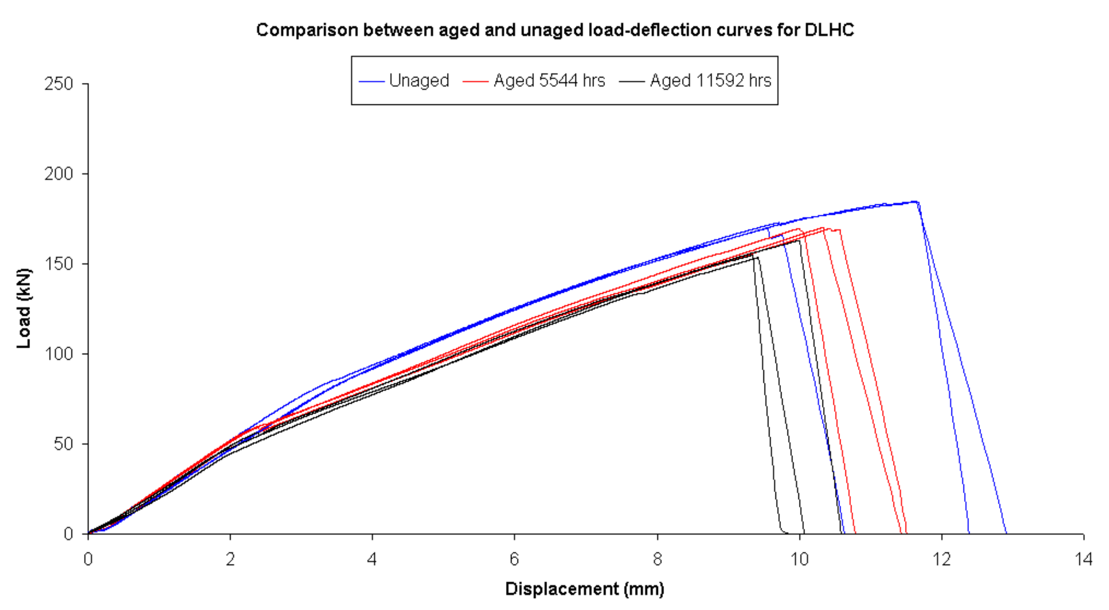

Figure 6.29 Comparison of tensile load-deflection response of unaged, aged 5544 hours and aged 11592 hours

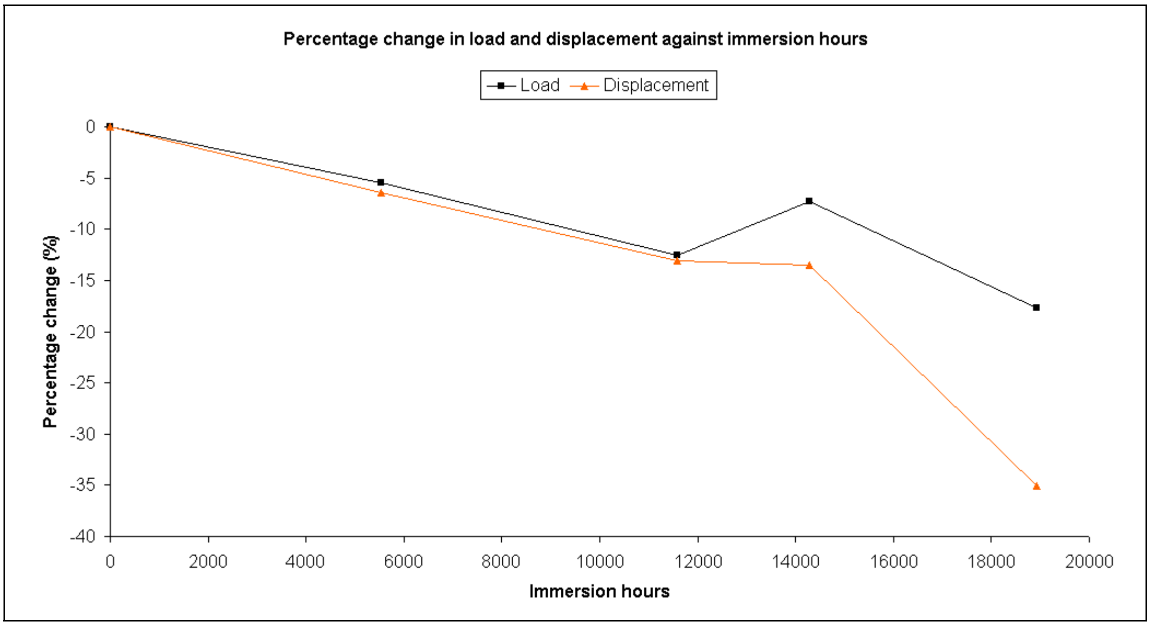

Figure 6.30 Percentage changes in failure load and failure displacement with increasing hours of ageing

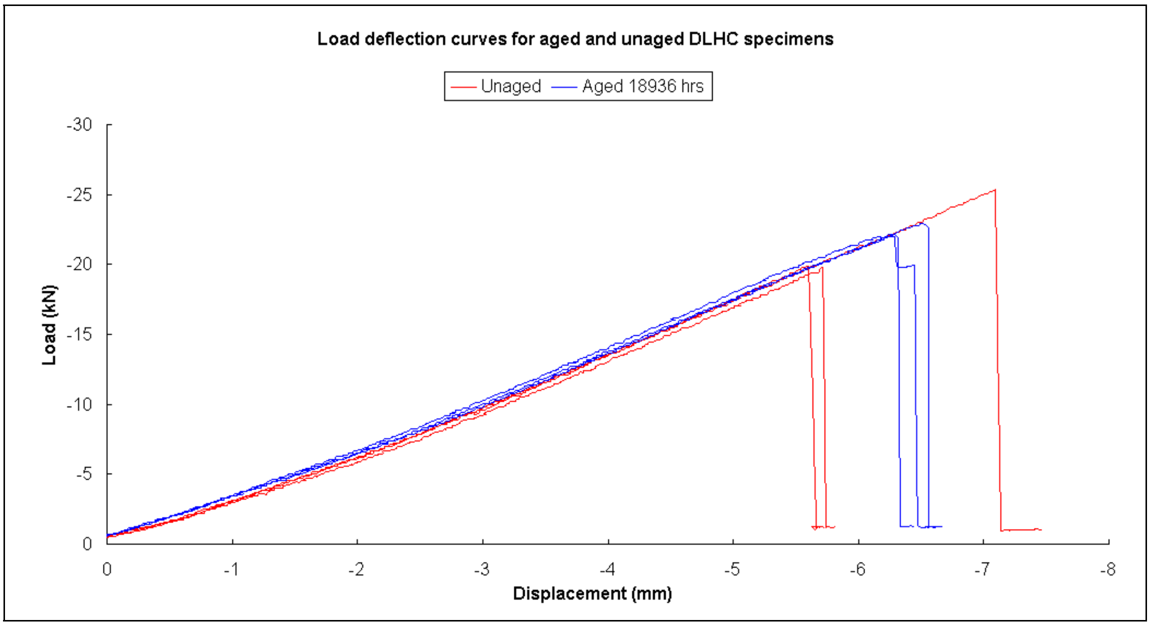

Figure 6.31 Load-deflection curves for DLHC specimens in 4-point bending unaged and aged 18936 hours

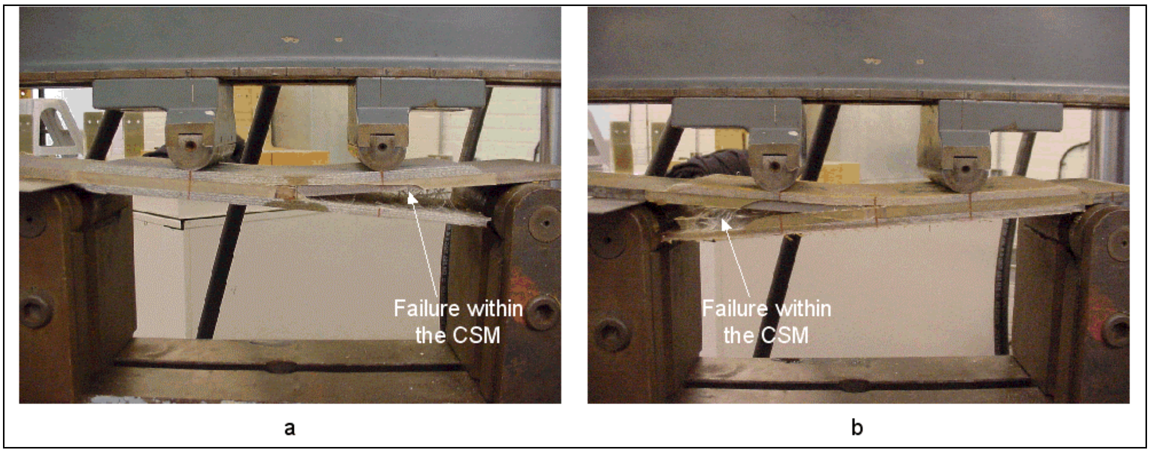

Figure 6.32 Pictures of DLHC failures in 4-point bending with (18936 hrs) and without ageing

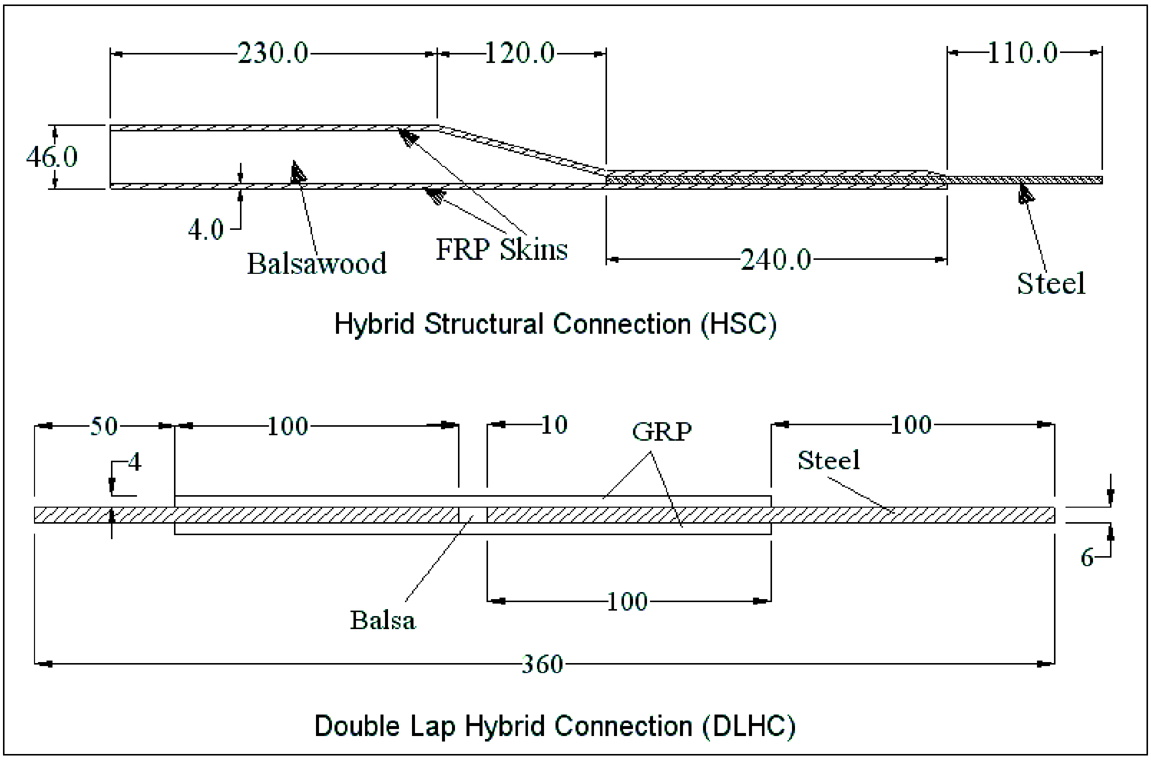

Figure 7.1 Geometry and materials in both the HSC and DLHC (mm)

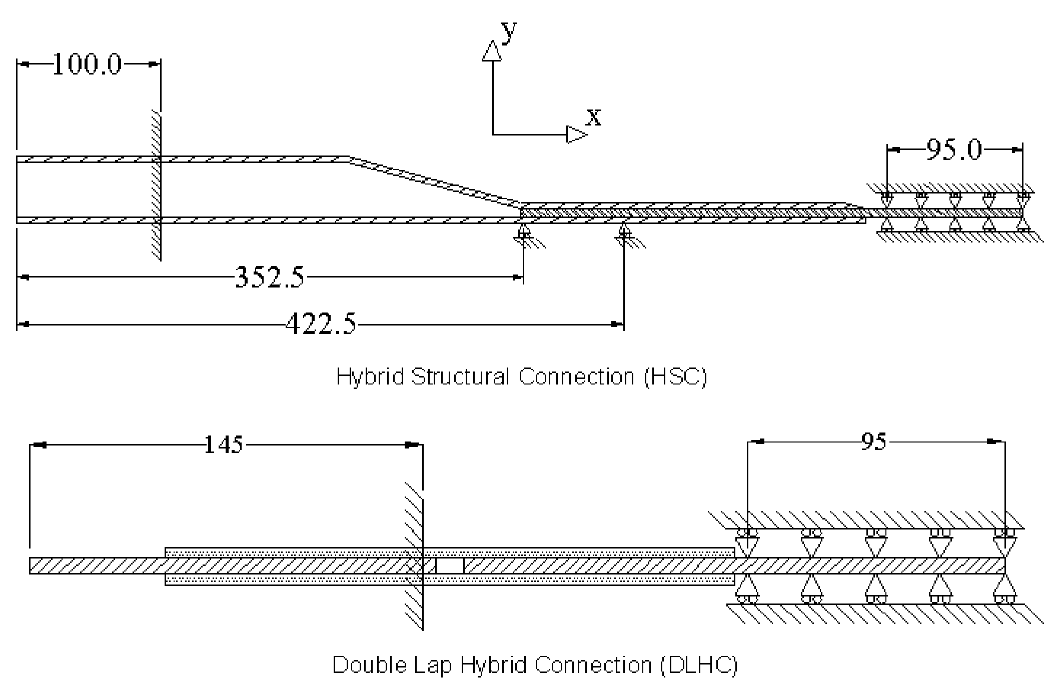

Figure 7.2 Boundary conditions for both the HSC and DLHC (mm)

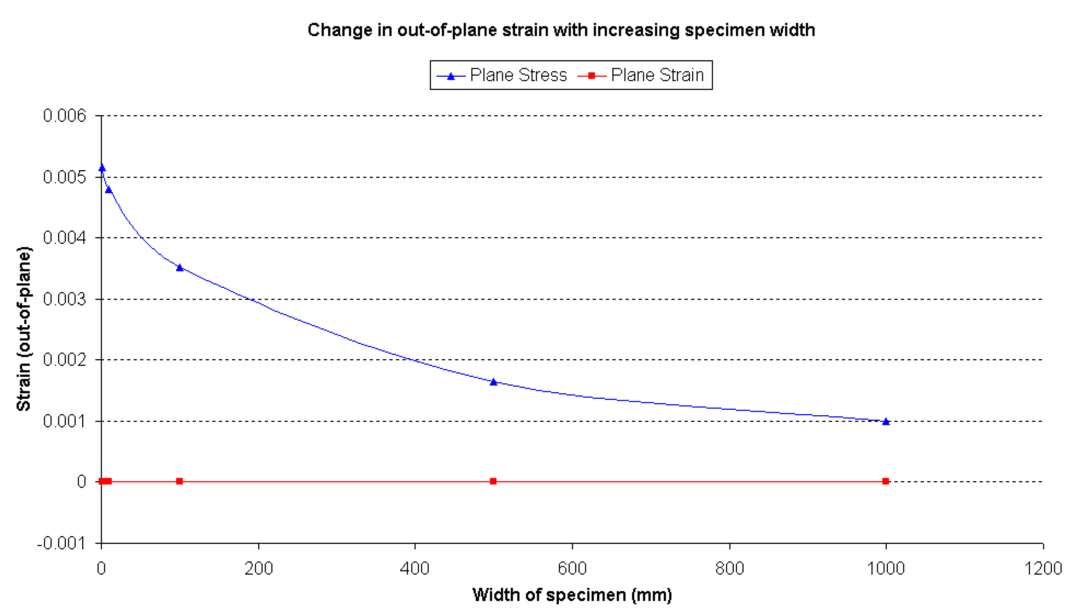

Figure 7.3 Out-of-plane strain against width

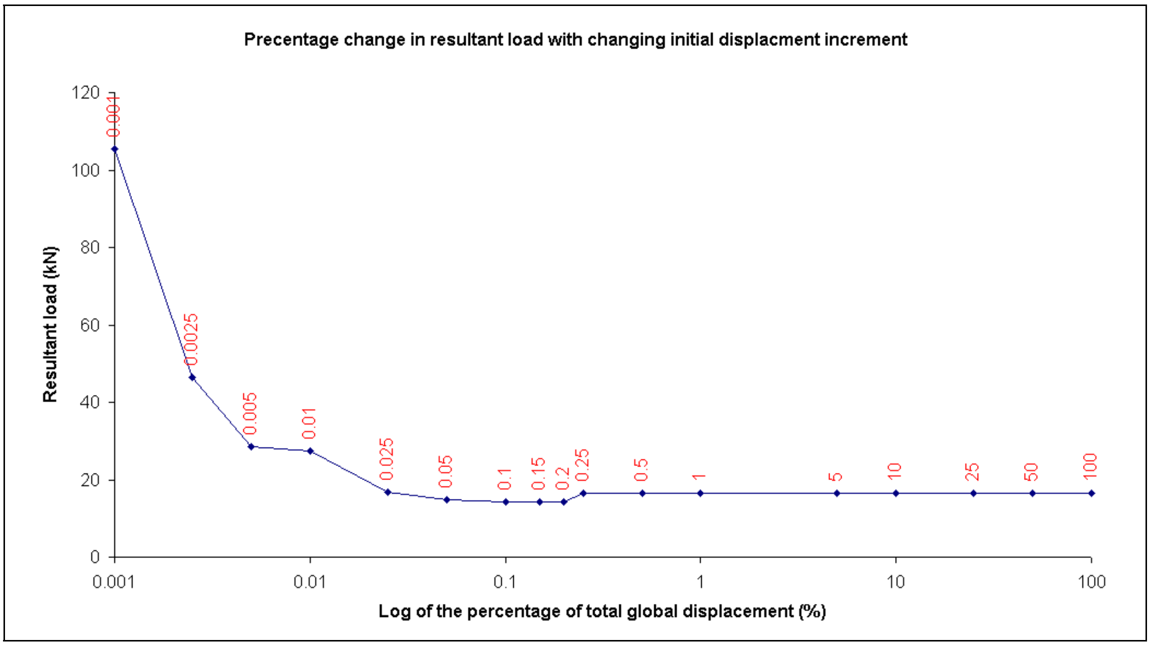

Figure 7.4 Influence of initial displacement increment size on final resultant load

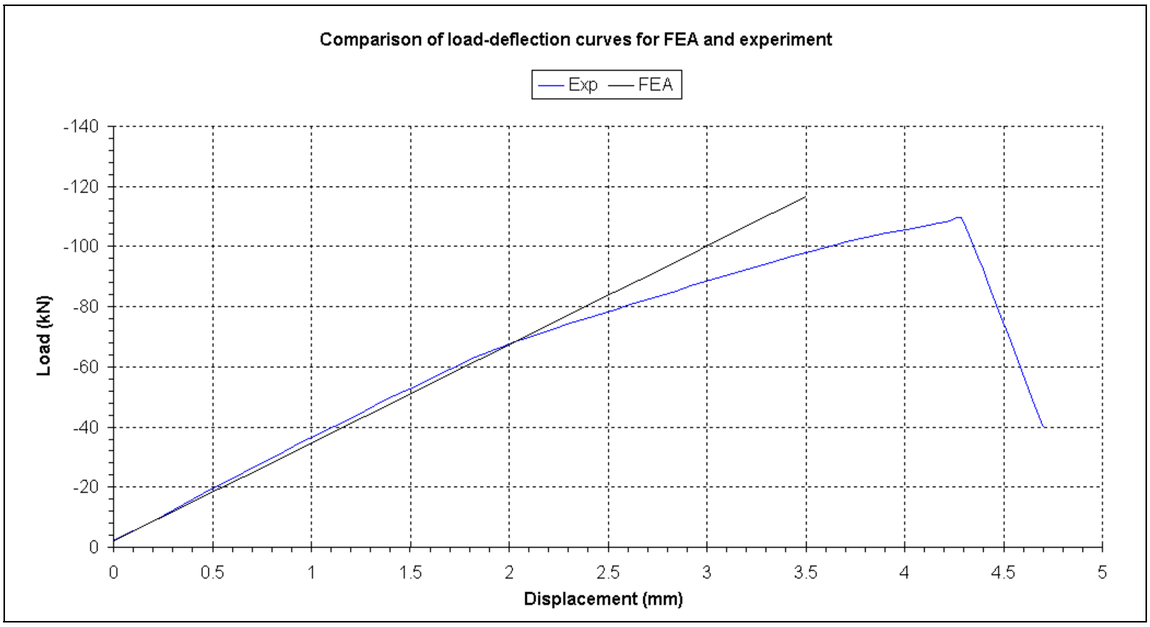

Figure 7.5 Finite element result compared to experimental result for HSC in compression

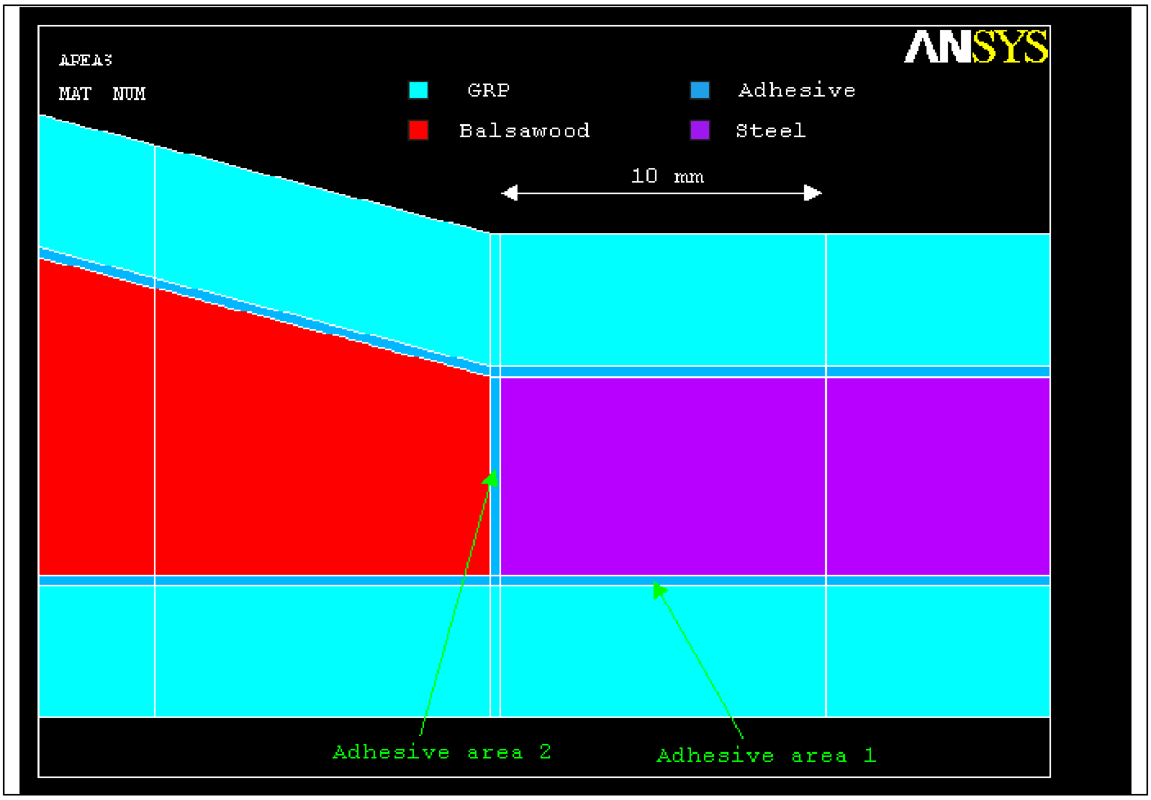

Figure 7.6 ANSYS model indicating the location of adhesive areas 1 and 2

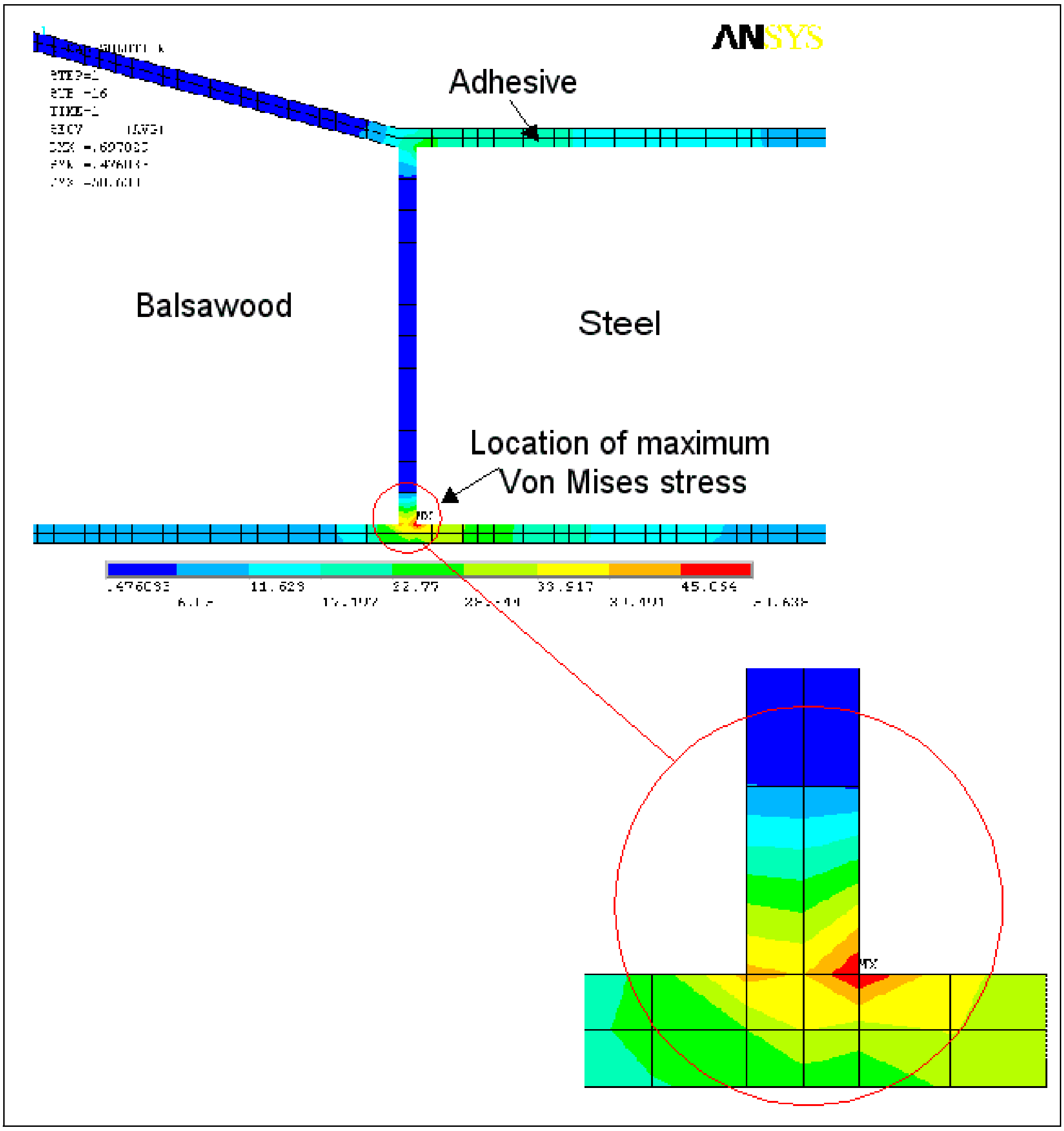

Figure 7.7 Location of the maximum Von Mises stress in the adhesive layer ($\sigma_{VM} \geq 50$ MPa)

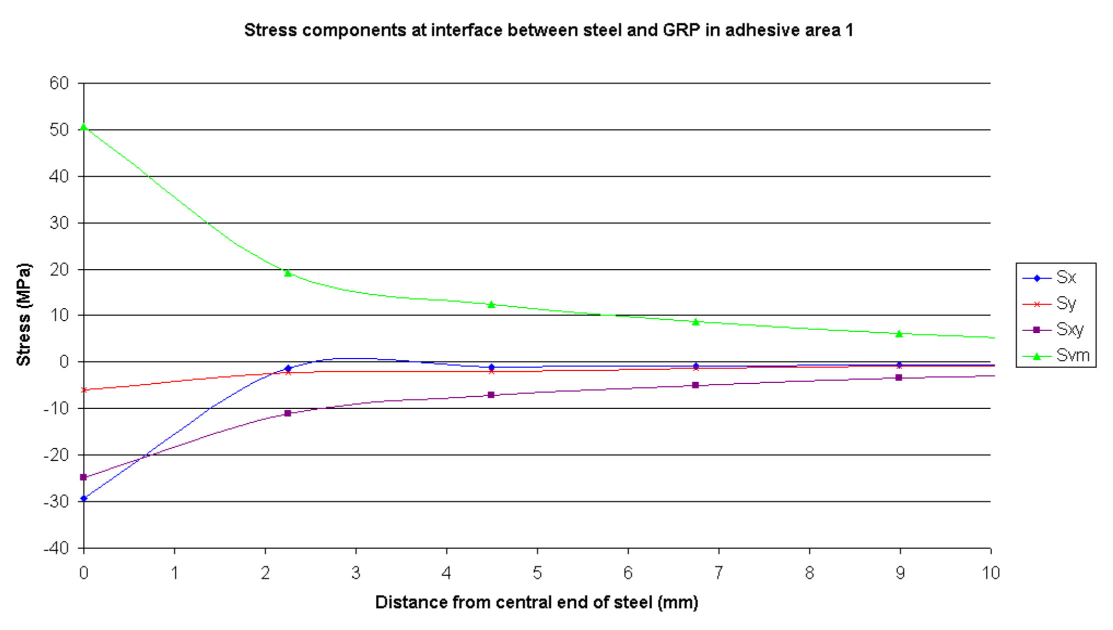

Figure 7.8 Stress components in adhesive area 1 (Fig. 7.6) at steel/adhesive interface for 0.72 mm displacement

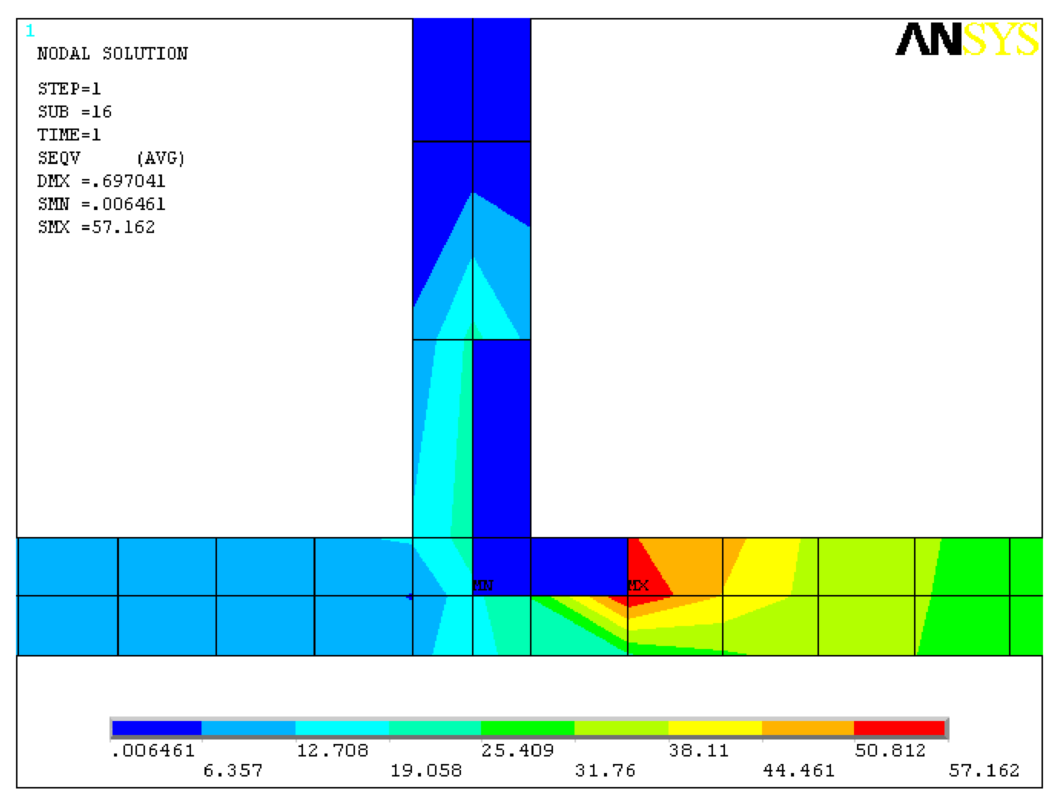

Figure 7.9 Adhesive elements with modified stiffness properties at location of maximum Von Mises stress (MPa)

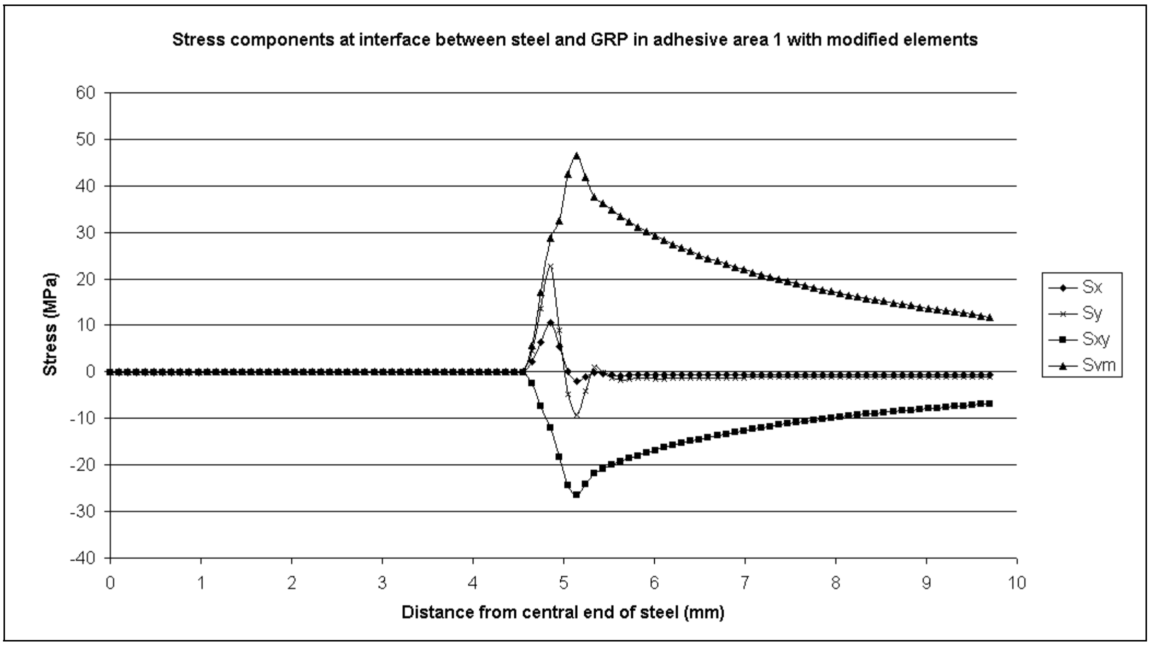

Figure 7.10 Stress components present at interface of steel and adhesive with modified element properties

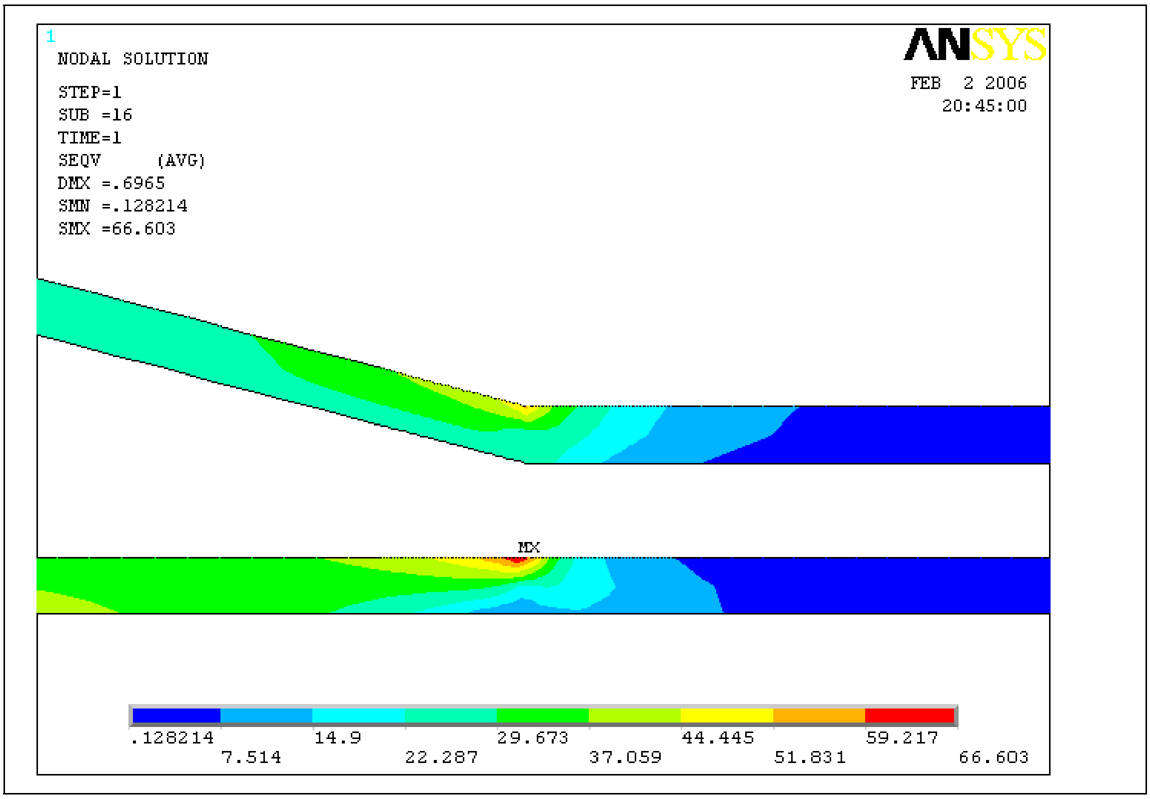

```
NODAL SOLUTION

STEP=1
SUB =16
TIME=1
SEQV      (AVG)
DMX =.6965
SMN =.128214
SMX =66.603
```

Figure 7.11 Von Mises stress in the GRP skins displacement where adhesive failure occurs (MPa)

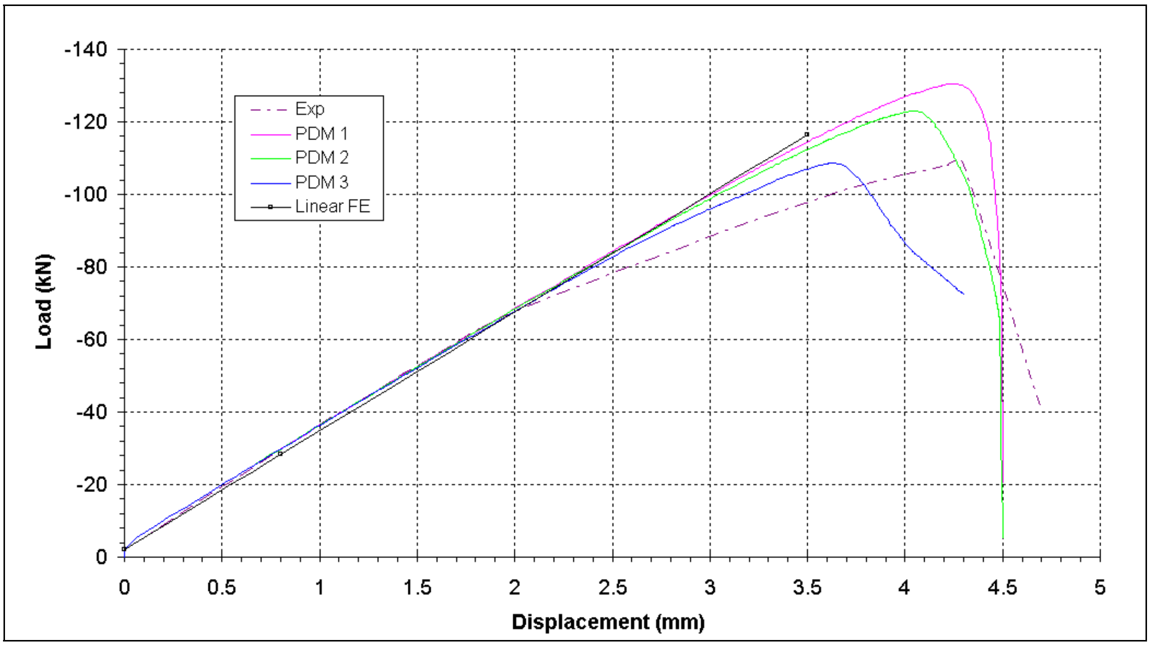

Figure 7.12 Comparison between the PDM and experimental load-deflection curves

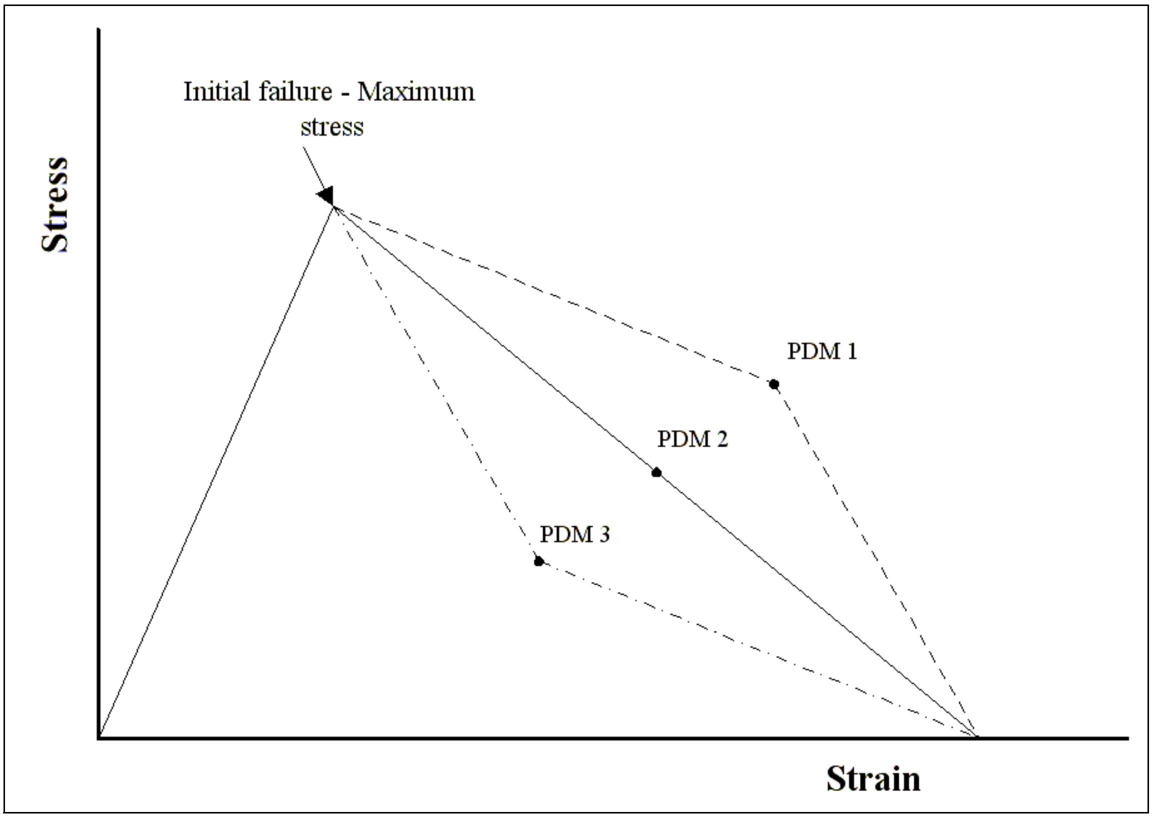

Figure 7.13 Stress reduction models for the progressive damage model

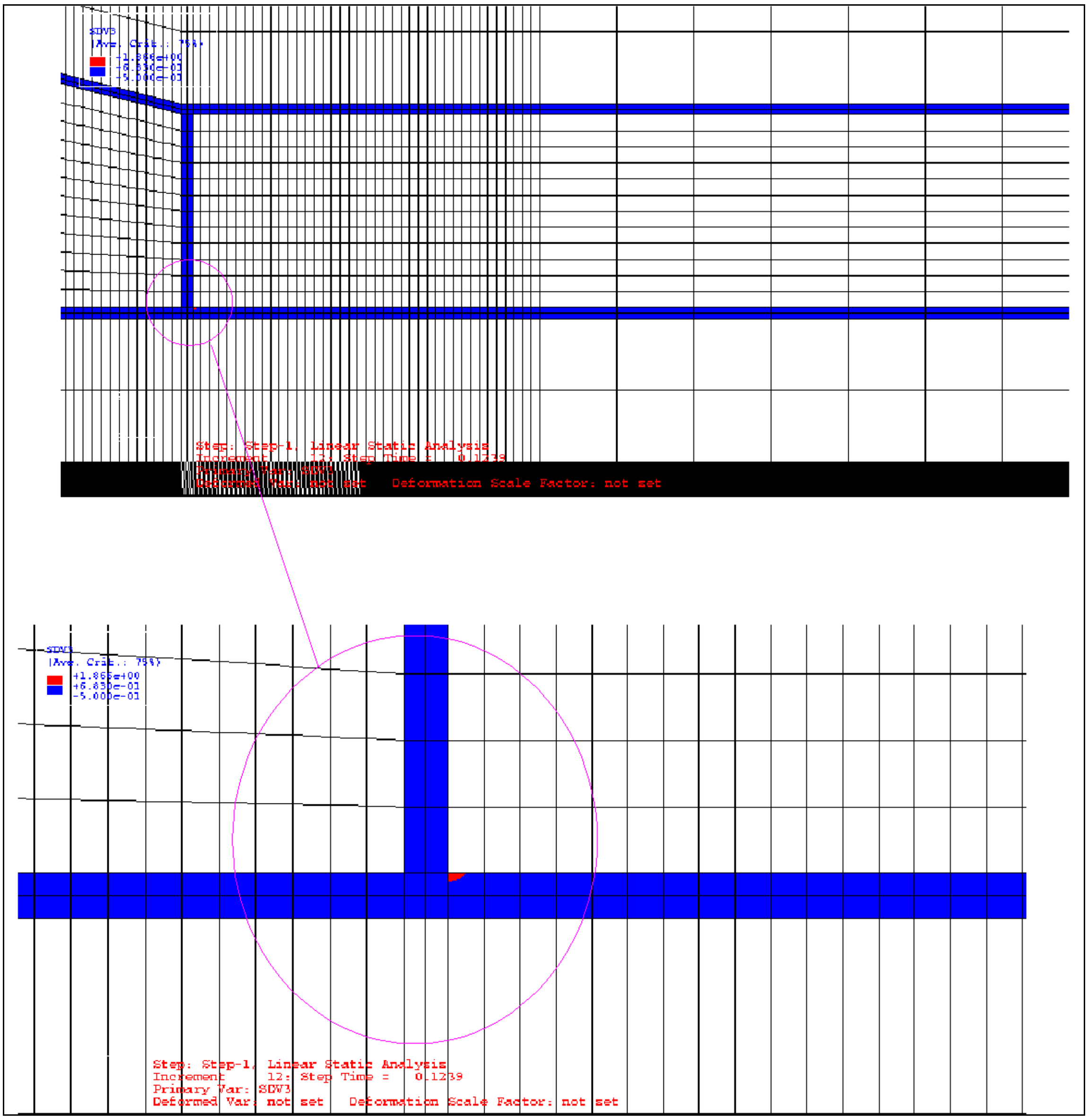

Figure 7.14 Location of first failure in the progressive damage model

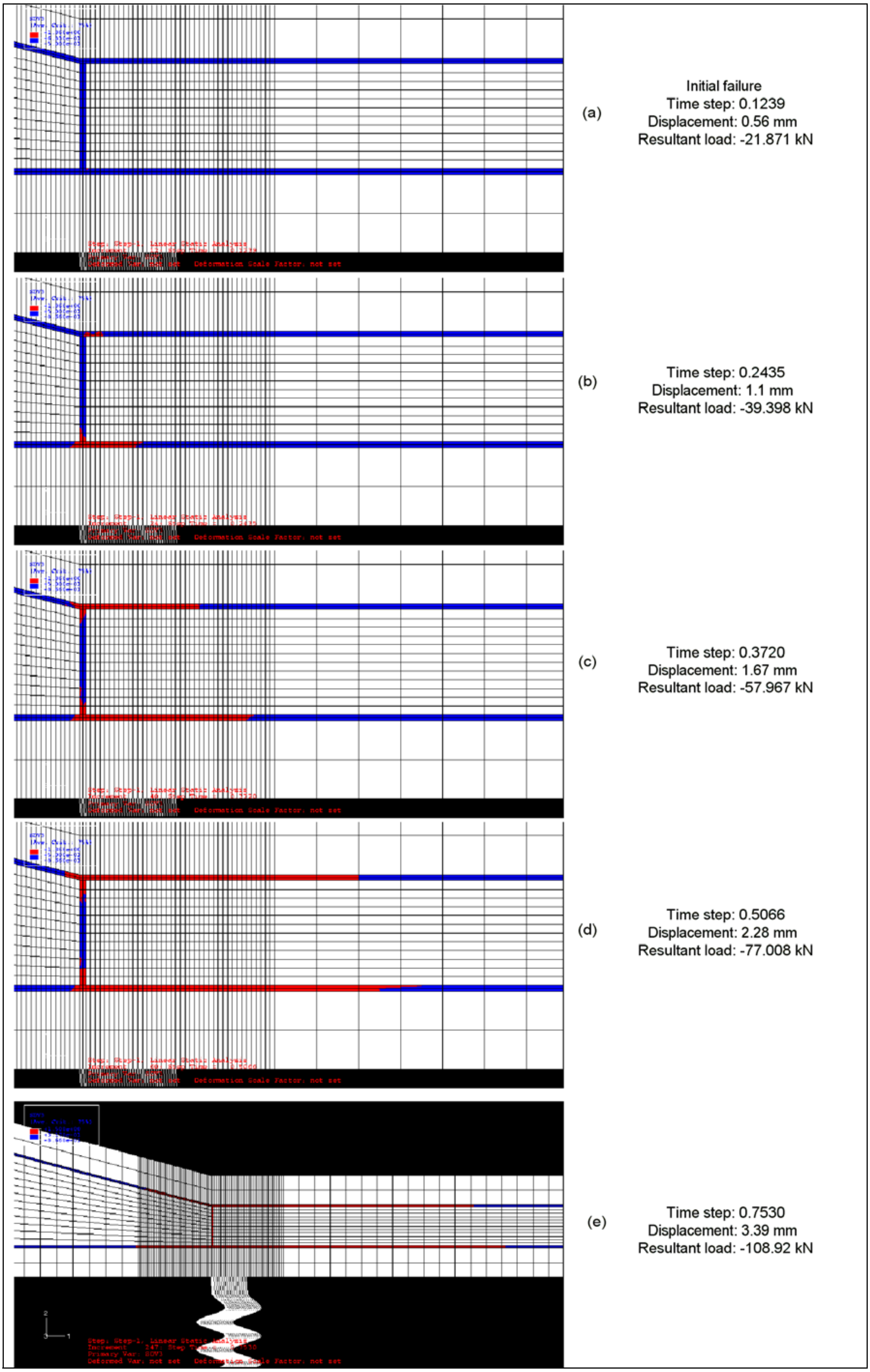

(a)

Initial failure
Time step: 0.1239
Displacement: 0.56 mm
Resultant load: -21.871 kN

(b)

Time step: 0.2435
Displacement: 1.1 mm
Resultant load: -39.398 kN

(c)

Time step: 0.3720
Displacement: 1.67 mm
Resultant load: -57.967 kN

(d)

Time step: 0.5066
Displacement: 2.28 mm
Resultant load: -77.008 kN

(e)

Time step: 0.7530
Displacement: 3.39 mm
Resultant load: -108.92 kN

Figure 7.15 Progression of damage in the joint

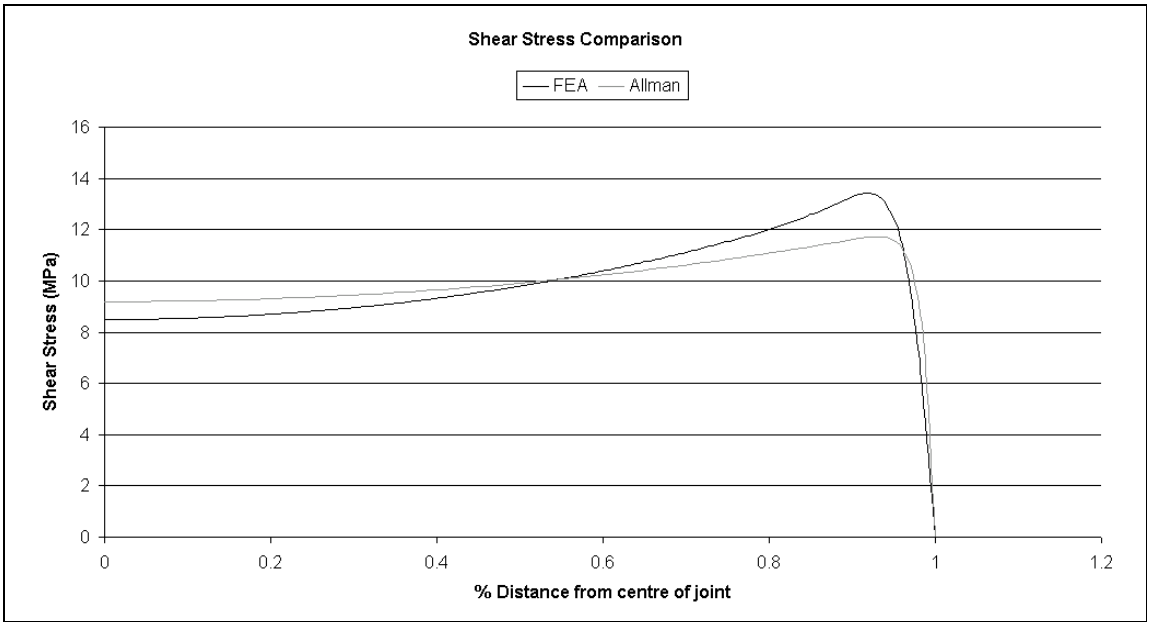

Figure 8.1 Comparison of shear stress between FEA and Allman for a single lap joint

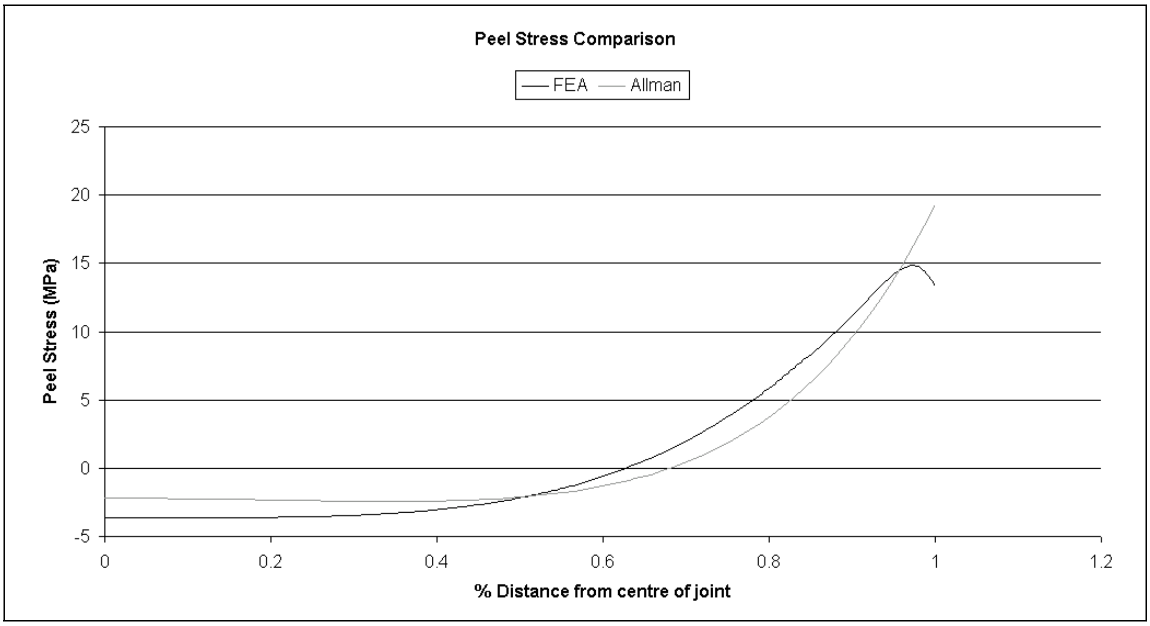

Figure 8.2 Comparison of peel stress between FEA and Allman for a single lap joint

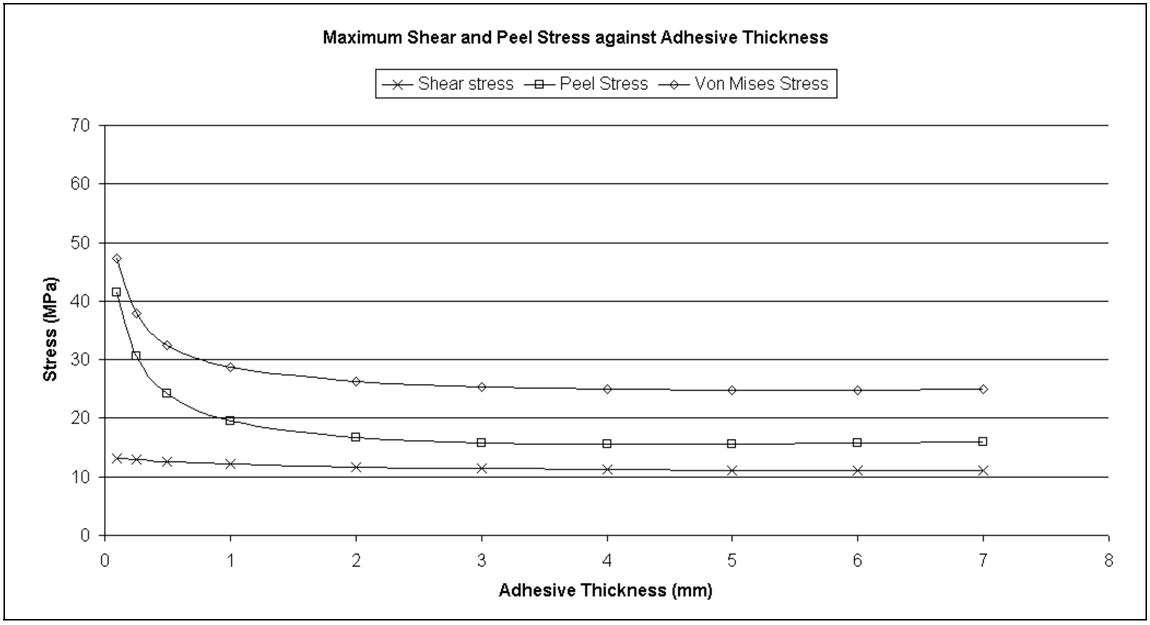

Figure 8.3 Maximum shear, peel and Von Mises stress against adhesive thickness using Allman's theory

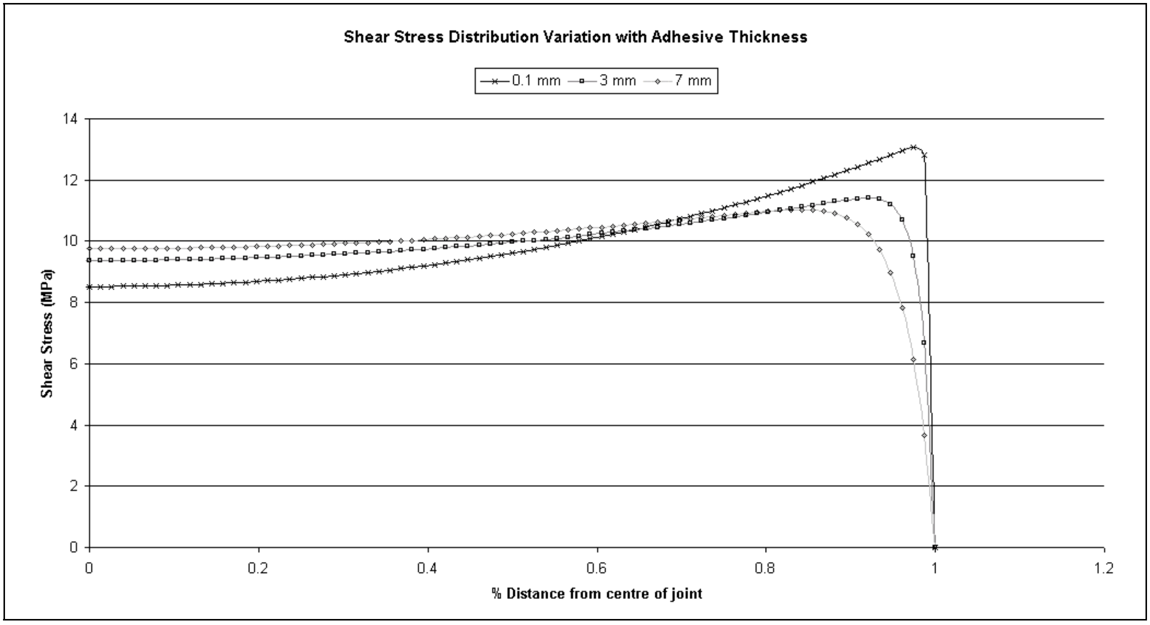

Figure 8.4 Shear stress distribution with variations in adhesive thickness using Allman's theory

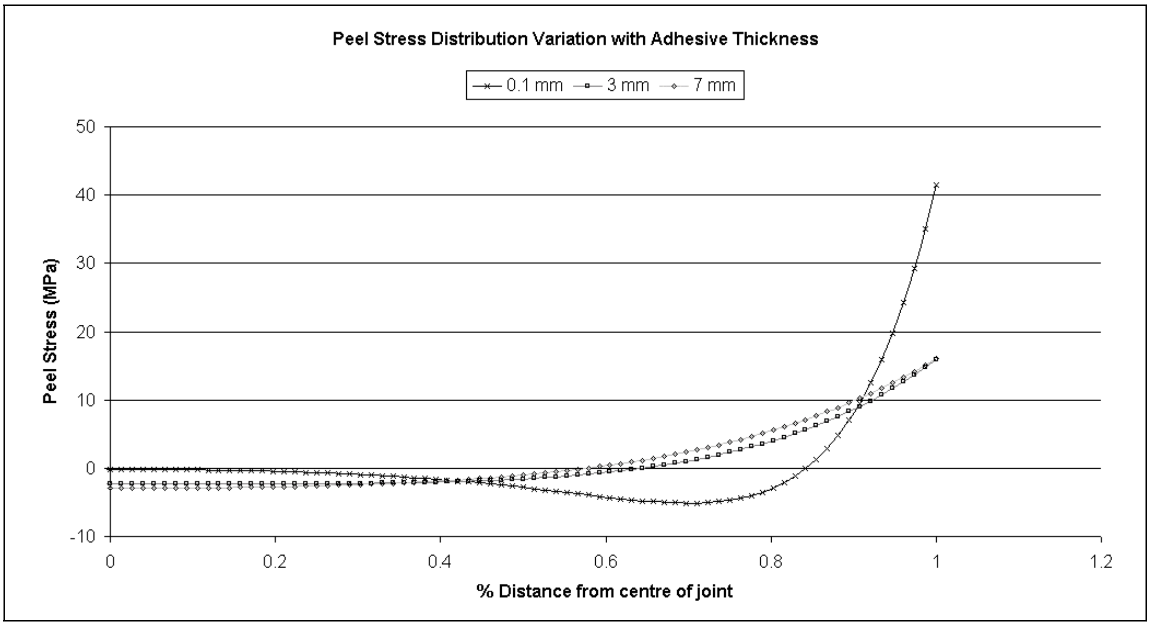

Figure 8.5 Peel stress distribution with variations in adhesive thickness using Allman's theory

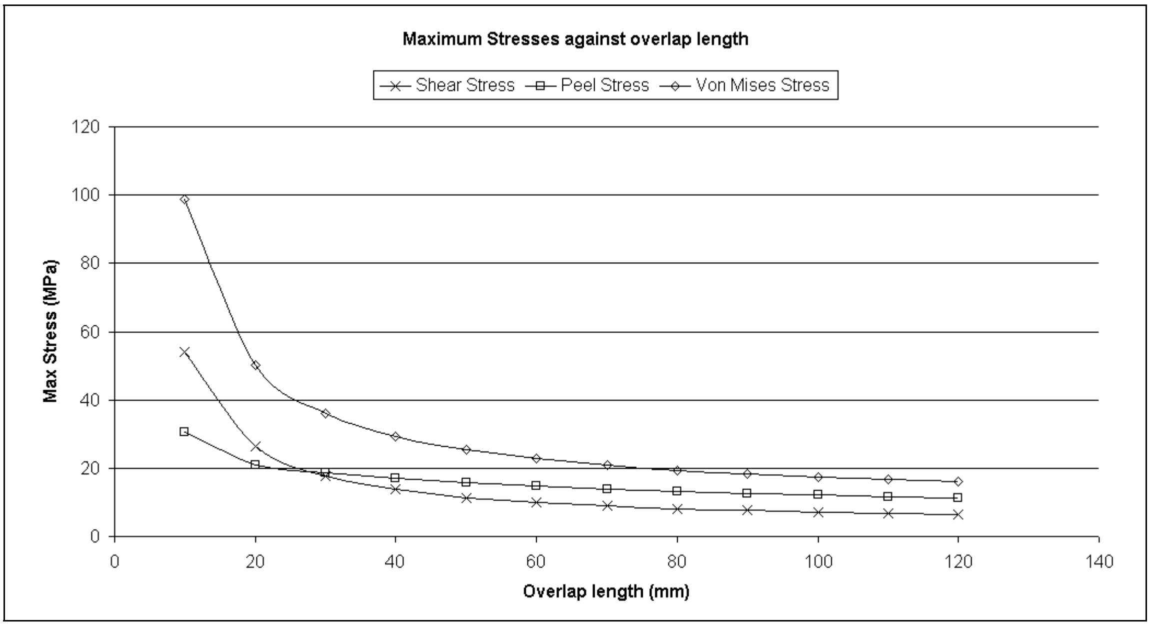

Figure 8.6 Maximum shear, peel and Von Mises stress against overlap length using Allman's theory

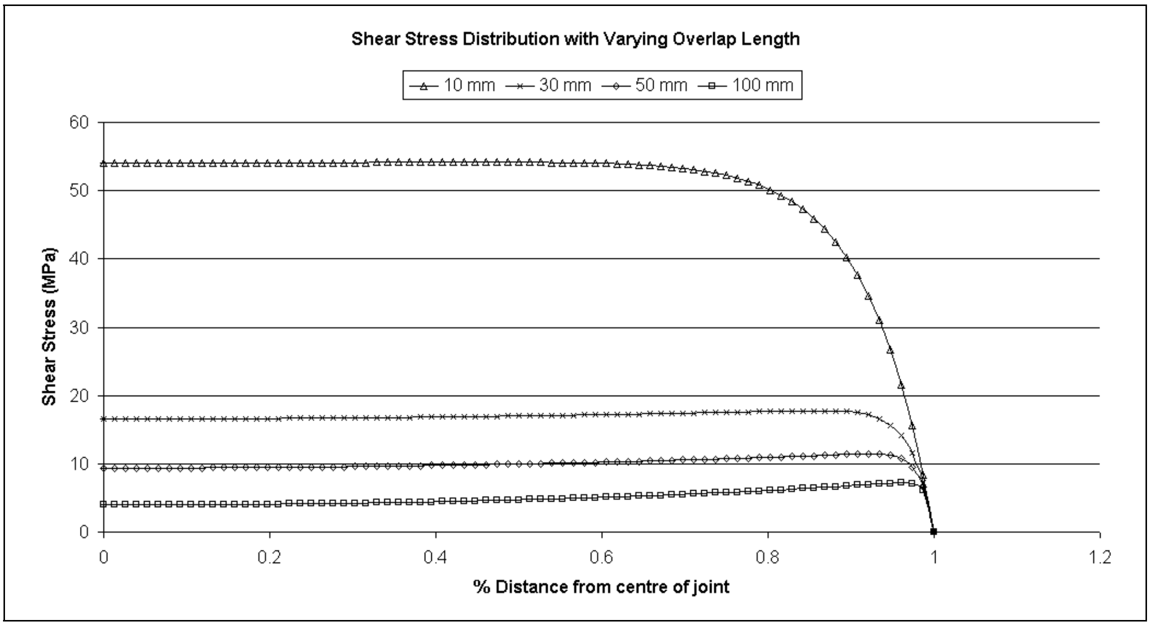

Figure 8.7 Shear stress distribution with variations in overlap length using Allman's theory

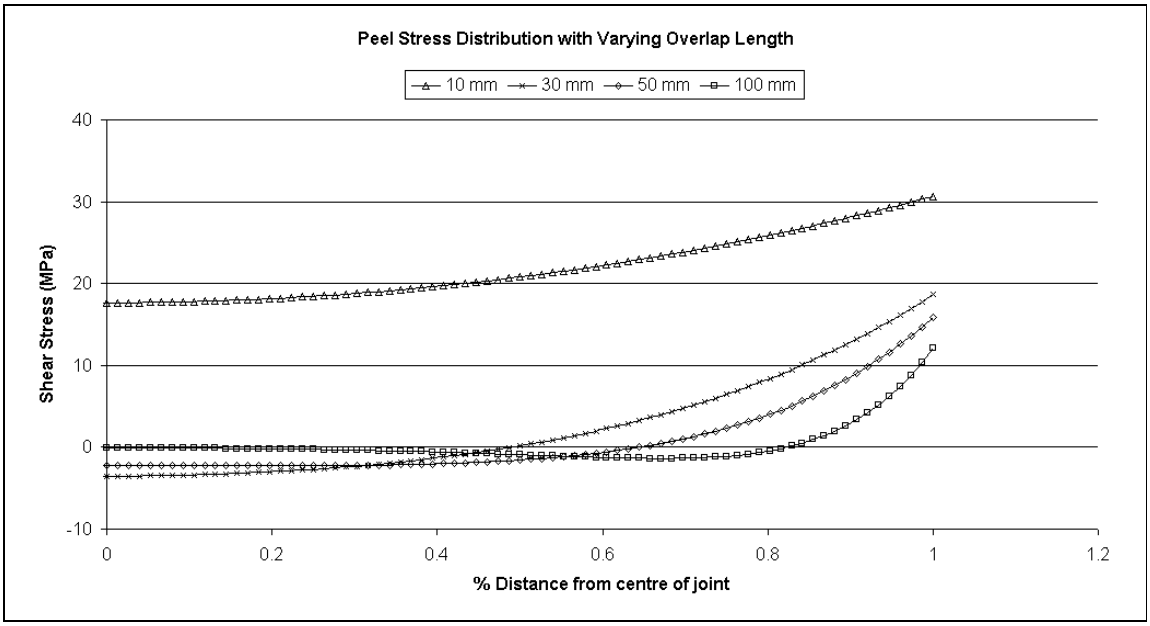

Figure 8.8 Peel stress distribution with variations in overlap length using Allman's theory

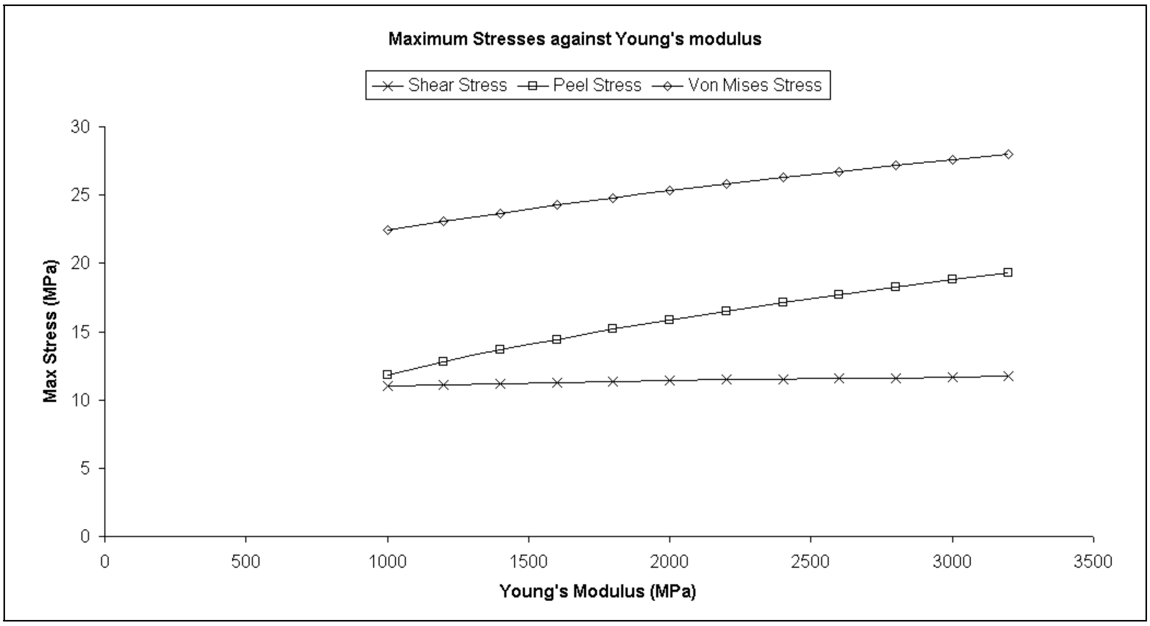

Figure 8.9 Maximum shear, peel and Von Mises stress with variations in Young's modulus using Allman's theory

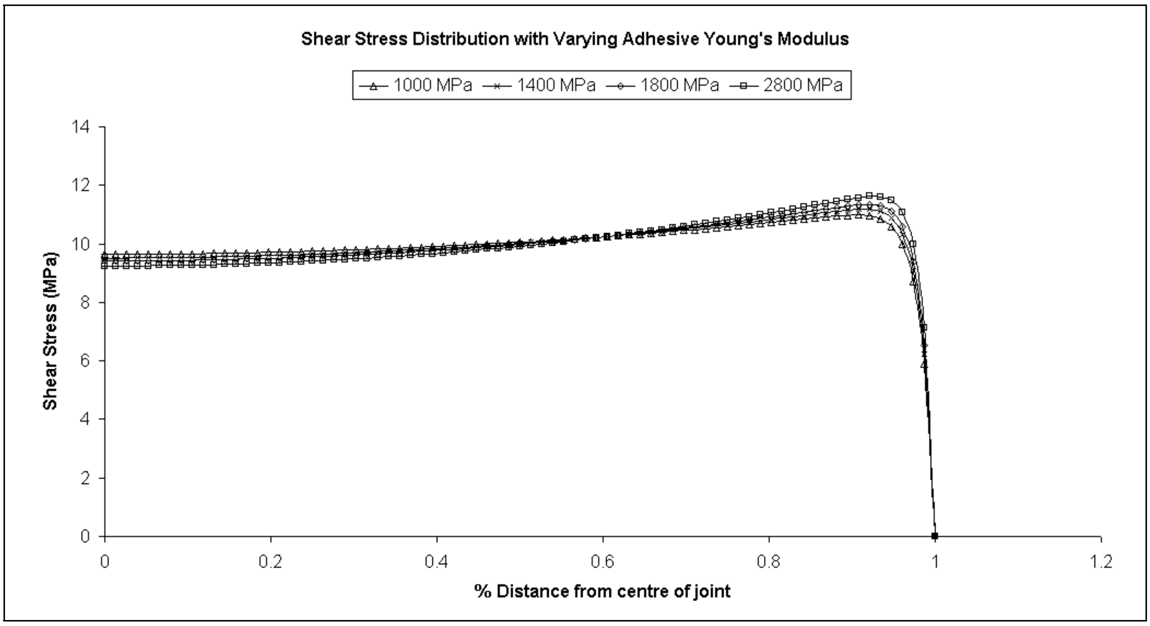

Figure 8.10 Shear stress distribution with variations in Young's modulus using Allman's theory

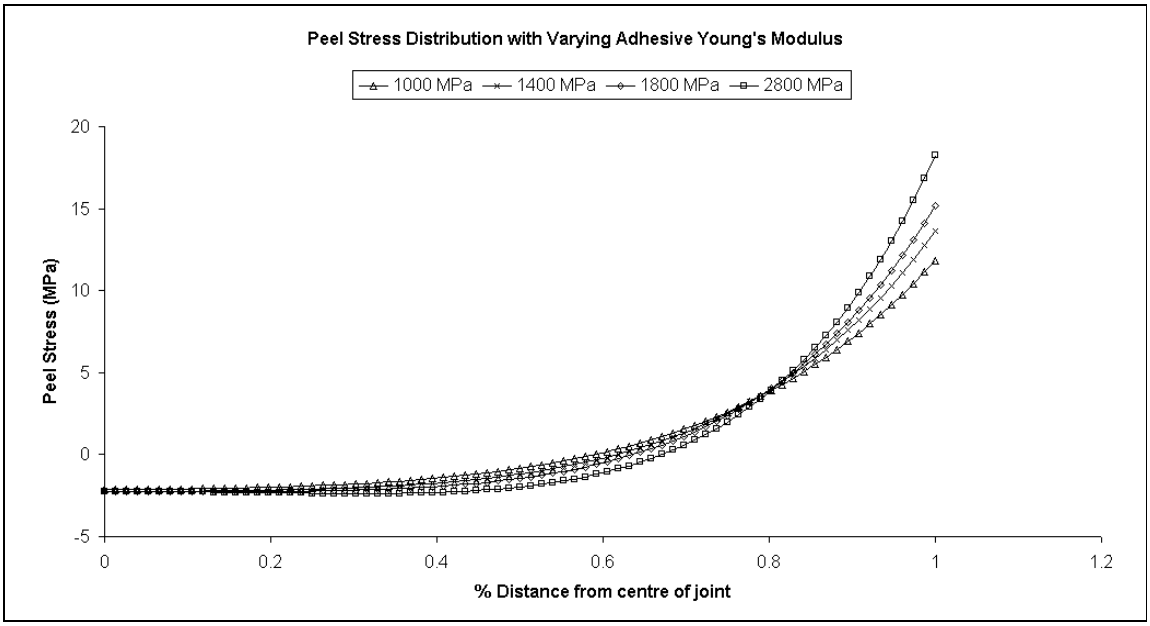

Figure 8.11 Peel stress distribution with variations in Young’s modulus using Allman’s theory

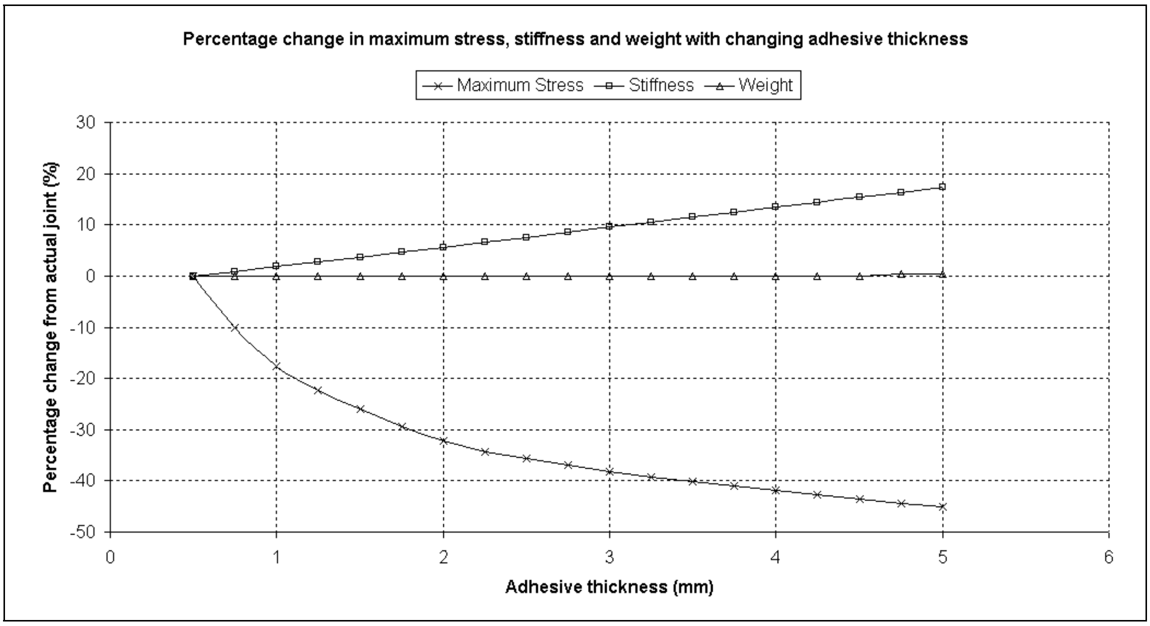

Figure 8.12 Percentage change from baseline of stress, stiffness and weight with changing adhesive thickness from FEA

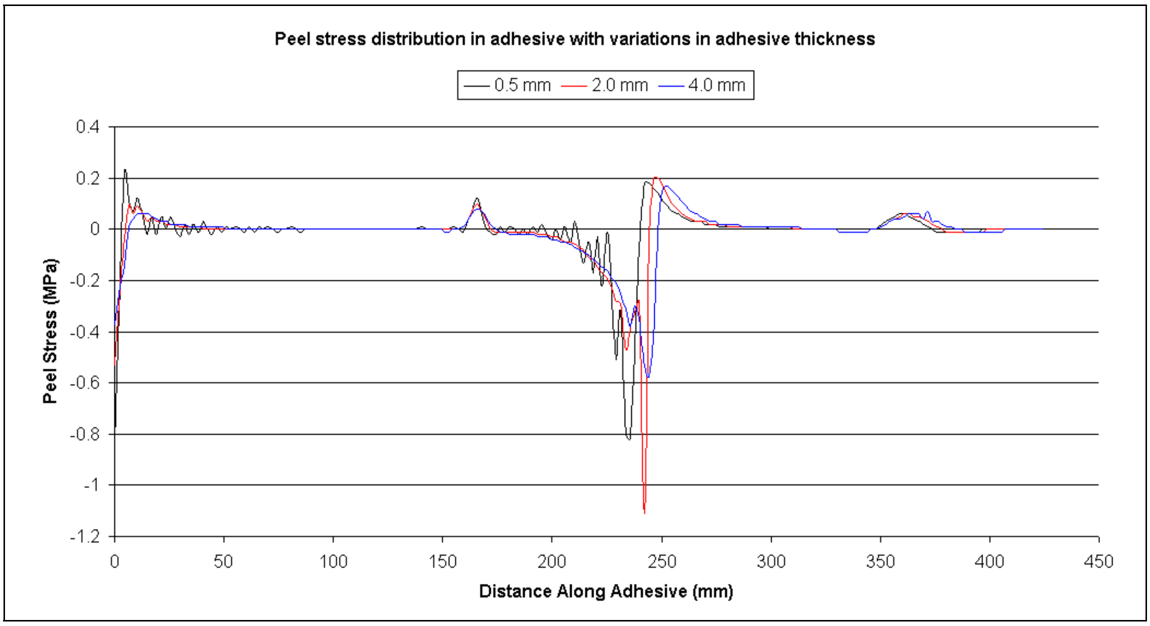

Figure 8.13 Peel stress distribution in adhesive layer with variations in adhesive thickness from FEA

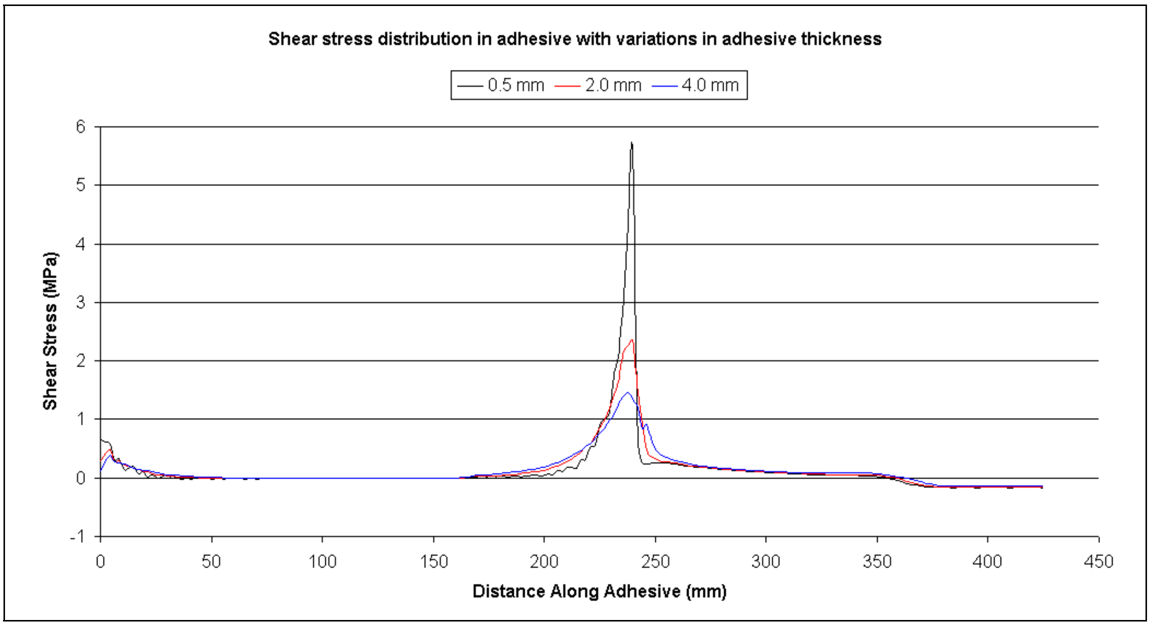

Figure 8.14 Shear stress distribution in adhesive layer with variations in adhesive thickness from FEA

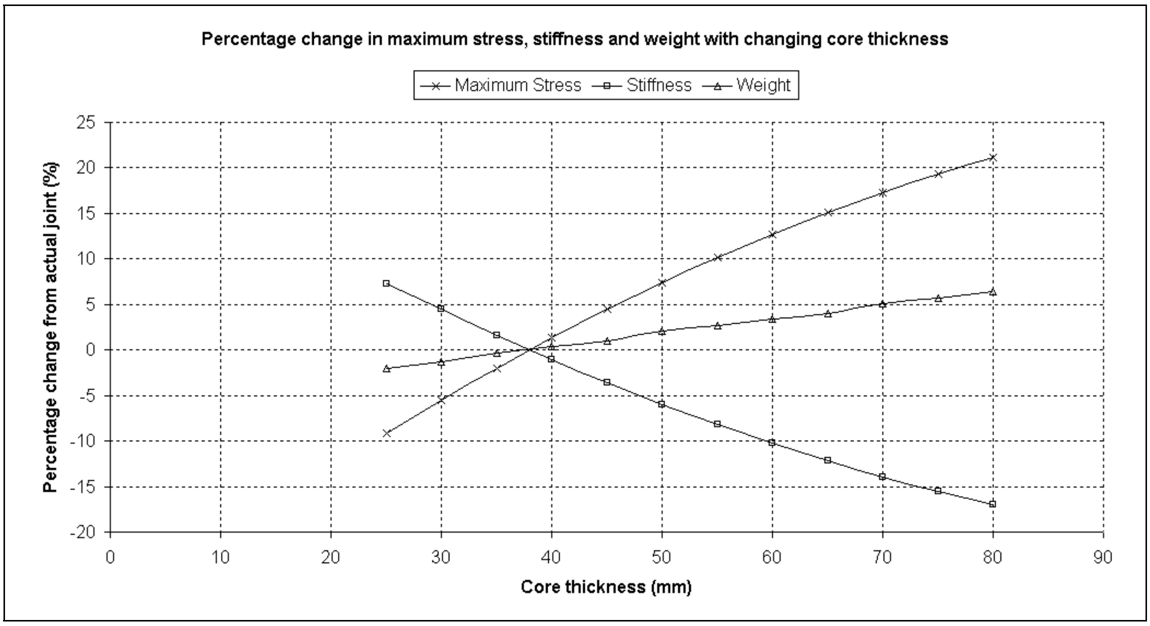

Figure 8.15 Percentage change from baseline of stress, stiffness and weight with changing core thickness from FEA

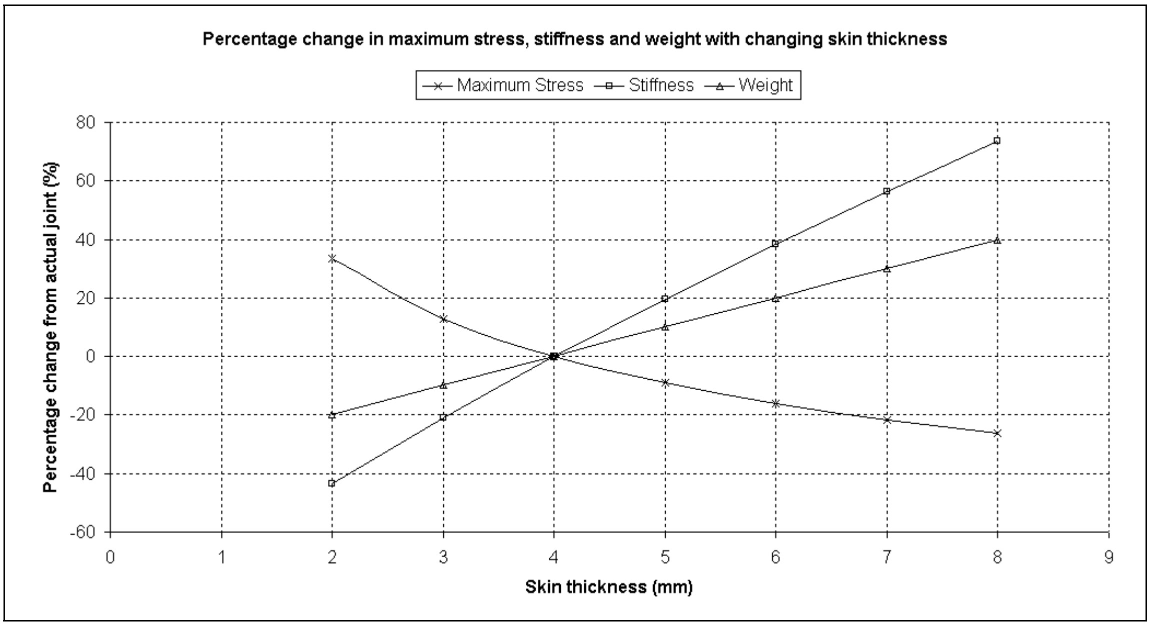

Figure 8.16 Percentage change from baseline of stress, stiffness and weight with changing skin thickness from FEA

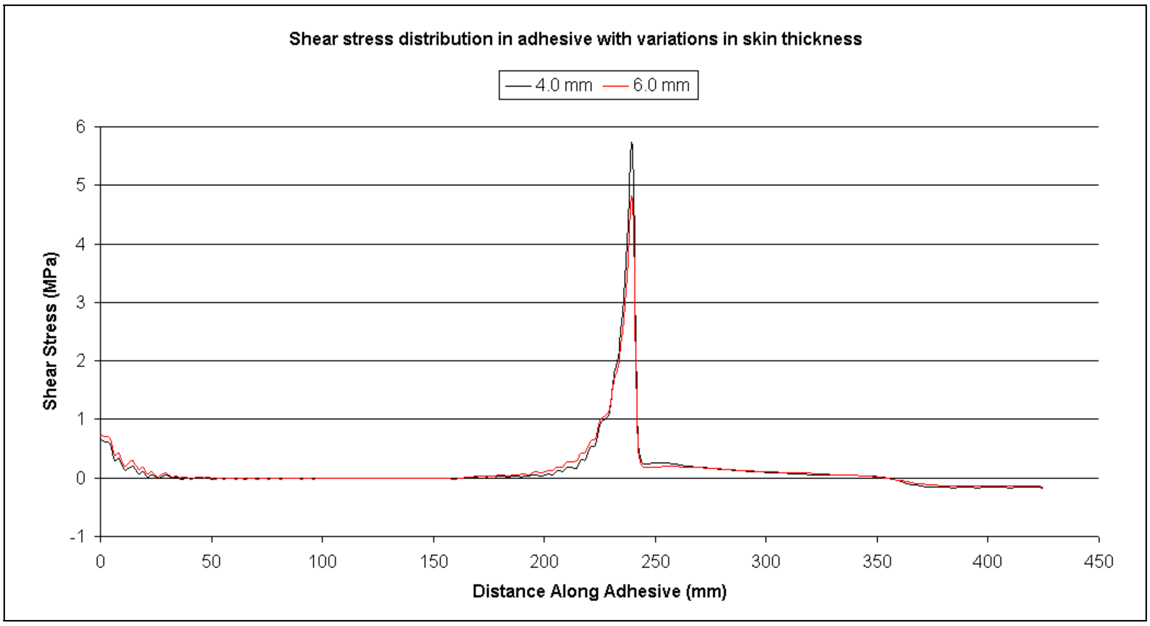

Figure 8.17 Shear stress distribution in adhesive layer with variations in adhesive thickness from FEA

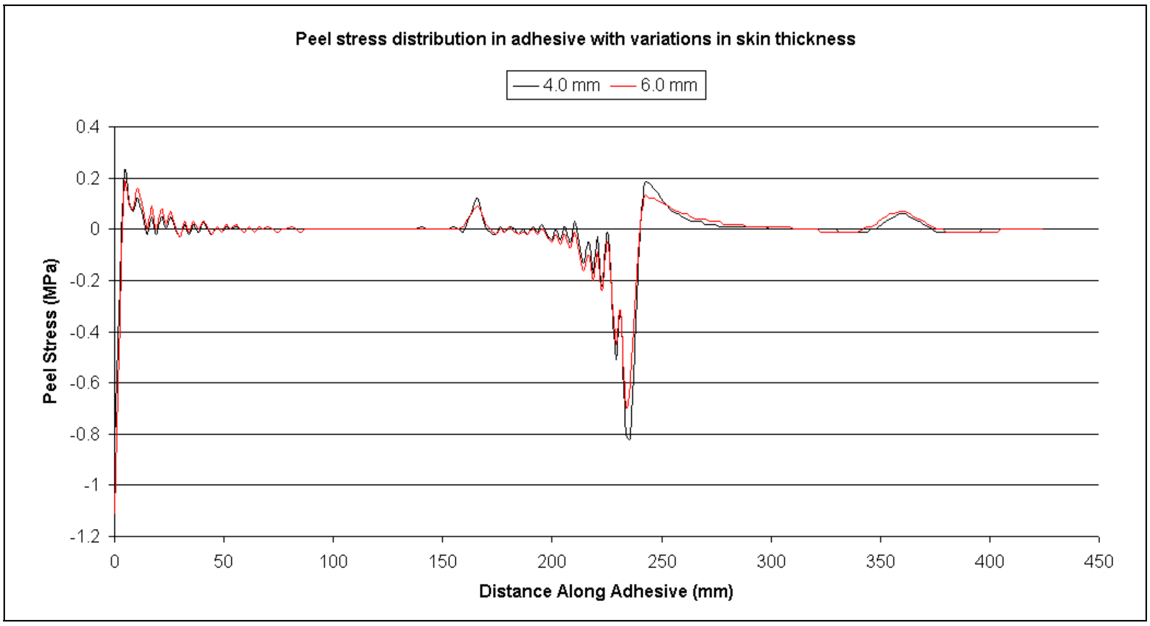

Figure 8.18 Peel stress distribution in adhesive layer with variations in adhesive thickness from FEA

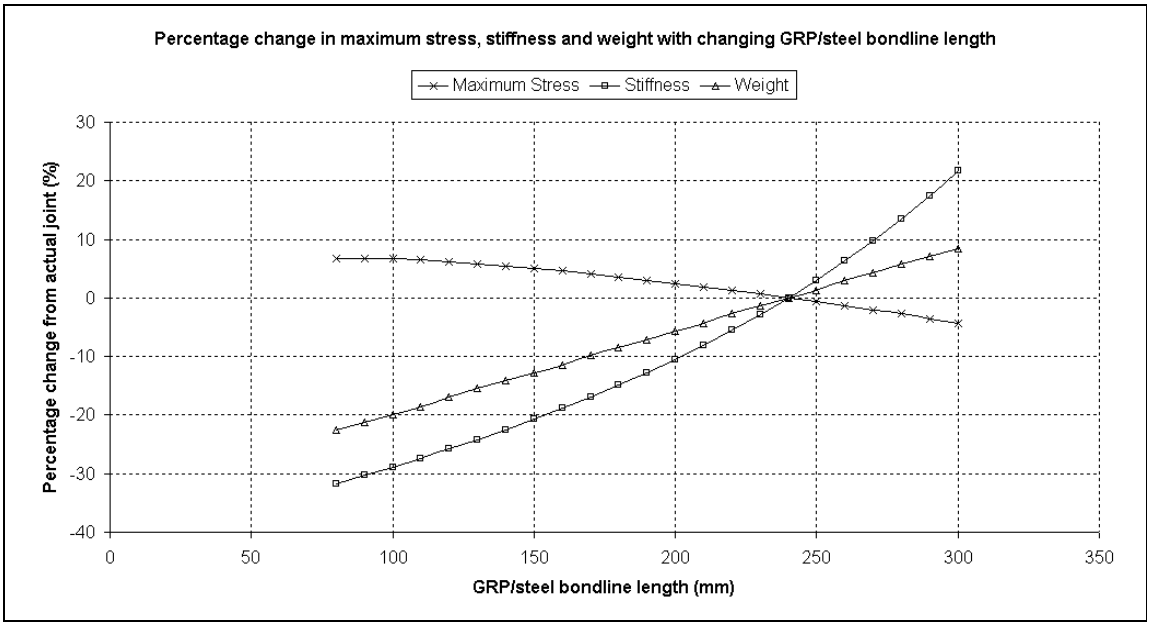

Figure 8.19 Percentage change from baseline of stress, stiffness and weight with changing GRP/steel bondline length from FEA

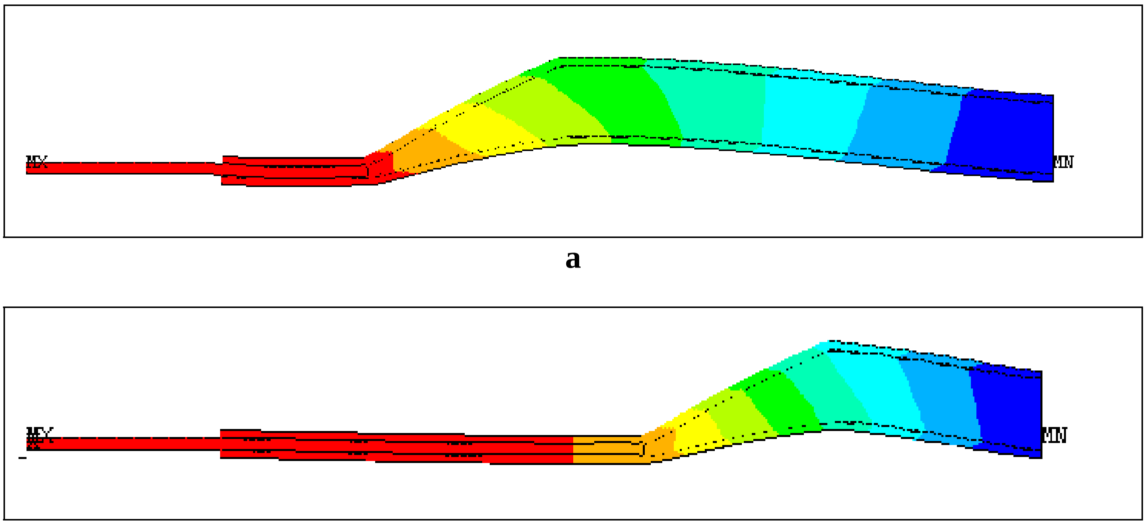

Figure 8.20 Comparison of the deformation of a short (a) and long (b) bond length from FEA

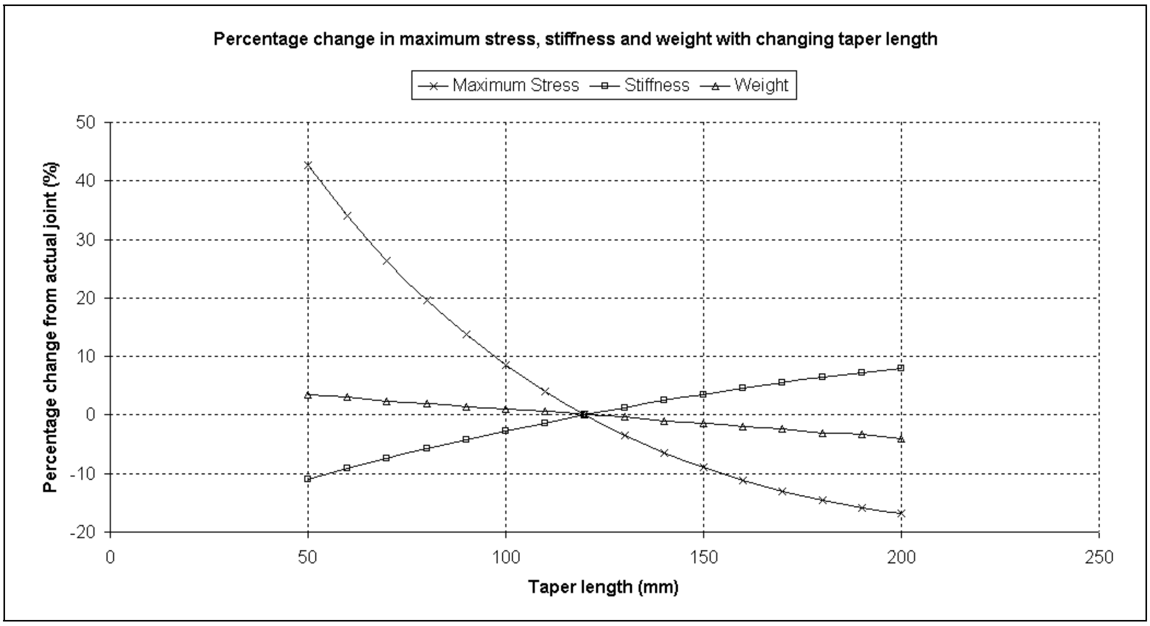

Figure 8.21 Percentage change from baseline of stress, stiffness and weight with changing taper length from FEA

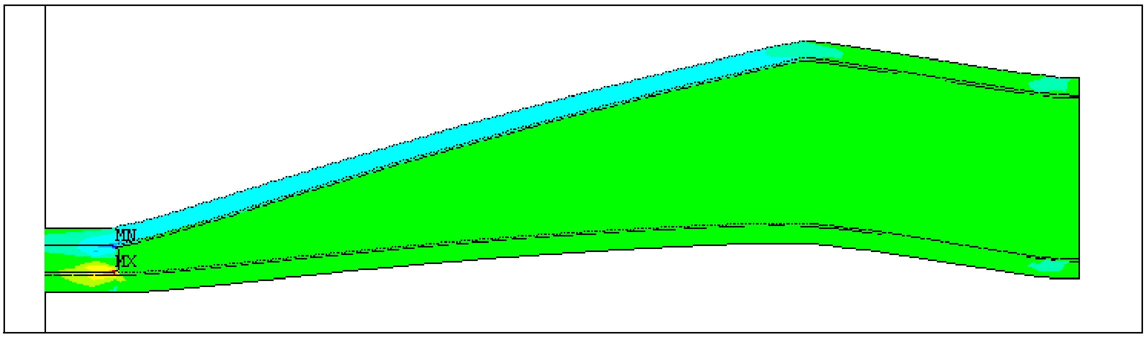

a

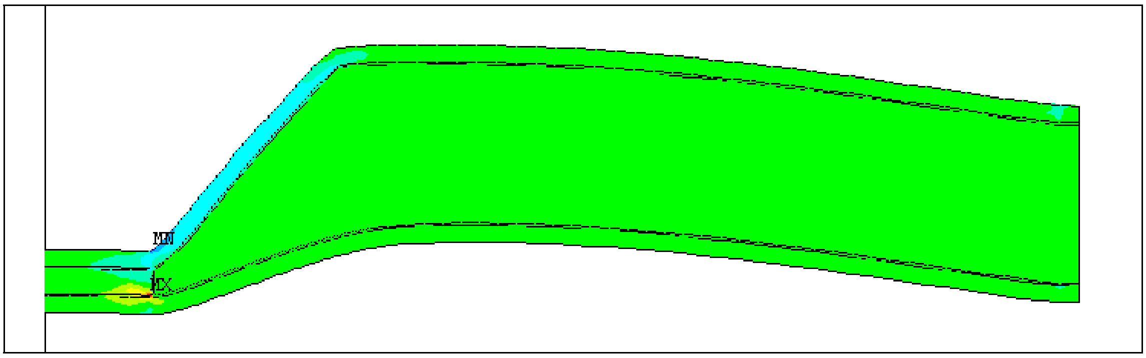

b

Figure 8.22 Lateral deflection (exaggerated) of long (a) and short (b) taper lengths from FEA

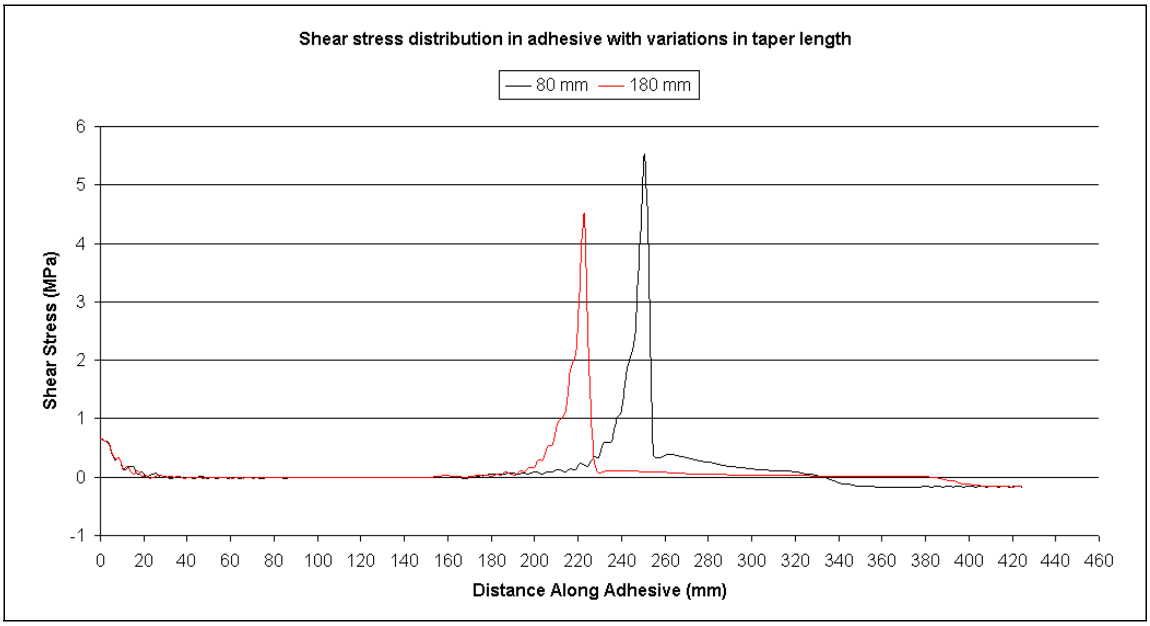

Figure 8.23 Shear stress distribution in adhesive layer with variations in taper length from FEA

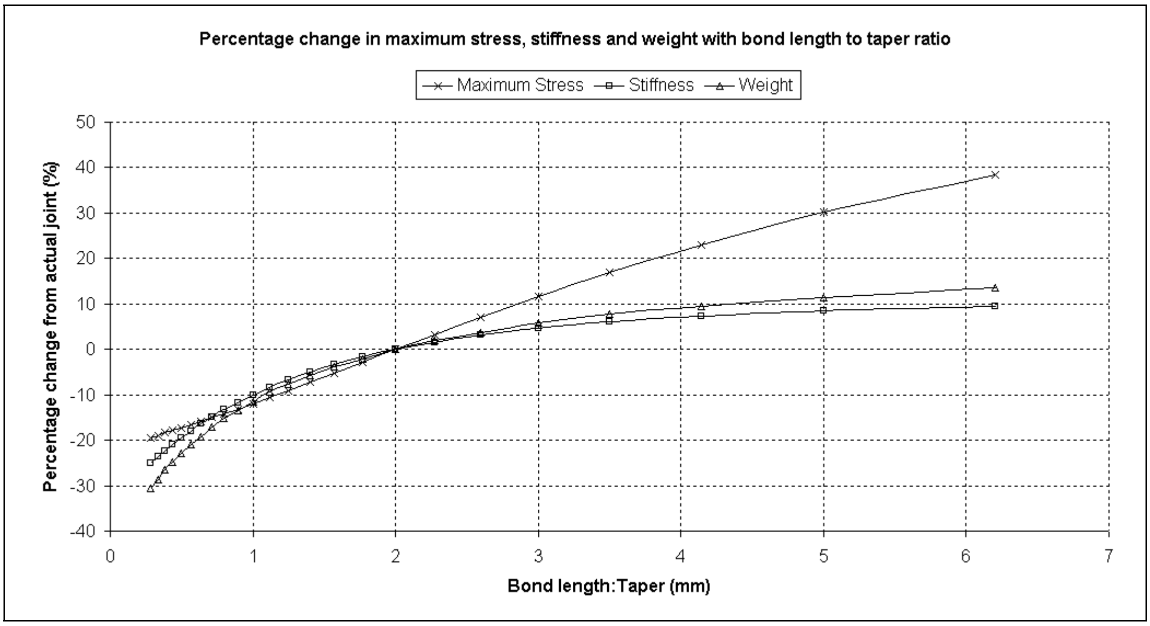

Figure 8.24 Percentage change from baseline of stress, stiffness and weight with bond length to taper ratio from FEA

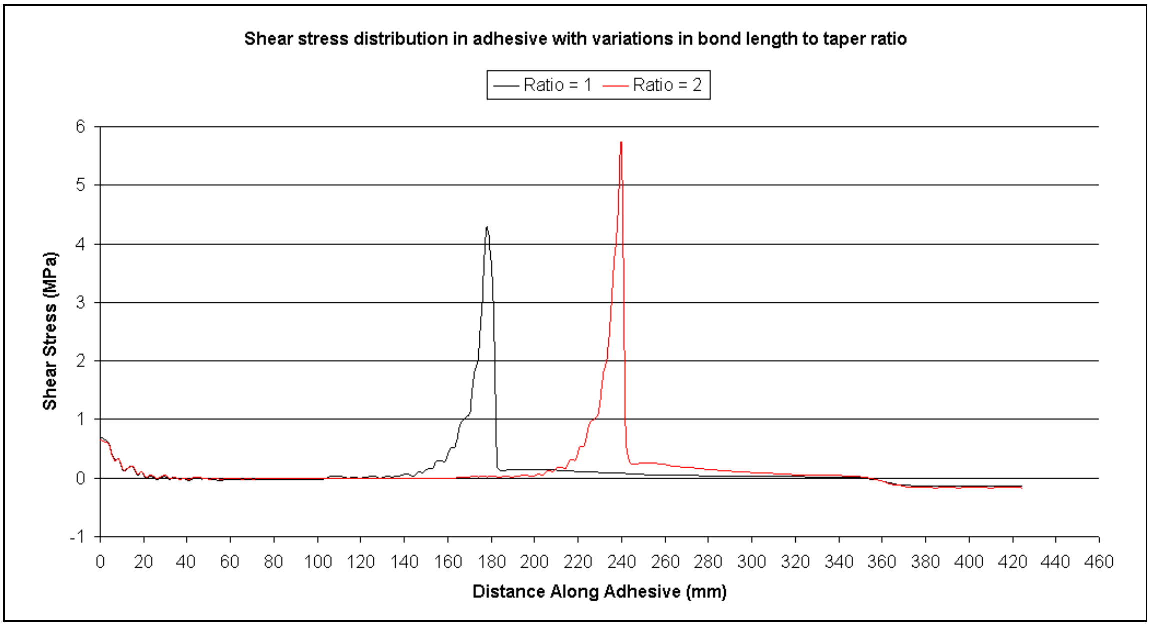

Figure 8.25 Shear stress distribution in adhesive layer with variations in bond length to taper ratio from FEA

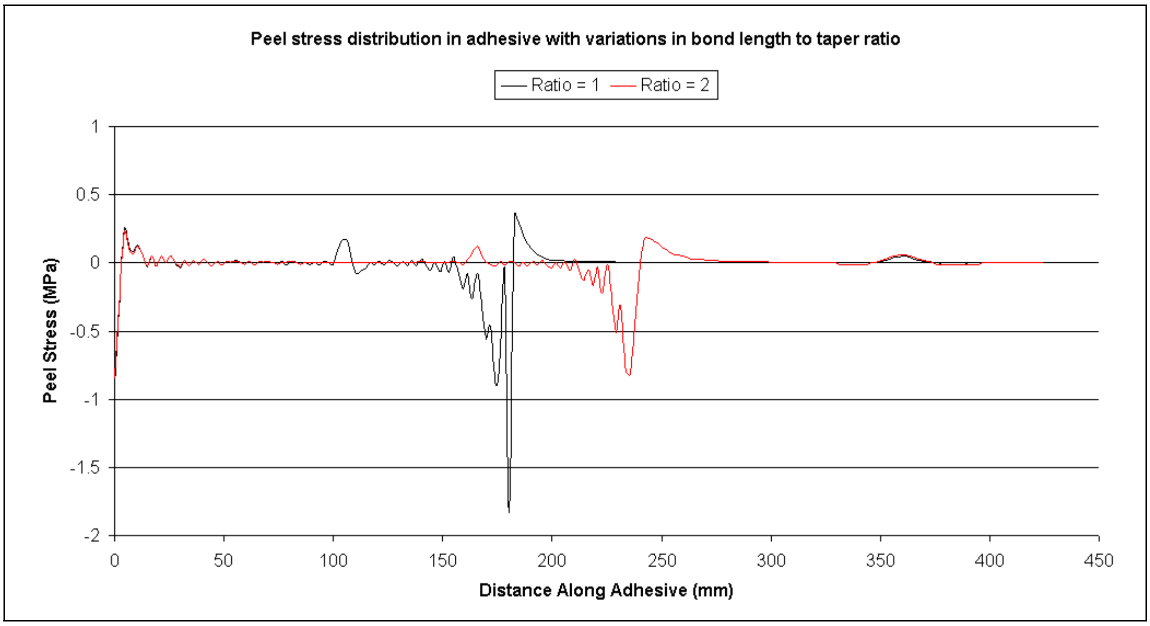

Figure 8.26 Peel stress distribution in adhesive layers with variations in bond length to taper ratio from FEA

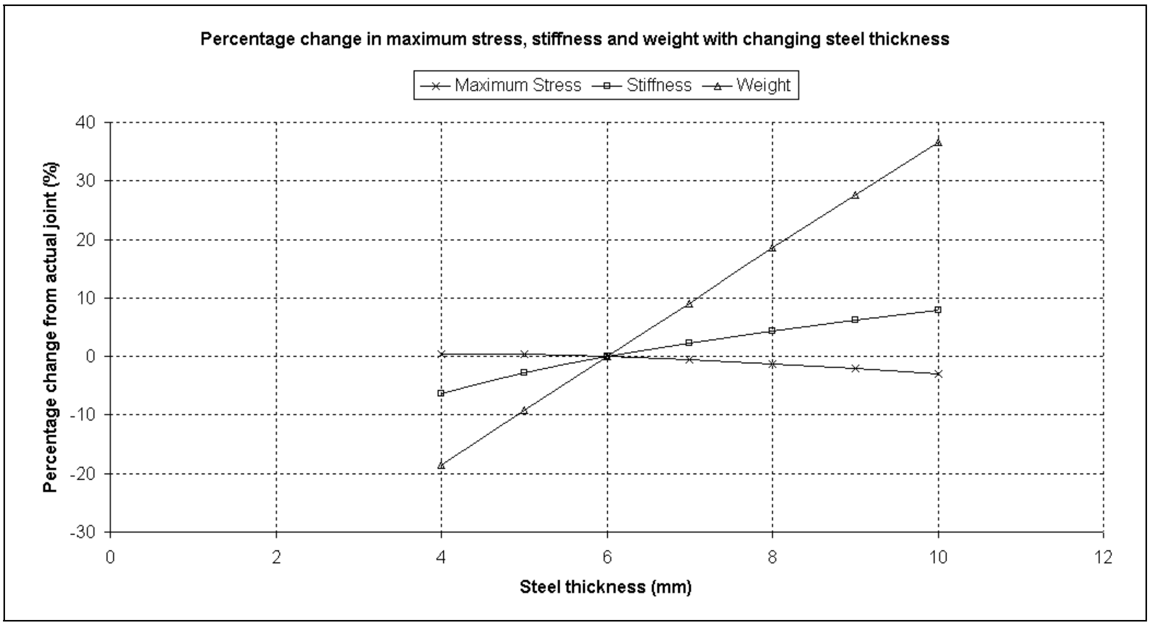

Figure 8.27 Percentage change from baseline of stress, stiffness and weight with changing steel thickness from FEA

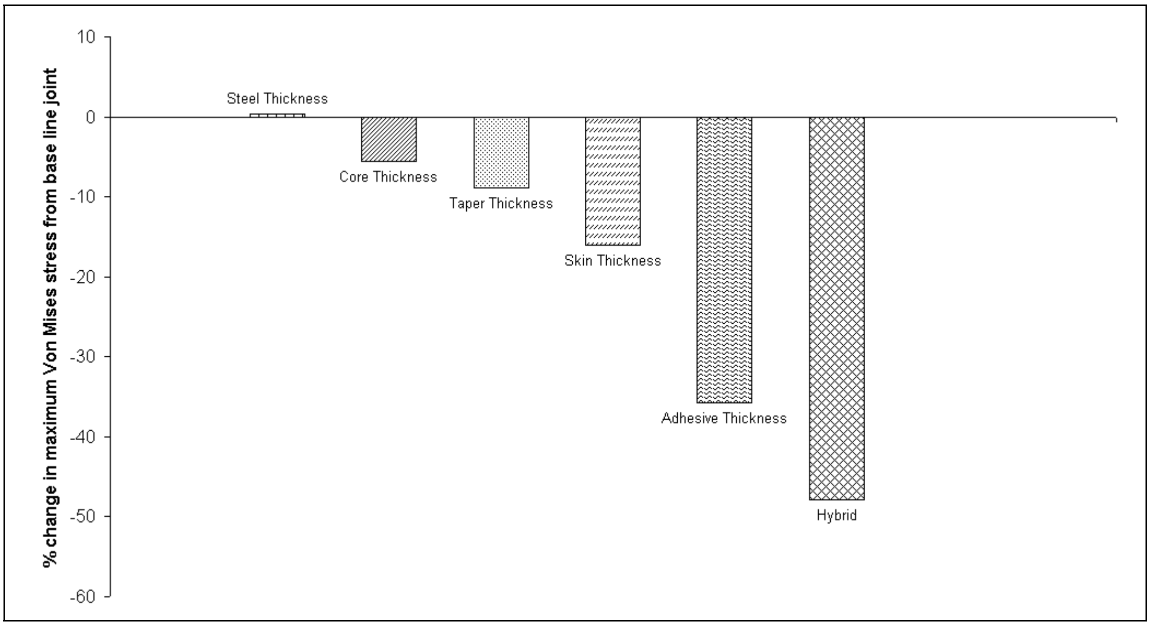

Figure 8.28 Comparison of changes to geometry on maximum Von Mises stress from FEA

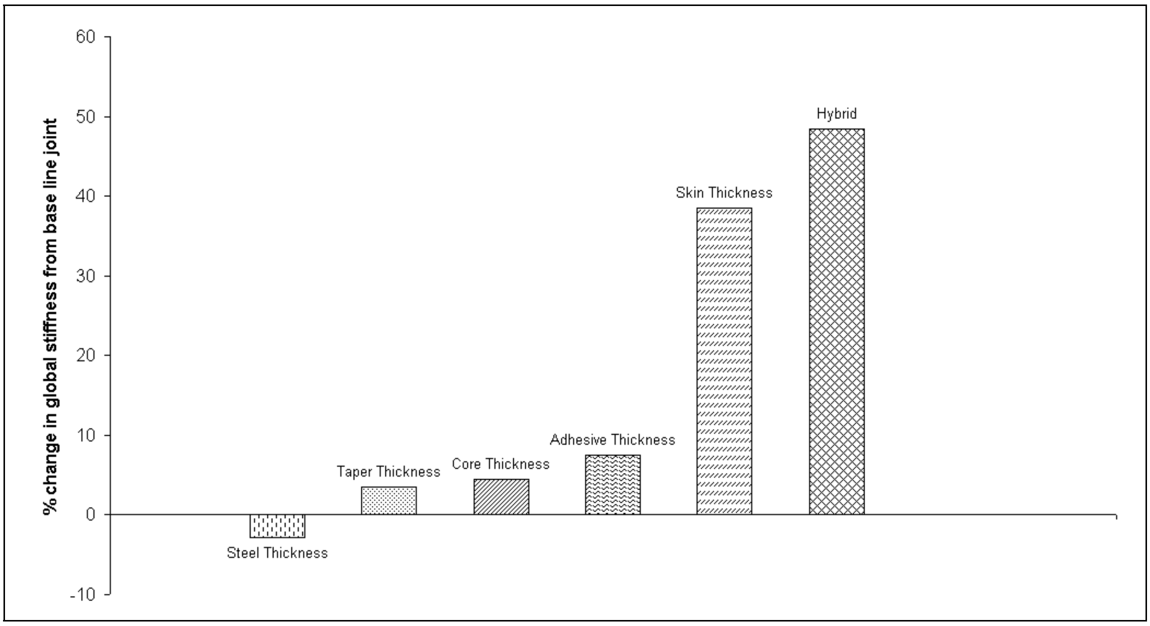

Figure 8.29 Comparison of changes to geometry on global stiffness from FEA

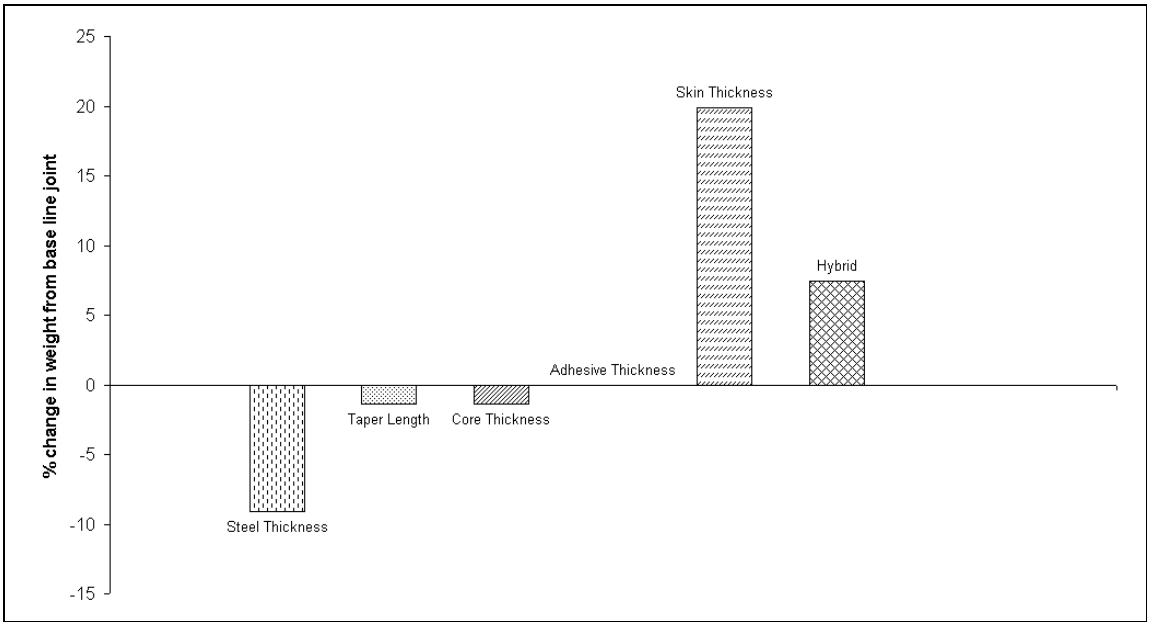

Figure 8.30 Comparison of changes to geometry on the weight of the joint from FEA

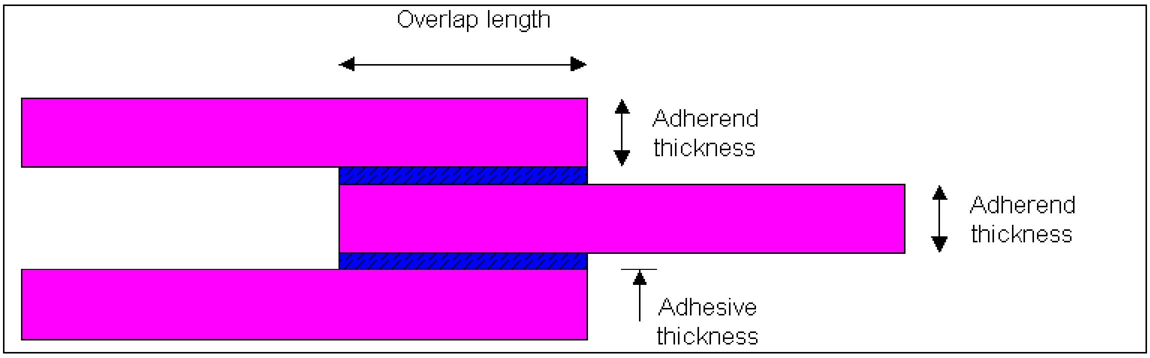

Figure 8.31 Schematic of double lap joint for optimisation test case

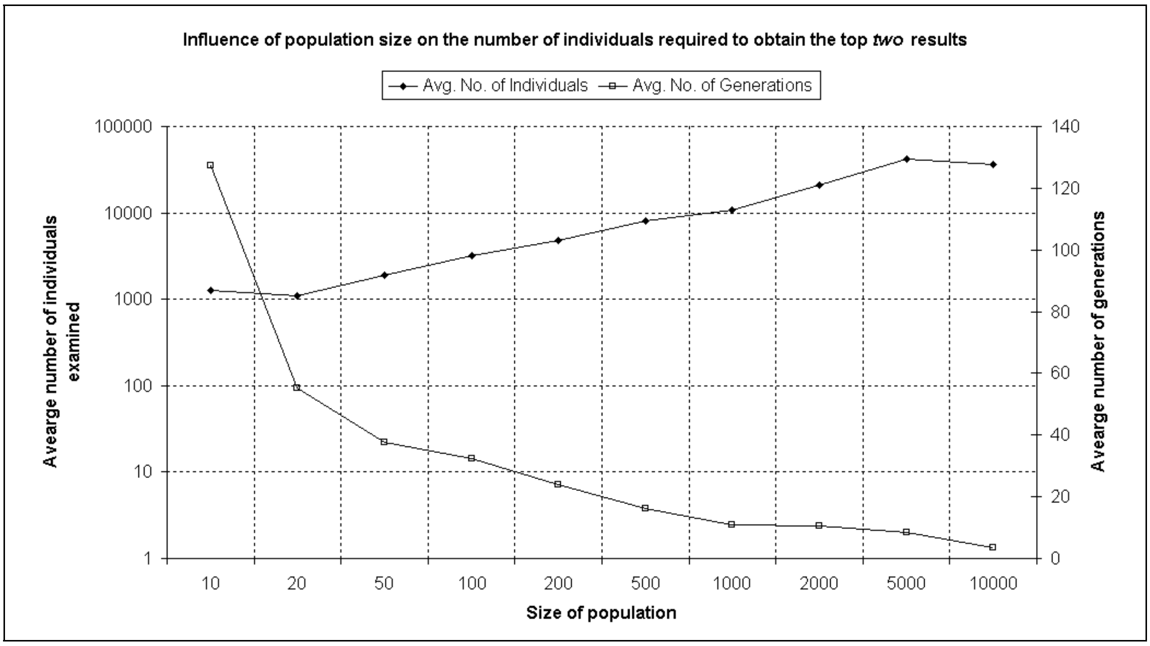

Figure 8.32 Influence of population size on GA performance

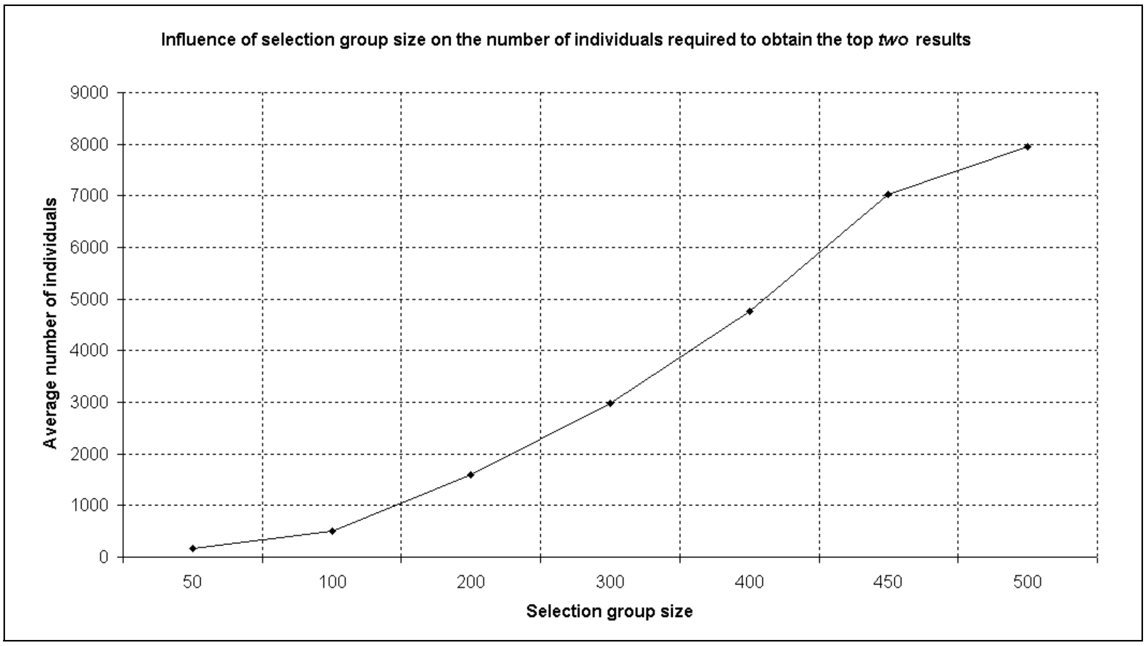

Figure 8.33 Influence of selection group size on GA performance

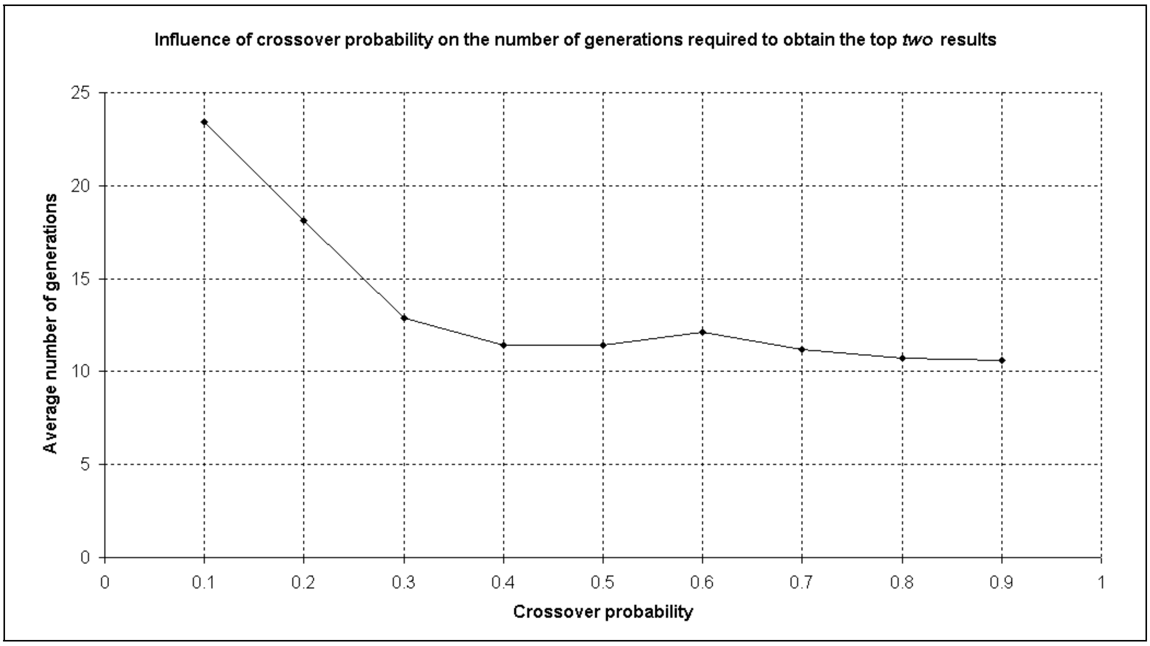

Figure 8.34 Influence of crossover probability on GA performance

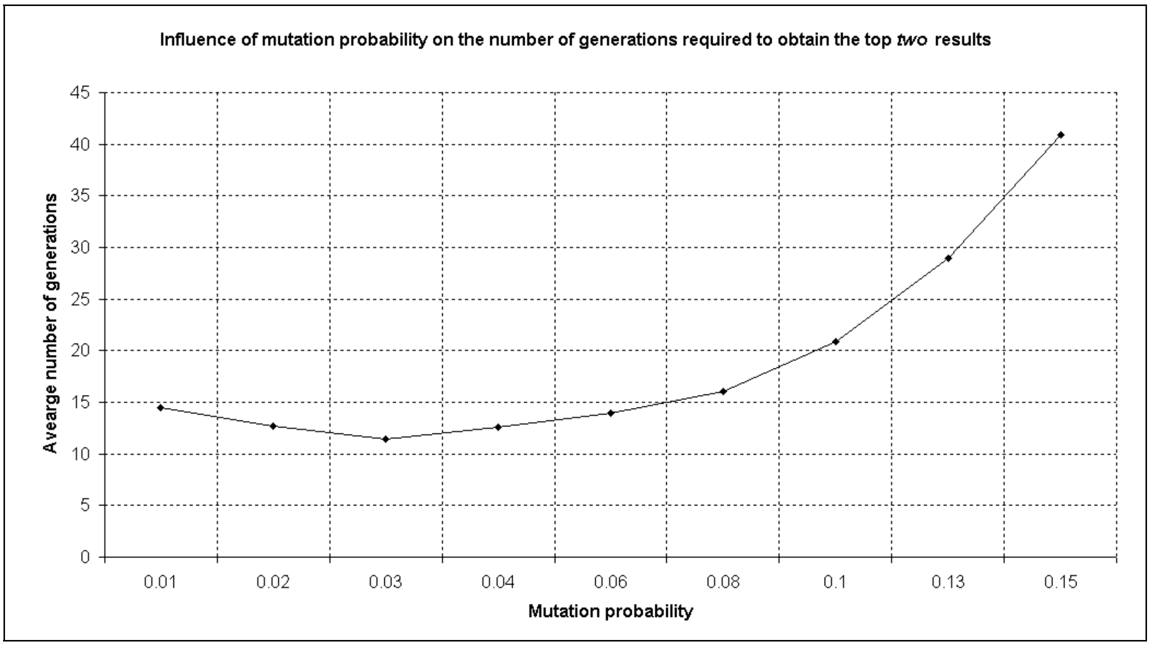

Figure 8.35 Influence of mutation probability on GA performance

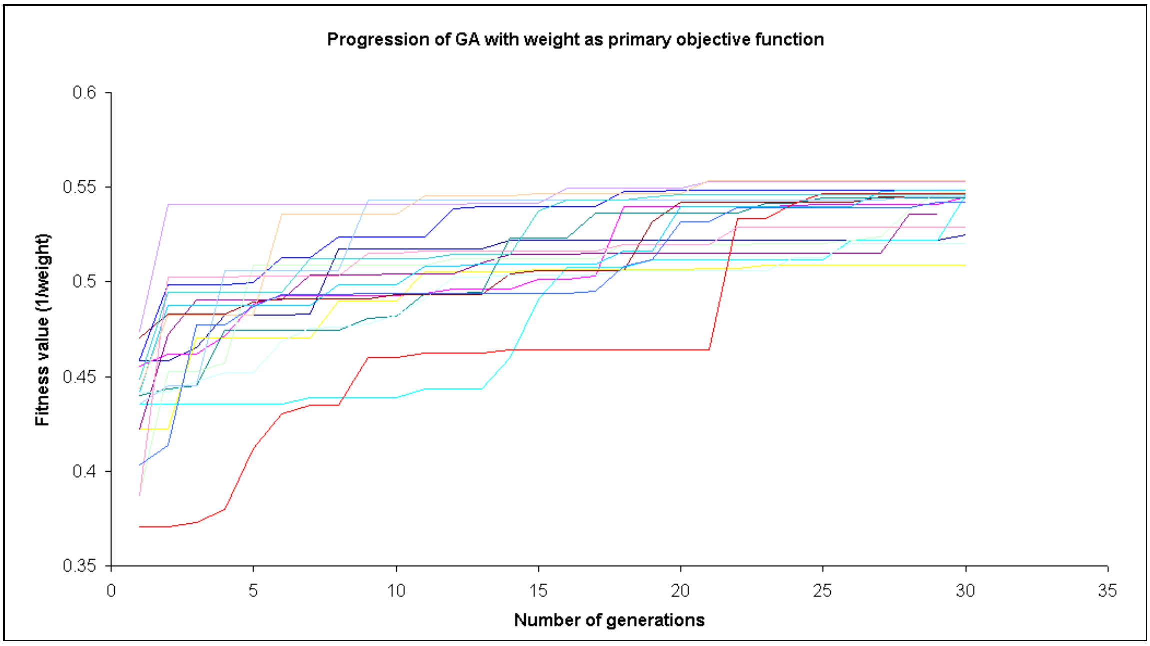

Figure 8.36 Progression of GA for repeated runs minimising weight

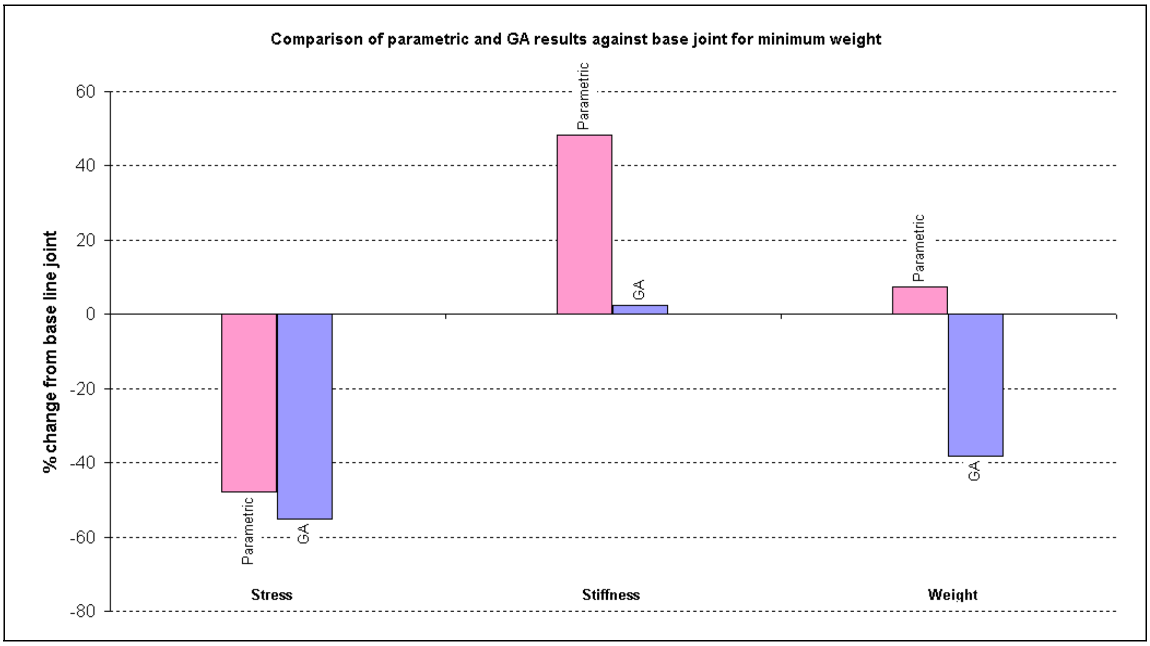

Figure 8.37 Percentage change in performance for parametric and GA results for minimum weight

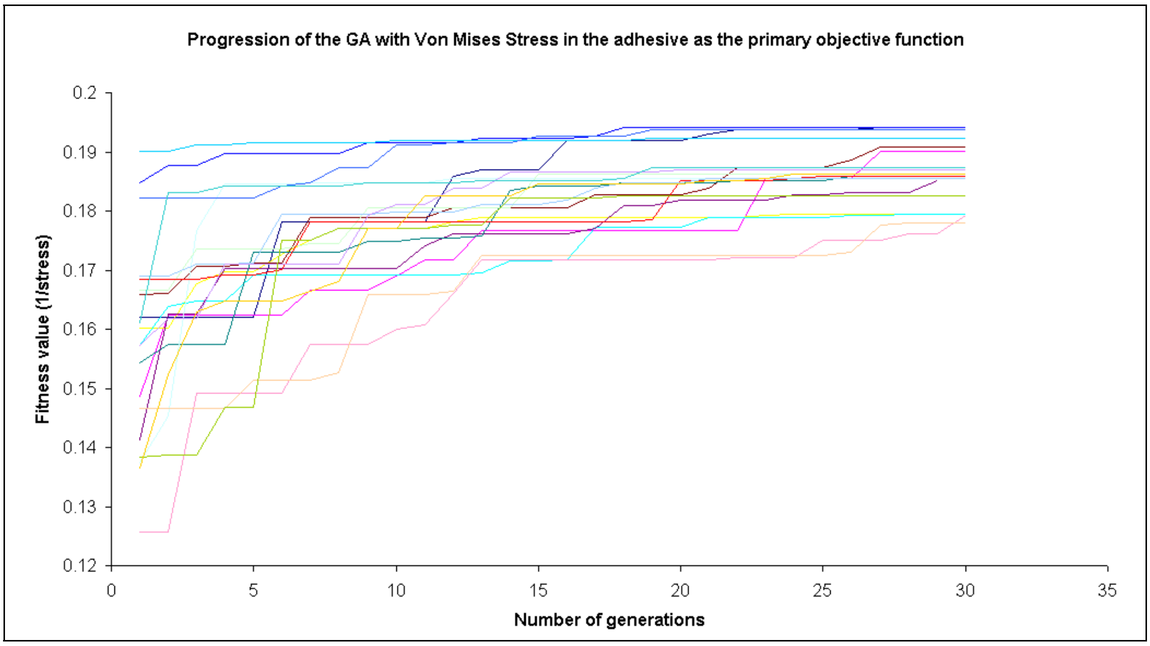

Figure 8.38 Progression of GA for repeated runs minimising Von Mises stress

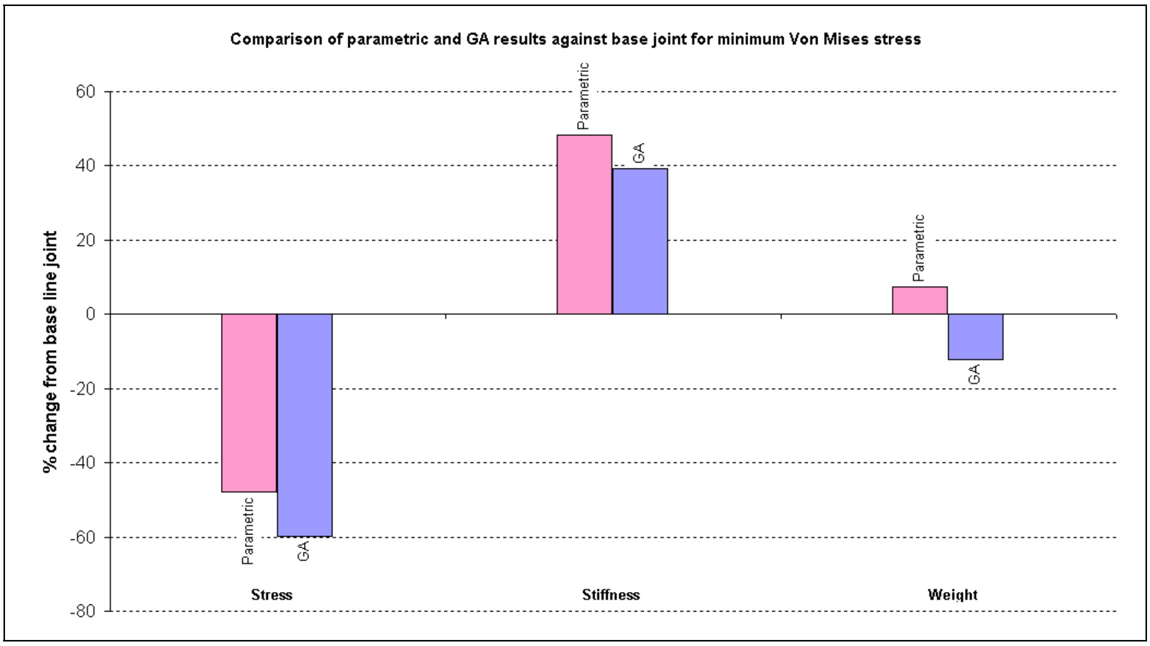

Figure 8.39 Percentage change in performance for parametric and GA results for minimum Von Mises stress

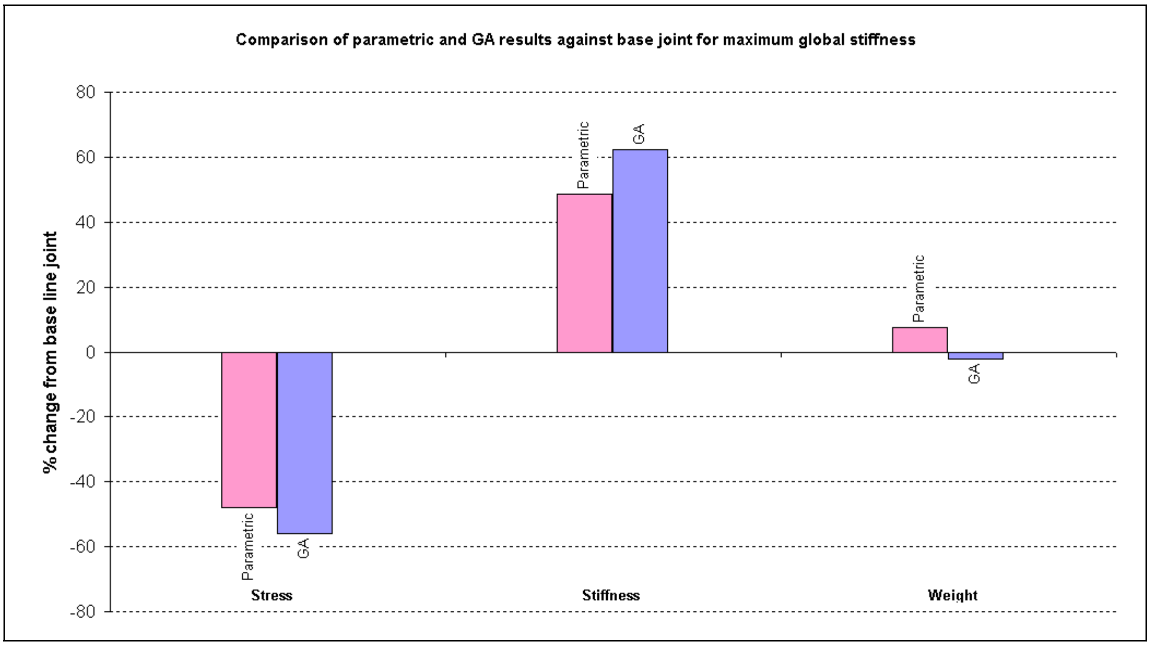

Figure 8.40 Percentage change in performance for parametric and GA results for maximum global stiffness

Appendix I General composite materials

Nature was the first producer of fibre-reinforced structures. A tree, for example, consists of long and strong cellular fibres running along the length of the trunk and branches parallel to the direction of the principal stresses. To this day wood remains one of man’s major structural materials. However, due to fibrous materials being anisotropic, they require much more complex analysis techniques to evaluate the strength or load carrying capabilities of a structure fabricated in this material. However, it is possible to design a composite material and a structure simultaneously resulting in a structure that can be more weight efficient than its metallic equivalent for a relatively small increase in cost [93].

Composite materials can be defined as the combination of two or more materials to create a single material that contains the properties of the individual components plus a number of additional properties associated with the combination. Traditionally, ships built using wooden timbers laid on a steel sub-frame were classed as composite ships. These ships were taking advantage of the formability and existing construction knowledge of wooden planking to provide the watertight outer skin and combining it with the strength and durability of a system of steel frames to provide ships that were both stronger and more durable.

Composite materials in the sense of fibre reinforced plastics began with the invention of the first real plastic ‘celluloid’ by John Wesley Hyatt in the United States of America in 1868. It wasn’t until 1909 that thermoset polymers were developed to rival the cellulosics that had dominated the plastics industry up until then. From 1905 to 1909 Dr. Leo H. Baekeland was working on phenol-aldehyde reactions, which were known about for a number of years. Mixing phenol and formaldehyde produced a condensation reaction, which in turn produced a hard, insoluble resin. However, at this time it was practically useless, as it could not be combined with any other materials. Baekeland used catalysts to control the condensation reaction and stop it at intervals to allow mixing with other materials before restarting the reaction. He patented this method for using the phenol-aldehyde reaction. This was essentially the first thermoset resin and is now known as a phenolic resin. The General Bakelite Company was started in 1910 and in 1922 it joined forces with Redmanol

Chemical Products Company before finally being bought by the Union Carbide and Carbon Corporation in 1939 marketing the Bakelite product. Initially the General Bakelite Company was the sole supplier of resins to the high-pressure laminators.

However, it was soon discovered that the resins, on their own, were too brittle and flexible to be used for structural members. In 1920 layers of Kraft paper were impregnated with phenolic resin resulting in the well-known product Formica. At this time the fibres being used in composite materials included papers and flax fibres and consisted mainly of cellulose materials. Water absorption becomes a major problem when cellular fibres are used as reinforcement e.g. water absorption in wood.

In 1942, low-pressure polyester resin systems had been developed and had become commercially available. They required only 13.8 Bar, 10 times less than previously required for successful curing of the adhesive. By the end of the Second World War, glass reinforced plastic (GRP) had been successfully used in structural applications. The combination of the glass fibres and the new low-pressure curing polyester resin provided a material with very attractive mechanical properties with high strength and stiffness to weight ratios. The number of applications of FRP began to expand rapidly and were to be found in a large number of industry sectors.

The introduction of styrene into the polyester resin has the effect of reducing its viscosity making it easier to handle and also allows for cross-linking of the resin during cure without the production of by-products. These resins can therefore be moulded without the need for pressure and are commonly referred to as ‘contact’ or ‘low pressure’ resins. Polyester resins are commonly found in two forms ‘Orthophthalic’ and ‘Isophthalic’. The former is the standard economical polyester resin. However the latter is now becoming the industry standard due to its superior water resistance.

Vinyl-ester resins are chemically similar to polyester, the main difference being the location of their reactive sites at the ends of the molecular chains. This allows the whole chain to withstand larger shock loading resulting in a tougher and more durable resin than polyester. In addition, vinyl-ester resins have fewer ester groups, the benefits being superior moisture resistance as it is the ester sites that lead to moisture degradation through hydrolysis.

Epoxy resins represent the most superior resins available at present. Epoxy resins are formed from long chain molecular structures, in a similar manner to vinyl-esters, both having reactive sites at the ends of the chains. However, the reactive sites are made up from epoxy groups rather than ester groups. The absence of the ester groups means that epoxy resins have excellent water resistant properties. Epoxy resins also contain two ring groups at its centre, this provides the molecular chains and hence a resin with excellent stiffness, toughness and heat resistant properties.

Developments in the reinforcements used to increase the load carrying capabilities of the relatively brittle resin systems described have also been under continuous development. Table I.1 outlines the tensile properties of a number of commonly used fibre reinforcements. Glass fibres were created by accident by a young researcher named Dale Kleist who was trying to fuse together two blocks of glass to create a vacuum tight seal. A jet of compressed air accidentally struck a piece of molten glass producing fine glass fibres. This research was continued by the company and the process of glass fibre manufacture was patented by the well known company Owens-Corning.

Table I.1 Tensile properties of commonly used reinforcement fibres

Product	Tensile Strength (MPa)	Tensile Modulus (GPa)
C-glass	3310	68.9
E-glass	3448	72.4
R-glass	4135	85.5
S-glass	4585	85.5-86.9
S2-glass	4890	86.9
Kevlar 49	3600-4100	131
Carbon (UHM)	2000	200+
Carbon (HS)	3500	90-150

Glass-fibre has since been woven or stitched into a huge range of cloths and fabrics with different fibre directions and mechanical properties. In addition, to the cloths and fabric, variations, there have been developments in the chemical make-up of the glass used to produce the fibres resulting in E-glass, C-glass, S-glass, R-glass and T-glass products, all with different mechanical and physical properties.

Aramid fibres, more commonly referred to by DuPont’s trade name ‘Kevlar’, are man made organic polymers. All aramid products have good resistance to impact, however, their compressive strength is similar to E-glass. In addition, to good tensile and impact mechanical properties, aramid fibres have good resistance to abrasion, chemical and thermal degradation. However, they do degrade slowly when exposed to ultraviolet light.

Carbon fibres provide the composite industry with the highest specific stiffness fibre commercially available. The fibres are grouped according to their modulus value. However, they are also the most expensive reinforcement product.

The present research does not attempt to extend the knowledge or technology of the materials currently available or commonly used to manufacture composite laminates, but to use the more economical products, namely E-glass fibre and vinyl-ester resin to extend the applications of composite materials.

Appendix II Publications

Boyd, S.W., Blake, J.I.R., Shenoi, R.A., and Kapadia, A., "Integrity of hybrid steel-to-composite joints for marine application," *Journal of Engineering for the Maritime Environment, Proceedings of the Institution of Mechanical Engineers, Part M*, **218**(M4):235-245, 2004.

Integrity of hybrid steel-to-composite joints for marine application

S W Boyd[1]*, **J I R Blake**[1], **R A Shenoi**[1] and **A Kapadia**[2]
[1]School of Engineering Sciences, University of Southampton, Southampton, UK
[2]Composite Technology Centre, VT Group (Halmatic), Portsmouth, UK

Abstract: There are many instances where the use of weight-saving polymer composite material for an entire structure is either too complex, too expensive or unfeasible. In these circumstances the use of a hybrid structure can incorporate the benefits of traditional (e.g. steel) construction coupled with the advantages of composite materials [e.g. glass-reinforced polymers, glass-reinforced plastic (GRP)] in weight-critical areas. A number of studies have been carried out on the static strength of hybrid steel-to-composite joints.

In the present study, an experimental investigation was undertaken into the fatigue life characterization of a hybrid steel-to-GRP joint. It was found that the fatigue data correlated well with the statistical-based Weibull cumulative distribution function. In addition, post fatigue (in-plane and out-of-plane) residual strength tests were undertaken to ascertain the joint structural performance after cyclic loading. Finite-element-based progressive damage analyses incorporating damage initiation and propagation characteristics, showed good correlation with experimental results.

Keywords: composite materials, hybrid steel-to-composite joints, fatigue life characterization, residual strength tests

1 INTRODUCTION

The application of hybrid metal-to-composite structures has been gaining momentum over the last number of years and their use can be found in a widening number of engineering disciplines. One initial use of metal-to-composite joints was in the repair of aluminium space frames with composite patches in the aerospace industry. With the large amount of experience in this field [**1**–**4**], the study of composite hybrid joints has been extended to applications in the land transport [**5**, **6**] and marine industries [**7**–**9**].

In the marine industry, reduced hull and superstructure weight increases payload for the same speed and power requirements and additionally allows for a more stable and effective operations platform for naval ships where seakeeping may be one of the prime objectives. Feasibility studies into the construction of composite superstructures for naval vessels began in the early 1980s [**9**]. Since then there has been increasing interest in the use of composite materials for naval superstructures. The French navy have implemented such a superstructure on their La Fayette class frigate in the form of a helicopter hangar [**7**]. Subsequently there has been increasing research interest in joints between steel and glass-reinforced plastic (GRP) for use in the hull–superstructure and hull–bulkhead joints [**8**, **10**–**11**].

Wright *et al.* [**8**] investigated a fibre-reinforced composite–steel connection for transverse ship bulkheads. These joints were tested in tension, compression, and lateral bending. They found that a suitable connection could be made and that symmetric rather than asymmetric joints provide better strength characteristics.

Clifford *et al.* [**10**] looked at very similar joints in lateral deflection. These specimens allowed investigation into the effect of joint geometry on structural performance, specifically the impact of the length of the steel insert on bending strength. By increasing the length of steel insert penetration into the core material the resulting failure moved from core failure to yielding of the steel.

Cao and Grenestedt [**11**] decreased the penetration of the steel insert in an attempt to both decrease the weight of the hybrid component and to reduce stress concentrations in critical areas. The failure occurred in a

The MS was received on 15 October 2004 and was accepted after revision for publication on 22 November 2004.

* *Corresponding author: Fluid Structure Interactions Research Group, School of Engineering Sciences, University of Southampton, Southampton, UK. email: sboyd@ship.soton.ac.uk*

similar manner to that observed by Clifford *et al.* [**10**] with yielding of the steel and shear failure of the core. Overall strength to failure was found to be approximately the same.

In the present study, an investigation is undertaken into the fatigue life characterization of a geometrically similar joint to those used in references [**7**–**11**]. Details of the joint are shown in Fig. 1. Although static and dynamic (shock/blast) loadings are of great importance, especially in naval vessels, it is assumed that the vessel must survive and operate for its required service life. This involves withstanding extremes of temperature and humidity cycling commonly found when operating in the Gulf/temperate regions and the day-to-day marine environment loadings such as accelerations due to wave motions. It is the latter that is discussed in the present research as being the prime generator of cyclic loading within the ship structure.

In addition, the residual strength of the joint, which is critical in terms of through-life ability of a vessel to withstand large instantaneous loading, is assessed in both axial compression and lateral externally applied bending. In-plane residual strength testing was carried out after fixed intervals of cyclic loading and out-of-plane residual strength was examined for differing fatigue crack lengths.

Numerical simulation of the static behaviour is undertaken incorporating progressive damage tools. The model is analysed using the ABAQUS suite of finite element (FE) software using Fortran-based user subroutines to implement the progressive damage analysis. Failure criteria for isotropic materials are used to identify initial failure and material property degradation is implemented to simulate the non-linear load–deflection behaviour observed in the experimental results.

2 JOINT DESIGN PHILOSOPHY

The hybrid joint used in the present study, shown in Fig. 1, is based on the design for the hangar to weather deck connections (Fig. 2) currently in service in the French navy on the La Fayette class frigates. The original joint was manufactured using hand lay-up techniques with a polyester resin. It was felt that the use of resin infusion would be an improvement both in quality of the final product and ease of mass production.

2.1 Materials

The materials used in the present study are a 3 × 1 twill weave 780 g/m^2 E-glass woven roving (Chomarat 800S4), vinylester resin (Dow Derakane 411–C50), 150 kg/m^3 balsa wood core (Baltek AL600–10 Contourcore) and 6 mm thick mild steel (D55).

The steel was delivered in its ‘black’ form, i.e. it had no weld-through primer on it. The steel surface was pretreated by shot blasting to SA2.5 standard, using chilled iron grit, G24. The steel was then acetone wiped to

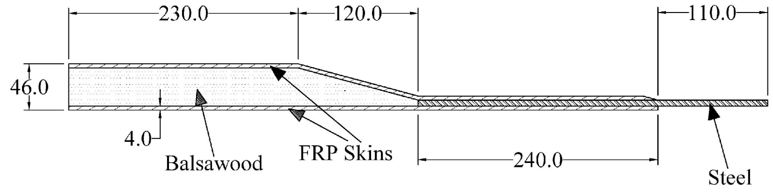

Specimen Thickness: 100mm

Fig. 1 Details of the hybrid joint used in the present study

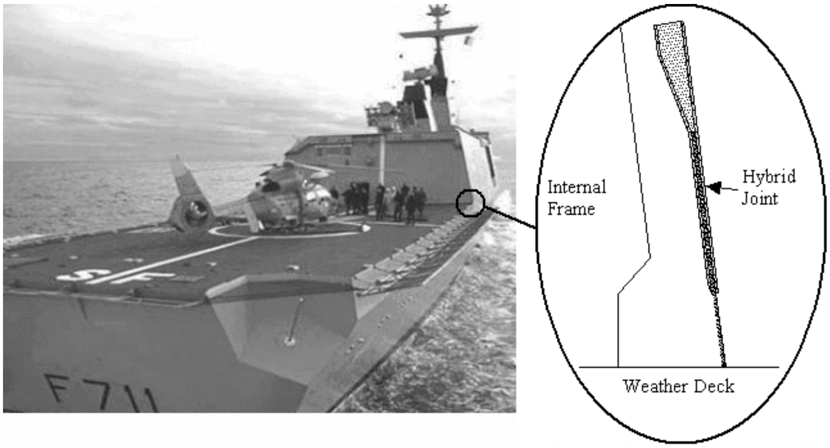

Fig. 2 Helicopter hangar on the French La Fayette class frigate (picture reproduced courtesy of DCN)

remove any debris from the blasting operation. Once the acetone had evaporated the steel was primed using catalyzed Derakane 411–45 vinylester resin. The resin was applied using a brush and the application was carried out within 4 h of shot blasting (generally accepted as an owner's requirement for paint).

2.2 Specimen manufacture

The initial step of the manufacturing process involves the surface preparation of the steel as described in section 2.1. It is generally accepted that shot blasting the bond surface prior to bonding is the most suitable method to prepare the steel for adhesive bonding.

The manufacture of the specimens was carried out as follows:

1. Apply release agent to the tool surface.
2. Lay-up distribution mat and peel-ply.
3. Lay-up eight layers of glass using adhesive spray to prevent movement of the reinforcement layers.
4. Lay-up steel and balsa.
5. Lay-up eight layers of glass using adhesive spray to prevent movement of the reinforcement layers.
6. Lay-up peel-ply, distribution mat and vacuum bag. Do not seal vacuum bag until the day of the infusion.
7. Apply 0.1 bar vacuum and ensure that reinforcement cloth is smooth and that balsa meets steel.
8. Ensure ambient temperature is above 16 °C.
9. Carry out a vacuum integrity test by applying 1 bar of vacuum and hold for 10 min. if any significant loss in vacuum (>0.07 bar) then check seal.
10. Pour resin, catalyst and accelerator into a clean bucket and mix well.
11. Release inlet and outlet clamps and allow resin to infuse the lay-up.
12. Once the resin has gelled, clamp resin inlet and leave under vacuum for 6 h.
13. Allow infusion to cure overnight and de-bag and de-mould sample.

3 EXPERIMENTAL SET-UP

3.1 Boundary conditions

It was important when testing the specimens to represent, as much as possible, the loading scenario that would be found in the full-scale structure. Due to the asymmetric geometry of the joint (Fig. 1) any load applied as a compressive force through the axis of the steel would produce a lateral bending force due to load eccentricity. Given that the design requirements on a naval vessel preclude excessive flexibility in this direction, it was felt that this was not representative of how the structure would behave in the real environment—the joint would be prevented from bending in this manner due to the internal framing of the superstructure. Figure 3 shows schematically how the specimen was constrained and loaded. In order to prevent the lateral bending, denoted in Fig. 3 by a deflection in the negative *y*-direction, a system of anti-bending guides was positioned near the steel/balsa interface. With the knowledge that fatigue tests were to be carried out in the future using the same experimental set-up, it was a concern that positioning rollers the length of the specimen to remove the lateral deflection could result in overworking of the joint through friction. While one roller would reduce the lateral deflection at the point at which it would be positioned, two rollers would ensure that the steel end of the specimen would remain in-axis, representing the boundary conditions anticipated in-service more accurately.

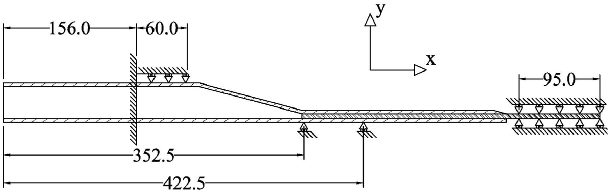

Fig. 3 Boundary conditions of the experimental specimen

The positions of the anti-bending guides were calculated using an FE analysis. The analysis involved observing the negative *y*-deflection for various roller positions. Initially the rollers were positioned equal distances either side of the steel/balsa interface (Fig. 4a). This resulted in the steel deflecting at its tip around the first of the rollers. It was observed that this roller position would lead to excessive peel forces at the steel/balsa/GRP interface resulting in premature failure. In order to prevent such bending of the steel, the rollers were positioned so as to support only the steel portion of the joint. This dramatically reduced the deformation at the rollers (Fig. 4b). Figure 5 shows the final position of the anti-bending guides.

3.2 Applied loads

The load was applied via a hydraulic ram controlled by an Instron 8800 controller. The ram was capable of producing 130 kN at maximum hydraulic pressure. Specific load was defined via a 250 kN load cell.

In the present study a compressive force was felt to be the most likely loading scenario encountered in the real structure. On a naval vessel, the use of this particular joint has direct application to the problem of mounting a lightweight GRP superstructure (typically a helicopter hangar) to a steel deck (Fig. 2). It is assumed that the hangar structure does not contribute to the global bending strength of the hull girder due to its length being considerably smaller than the overall length of the hull, and it is decoupled from the hull girder due to the differences in elastic modulus of the materials used for the hull and hangar. Therefore, only forces induced by

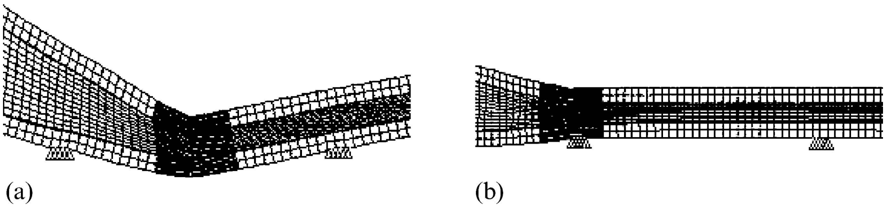
(a) (b)

Fig. 4 (a) Anti-bending guides equidistant from steel/balsa interface (scaled deflection). (b) Anti-bending guides supporting only the steel (scaled deflection)

Fig. 5 Position of anti-bending guides

the structure's own weight and accelerations due to motion are considered significant. With the vessel at rest and in calm water, the joint will experience only a compressive force equal to the apportioned weight of the hangar structure and any ancillary equipment mounted on it. The generation of tensile forces on the other hand, while unlikely, is not inconceivable. When the vessel is underway and is sailing in seas rather than calm water, it will experience motions in all six degrees of freedom. These motions translate to the connection between the hull of the vessel and the hangar superstructure. Assuming the hangar is located on the after-deck of the ship, for the connection to experience a tensile load or at most a relief of the compression loading due to the hangar's structural weight, the aft end of the ship needs to experience one negative g for weightlessness or greater for tensile load. This scenario would be possible if the aft end of the ship were in free fall from coming off the back of a wave, but in reality this is highly unusual.

It is feasible that either the port or starboard side of the structure would be subjected to one or more negative g during roll. The size of the tensile force would be related to the position of the neutral axis of the hangar structure and the roll rate, but again it is highly unlikely that one negative g will be experienced in reality and only a combination of roll and heave may in extreme circumstances produce enough acceleration to cause the structure to be weightless.

From the discussion of realistic loading scenarios described above, the most likely force to be encountered by the hybrid metal composite joint is, therefore, compressive and to this end the testing of the fatigue life of the joint has been carried out in compression.

3.3 Test programme

The first phase of testing of the hybrid joint is to determine the ultimate static compressive strength of the joint. This will identify the maximum load amplitude for the fatigue test phase.

Fatigue life characterization of the hybrid joint at various load amplitudes in compression load cycles is carried out in the second test phase. A zero-compression test allows for the most extreme form of cyclic compression loading for a given mean load level and the greatest flexibility in the choice of load amplitude. Through characterizing the fatigue life, the endurance limit of the hybrid joint can be determined as well as identifying the number of cycles (N) to failure for the subsequent axial (loading applied in the plane of the steel insert) residual strength tests.

The third test phase investigates the residual strength of the hybrid joint. Two tests were carried out in this phase. The first was an axially compressive residual strength test where specimens were prepared by fatigue cycling to a fraction of the total number of cycles to failure for a given load amplitude. The second residual strength test was carried out in fully encastred four-point bending where, in this instance, the specimens were prepared by fatigue cycling axially at a fixed load amplitude to produce cracks of differing lengths.

4 RESULTS

4.1 Static testing

The specimens tested for static strength were loaded under position control to pick up any stress relief, the rate of deflection set to approximately 0.5 mm/min. Ultimate compressive failure occurred at 108 kN. It is known that any axially loaded joint will develop high stress concentrations at the ends of the jointed region. In the present study additional stress concentration will be present due to the load eccentricity and subsequent internal bending (global bending has already been removed by the anti-bending guides). Thus, it is assumed that the most highly stressed region of the joint should be located at the steel/balsa interface and in particular on the flat side. It is in this region that the initial crack was observed. The crack then propagated along the steel/GRP interface on the flat side. It is expected that the cause of the initial crack is due to peel forces caused by the load path eccentricity. This crack extends due to mode I crack opening until the anti-bending guides are approached. From this point on the crack extends due to mode II shearing of the adhesive layer.

The load–deflection curve of ultimate compressive failure can be seen in Fig. 6. The ultimate compressive strength (UCS) of the joint is 108 kN, however for the purpose of maximum cyclic load levels, a nominal compressive strength (UCS_{nom}) is taken as 100 kN. The nominal value of ultimate compressive strength was chosen due to limited numbers of specimens for experimental testing statically. The 100 kN UCS_{nom} provides a conservative limit for maximum cyclic load levels and equates to an expected experimental scatter level of 8 per cent.

4.2 Fatigue life characterization

The fatigue life characterization tests carried out in this phase of the programme are outlined in Table 1. The first tests described in Table 1 were designed to assess the structural response of the joint over a long period of time, allowing for a careful observation of anticipated crack growth, stiffness degradation and energy dissipation. The lack of existent data available on these joints and the very limited number of specimens available for a pure fatigue analysis (i.e. without the residual strength testing) meant that the test matrix had to be evolutionary in nature.

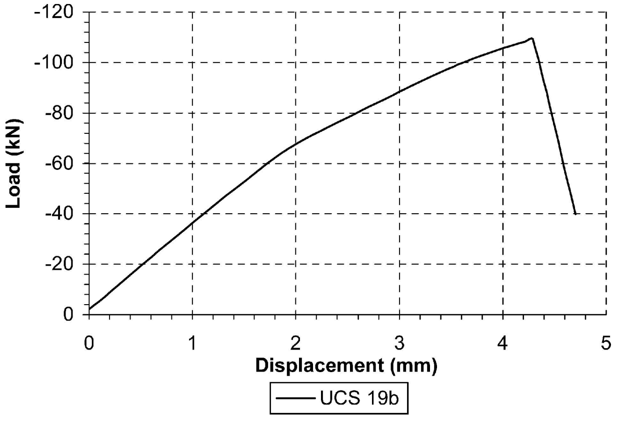

Fig. 6 Static compression load–deflection curve

Table 1 Fatigue test programme

Test No.	Description	Specimen	Load amplitude (kN)
1	17–34% UCS_{nom}	12a	8.6
2	34–69% UCS_{nom}	12b	17.2
3	0–86% UCS_{nom}	13a	43.0
4	0–69% UCS_{nom}	14a	34.4
5	0–60% UCS_{nom}	14b, 15a	30.1
6	0–51% UCS_{nom}	13b	25.8
7	0–77% UCS_{nom}	15b, 16a	38.7

During the tests, data on the load and deflection of the specimen were acquired for one cycle in every 100. The resulting output data were analysed to investigate any stiffness degradation during the fatigue life. The stiffness of the joint was obtained by fitting a straight line to the hysteresis loop of the load–deflection curve and obtaining the gradient. In addition, the area inside the hysteresis loop is plotted against the number of cycles. A change in this area indicates a release of energy, possibly due to damage within the joint [**12**].

Tests 1 and 2, from Table 1, were carried out at relatively low loads and load amplitudes. After 10^6 cycles at 1 Hz test 1 was stopped. There were no visual indications of damage. The joint was tested to failure under axially compressive static load. The resulting strength was 100 per cent of the UCS. In addition, and shown in Fig. 7, there was no significant loss in stiffness or dissipation of energy, both of which can be a measure of damage. The implication of tests 1 and 2 is that in order to obtain fatigue failure of the hybrid joint, higher mean load levels and/or higher load amplitudes would be required.

Specimen 13a (test 3) was subjected to a load amplitude of 43 kN, equivalent to 0–86 per cent of the UCS_{nom}. Figure 8 shows the stiffness change and energy release against number of cycles and unlike the low amplitude/low mean load levels of tests 1 and 2, there is a significant loss in stiffness and a corresponding increase in energy release prior to ultimate failure at approximately 1700 cycles.

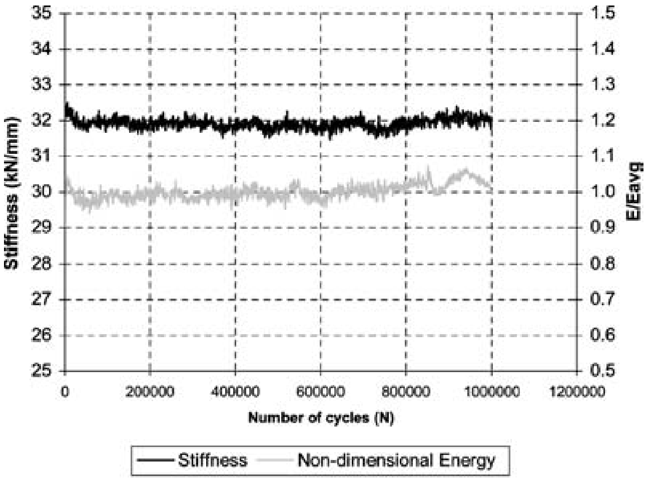

Fig. 7 Stiffness and energy results versus number of cycles for 17–34 per cent of UCS_{nom}

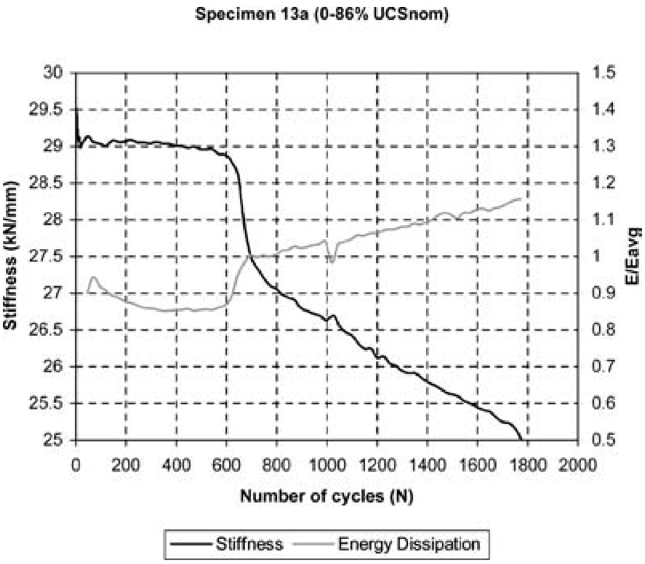

Fig. 8 Stiffness and energy dissipation of specimen 13a under 0–86 per cent UCS_{nom} fatigue cycle

The load amplitude of the fatigue tests was systematically reduced in order to obtain the fatigue endurance limit. Tests were carried out at load amplitude P_a equal to 38.7 kN, 34.4 kN, 30.2 kN and 25.8 kN. The stiffness and energy plots for all these tests exhibit a loss in stiffness and corresponding increase in energy release during their fatigue life. However, while higher load amplitudes induced total failure, the specimen subjected to the lowest load amplitude remained intact, albeit with visual signs of failure, past 3.5×10^6 cycles. Given this fact, it was assumed that the fatigue endurance limit of the hybrid joint was at, or close to, a load amplitude of 25 per cent UCS_{nom}.

In addition, the results indicate that the fatigue life of the hybrid joint is dependent on the load amplitude rather than the mean load. The specimen in test 1 was subjected to a load amplitude of 17 per cent UCS_{nom} and a mean load of 26 per cent UCS_{nom}. This applied loading did not appear to cause any damage to the hybrid joint even after 10^6 cycles. In contrast increasing the load amplitude to 26 per cent UCS_{nom} for the same mean load caused visual signs of failure (test 6) after 10^6 cycles. For only a marginal increase in mean load (approximately 30 per cent UCS_{nom}) but with a still greater increase in load amplitude to 30 per cent UCS_{nom} (test 5), complete specimen failure occurred between 10^5 and 10^6 cycles.

Figure 9 shows the fatigue life curve of the hybrid joint in terms of load amplitude P_a and number of cycles ($\log_{10} N$). A representation of the whole life of the joint may be described by a number of discrete functions. Figure 9 shows a discrete logarithmic function representing the experimental data without consideration of the static test case. The level of correlation between the chosen logarithmic function and the experimental data is high, with a variance accounted for value, VAC or R^2, equal to 0.95. A more appropriate and useful function to represent the data would be continuous in nature. A Weibull cumulative density function, $W(N)$, commonly used to describe the fatigue behaviour of composite structures [**13**, **14**] is, therefore, also presented in Fig. 9. The Weibull function is defined from the UCS and is fitted using the shape, β, and scale, η, parameters as described in equation (1). These parameters are selected so as to provide a minimum value of error through the least squares approach. The correlation between the experimental data and the function used to fit the data is very good with an R^2 value also equal to 0.95, validating the use of the Weibull function to describe the as-determined fatigue life of the hybrid joint. It must be noted that the function is based upon a fatigue load endurance limit of 25 per cent of UCS_{nom}. However, a more accurate identification of the endurance limit would be expected to provide a better curve fit to the experimental data.

$$W(N) = \text{UCS} - (\text{UCS} \cdot e^{-(N/\eta)^{\beta}}) \tag{1}$$

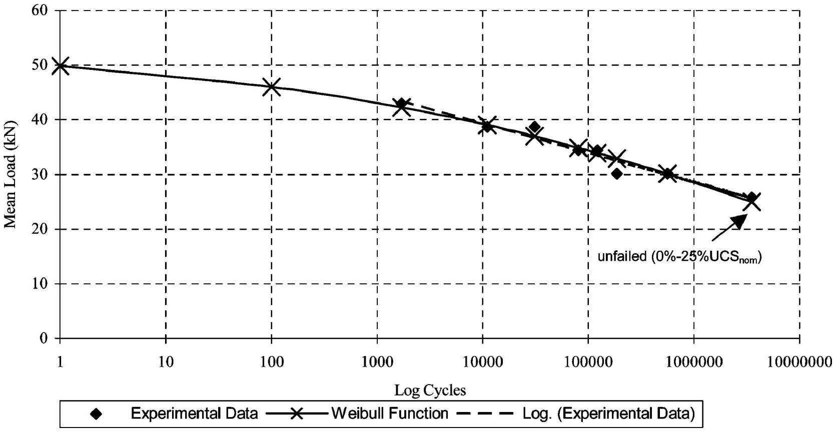

Fig. 9 Fatigue life curve for hybrid joint with respect to mean load

The curve obtained from the present study is typical of those obtained from fatigue characterization of composite materials [**17**]. The goodness of fit of the Weibull cumulative density function provides confidence in predicting the joint life and the corresponding probability density function can predict the probability of failure for any given load amplitude.

4.3 Residual strength testing

Residual strength tests allow the evaluation of remaining strength in a structure after a given life cycle. In the present study the hybrid joint has been subjected to fatigue cycles, equivalent to those used for fatigue life characterization in section 4.2, to represent a portion of the structure's life. Two residual strength tests were performed: in-plane and out-of-plane. The in-plane tests consisted of fatiguing the hybrid joint to a predetermined fraction of its number of cycles to failure, N. The joint was subsequently tested in axial compression to failure. Load and deflection were monitored. The out-of-plane tests involved fatiguing the hybrid joint in order to create a crack in the specimen of a predetermined length. The joint was then tested in four-point bending with fully encastred end conditions as shown in Fig. 10. This loading was chosen to represent an external force applied normal to the surface of the superstructure. The fully encastred end conditions provide a conservative estimate of the lateral residual bending strength of the hybrid joint and were chosen to best represent the boundary conditions expected in the full-scale structure. The steel end would be welded to the weather deck and would most likely incorporate some kind of bracket to provide additional reinforcement. The composite sandwich end would be expected to be attached to a longitudinal stiffener, both of which could be represented by fully clamped end conditions.

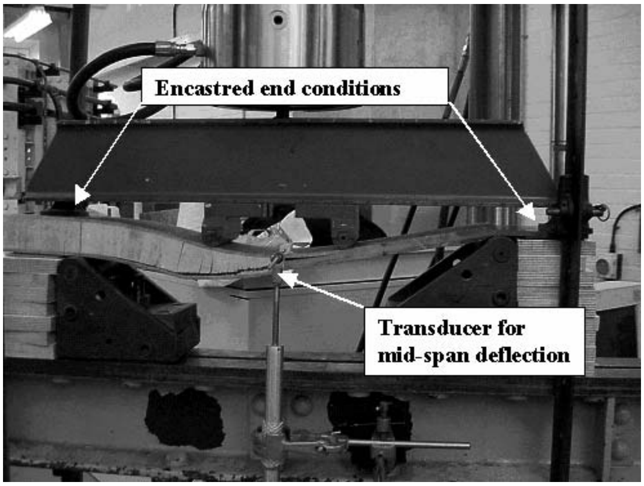

Fig. 10 Out-of-plane residual strength test set-up

It was found in the fatigue life characterization that there was significant scatter in the resultant number of cycles to failure N at a given load amplitude. This led to a lack of confidence in the choice of the N value to be used in the in-plane residual strength tests. This variability in the fatigue behaviour of the hybrid joint resulted in more damage being observed in the specimen tested to one-third ($N/3$) of its N value than the specimen tests to two-thirds ($2N/3$). However, this phenomenon is not represented in the results of the in-plane residual strength tests, where no difference was observed in the residual strength value.

While the in-plane residual strength results are not presented here it was found that the strength of a fatigued specimen was 100 per cent of the static UCS_{nom}, equivalent to 92 per cent of the single compressive strength value obtained in section 4.1, under axial loading. Following the assumption made in section 4.1, once the crack is beyond the second anti-bending guide, crack propagation extends due to mode II shearing. This implies that the shear strength of the adhesive layer dictates the failure load of the joint. Regardless of the number of cycles and extent of visible cracking, residual strength remains dependent on the shear area remaining.

The out-of-plane residual strength tests were performed on specimens containing fatigue cracks of predetermined length. All fatigue cracks were created by cycling with a load amplitude of 34.4 kN (34 per cent of UCS_{nom}) at 1 Hz. The bending tests were carried out using a 100 kN Instron test frame with an 8800 controller. Load, cross-head displacement and mid-span displacement were acquired via a Strawberry Tree data shuttle and DasyLab software. The crack lengths and corresponding residual strength results are presented in Table 2. A graph of initial joint stiffness against crack length is shown in Fig. 11. From this figure there appears to be a trend of stiffness reduction with increasing crack length. Figure 12 shows the full load displacement plot for specimen 22a (50 mm crack length). There are a number of points of stress relief in this graph and these correspond to the specific failures within the joint (description of the events in Fig. 12 are given in Table 3). The out-of-plane failure of the hybrid joint is shown graphically in Fig. 13. The results presented in Table 2 indicate that residual strength remains at 100 per cent regardless of the length of the fatigue crack. However,

Table 2 Out-of-plane residual strength test results

Specimen	Crack length (mm)	Residual strength (kN)	Mid-span deflection (mm)
23a	0	11.4	14.1
22a	50	11.4	12.0
20a	75	11.3	16.0
19b	115	12.7	20.7
23b	145	11.1	13.7

Table 3 Out-of-plane residual strength test events

Event	Observation	Load (kN)	Disp. (mm)
0 to A	Tip of balsa within the taper begins to make cracking sounds as load is increased. The GRP begins to debond from the steel on the taper side at the centre of the joint	0–11.4	0–12.0
A to B	Once the crack on the taper side (steel/GRP interface) exceeds a critical length, load is released as the GRP/balsa interface parts along the length of the taper on the taper side	11.4–7.9	12.0–12.7
B to C	The remaining balsa outside the taper region is put under stress as the load rises	7.9–10.1	12.7–19.9
C to D	The GRP/balsa interface parts along the entire length of the interface on the taper side	10.1–6.9	19.9–22.3
D to E	Load rises over a large increase of displacement as the existing fatigue crack is opened and increased by a further 10 mm	6.9–10.3	23.3–46.2

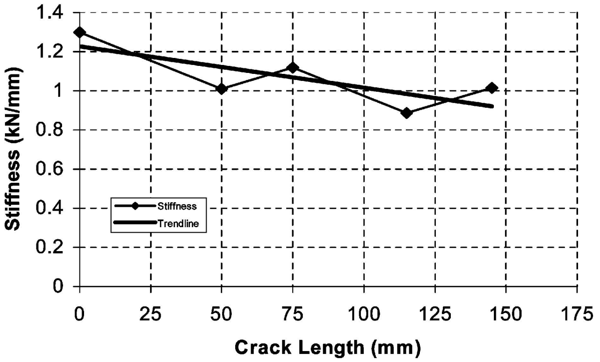

Fig. 11 Initial bending stiffness against crack length

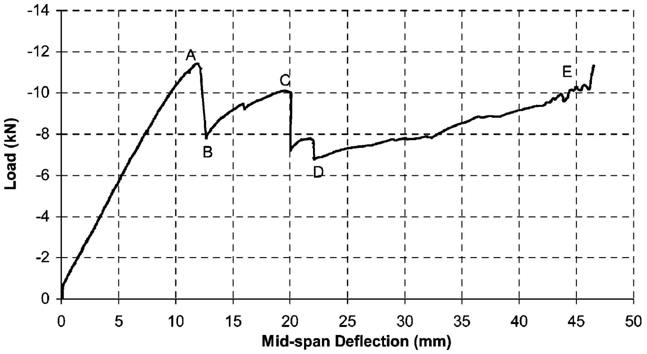

Fig. 12 Load displacement for residual strength test containing a 50 mm crack

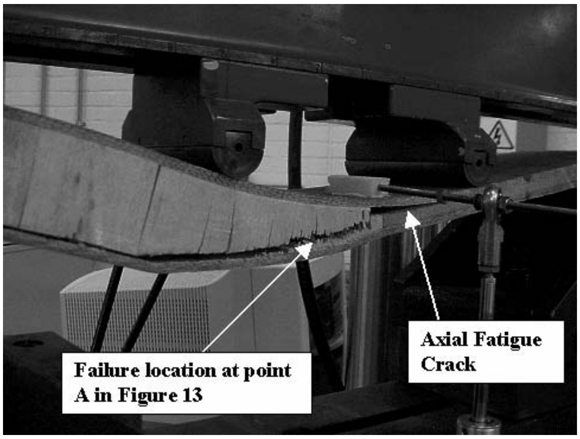

Fig. 13 Failure of joint in four-point bending

due to the joint being fully encastred, the steel near the end clamp yields. This causes a peel stress at the steel end of the GRP overlap on the flat side and begins a debond at this interface. If the fatigue crack were sufficiently long that the fatigue crack and the bending crack resulted in a complete debond of the GRP/steel interface on the flat side, the stiffness and hence the ultimate strength of the joint might be reduced. However, with the fatigue crack tip being sufficiently far away from the end of the overlap, and limitations in the experimental test rig, the two cracks did not converge hence the joints all fail due to a debond between the GRP and balsa on the taper.

5 NUMERICAL MODELLING

In an attempt to more clearly understand the failure mechanisms within the hybrid joint and to observe and predict the damage progression, a numerical model with the facilitation for progressive damage modelling (PDM) was developed. The model analyses the stresses within the increasingly loaded structure and if necessary readjusts local stiffness according to predefined failure criteria. This tool was developed to look at static failure of the joint and to take into account the non-linear nature of the load–deflection relationship observed from experiment.

5.1 General

Numerical modelling of the hybrid joint is carried out using the finite element package ABAQUS 6.2. The joint is divided into four distinct areas: GRP, balsa, steel and the resin-rich layer between the steel and GRP substrates. In the context of this work this resin-rich layer is defined as the adhesive layer. The PDM-user subroutine is only used to define the material properties and stresses for the adhesive layer as it was observed from the experimental tests that the joint failure occurred only in this region.

The mechanical properties of each region are defined in Table 4, where the x, y and z subscripts refer to the in-plane, through thickness and out-of-plane material

Table 4 Material properties for numerical model

	Material			
Property	GRP	Balsa	Adhesive	Steel
E_x (MPa)	20 600	56.951	2944.7	209 000
E_y (MPa)	6770	2965	2944.7	209 000
E_z (MPa)	20 600	56.951	2944.7	209 000
G_x (MPa)	3030	147	–	–
G_y (MPa)	3030	147	–	–
G_z (MPa)	3030	147	–	–
ν_{xy}	0.231	0.01	0.36	0.29
ν_{xz}	0.171	0.23	0.36	0.29
ν_{yz}	0.231	0.24	0.36	0.29
σ_T (MPa)	–	–	50	–

directions of the laminate, respectively. The model is constructed using eight-node quadrilateral, solid elements. Due to the joint's geometry the analysis has been simplified into a two-dimensional (2D) plane stress with thickness problem. The boundary conditions for the numerical model were kept as close as possible to those used experimentally, see Fig. 2.

5.2 Linear response

A linear analysis was conducted to assess the correlation between initial experimental and numerical stiffness of the joint. The hybrid structure was subjected to a global displacement of 4.5 mm with a resultant load of 150 kN, considerably higher than the failure load achieved experimentally. However, good correlation between experimental and numerical stiffness was achieved in the linear region. There was a clear point of divergence between the results at a deflection of approximately 2.0 mm. Based on this result it was felt that a non-linear material model would take into account the loss in global stiffness of the joint at higher deflections.

In addition the linear model has been used to increase understanding of the failure mechanisms of the hybrid joint. It was observed during the experimental results that failure, during the in-plane testing, proceeded along the flat side of the joint at the interface between the steel and the GRP from the centre to the steel end. The linear numerical model indicates that the area of highest stress is concentrated at the same location. By introducing a progressive damage model the path of failure can be modelled and compared with that observed experimentally.

For the out-of-plane residual strength numerical model the location of the major stress concentration is also located at the interface of the steel, GRP and balsawood on the flat side. By removing a given number of resin elements in the adhesive layer to represent the presence of a fatigue crack, the stress concentration re-locates in the adhesive as the debonds appear. With just the fatigue crack on the flat side of the GRP/steel interface the major stress concentration is located at the GRP/steel interface on the taper side. Once the crack extends along this interface the major stress concentration moves to the GRP/balsa interface on the taper side. This is the location of the first of the stress relief events described in Table 3. Figure 14 shows the location of the stress concentration in the numerical model with cracks on both GRP/steel interfaces.

5.3 Non-linear material model

Implementation of the non-linear material model involved the inclusion of a 'user subroutine' to define material properties and hence stresses in each of the elements of interest.

For any chosen Young modulus and Poisson ratio used to define the isotropic nature of the adhesive layer, the incremental stress can be calculated using the equation

$$\{\sigma\}_N = [\mathbf{C}]_N \{\varepsilon\}_N \tag{2}$$

where N is the increment number and $[\mathbf{C}]$ is the constitutive matrix of material properties. The total stress in the element is given by

$$\{\sigma\}_{\text{total}} = \sum_{i=1}^{N} \{\sigma\}_i \tag{3}$$

5.3.1 Damage modelling

In order to assess any possible damage to the adhesive layer due to incremental loading the resultant stresses obtained from equation (2) can be analysed using well-known failure criteria for isotropic materials such as maximum stress/strain, maximum shear stress or shear strain energy theories.

In the present study the shear strain energy theory, more commonly known as the von Mises failure criteria [**15**], is used. This states that failure will occur if the strain energy exceeds the strain energy at failure under

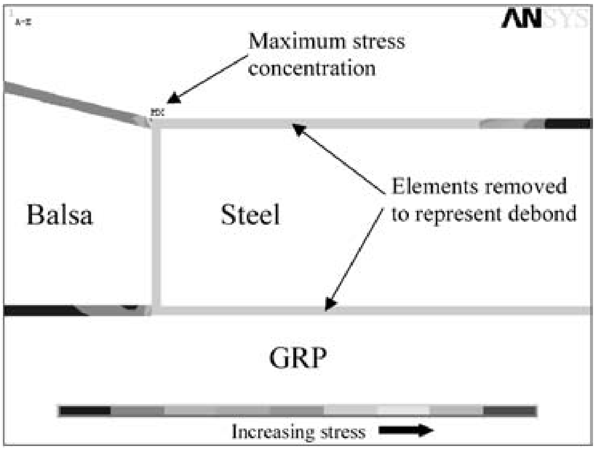

Fig. 14 Position of major stress concentration after steel/balsa interface failure in four-point bending

simple tension and from basic theory [**16**] is defined as

$$\sqrt{\sigma_1^2+\sigma_2^2-\sigma_1\sigma_2} \geqslant \sigma_t \tag{4}$$

where σ_1 and σ_2 are the major and minor principal stresses, respectively, and σ_t is the tensile strength of the resin used in the adhesive layer. In the present study the tensile strength of the resin is used to evaluate failure according to equation (4) and is given in Table 4.

5.3.2 Material property degradation

It can be stated for all but the most brittle materials that, when the stress in a material causes the failure criteria to be exceeded, the reduction in material properties is not instantaneous. Tests carried out to British Standard BS 2782 (Part 3, Methods 320A–320F) were conducted on bulk castings of the adhesive. The results indicate that the adhesive does not behave in a purely brittle manner. Historically there are three commonly used material degradation models: instantaneous [**17**], gradual [**18**] and constant stress [**19**]. The examination of the global stiffness reduction of the hybrid joint appears to tend toward a gradual reduction model. However, in order to define this scenario within the user subroutine of material property definition, the gradual reduction method results in a negative Young modulus, ultimately causing numerical problems associated with the global finite element equations. To overcome this the stress in the element is reduced to represent a negative Young modulus. This can be carried out using either a linear or non-linear reduction model.

By investigating the effect of differing functions for stress reduction using a piecewise linear system, an approximation to the true function can be identified. Three points can be determined from knowledge of the strain in each element at the point at which the failure criteria are exceeded. The first point is where the initial failure criteria are exceeded and the third is the complete failure point. The middle point defines the approximate function shape (see Fig. 15).

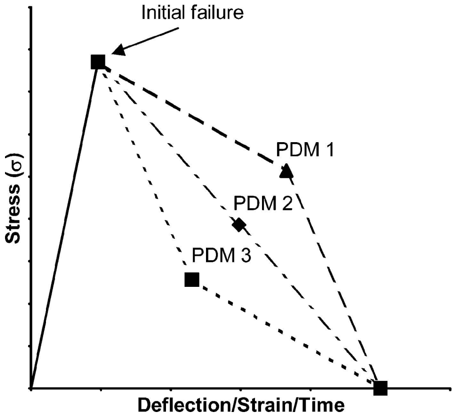

Fig. 15 Stress reduction models

5.4 Numerical results

It should be noted that progressive cracks may have an effect on the behaviour of the structure: this is modelled normally using fracture mechanics principles. In the context of this paper, however, the focus is on strength issues and failure based on strength methods and criteria. The results obtained from the numerical model are given in Fig. 16. This graph shows the experimental load–deflection curve compared with a linear finite element result and three non-linear results. The non-linear results have used the three differing stress reduction models as shown in Fig. 15.

As discussed in section 5.2, there is a clear point of divergence between the predicted linear response and experimental observation at 2 mm deflection. The non-linear PDM successfully identifies this point of divergence for all three stress reduction models. Furthermore, beyond a global displacement of 2 mm the correlation between the presented non-linear numerical results and the experimental result, depending on the choice of post-failure material function (see Fig. 15), represents a compromise between excellent prediction of failure load and excellent prediction of failure strain.

The progressive damage model clearly indicates the path of failure in the joint as the stresses in the adhesive layer combine to exceed the failure criteria. Figure 17 shows the position of the first point of failure of the joint. Its location is at the interface of the steel, balsawood and GRP on the flat side of the hybrid joint. It is in this location that the first experimentally observed crack occurs, subsequently leading to the GRP/steel debond. In the case of the tested specimens subsequent increased loading led to crack propagation along the flat side in the steel/GRP interface. The numerical model successfully identified this phenomenon.

6 CONCLUSIONS

In this study the fatigue life for a hybrid steel-to-GRP joint has been characterized. It was found that a Weibull cumulative density function correlated well with experimental data for the hybrid joint, a function commonly associated with the description of the fatigue life of composite materials. Confident use of the Weibull function in relation to the structural performance of the hybrid joint allows for fatigue life prediction and determination of the probability of failure for a given load amplitude.

The axial residual strength tests carried out on the hybrid joint indicate that damage caused by in-plane fatigue loading has little influence on the ultimate failure load of the joint in axial compression. In addition there is very little reduction in stiffness of the joint observed in lateral bending with increasing axially induced fatigue damage.

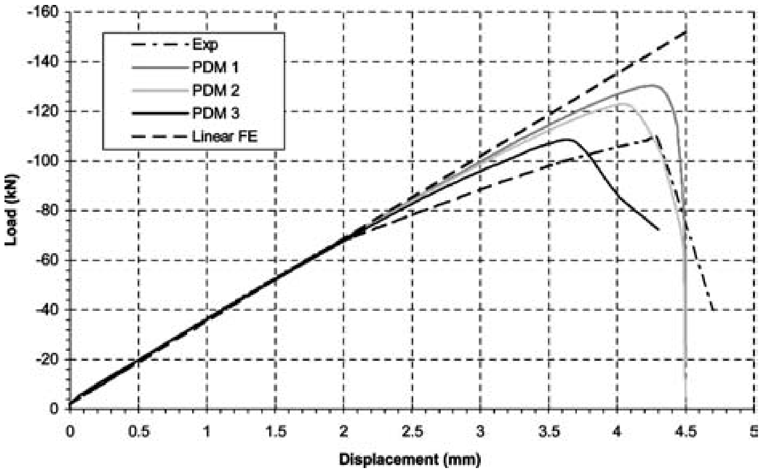

Fig. 16 Numerical versus experimental load–deflection curves

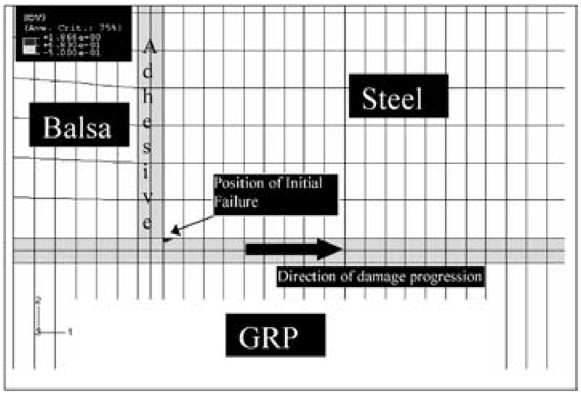

Fig. 17 Position of initial failure and direction of damage propagation (within adhesive layer at the interface between GRP/steel/balsa, flat side of specimen)

The numerical analyses provide insight into the failure mechanisms present in the hybrid joint. The linear analysis indicated a very good correlation of experimental and numerical joint stiffness for the linear portion of the load–deflection curve. The progressive damage model accurately represented the displacement at which the load–deflection curve becomes significantly nonlinear.

The progressive damage model, in association with the three presented stress reduction models provided and depending on the choice of stress reduction model, provides excellent agreement with experiment of either failure load or failure strain. Continuing investigation into more appropriate stress reduction models would lead to a better compromise between prediction of both ultimate failure load and strain.

ACKNOWLEDGEMENTS

The authors gratefully acknowledge the EUCLID RTP3.21 Programme and the UK Ministry of Defence for funding of this research. Discussions with project partners, particularly colleagues at QinetiQ, Vosper Thornycroft (VT), University of Newcastle upon Tyne and Det Norske Veritas (DNV) have been very beneficial to the authors' work.

REFERENCES

1 **Baker, A.** Repair of cracked or defective metallic aircraft components with advanced fibre composites—an overview of Australian work, *Composite Structure*, 1984, **12**, 153–181.

2 **Baker, A., Chester, R., Davis, M., Roberts, J.** and **Retchford, J.** Reinforcement of the F-111 wing pivot fitting with a boron/epoxy doubler system—materials engineering aspects, *Composites*, 1993, **24**, 511–521.

3 **Ong, C. L.** and **Shen, S. B.** Some results on metal and composite patch reinforcement of aluminium honeycomb panel, *Theor. Appl. Fracture Mech.*, 1991, **16**(2), 145–153.

4 **Naboulsi, S.** and **Mall, S.** Characterisation of fatigue crack growth in aluminium panels with a bonded composite patch, *Composite Structs*, 1997, **37**(3/4), 321–334.

5 **Shin, K. C., Kim, Y. G., Lee, D. G.** and **Choi, J. M.** Adhesively bonded lap-joints for composite-steel shell structure of high-speed vehicles, *Composite Structs*, 1997, **38**(1–4), 215–227.

6 **Choi, J. H.** and **Lee, D. G.** Torque capacity of co-cured tubular lap joints, *J. Composite Mater.*, 1997, **31**(14), 1381–1396.

7 **Le Lan, J. Y., Parneix, P.** and **Gueguen, P. L.** Composite material superstructures, International Conference on *Nautical Construction with Composite Materials*, Paris, France, 1992.

8 **Wright, P. N. H., Wu, Y.** and **Gibson, A. G.** Fibre reinforced composite-steel connections for transverse ship bulkheads, *Plast., Rubb. Composites*, 2000, **29**(10), 549–557.

9 **Mouritz, A. P., Gellert, E., Burchill, P.** and **Challis, K.** Review of advanced composite structures for naval ships and submarines, *Composite Structs*, 2001, **53**, 21–41.

10 **Clifford, S. M., Manger, C. I. C.** and **Clyne, T. W.** Characterisation of a glass-fibre reinforced vinylester to

steel joint for use between a naval GRP superstructure and a steel hull, *Composite Structs*, 2002, **57**(1–4), 59–66.

11 **Cao, J.** and **Grenestedt, J. L.** Test of a redesigned glass-fibre reinforced vinyl ester to steel joint for use between a naval GRP superstructure and a steel hull, *Composite Structs*, 2003, **60**, 439–445.

12 **Shenoi, R. A., Read, P. J. C. L.** and **Hawkins, G. L.** Fatigue failure mechanisms in fibre-reinforced plastic laminated tee joints, *Int. J. Fatigue*, 1995, **7**(6), 415–426.

13 **Burman, M.** and **Zenkert, D.** Fatigue of foam core sandwich—1: undamaged specimens, *Int. J. Fatigue*, 1997, **19**(7), 551–561.

14 **Lee, J., Harris, B., Almond, D. P.** and **Hammett, F.** Fibre composite fatigue—life determination, *Composites Part A*, 1997, **28A**, 5–15.

15 **von Mises, R.** Mechanik der fasten Koerper im plastisch deformablen Zustand, *Goettinger Nachrichten, Math-Phys*, 1913, 582.

16 **Megson, T. H. G.** *Structural and stress analysis*, 1996 (Arnold, London, UK).

17 **Murray, Y.** and **Schwer, L.** Implementation and verification of fibre-composite damage models, *Failure Criteria and Analysis in Dynamic Response*, 1990, AMD 107, pp. 21–30 (ASME).

18 **Petit, P. H.** and **Waddoups, M. E.** A method of predicting the nonlinear behavior of laminated composites, *J. Composite Mater*., 1969, **3**, 2–19.

19 **Hahn, H. T.** and **Tsai, S. W.** On the behaviour of composite laminates after initial failures, *Astronaut. Aeronaut*., 1983, **12**, 58–62.